



Instituto de Física de Cantabria
Departamento de Física Moderna
Universidad de Cantabria

Influence of active galactic nuclei properties on their optical classification

**Influencia de las propiedades de los núcleos
galácticos activos en su clasificación óptica**

Memoria presentada para optar al título de Doctor en Ciencia y
Tecnología por la Universidad de Cantabria

por

Lorenzo Barquín González

Bajo la supervisión de Silvia Mateos Ibáñez y Francisco J. Carrera Troyano

Declaración de autoría

Silvia Mateos Ibáñez

Doctora en Ciencias Físicas e Investigadora Científica del Consejo Superior de
Investigaciones Científicas

y

Francisco J. Carrera Troyano

Doctor en Ciencias Físicas y Catedrático de la Universidad de Cantabria

CERTIFICAN que la presente memoria

Influencia de las propiedades de los núcleos galácticos activos en su clasificación óptica

ha sido realizada, bajo su dirección, por **Lorenzo Barquín González**, y constituye su tesis para optar al grado de doctor por la Universidad de Cantabria. Consideran que esta memoria contiene aportaciones suficientes para constituir la tesis doctoral del interesado. Asimismo, emiten su conformidad para que la presente memoria sea depositada y se celebre, ulteriormente, la correspondiente lectura y defensa.

En Santander, a 17 de Junio de 2024,

Fdo.: Dra. Silvia Mateos Ibáñez

Fdo.: Dr. Francisco J. Carrera Troyano

A mis padres y a Eva; que tanto me han apoyado estos años.

Agradecimientos

Hace más de cuatro años desde que comencé este viaje que es el doctorado, y algunos más desde que entre por primera vez en el IFCA a estudiar los AGNs. Desde entonces, han pasado muchas cosas: una pandemia mundial, guerras, la película de Barbie... He compartido estos años con muchas personas que me han acompañado durante esta fase de mi vida y han hecho que, aunque el mundo se haya vuelto más loco, yo siga más o menos cuerdo y a las que quiero agradecer con esta sección.

Antes que nada, quiero agradecer a mis directores, Silvia y Francisco. Desde que llamé por primera vez al despacho de Silvia para interesarme por el trabajo de fin de grado, no han hecho más que ayudarme y guiarme, respondiendo con paciencia a mis innumerables preguntas. Gracias a su tutela he podido aprovechar al máximo estos años, y sin su apoyo esta tesis no habría sido posible.

También quiero agradecer el buen recibimiento que he recibido por la gente que forma o ha formado parte del grupo de AGNs y Galaxias del IFCA. En este grupo me he sentido como en casa. Especialmente quiero agradecer a Amalia que me ha ayudado en más de una ocasión, muy especialmente con los enrevesados espectros infrarrojos, y a Nacho, que defendió su tesis poco después de que yo empezara la mía y me ayudó durante los primeros meses a acostumbrarme con el trabajo de análisis.

No puedo olvidarme de mis compañeros de despacho, Giorgos y Koushika. Han sido ambos una gran compañía estos años, y Koushika en particular una gran compañera de viajes que me ha descubierto la deliciosa gastronomía de Tamil Nadu y con la que espero mantener el contacto. ¡Mucho ánimo con lo que te queda de doctorado!

Por último, pero no menos importante, quiero dar las gracias a mis padres, a mi hermana, a mis amigos y a Eva. Gracias por estar ahí todos estos años, vuestros ánimos y apoyo incondicional han sido la mayor ayuda que podía haber pedido.

Resumen

Los Núcleos Galácticos Activos (por sus siglas en inglés, AGNs) son los fenómenos persistentes más luminosos del Universo observable y emiten grandes cantidades de radiación a lo largo de todo el espectro electromagnético. La emisión de los AGNs se origina por la acreción a un agujero negro supermasivo (SMBH) con masa $> 10^6 M_{\odot}$, un tipo de objeto que hoy en día se cree que se encuentra en el centro de la mayoría, si no todas, las galaxias. El estudio de los AGN es una pieza clave para poder comprender la formación y evolución de las galaxias, ya que sus propiedades están correlacionadas con las de la galaxia que los alberga.

La explicación más aceptada para la diversidad aparente de los AGNs es el Modelo Unificado de AGNs. Entre otros éxitos, ha sido capaz de explicar las diferencias observadas en los espectros ópticos de ciertos AGN y la clasificación asociada de los mismos en tipos 1, con la detección de líneas de emisión anchas ($\text{FWHM} > 1000 \text{ km s}^{-1}$) y estrechas ($\text{FWHM} < 1000 \text{ km s}^{-1}$), y tipos 2, con la detección sólo de estas últimas. En este modelo, una estructura de gas y polvo toroidal conocida como el toro, bloquearía ciertas líneas de visión impidiendo la observación de la región nuclear, mientras otras no serían afectadas. Sin embargo, el Modelo Unificado no proporciona una respuesta satisfactoria acerca de qué propiedades físicas provocan la subclasificación de los AGN tipo 1 en subtipos 1.0, 1.2, 1.5, 1.8 y 1.9, definidos en base a las diferencias en el cociente de flujos de $[\text{OIII}]5007\text{\AA}$ y la componente ancha de $\text{H}\beta$. En esta tesis hemos tratado arrojar luz sobre esta cuestión. En particular, nos hemos centrado en la investigación del efecto sobre la clasificación de la extinción, la luminosidad del AGN y de la galaxia anfitriona, y la intensidad intrínseca de las líneas de emisión estrechas y anchas. Esta tesis constituye el primer estudio sistemático en la literatura de todas estas propiedades realizado en una misma muestra con una función de selección bien definida.

Para llevarlo a cabo, obtuvimos nuestra muestra de trabajo de la *Bright Ultra-hard XMM-Newton Survey* (BUXS), una muestra de AGNs compuesta por 258 fuentes brillantes en rayos X (con flujos por encima de $6 \times 10^{-14} \text{ erg s}^{-1} \text{ cm}^{-2}$ a energías mayores que 4 keV) detectadas con XMM-Newton. Utilizando una combinación de información fotométrica que abarca desde el ultravioleta hasta el infrarrojo medio y espectros de rayos X, ópticos y del infrarrojo cercano (NIR), pudimos construir una muestra multi-longitud de onda compuesta por 159 AGN con una clasificación espectroscópica óptica completa, robusta y uniforme, es decir, basada en el mismo conjunto de líneas de emisión para todos los objetos. Nuestra muestra cubre luminosidades intrínsecas en rayos X (definida a energías 2 – 10 keV en el sistema de referencia en reposo) de $10^{42} - 10^{46} \text{ erg s}^{-1}$ y *redshifts* entre 0.05 y 0.75, llegando a valores superiores a los de estudios similares anteriores.

Usando la información fotométrica, hemos construido las distribuciones espectrales de energía (SED) de nuestras fuentes. Hemos descompuesto las SED observadas en la suma de emisión de la galaxia anfitriona y del AGN, esta última combinación de la emisión del disco de acreción y del toro. Para llevar a cabo los ajustes se utilizó la herramienta *SED Analysis using Bayesian Statistics* (SEABASs). A partir de estos ajustes, hemos obtenido el contraste observado del AGN sobre total (AGN más galaxia anfitriona), la extinción total óptica/ultravioleta en la línea de visión, la luminosidad de la galaxia y del AGN.

A la vez, hemos llevado a cabo el ajuste de los espectros ópticos y en el infrarrojo cercano de nuestras fuentes. Para ello, se desarrolló un código original con capacidad para ajustar un modelo compuesto por varios componentes del continuo de AGN y galaxia y de líneas de emisión estrechas y anchas. Este código nos permitió determinar con fiabilidad la significancia de la detección de las componentes anchas de las líneas de emisión, evitando al mismo tiempo ajustar un modelo excesivamente complejo. A partir de estos ajustes, obtuvimos las propiedades de las líneas de emisión, como el flujo y la anchura, y la clasificación intermedia de nuestros AGNs.

Hemos estudiado primero el efecto del contraste y las propiedades asociadas con el contraste en la determinación del subtipo. El contraste muestra una clara disminución con el subtipo, distinguiéndose dos grupos principales: uno conformado por 1.0s, 1.2s y 1.5s (1.0 – 5s) y otro por 1.8, 1.9s y 2s (1.8 – 9/2s). Esta diferencia se debe, en parte, a un aumento de la extinción que sigue la misma tendencia. Para los AGNs con bajos niveles de extinción ($E(B - V) < 0.65$) encontramos que la mayoría de la extinción detectada, si no toda, puede asociarse a material de la galaxia. Para los demás, la extinción debe contar una importante contribución de material circumnuclear.

El 50% de los 1.9s y 2s carecen de suficiente extinción para explicar la no detección de líneas de emisión anchas en su espectro óptico/NIR, implicando la necesidad de la presencia de un efecto adicional. Nuestros hallazgos muestran que los 1.8 – 9/2s se encuentran preferentemente en galaxias con luminosidades mayores, mientras que los AGNs muestran luminosidades intrínsecas similares a los 1.0 – 5s. En consecuencia, en estos AGNs el cociente entre luminosidades AGN/galaxia anfitriona disminuye, dificultando la detección de la emisión de las líneas de emisión anchas.

Sin embargo, estos resultados no explican el origen de los tipos intermedios de 1.0 a 1.5. Para entenderlos hemos estudiado el efecto de la luminosidad relativa a la del AGN de las componentes anchas de $H\beta$ y $H\alpha$ y de $[OIII]5007\text{\AA}$ en la determinación de la clase. No encontramos diferencias en la luminosidad relativa de la componente ancha de $H\beta$ entre 1.0s, 1.2s y 1.5s. Se obtuvieron resultados similares al considerar en su lugar la componente ancha de $H\alpha$. También se estimó para los 1.9s de baja extinción el flujo esperado para la componente ancha de $H\beta$ a partir de la línea $H\alpha$, teniendo en cuenta la relación intrínseca esperada entre ambas. De esta manera se pudo tener en cuenta las componente

anchas de $H\beta$ más débiles, que pudieran haber escapado detección. Con estas estimaciones se reclasificaron estos objetos como 1.0/1.2/1.5/1.8. Aun con su inclusión, no se encontraron diferencias significativas entre 1.0s, 1.2s y 1.5s. Sin embargo, encontramos un indicio de una disminución de la luminosidad relativa de $H\beta$ para los 1.8s. Así mismo, se halló una clara disminución de la luminosidad relativa de las líneas de emisión estrechas con el subtipo para 1.0s, 1.2s y 1.5s, usando como referencia $[OIII]5007\text{\AA}$. Junto a esta, se encontró una relación entre la luminosidad relativa de $[OIII]5007\text{\AA}$ y la luminosidad del AGN, pero no tan fuerte la anterior. Encontramos improbable que esta tendencia con el subtipo esté relacionado con cambios en la extinción sufrida por las líneas de emisión estrechas, con contaminación proveniente de la galaxia anfitriona o con variabilidad, estando más probablemente relacionado con un aumento del factor de cobertura de la región de emisión de las líneas estrechas (NLR) con el subtipo.

En resumen, esta tesis ha demostrado que la clasificación intermedia de los AGN tiene un origen complejo, y que no existe un único parámetro que pueda explicar las diferencias observadas. Así, por un lado, la combinación de un aumento de la extinción y una disminución de la relación de luminosidad AGN/galaxia, impulsada principalmente por un aumento de la luminosidad de la galaxia anfitriona, constituye la principal razón de la clasificación de los AGN en los subtipos 1.0 – 5 y 1.8 – 9/2. Por otro lado, un aumento de la intensidad intrínseca de las líneas de emisión estrechas, en particular de $[OIII]5007\text{\AA}$, es el principal responsable de la clasificación de los AGN en los subtipos 1.0, 1.2 y 1.5. Estos descubrimientos implican la necesidad de la inclusión de parámetros adicionales en el Modelo Unificado para explicar las observaciones, en particular, la luminosidad de la galaxia y de las propiedades de la NLR.

En futuro trabajos se trataría de ampliar los resultados aquí presentados mediante el estudio del impacto de la masa del SMBH y el ratio de Eddington en la clasificación. Para ello, se obtendrían la masa del SMBH a partir de su relación con las propiedades de líneas anchas para los 1.0 – 9s y con la masa estelar de la galaxia para los 2s. Así mismo, se trataría de obtener mediciones directa de las propiedades de la NLR (parámetro de ionización, densidad electrónica y factor de cobertura) a partir de la comparativa de la anchura equivalente de las líneas de emisión $[OIII]4363\text{\AA}$, $[OIII]5007\text{\AA}$ y la componente estrecha de $H\beta$ con modelos teóricos.

Abstract

Active Galactic Nuclei (AGN) are the most luminous persistent phenomena in the observable Universe, emitting vast amounts of radiation all over the electromagnetic spectrum. AGN are fuelled by the accretion onto supermassive black holes (SMBHs) with masses $> 10^6 M_{\odot}$, which nowadays are believed to be in the centre of every massive galaxy. AGN have become a fundamental piece to understanding the formation and evolution of galaxies, as the properties of their SMBHs are tightly correlated with those of their host galaxies.

The most accepted explanation for the perceived diversity of AGN is the Unification Model. Among other achievements, it successfully explains the differences in the optical spectra between certain AGN and the associated classification into type 1, characterised by the detection of broad ($\text{FWHM} > 1000 \text{ km s}^{-1}$) and narrow ($\text{FWHM} < 1000 \text{ km s}^{-1}$) emission lines, and type 2, distinguished by the detection of solely the latter. In this model, a toroidal structure of gas and dust, known as the torus, would block certain emission lines, hampering the observation of the nuclear region, while others would be unaffected. However, the Unification Model does not provide a satisfactory answer on which physical properties are driving the subclassification of type 1 into subtypes 1.0, 1.2, 1.5, 1.8, and 1.9, based on the flux ratio of $[\text{OIII}]5007\text{\AA}$ and the broad component of $\text{H}\beta$. In this thesis, we aimed to shed light on this issue. In particular, we focused on the effect of extinction, AGN and host galaxy luminosities and relative luminosity with respect to the AGN luminosity of narrow and broad emission lines. This thesis is the first systematic study in the literature of these properties on the same sample with a well-defined selection function.

To achieve it, we drew our working sample from the Bright Ultra-hard XMM-Newton Survey (BUXS), an AGN sample composed of 258 X-ray bright (with fluxes greater than $6 \times 10^{-14} \text{ erg s}^{-1} \text{ cm}^{-2}$ at higher energies than 4 keV) sources detected with XMM-Newton. Using a combination of photometry information ranging from ultraviolet to mid-infrared and X-ray, optical, and near-infrared (NIR) spectra, we were able to construct a multi-wavelength sample composed of 159 AGN with complete, robust and uniform (based on the same set of emission lines for all objects) optical spectroscopic classification. The sample spans a rest-frame 2 – 10 keV X-ray luminosity range of $10^{42} - 10^{46} \text{ erg s}^{-1}$ and redshifts between 0.05 and 0.75, a higher boundary than previous similar studies.

Using the photometry information collected, we built the spectral energy distributions (SED) of our sources. We decomposed the SEDs into a combination of host galaxy and AGN, with the latter including the accretion disk and torus emission components. To carry out the fits, we used the tool *SEd Analysis using Bayesian Statistics* (SEABASs). From these fits, we obtained the observed AGN over total (AGN plus galaxy) contrast, the total optical/ultraviolet line-of-sight extinction, and the host galaxy and AGN intrinsic luminosities.

At the same time, we fitted the optical and NIR spectra of our sources. We developed an original code capable of fitting a progressively more complex model composed of several AGN/galaxy continuum and narrow and broad emission line components. The code allowed us to reliably determine the significance of the detection of the broad emission lines while avoiding overfitting. We obtained the emission line properties, like flux and width, and a robust intermediate classification.

We first studied the effect of observed contrast and contrast-related properties on the subtype determination. The contrast exhibits a clear decline with subtype, distinguishing two main groups: one composed of 1.0s, 1.2s, and 1.5s (1.0 – 5s) and the other of 1.8s, 1.9s y 2s (1.8 – 9/2s). This difference is partly driven by an increase in extinction following the same trend. For AGNs with low extinction ($E(B - V) < 0.65$), we find that most, if not all, of the detected extinction can be associated with material in the host galaxy. For the rest, the extinction must have a significant contribution from material at circumnuclear scales.

Fifty percent of 1.9s and 2s lack sufficient extinction to explain the non-detection of detection of broad emission lines, unveiling the necessity of an additional effect. Our findings show that 1.8 – 9/2s preferentially reside in host galaxies with higher luminosities while displaying similar intrinsic AGN luminosities to 1.0 – 5s. Consequently, the AGN to host galaxy luminosity ratio diminishes, hindering the detection of the broad emission lines.

However, these results do not explain the origin of the intermediate subtypes from 1.0 to 1.5. To understand them, we studied the effect of the broad and narrow emission line relative luminosity on the subtype determination, using broad $H\beta$ and $H\alpha$ and $[OIII]5007\text{\AA}$. We found no differences in the intrinsic intensity of the broad component of $H\beta$ between 1.0, 1.2 and 1.5 subtypes. Similar results were found when we considered instead the broad component of $H\alpha$. We estimated the intensity of the broad component of $H\beta$ from the $H\alpha$ observation for 1.9s with low extinction to account for the weakest broad $H\beta$ lines, which could have avoided detection. With these estimations, we reclassified them as 1.0/1.2/1.5/1.8. Even when these objects are included, we still did not find any significant difference between 1.0s, 1.2s and 1.5s. However, we found that the relative intensity of $H\beta$ might be lower in 1.8s than in 1.0 – 5s.

We found a clear decrease of the narrow emission line relative luminosity with increasing subtype for 1.0s, 1.2s and 1.5s, as traced by $[OIII]5007\text{\AA}$. We also detected a decrease of the relative luminosity of $[OIII]5007\text{\AA}$ with the AGN luminosity, but not as strong as the former. We found that the trend with subtype is unlikely to be related to changes in the extinction suffered by the narrow emission lines, contamination from the host galaxy or variability. Our results suggest that it is most probably related to an increase in the covering factor of the narrow-line emitting region (NLR) with increasing subtype.

To sum up, this thesis showed that the intermediate classification of the AGN has a complex origin, and not a single parameter can explain the subtype differences. Therefore, we con-

clude that, on the one hand, the subtype classification into 1.0 – 5 and 1.8 – 9/2 is mainly driven by the combination of increasing extinction and decreasing AGN/galaxy luminosity ratio, primarily due to the rising luminosity of the host galaxy. At the same time, on the other hand, there is an increase in the relative luminosity of the narrow emission lines, particularly [OIII]5007Å, which is responsible for the subtype classification between 1.0, 1.2 and 1.5. These findings imply the need for the inclusion of additional parameters in the Unification Model to explain the observations, particularly the luminosity of the host galaxy and the properties of the NLR.

Future work would seek to expand the results presented here by studying the impact of the SMBH mass and the Eddington ratio on classification. For this purpose, the mass of the SMBH could be derived from its relation with the broad line properties for the 1.0 – 9s and with the stellar mass of the galaxy for the 2s. Additionally, direct measurements of the NLR properties (ionisation parameter, electron density and coverage factor) would be obtained by comparing the measured equivalent width of the [OIII]4363Å, [OIII]5007Å and the narrow H β emission lines with theoretical models.

Contents

Declaración de autoría	iii
Agradecimientos	vii
Resumen	ix
Abstract	xiii
1 Introduction	1
1.1 AGN Phenomenology	1
1.1.1 Spectral energy distribution of AGN	4
1.2 AGN Classification	7
1.3 Unification Model of AGN	10
1.4 Current understanding of optical spectroscopic subtypes	14
1.5 Aims and structure of this thesis	16
2 Multi-wavelength surveys	19
2.1 X-rays: XMM-Newton	19
2.2 Ultraviolet: GALEX	21
2.3 Optical: Sloan Digital Sky Survey	23
2.4 Near-infrared	24
2.4.1 VISTA	24
2.4.2 2MASS	25
2.4.3 UKIRT	25
2.5 Mid-infrared: WISE	26
3 The BUXS AGN Sample	29
3.1 Sample definition	29
3.2 Optical counterpart identification and spectroscopic follow-up	30
3.3 Spectral energy distribution construction	34
4 Data reduction and fitting	39
4.1 Optical spectral reduction	39
4.2 EMIR spectral reduction	40
4.3 Analysis of the optical/NIR spectra	43
4.3.1 Fitting software	44

4.3.2	Spectral models	46
4.3.3	Fitting regions	49
4.4	Analysis of the SEDs	55
5	Results of this thesis	61
5.1	AGN sample properties	62
5.2	Analysis of aperture effect in subtype determination	65
5.3	Contrast related properties	68
5.3.1	Observed contrast	68
5.3.2	Optical extinction	70
5.3.3	AGN and host galaxy luminosity	74
5.3.4	AGN over host galaxy luminosity ratio	77
5.4	Emission line luminosities	79
5.4.1	Relative luminosity of the broad emission lines	80
5.4.2	Relative luminosity of the [OIII]5007Å emission line	84
5.4.3	Origin of the [OIII]5007Å relative luminosity increase with subtype	86
6	Conclusions and future work	89
6.1	Contrast-related properties as main drivers of 1.0/1.2/1.5 and 1.8 – 9/2 classes	90
6.2	Differences in relative luminosity of [OIII] for 1.0s, 1.2s and 1.5s	91
6.3	Future work	92
A	X-rays spectral analysis	97
B	Statistical tests	105
B.1	Significance levels	105
B.2	F test	106
B.3	Kolmogorov-Smirnov test	106
B.4	Anderson-Darling test	108
B.5	Kendall rank correlation coefficient test	108
C	Working sample spectra and results lists	111
	Bibliography	119

Chapter 1

Introduction

More than eighty years ago, [Seyfert \(1943\)](#) reported the presence of very broad, strong, and highly excitation emission lines in the optical spectra of the nucleus of six *spiral nebulae* (now well-identified as galaxies). However, this first discovery was largely ignored until [Baade & Minkowski \(1954\)](#) found the similarities of the spectra between these sources and the Cygnus A radio source. The work of [Schmidt \(1963\)](#) confirmed the observed emission lines were redshifted nebular lines and consequently ascertained their extra-galactic nature. These and other results on similar dates opened up the study of a new kind of highly luminous astronomic phenomenon, the Active Galactic Nucleus (AGN).

In this chapter, we will present a summary of the current knowledge about AGN that is most relevant to this thesis. In Sect. [1.1](#), we will describe what AGN are, enumerate their most significant properties, explain the motivation for their study, and describe their observed emission. We will then introduce the typical criteria used to classify AGN in Sect. [1.2](#), focusing on the optical spectroscopic classification. Next, in Sect. [1.3](#), we will explain the Unification Model of AGN and describe its importance in understanding the observed AGN emission and classifications. In Sect. [1.4](#) we will describe the current understanding of the AGN optical spectroscopic subtypes. Finally, we will introduce in Sect. [1.5](#) the aims of this thesis and outline its structure.

1.1 AGN Phenomenology

AGN are the most luminous persistent phenomena in the observable Universe. AGN have bolometric luminosities¹, L_{BOL} , ranging from 10^{41} erg s⁻¹ to 10^{48} erg s⁻¹ ([Padovani et al., 2017](#)), comparable to or even higher than those of quiescent galaxies ($L_{\text{BOL}} < 10^{43}$ erg s⁻¹, [Bell & de Jong 2001](#)). Additionally, AGN show strong emission all over the electromagnetic spectrum, from gamma rays to radio wavelengths ([Padovani et al., 2017](#)).

¹The bolometric luminosity of an object corresponds to the total energy per unit of time emitted along the whole electromagnetic spectrum.

AGN also frequently show variability, on time scales from years to minutes depending on the region of the electromagnetic spectrum studied (Ulrich et al., 1997; Mateos et al., 2007; LaMassa et al., 2015; Hernández-García et al., 2015). According to the shortest detected time scales of variability, especially in X-rays, the origin of the luminosity is a very compact region of the order of the size of the Solar System (Padovani et al., 2017). Furthermore, not only high luminosities have been observed, but also a high concentration of mass has been estimated to reside in this region through different techniques (Neufeld et al., 1994; Yu & Lu, 2004; Peterson & Bentz, 2006).

Accretion is the only process that is efficient enough to explain the observed high energy density. Consequently, it is widely accepted that the source of the AGN emission must be a supermassive black hole (SMBH, with $M > 10^6 M_{\odot}$ and M_{\odot} corresponding to the mass of the Sun) actively accreting. However, not all SMBHs are actively accreting matter, like the SMBH in the centre of the Milky Way (Sagittarius A*, with $M \approx 4 \times 10^6 M_{\odot}$, Gravity Collaboration et al. 2023), and consequently, they are not detected as AGN.

There is plenty of evidence that most, if not all, galaxies are hosts to a SMBH in their nucleus (Magorrian et al. 1998; Kormendy & Gebhardt 2001 and reference therein). One of the most surprising discoveries of the last 20 years was the strong relations found between the properties of the SMBH and their host galaxies. There are well-established relations between the SMBH mass with the stellar velocity dispersion (Gebhardt et al., 2000; Ferrarese & Merritt, 2000; Tremaine et al., 2002), the stellar mass (Graham et al. 2001; Häring & Rix 2004; Schutte et al. 2019; see top plot of Fig. 1.1) and the luminosity of the host galaxy bulge (Kormendy & Richstone, 1995; Marconi & Hunt, 2003; Gültekin et al., 2009). What is even more, the evolution of star formation across cosmic time parallels that of SMBH accretion rate (Bongiorno et al., 2007; Kormendy & Ho, 2013; Madau & Dickinson, 2014), as can be seen in the bottom plot of Fig. 1.1.

These relations strongly suggest a hand-in-hand evolution of the host galaxy and SMBH, although it is not clear yet how one influences the other. Some hypotheses are radiation pressure of the AGN on the material feeding it and on the star formation in the host galaxy (Fabian, 2012), the influence of mechanical feedback from powerful AGN jets (Gaspari et al., 2012; McNamara & Nulsen, 2012), or an external process regulating both the growth of galaxy and SMBH, like accretion from the intergalactic medium (Mullaney et al., 2012). Given the previous observations, AGN are nowadays not considered a type of object but rather a state all galaxies go through at some point in their evolution that can be activated by different mechanisms, such as galaxy mergers (Hopkins et al., 2008; Hirschmann et al., 2010), galaxy interaction with the intercluster medium (Byrd & Valtonen, 1990; Marshall et al., 2018) or instabilities in the galactic disk (Schulz & Struck, 2001; Younger et al., 2008).

As AGN are highly luminous and long-lived, we can detect them at large distances. In fact, AGN with high redshift ($z = 3 - 7$) were detected with the X-ray observatory Chandra

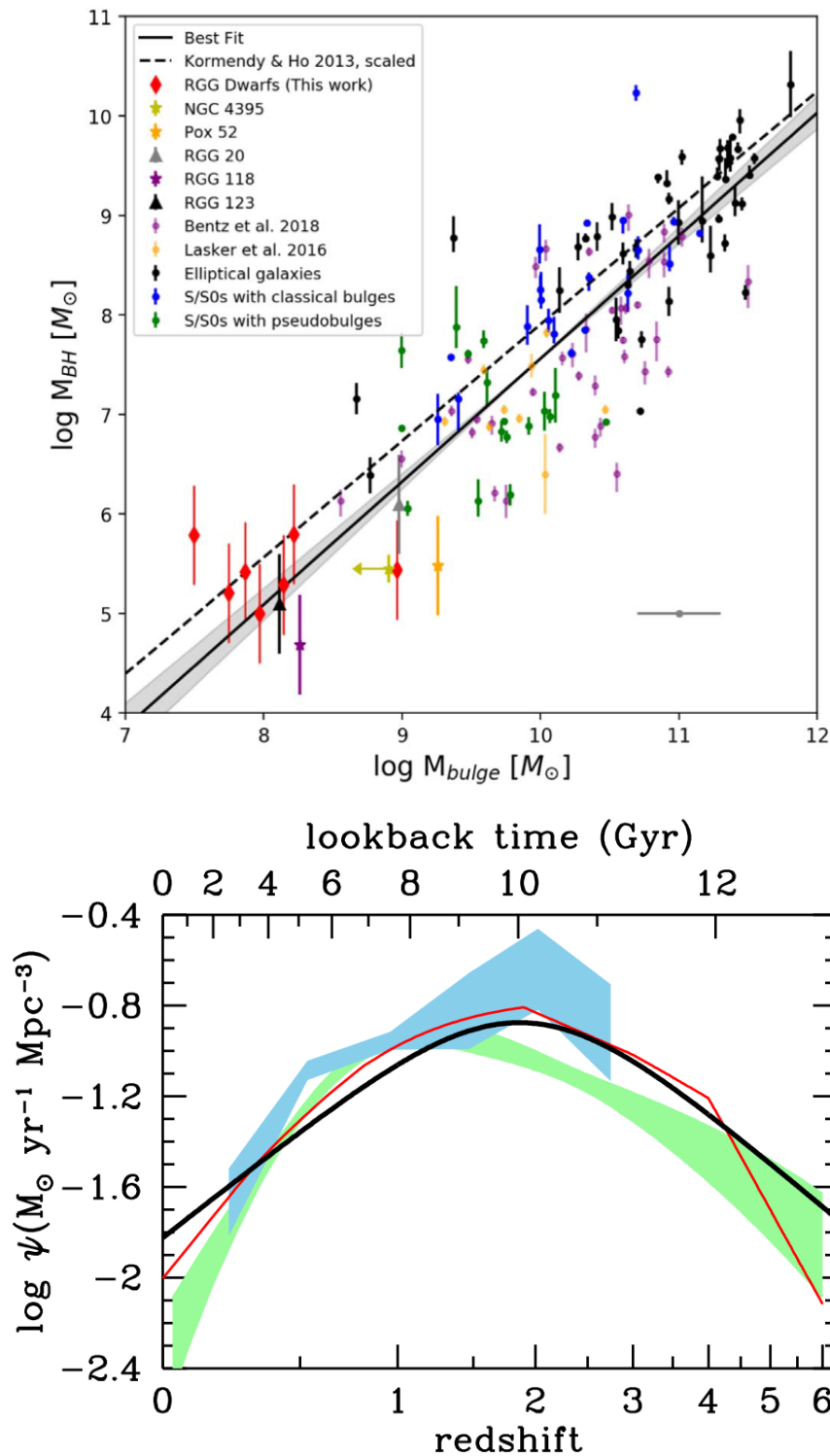


Figure 1.1: (Top) Mass of the SMBH versus the stellar mass of the bulge of its host galaxy (coloured points) and fitted relations between both parameters (dashed and solid lines). Obtained from [Schutte et al. \(2019\)](#). (Bottom) The history of star formation in galaxies (black solid line) and the growth history of SMBH, as revealed from X-rays (red line and green shadowed area) and infrared surveys (blue shadowed area). Obtained from [Madau & Dickinson \(2014\)](#).

(Vito et al., 2018; Nanni et al., 2018; Sandoval et al., 2023). The most recent James Webb Space Telescope has detected AGNs at infrared wavelengths at redshifts $z \approx 10$ when the Universe was only 3% of its current age (Maiolino et al., 2023, 2024; Castellano et al., 2024).

Therefore, the combination of their ubiquity all over the Universe, the large range of redshifts they are found in, and the fundamental impact of the accreting SMBHs on the evolution of their hosts make the study of AGN fundamental to understanding not only the galaxy formation and evolution but also the history of the Universe.

1.1.1 Spectral energy distribution of AGN

The representation of the emission versus frequency of an object is known as its Spectral Energy Distribution (SED). The average SED of an unobscured AGN is shown in Fig. 1.2. It is relatively flat from far-infrared to X-rays when using νf_ν^2 units. In this section, we will describe the observed emission of AGN moving from the longest to the shortest wavelengths and the selection techniques associated with each range. The origin of the emission at every wavelength will be explained later, in Sect. 1.3.

- **Radio:** typically defined from tens of GHz to 10 MHz, is well described by a power law, $f_\nu^3 \propto \nu^{-\alpha_R}$. It is extended and originates in jets extending from kiloparsecs to megaparsecs (Schwartz et al., 2003; Blandford et al., 2019). The shape of the radio spectrum depends on whether the emission is core-dominated (most radio emission originated near the AGN centre) or lobe-dominated (most radio emission originated in hot spots far from the AGN centre). In the first case, the observed spectrum is flatter ($\alpha_R \sim 0$), while it is steeper ($\alpha_R \sim 0.8$) in the latter (Kimball & Ivezić, 2008). Detection of luminous radio sources can be almost unequivocally associated with AGN, making it a reliable method to detect them (Mushotzky, 2004). However, radio emission is strong in $\lesssim 10\%$ of AGN, while for the rest it is three orders of magnitudes smaller than the emission at optical wavelengths (Padovani, 2016).
- **Infrared:** It covers wavelengths from 500 μm to 1 μm . The spectral shape is characterized by a power law, $f_\nu \propto \nu^{-\alpha_{I1}}$ with an $\alpha_{I1} \sim 1$ (Alonso-Herrero et al., 2001) at 1 – 10 μm , by a bump at 10 – 30 μm and at larger wavelengths by a steep decline modelled with a power law, $f_\nu \propto \nu^{-\alpha_{I2}}$ with an index $\alpha_{I2} > 3$. In AGN with a strong radio emission, the far-infrared (FIR) emission differs and it is described by a power law with a index close to 2.5 (Risaliti & Elvis, 2004).

IR emission is usually used to identify AGN using both photometry and spectrometry. With the former, AGN can be selected employing IR colors i.e., a relation of monochromatic flux ratios. These rely on the fact that the AGN with the most luminous IR emission have a characteristic color that differentiate them from other IR

² νf_ν correspond to the observed flux f_ν at frequency ν multiplied by the frequency.

³ f_ν correspond to the flux density at frequency ν .

sources (quiescent galaxies, starburst galaxies...) (Stern et al., 2005; Mateos et al., 2012; Assef et al., 2013). Objects can also be identified as AGN using IR photometry if the observed SED at $< 10 \mu\text{m}$ follows a power law shape, as expected in AGN (Alonso-Herrero et al., 2006; Donley et al., 2007, 2012). MIR spectra can be used to identify AGN based on certain properties like the presence of high ionisation emission lines like [Ne V], [Ne II] or [O IV], the equivalent width of polycyclic aromatic hydrocarbons (PAH) features or the strength of the silicate absorption at $9.7 \mu\text{m}$ (Armus et al., 2007; Alonso-Herrero et al., 2014).

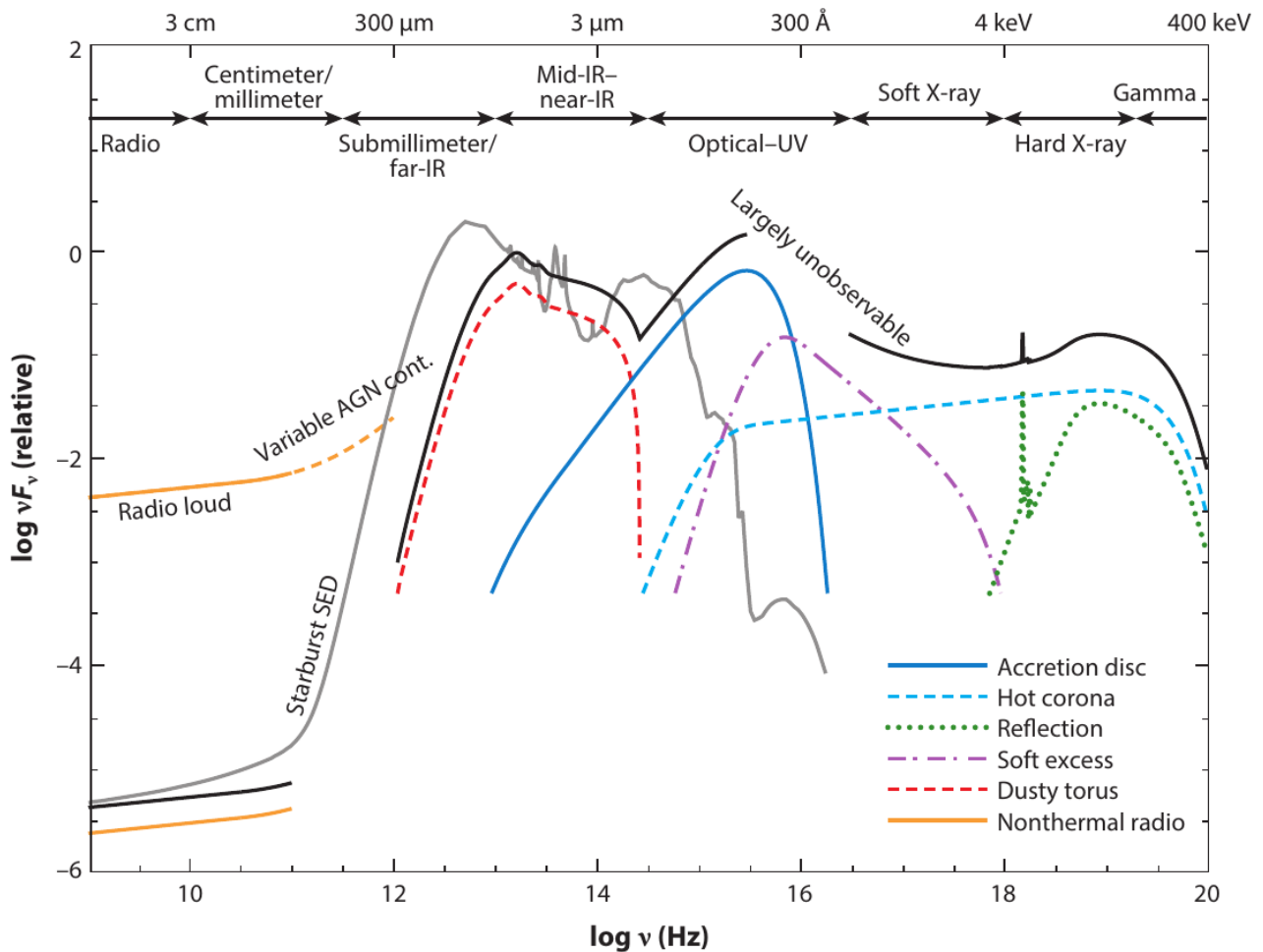


Figure 1.2: Average spectral energy distribution of an unobscured AGN (black solid line) and the components in each wavelength range (coloured dashed lines). The SED of a star-forming galaxy (grey solid curve) is included for comparison. Obtained from Hickox & Alexander (2018), previously adapted from Harrison (2014).

- **UV/Optical:** the bulk of the AGN emission is concentrated at UV/optical wavelengths ($8000 \text{ \AA} - 1000 \text{ \AA}$). The UV/optical emission usually corresponds to the peak of AGN luminosity and can account for up to $\sim 50\%$ of its bolometric luminosity of the AGN. The integrated UV/optical emission can be described with a multi-black

body spectrum, usually approximated with a power law, $f_\nu \propto \nu^{-\alpha_O}$, with typical indexes $\alpha_O \sim -0.5 - 0.3$ and a blue excess at the wavelengths $\lesssim 3000 \text{ \AA}$ (Koratkar & Blaes, 1999).

Additionally, the blending of certain emission line families gives rise to the appearance of pseudo-continua. The two most relevant are the one formed by the FeII transitions, which significantly contributes to the observed flux from UV to wavelengths close to $H\beta$, and the one formed by high-order Balmer emission lines, which has a significant contribution mostly at UV wavelengths.

In the optical range, a myriad of permitted, semi-forbidden, and forbidden emission lines can also be detected, broadly classified into narrow and broad emission lines. The narrow lines have widths $< 1000 \text{ km s}^{-1}$ and both permitted and forbidden narrow emission lines are found. The broad emission lines have widths $\geq 1000 \text{ km s}^{-1}$, reaching values of tens of thousands of kilometres per second, and only broad permitted emission lines are detected. We will keep for the rest of the thesis this definition of narrow and broad emission lines.

The detection of broad emission lines is used to unambiguously identify an AGN. However, their sensitivity to extinction along the line of sight and the cost of carrying out spectroscopic observations limit their use for AGN identification in large surveys. Using UV/optical photometric data, blue colours can be used to distinguish between, preferentially, unobscured AGN and non-active galaxies (Schmidt & Green, 1983; Richards et al., 2002).

- **X-rays:** the X-rays in AGN are usually understood as the emission in the 0.2–200 keV energy band. Its main component is a broad band (1–100 keV) continuum well modelled with a power law $f_\nu \propto \nu^{1-\Gamma_X}$, with $\Gamma_X = 1.9$ being the typical photon index⁴ value found for AGN (Caccianiga et al., 2004; Tozzi et al., 2006; Mateos et al., 2010; Corral et al., 2011). In $\sim 50\%$ of the AGN at $< 2 \text{ keV}$, an excess over the extrapolation of the power law is found, usually known as the soft excess and modelled with a black body spectrum with temperatures in the range $\sim 0.1\text{--}0.2 \text{ keV}$ (Beckmann & Shrader, 2012; Boissay et al., 2016).

Other important features found in the X-ray spectra and not well described by the power law are the Compton reflection hump, which has a complex modelling, and strong emission lines, of which the FeK_α emission line at 6.4 keV is the most prominent (Levenson et al., 2006; Nandra et al., 2007). These two features are more relevant in highly absorbed X-ray spectra. The FeK_α line can show two components: a narrow ($\sim 2000 \text{ km s}^{-1}$) and a broadened relativistic component (Ricci et al., 2014; Liu et al., 2016a).

⁴The photon index, Γ_X , is related to the energy index, α_X , of a power law as $\Gamma_X = 1 + \alpha_X$

As the X-ray emission is universal in AGN, it can be used to identify them. Furthermore, pointlike sources in host-galaxies (mostly X-ray binary stars) can only reach X-ray luminosities at rest-frame 2–10 keV up to 10^{42} erg s⁻¹. Consequently, any pointlike source found with higher luminosities is unequivocally identified as an AGN.

- **Gamma-rays:** the gamma-ray emission ($E_\gamma > 100$ MeV) is only detected in AGN with radio jets. The spectra of AGN at these energies are usually modelled as a power law with a stepped photon index in the range of $\Gamma_\gamma = 1.5 - 3$ (Madejski & Sikora, 2016). AGN selection in current gamma-rays surveys gives samples of high reliability but is restricted to AGN with strong jets.

1.2 AGN Classification

Although the previously described SED is the average for non-obscured AGN, there can be significant changes among them. For example, not all AGN show strong radio emission, and the broad emission lines detected in the optical range are absent in a significant fraction of AGN. Using these observable differences, several classification criteria were created.

For example, the most classical way to separate AGN is according to their luminosity. The most luminous ($L_{\text{BOL}} > 10^{45}$ erg s⁻¹) are nowadays known as Quasars (QSO), while the rest are identified as Seyfert. As AGN can be detected at all wavelengths, this has led to an ever-increasing number of potential AGN classifications, even for a single object. For example, classification can be based on properties on radio (radio-loud or radio-quiet, Blazar or non-Blazar...), X-rays (Compton thick) or optical (type 1 and 2) wavelengths. Some examples of usual AGN classifications and their definition criteria are shown in Tab. 1.1

We have focused on one of the most used classifications, the optical spectroscopic classification of AGN that differentiates AGN between type 1 and type 2 based on the properties of the observed emission lines in the UV/optical spectrum:

- **Type 1:** as stated in Sect. 1.1, AGN may show several strong, highly excited emission lines in the rest-frame UV/optical range. We identify as type 1 those AGN in which we detect both broad permitted and narrow permitted and forbidden emission lines. The most typical broad emission lines used for identifying type 1 AGN at $z \lesssim 1$ are MgII λ 2798, H β , and H α .

In the spectra of type 1 AGN a strong blue continuum is also detected, corresponding to the direct observation of the accretion disk's thermal emission (see Sect. 1.3). The top panel of Fig. 1.3 shows an example of the optical spectrum of a typical type 1 AGN.

- **Type 2:** AGN are classified as type 2 when only narrow permitted and forbidden emission lines are detected in their rest-frame UV/optical spectra. In type 2 AGN, neither the broad emission lines nor the strong blue continuum are present. An example of the spectrum of a type 2 AGN can be seen in the bottom plot of Fig. 1.3.

In type 2 AGN, the observed continuum is usually dominated by the integrated emission of the host galaxy. However, narrow emission lines are usually intense and show different flux ratios than those produced by the host galaxy (stellar emission, supernova remnants...). The flux ratios depend of the shape of the spectrum of the ionizing source, very different for non-active galaxies and the intense radiation from the accretion disk of the AGN, and they are usually used to differentiate type 2 from non-active galaxies. The most common method, the Baldwin-Phillips-Terlevich (BPT; [Baldwin et al. 1981](#)) diagram, uses the flux ratio of [OIII]5007Å over the narrow component of H β and of [NII] λ 6585 over the narrow component of H α .

Class (1)	Meaning (2)	Main properties (3)
Sey1	Seyfert 1	Broad and narrow lines in UV/optical
Sey2	Seyfert 2	Only narrow lines in UV/optical
QSO	Type 1 quasar	High luminosity Sey1
QSO2	Type 2 quasar	High luminosity Sey2
RL AGN	Radio-loud AGN	$f_B/f_{5\text{ GHz}} \geq 10$
RQ AGN	Radio-quiet AGN	$f_B/f_{5\text{ GHz}} > 10$
FR I	Fanaroff-Riley Type I	Nucleus-dominated radio emission
FR II	Fanaroff-Riley Type II	Lobe-dominated radio emission
Blazar	-	Highly polarized, variable and nothermal continuum
BL Lac	BL Lacertae Object	Blazars without emission lines detected
Type 1	-	Sey1 and QSO
Type 2	-	Sey2 and QSO2

Table 1.1: Examples of some usual classifications that make up the AGN zoo. **Col. 1:** class name; **Col. 2:** meaning of the identification; **Col. 3:** classification criteria used for their definition. f_B corresponds to the flux on the B-band. Adapted from [Padovani et al. \(2017\)](#).

After identifying type 1 and type 2 AGN, [Osterbrock \(1977\)](#) demonstrated that there is a broad distribution of flux ratios between the broad and narrow components of H β among type 1 AGN. This revealed that the relative intensity of broad and narrow emission lines in AGN is not constant. Using this ratio, type 1 AGN can be sub-classified as 1.0, 1.2, 1.5, 1.8 and 1.9 ([Osterbrock, 1977, 1981](#)).

Since then, several criteria have been proposed to account for the relative intensity of broad and narrow emission lines, each using a different set of emission lines. For example, [Whittle \(1992\)](#) used the ratio between the total flux of H β (broad and narrow) and [OIII]5007Å. [Winkler \(1992\)](#) instead used the ratio total flux of H β and total flux of the [OIII] doublet, while [Stern & Laor \(2012\)](#) used a classification based on the flux ratio between the narrow and broad components of H α .

Here, we have classified our AGN following a criterion based on that of [Whittle \(1992\)](#). To differentiate between subtypes, we have used the flux ratio of [OIII] λ 5007Å over the broad component of H β instead of the whole profile of H β (narrow+broad) as in [Whittle \(1992\)](#). We followed our approach to trace the relative intensity between narrow and broad emission lines, as they came from different regions and suffer different levels of extinction. Using $R = f([\text{OIII}]\lambda 5007)/f(\text{bH}\beta)$, the subtypes are defined as follows:

- **Subtype 1.0:** when $R \leq 0.3$;
- **Subtype 1.2:** when $0.3 < R \leq 1$;
- **Subtype 1.5:** when $1 < R \leq 4$;
- **Subtype 1.8:** when $R > 4$;
- **Subtype 1.9:** no broad component of H β is detected, but a broad H α is detected

In Fig. 1.3, we show examples of rest-frame optical spectra for subtypes 1.0, 1.2, 1.5 and 1.9 and type 2 taken from the AGN sample used in this thesis (see Chapter 3 for more details).

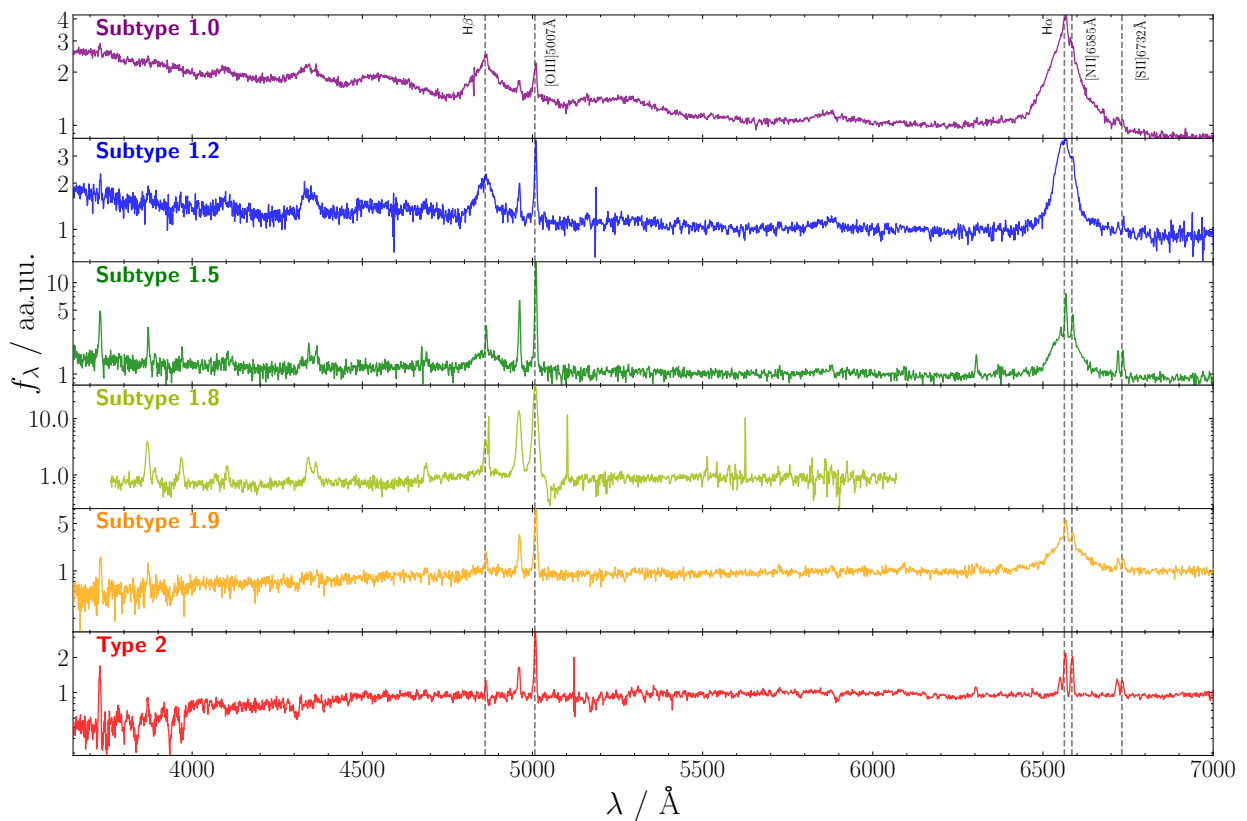


Figure 1.3: Rest-frame optical spectra of AGN with different optical spectroscopic classifications. Vertical dashed lines correspond to the rest-frame emission wavelength of typical broad and narrow emission lines. All spectra have been normalized to their observed emission at rest-frame 6000 Å.

1.3 Unification Model of AGN

Up to this point, the observed emission of AGN has been described as complex, showing significant variations between objects. However, all AGN are believed to share the same physical processes and structures. To explain this apparent paradox, the Unification Model was developed.

[Antonucci \(1993\)](#) was the first to present a unification model for AGN, the Straw Person Model (SPM), to explain the AGN dichotomy into type 1 and type 2. In this model, a toroidal structure of gas and dust coplanar with the accretion disk, called torus, is surrounding the nuclear region of the AGN obscuring certain lines of sight, making it difficult to detect the nuclear emission. Identification as type 1 or type 2 would depend only on the inclination of the line of sight with respect to the symmetry axis of the accretion disk: at low inclinations (face-on) the accretion disk would be directly observed while a high inclinations (side-on) the torus would obscure it. [Urry & Padovani \(1995\)](#) extended the model to explain the different radio emission properties of AGN by including a relativistic jet of charged particles perpendicular to both accretion disk and torus. In this model, the properties of the radio emission depend on the inclination angle between the observer and the emission of the jet.

Since then, the Unification Model has evolved, showing the necessity of including more parameters like the AGN luminosity ([Lawrence, 1991](#); [Beckmann et al., 2009](#); [Mateos et al., 2017](#)), accretion properties ([Hickox et al., 2009](#); [Ricci et al., 2017](#)) or the covering factor⁵ of the torus ([Nenkova et al., 2008](#); [Elitzur, 2012](#); [Mateos et al., 2016](#)).

Nowadays, the description of an AGN includes multiple structures at different scales, shown in [Fig. 1.4](#). These structures are, from the innermost region of the AGN to the outermost:

- **SMBH:** the SMBH is the central engine of the AGN, with $M > 10^6 M_{\odot}$. Its mass can be estimated either from the stellar velocity dispersion (using the relations introduced in [Sect. 1.1](#)) or through the intensity and width of the broad emission lines ([Greene & Ho, 2005](#); [Trakhtenbrot & Netzer, 2012](#); [Mejía-Restrepo et al., 2016, 2022](#)). Its accretion rate can also be characterized through the comparison of the bolometric luminosity of the AGN with the Eddington luminosity⁶, L_{Edd} , of the SMBH, assuming accretion efficiencies of $\epsilon \sim 0.1$ ([Marconi et al., 2004](#)).
- **Accretion disk:** it is formed by the material falling into the SMBH. It is typically optically thick and geometrically thin ([Laor & Netzer, 1989](#); [Hubeny et al., 2001](#)), except maybe for the AGN at the lowest luminosities ([Narayan, 2005](#); [Ho, 2008](#)). The accretion disk has an estimated outer radius of $\sim 10^{-2}$ pc ([Hawkins, 2007](#)). It is responsible for the bulk of the AGN emission at UV/optical wavelengths.

⁵The covering factor corresponds to the fraction of sky covered by the torus as seen by the SMBH.

⁶The Eddington luminosity corresponds to the luminosity that an AGN emits once the balance between radiation and gravity is reached. Assuming a medium composed only of hydrogen, it is related to the mass of the SMBH as $L_{Edd} = 1.26 \times 10^{38} (M/M_{\odot}) \text{ erg s}^{-1}$

The radiation of the accretion disk is of thermal origin. As the material falls into the SMBH, it loses the angular momentum due to its viscosity, which causes it to heat. The inner part of the disk reaches temperatures of $T \sim 10^{6-7}$ K, emitting at UV wavelengths or even soft ($E < 2$ keV) X-ray energies, while the outer parts are colder ($T \sim 10^{3-4}$ K) and emit at optical and near-infrared (NIR) wavelengths (Wang & Zhou, 1996).

- **Hot corona:** the corona is hot plasma composed of very energetic (100 keV – 1 MeV) electrons reaching temperatures of $T \sim 10^9$ K (Di Matteo et al., 1997) situated over the inner regions of the accretion disk. The corona is responsible for the primary X-ray radiation. When the UV/optical photons of the accretion disk interact with the relativistic electrons of the corona, they experience an inverse Compton effect and are promoted to higher energies. This close relation between the accretion disk and the corona is supported by the tight relation found between X-ray and UV luminosity (Lusso et al., 2010, 2012; Duras et al., 2020).

It is believed that the disk is the region where at least part of the Compton reflection hump observed in X-rays originates as a result of the reflection of the emission from the corona (Turner & Miller, 2009). Additionally, the relativistic FeK $_{\alpha}$ emission line detected in some AGN is produced by fluorescence of material located in the inner regions of the accretion disk (Liu et al., 2016b). The narrow component is believed to be originated at circumnuclear scales (see "torus" below).

- **Broad line region (BLR):** the BLR is a region formed by clouds of highly-excited gas at high temperatures ($T \sim 2 \times 10^4$ K; Popović 2003). Using reverberation mapping techniques, the BLR has been estimated to be placed around the corona and accretion disk at a close distance ($r \sim 0.01-1$ pc; Netzer 2015). The broad emission lines detected in the UV/optical spectra are produced in the BLR as the accretion disk UV photons are absorbed by the gas and re-emitted as emission lines.

The broad nature of these lines is due to a Doppler effect caused by the rapidly movement ($v > 1000$ km s $^{-1}$) of the clouds in the gravitational potential of the SMBH. At the same time, as no forbidden lines are detected, it is inferred that the density of these clouds must be high ($n_e = 10^8-10^{10}$ cm $^{-3}$, Netzer 1990).

- **Torus:** surrounding the SMBH, accretion disk, hot corona and BLR (all of them collectively known as the nuclear region of the AGN), there is a toroidal structure composed of gas and dust commonly known as the torus, extending up to a few parsecs (Alonso-Herrero et al., 2011; García-Burillo et al., 2016). The torus was initially proposed to be a smooth dust structure, but recent results showed that the dust is either distributed in optically thick dense clouds (Tristram et al., 2007; Nenkova et al., 2008; Elitzur, 2012) or a combination of a smooth distribution and clouds (Stalevski et al., 2012; Assef et al., 2013).

The torus has been traditionally proposed as the origin of the IR radiation: the radiation produced in the nuclear region is absorbed, heating the dust, and then it is re-emitted as infrared thermal radiation. The wide range of wavelengths covered is a consequence of the range of temperatures in the dust. The material closest to the nuclear region is at the highest temperatures ($T > 1500$ K, [Granato et al. 1997](#); [Netzer 2015](#)) and is responsible for the shortest NIR radiation, while the farthest regions are colder, as less UV/optical radiation reaches them, and emit at mid-infrared (MIR) and FIR wavelengths. It is important to note that recent studies suggest that the IR radiation might not be emitted only by material in the torus, but also by dust in AGN-driven polar winds travelling in directions perpendicular to the accretion disk ([Hönig & Kishimoto, 2017](#)).

The torus is the main ingredient of the Unified Model to explain the type 1/type 2 dichotomy, providing an anisotropic obscuration of the nuclear region. If the line of sight of the observer is intercepted by material in the torus, the optical radiation from the nuclear region will be absorbed, making both the blue emission of the disk and the broad emission lines unobservable and such AGN would be classified as type 2. In any other case, both components would be directly observable, and the AGN would be classified as type 1. High energy X-ray emission from the corona is usually still detected, as it is less affected and only partly absorbed by the torus. However, if the neutral hydrogen column density⁷ of the torus is high enough it could affect X-rays, specially at the lowest energies. This kind of AGN are known as Compton-thick. The torus is also believed to be the origin of the narrow component of the FeK $_{\alpha}$ emission line at 6.4 keV, due to the reprocessing of X-ray photons by neutral material, and at least part of the Compton reflection hump ([Turner & Miller, 2009](#)).

In the Straw Person Model framework, it is assumed that all AGN have the same torus properties, and the type 1/2 dichotomy is determined only by an inclination effect plus the probability of the line of sight being intercepted by a cloud. However, recent studies have shown that the torus may be different for type 1/2 AGN and may depend on AGN properties such as luminosity or Eddington ratio⁸ ([Kishimoto et al., 2011](#); [Alonso-Herrero et al., 2011](#); [Ramos Almeida et al., 2011](#); [Mateos et al., 2016](#); [Ramos Almeida & Ricci, 2017](#); [Hickox & Alexander, 2018](#)).

- **Narrow line region (NLR):** The NLR, like the BLR, is formed by clouds of highly ionized gas. However, these clouds are situated far from the nuclear region of the AGN, at distances from $r \sim 10$ pc to hundreds or even thousands of parsecs ([Netzer, 2015](#)). In these clouds, the narrow emission lines are produced when the UV nuclear radiation is absorbed and re-emitted.

⁷The neutral hydrogen column density, N_{H} , is defined as to the equivalent number of atoms of neutral hydrogen per unit of surface, and it is used to describe the absorption in the line of sight.

⁸The Eddington ratio, λ , corresponds to the ratio between the bolometric and Eddington luminosities.

Similarly to their broad counterparts, the width of the narrow emission lines is also produced by Doppler broadening, but as the NLR is placed further away from the SMBH than the BLR, the velocity of the clouds (and consequently the width of the lines) is lower. The presence of both permitted and forbidden transitions reveals that the density of the NLR clouds is also lower ($n_e = 10^3\text{--}10^6 \text{ cm}^{-3}$, [Netzer 1990](#)) than that of the BLR. Emission of the NLR is not affected by the torus, as the material is located farther away from the SMBH than the torus.

- **Jet:** deep radio surveys have shown that jets are more common than previously thought. However, only $\sim 10\%$ of AGN present strong relativistic jets ([Padovani, 2016](#)). AGN jets are a collimated plasma of very energetic particles launched from sub-parsec scales up to distances of kilo-parsecs or even mega-parsecs ([Schwartz et al., 2003](#)). The strong magnetic field that forms the jet induces the electrons and protons to spiral around magnetic field lines producing synchrotron emission, liberating the radio emission and the non-thermal FIR emission detected in radio-loud AGN. When the jet is aligned with the line of sight, relativistic beaming produces a flat spectrum without UV/optical emission lines and the classification of the source as a Blazar.

The jet is also believed to be the source of the gamma-ray emission detected in AGN. However, the origin of this emission is not clear, with theories explaining it as synchrotron emission of high-energy protons ([Böttcher et al., 2013](#)) or inverse Compton scattering inside the jet ([Aharonian, 2000](#)), among others.

Unification Models have been successful in explaining type 1 and type 2 AGN and predicting their properties: obscuration is larger for type 2 AGN ([Caccianiga et al., 2008](#); [Burtscher et al., 2016](#); [Koss et al., 2017](#); [Oh et al., 2022](#)), optical and X-rays obscuration are usually well correlated ([Caccianiga et al., 2004](#); [Schnorr-Müller et al., 2016](#); [Oh et al., 2022](#)) and type 2 AGN usually show more dust emission than type 1 ([Granato et al., 1997](#)). Moreover, the torus has been resolved using the Atacama Large Millimeter/Submillimeter Array (ALMA)⁹ in several local AGN ([García-Burillo et al., 2016](#); [Alonso-Herrero et al., 2018](#); [Combes et al., 2019](#); [García-Burillo et al., 2021](#)).

Furthermore, the finding of hidden type 1 AGN is considered a strong support of the Unification Model. These AGNs are classified as type 2. However, broad emission line components are found when they are observed in polarised light ([Antonucci & Miller, 1985](#); [Moran et al., 2000](#); [Ramos Almeida et al., 2016](#)). The explanation for this phenomenon is that although the torus may be obscuring the BLR, it also scatters some of the BLR photons toward the line of sight of the observer. As scattered photons are polarized, they can be distinguished from non-scattered unpolarized light.

However, the Unification Model has been challenged by some observations. A significant

⁹ALMA is a interferometer radio telescope capable to observe in 8 bands covering from 110 Ghz to ~ 950 Ghz and with resolutions ranging from $4.3''$ to $0.5''$.

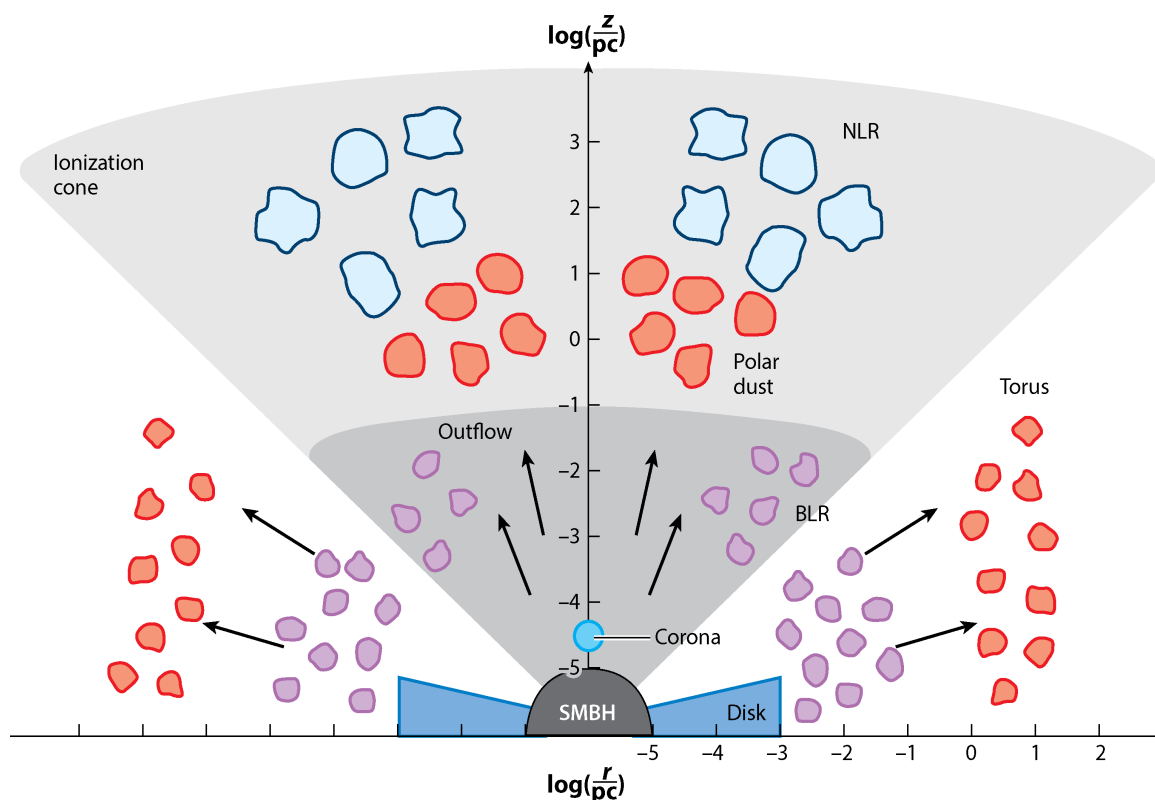


Figure 1.4: Scheme of the different AGN structures. The disk, corona and torus (including the polar dust) components are coloured to match the colouration of their emission in Fig. 1.2. Obtained from [Hickox & Alexander \(2018\)](#), previously adapted from [Ramos Almeida & Ricci \(2017\)](#).

fraction of type 2 AGN have been found to be unobscured in X-rays ([Mateos et al., 2005a,b](#); [Merloni et al., 2014](#); [Mateos et al., 2015](#); [Liu et al., 2016a](#); [Ordovás-Pascual et al., 2017](#); [Koss et al., 2017](#); [Oh et al., 2022](#)).

Some of the AGN with lowest luminosities are also suspected to not be able to sustain a BLR at all, the so-called true type 2 ([Bianchi et al., 2008](#); [Panessa et al., 2009](#); [Elitzur & Ho, 2009](#)). However, results such as the detection of a broad component in the true type 2 candidate NGC 3147 ([Bianchi et al., 2019](#)), call into question their nature.

1.4 Current understanding of optical spectroscopic subtypes

The Unification Model of AGN provides a first-order explanation for the origin of the type 1 and 2 dichotomy as an obscuration effect regulated by the probability of the observed line of sight being intercepted by the torus. However, it does not address which physical parameters are driving the intermediate optical spectroscopic classification of type 1 AGN into subtypes 1.0, 1.2, 1.5, 1.8 and 1.9.

A straightforward interpolation between type 1 and type 2 AGN might imply that subtypes are linked to an increasing nuclear obscuration within this framework. As the subtype increases, the observed broad component decreases, while the intensity of the narrow emission lines remains constant, as they originate far from the nuclear region. In fact, previous works have identified differences in both optical extinction and X-ray absorption between classes (Goodrich, 1995; Alonso-Herrero et al., 2003a; Schnorr-Müller et al., 2016; Burtscher et al., 2016; Koss et al., 2017; Jaffarian & Gaskell, 2020; Oh et al., 2022).

The most common explanation for the increasing extinction with class is that the line of sight of the observer grazes the edge of the torus, until is completely blocked in type 2. However, other torus properties may be changing and affecting the extinction measured between classes like, for example, its covering factor, which has been found to have a higher value in type 2 than type 1 (Ramos Almeida et al., 2011; Alonso-Herrero et al., 2011; Ichikawa et al., 2015; Mateos et al., 2016; García-Bernete et al., 2019; Barquín-González et al., 2020; Ricci et al., 2023).

While several studies locate the obscuring material at circumnuclear scales (Heard & Gaskell, 2016; Lu et al., 2019; Calistro Rivera et al., 2021), it could also be that the increase of obscuration detected is associated to the gas and dust in the host galaxy (Alonso-Herrero et al., 2003b; Baron et al., 2016; Gkini et al., 2021; Alonso-Tetilla et al., 2024). In fact, previous studies showed that 1.8/1.9/2s are preferentially found in edge-on galaxies and prone to suffer higher levels of host galaxy extinction than 1.0/1.2/1.5s (Maiolino & Rieke, 1995; Winter et al., 2009; Koss et al., 2011).

However, the extent of the role of extinction and/or galaxy contamination in subtype determination is not completely clear. A population of unobscured 1.8 – 9 and type 2 was found, which directly challenges the Unification Model (Caccianiga et al., 2004; Trippe et al., 2010; Mateos et al., 2015; Koss et al., 2017; Oh et al., 2022; XueGuang, 2023).

Several surveys at optical, infrared and X-ray wavelengths have shown that type 2 AGN have preferably lower luminosities than type 1 AGN (Della Ceca et al., 2008; Burlon et al., 2011; Ueda et al., 2014; Koss et al., 2017; Suh et al., 2019). If the same happens for the different subtypes, it will reduce the strength of the AGN observed features, reducing the AGN/host contrast at UV/optical wavelengths and making more difficult the detection of the emission from the BLR.

Variations in AGN luminosity between subtypes can also lead to differences in obscuration properties. According to receding torus models, the AGN luminosity would affect the torus geometry, decreasing its covering factor with increasing AGN luminosity (Lawrence, 1991; Beckmann et al., 2009; Mateos et al., 2017).

Another reason the subtype may change is differences in the relative luminosity with respect of the AGN luminosity of the broad and/or narrow emission lines. Stern & Laor (2012)

found an increase in the intensity of [OIII]5007Å with the AGN luminosity, this effect could be a consequence of a decrease in the covering factor of the NLR with AGN luminosity.

At the same time, [Elitzur et al. \(2014\)](#) suggested that the relative luminosity with respect of the AGN luminosity of the broad emission lines follows an evolutionary sequence, decreasing with decreasing subtype and AGN luminosity. They explain this trend in the disc-wind model, where the covering factor of the BLR decreases with decreasing luminosity. This model even predicts a specific luminosity beyond which the AGN can no longer sustain a BLR. The disc-wind model is usually proposed as an explanation of the changing-look AGN, objects for which the observed subtype can sometimes change between observations ([Denney et al., 2014](#); [LaMassa et al., 2015](#); [McElroy et al., 2016](#); [Li et al., 2022](#)).

At the same time, differences could also arise in host galaxy properties. Previous studies have found that type 2s live in host galaxies with higher stellar mass than type 1s ([Zou et al., 2019](#); [Mountrichas et al., 2021](#); [Koutoulidis et al., 2022](#)). However, the significance of this difference is still debated ([Kauffmann et al., 2003](#); [Merloni et al., 2014](#); [Bornancini & García Lambas, 2018a](#)). The higher stellar mass of the host galaxy is expected to be associated with a higher luminosity, producing a decrease in the observed contrast, which would translate into the observed subtype differences.

It is clear that the current picture of the intermediate optical classification is complex, and the combined impact of the different parameters in the subtype class still needs to be clarified. The most likely explanation is that multiple parameters are driving the classification, and it may be that even different subtypes have different parameters responsible for their origin.

1.5 Aims and structure of this thesis

The Unification Model is able to explain in first order the origin of type 1 and 2 classification as an effect of inclination and the probability of the line of sight being intercepted by a material of the torus. However, we still lack a complete explanation of the origin of the intermediate optical spectroscopic classification of AGN into 1.0, 1.2, 1.5, 1.8 and 1.9. Although several works in the literature have studied differences between subtypes, they have focused on the study of only one parameter or used small samples with not well defined selection functions. Consequently, a systematic study of the properties driving the subtype determination with a large well characterized AGN sample is absent. Studying the origin behind the observed classification of AGN can greatly help to understand the AGN structure and their properties. For example, the effort to explain the clear dichotomy of AGN between type 1 and type 2 played a key role in developing the Unification Model.

In this study, we aimed to reveal what physical properties play a leading role in the optical spectroscopic intermediate classification. We focused on identifying, for the first time, the effect on the subtype classification using of the following properties on a same sample with a well defined selection function:

- Optical extinction, both of nuclear origin and associated with the host galaxy.
- AGN intrinsic luminosity
- Host-galaxy luminosity
- Relative luminosity with respect to the AGN luminosity of the narrow and broad emission lines in the UV/optical range.

To do so, we compared the individual distributions of these parameters between subtypes and calculated the significance of the differences found. When we found that more than one parameter could play a significant role, we studied their 2D relations to disentangle the effects and identify potential combined effects properly.

The structure for the rest of the thesis is as follows. Chapter 2, describes the photometric and spectroscopic surveys we used, ranging from X-ray to mid-infrared, that allowed us to use a multi-wavelength approach in our work. In Chapter 3, we will describe the AGN sample used, the Bright Ultra-hard XMM-Newton Survey (BUXS; Mateos et al. 2012, 2015) sample. BUXS is a unique flux-limited X-ray-selected AGN sample comprising 256 AGN with a wide range of luminosities and redshift. In this chapter, we will also explain the optical counterpart identification, spectroscopic follow-up and spectral energy distribution (SED) construction.

In Chapter 4, we will describe the reduction of the NIR spectra and the fitting process of the spectral and photometric data. The spectroscopic information allowed us to obtain reliable estimations of the emission line properties and optical spectroscopic intermediate classification. The photometric data was used to obtain the total extinction in the line of sight and the luminosity of the AGN and the host galaxy. Using both data sets simultaneously also allowed us to refine our results by comparing the results. After the analysis, we obtained a working sample of 165 AGN with an almost complete (96%) and uniform (i.e., based on the same set of lines for all objects) classification. Thanks to these properties, our study will not suffer from biases related to classification incompleteness, which are more severe for subtypes 1.9 and 2, as their AGN characteristic emission is fainter, and subtype and redshift are more difficult to determine. This makes our dataset ideal for this study, while the large sample size ensures we can extract robust statistical conclusions from comparing subtypes.

In Chapter 5, we will show the results obtained in this thesis and quantify the significance of the trends and differences detected. Finally, in Chapter 6, we will summarize our conclusions and propose some research lines as a follow-up to this work.

Through this work, we will report errors at 1σ confidence level, and we adopt a cosmology with a mass density parameter $\Omega_M = 0.3$, an effective mass density of the dark energy $\Omega_\Lambda = 0.7$ and a Hubble constant $H_0 = 70 \text{ km s}^{-1} \text{ Mpc}^{-1}$.

Chapter 2

Multi-wavelength surveys

Multi-wavelength studies are nowadays fundamental to fully understanding the inner structure of AGN. As introduced previously, AGN emit all over the electromagnetic spectrum, and emissions at different wavelengths originate in different regions. Consequently, if we observe the AGN at various wavelengths, we can probe multiple parts, allowing us to study all of them or isolate the emission from one of them.

In this thesis, we have also followed a multi-wavelength approach. We have used data ranging from mid-infrared wavelengths to X-ray energies to construct the parent sample, decompose the observed emission into components, and study the effect of different observable parameters in the optical subtype determination. Moreover, we have used both photometric and spectroscopic data to analyse all objects, allowing a more thoughtful study of the AGN emission properties.

In this chapter, we will introduce the multi-wavelength instrumentation and associated surveys used in this work, moving from the shortest wavelengths to the longest: X-rays in Sect. 2.1, UV in Sect. 2.2, optical in Sect. 2.3, NIR in Sect. 2.4 and MIR in Sect. 2.5. At the end of the chapter, we will summarise the most important information about the filters used by the photometric surveys in Table 2.1.

2.1 X-rays: XMM-Newton

The X-ray Multi-mirror Mission - Newton (XMM-Newton; [Jansen et al. 2001](#)) is a space observatory launched by the European Space Agency (ESA) on 10 December 1999 to study cosmic X-ray sources. It is still carrying out observations. XMM-Newton carries three instruments on board: an optical/UV Monitor Telescope ([Mason et al., 2001](#)), the European Photon Imaging Camera (EPIC; [Turner et al. 2001](#), [Strüder et al. 2001](#)) and the Reflection Grating Spectrometer (RGS; [Den Herder et al. 2001](#)). In the present work, we have relied on observations taken with the EPIC camera.

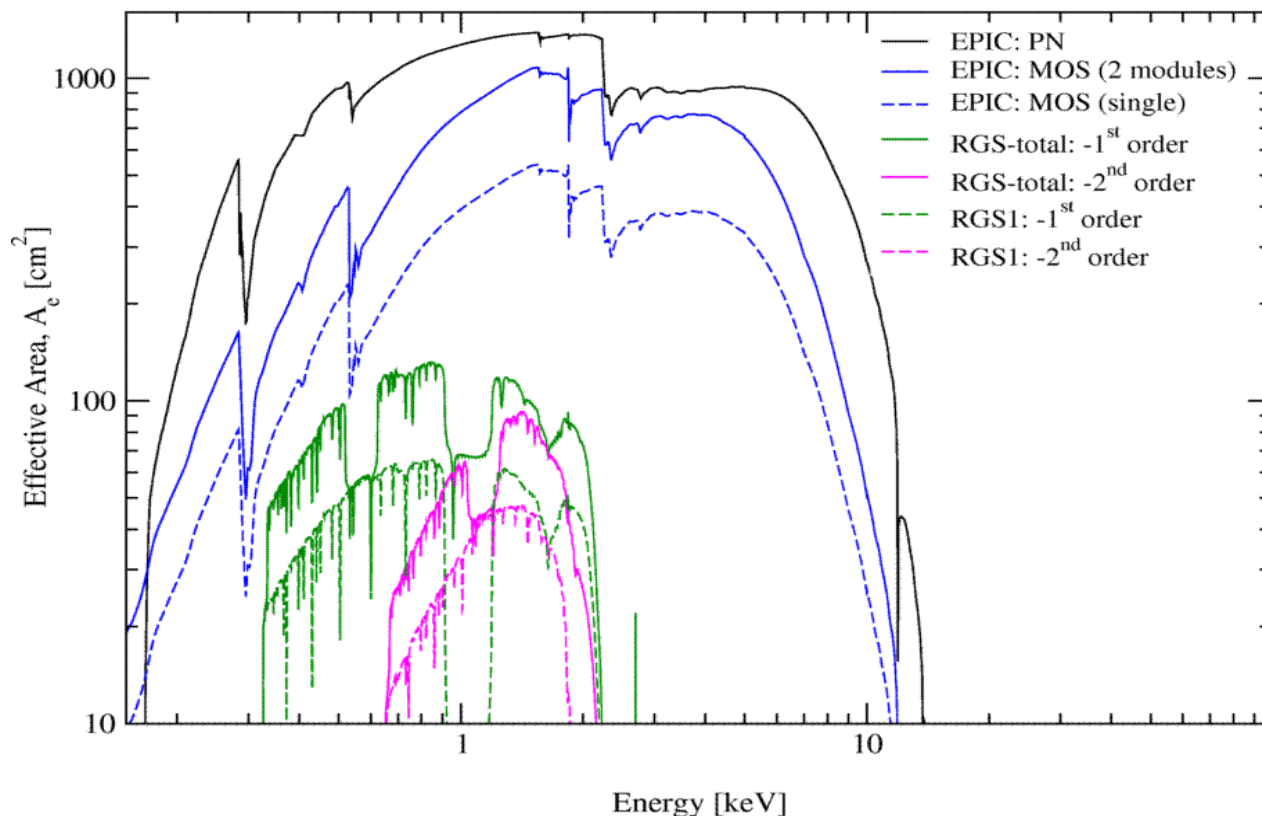


Figure 2.1: On-axis effective area of the XMM-Newton mirror for the EPIC-pn, EPIC-MOS and RGS instruments. It corresponds to the detectors with the open filter. Source: https://xmm-tools.cosmos.esa.int/external/xmm_user_support/documentation/uhb/effareaonaxis.html

The EPIC camera is composed of three X-ray CCD cameras, each installed behind one of the three X-ray telescopes on board XMM-Newton. Two of the cameras are built around Metal Oxide Semi-conductor CCD arrays (EPIC-MOS), and the third was developed using pn CCDs (EPIC-pn). The EPIC-MOS cameras are mounted in the same two telescopes as the RGS and both instruments share the incident light while the EPIC-pn camera receives all the light that reaches the telescope where it is mounted. All three cameras were developed to be photon counting, i.e., able to detect the direction and energy of incoming photons. This way, they can provide both extremely sensitive imaging observations when integrating all photons received and X-ray spectra with moderate spectral resolution ($E/\Delta E \sim 20 - 50$).

The EPIC camera efficiently covers an energy range from 0.1 to 15 keV and achieves a moderate angular resolution of 6 arcsec (FWHM of PSF) in a field-of-view approximately circular with 30 arcmin diameter. The on-axis net effective area¹ of the instruments on-board XMM-Newton is shown in Fig. 2.1. It can be seen that the XMM-Newton mirrors are most efficient in the 0.1 – 10 keV range, with the effective area dropping significantly at higher energies.

¹The effective area is essentially the efficiency times the collecting area of the telescope, i.e., the conversion between photons per square centimetre and counts.

Every time an observation of the sky is carried out with the EPIC camera, around 30 to 100 objects are detected inside its field-of-view, most of them AGN, as illustrated in Fig. 2.2. All those detections not correspondent to the main target of the observation are known as serendipitous detections. As XMM-Newton makes around 600 observations per year (covering ~ 100 sq. deg.), the number of serendipitous unique sources grows at the rate of ~ 30000 per year. Creating a catalogue out of the vast amount of XMM-Newton detections is one of the main goals of the Survey Science Centre (SSC).

The SSC is an international consortium composed of institutes² in Spain, the UK, Germany and France and associated scientists in Europe, USA and Japan. The SSC was founded to be in charge of the pipeline processing of XMM-Newton observation, to develop the official science analysis software for XMM-Newton, identify the detected sources in each observation and build and publish X-ray source catalogues (Watson et al., 2001). In 2012, the first two tasks were migrated to the XMM-Newton Science Operations Centre (SOC) based at the European Space Astronomy Centre (ESAC) in Spain, with the SSC focusing on the last two tasks. The SSC has periodically published catalogues composed of serendipitous detections of X-ray sources: the XMM-Newton Serendipitous Source Catalogues (Watson et al., 2009; Rosen et al., 2016; Webb et al., 2020). A more detailed description of the SSC and access to the published Serendipitous Source Catalogues are available on its website: <http://xmmssc.irap.omp.eu/>.

We have used data extracted from observations employed to construct these catalogues to both define the sample and obtain the associated X-ray spectroscopy. The source detection and fitting process of the X-ray spectra data from these catalogues will be described in Sect. 3.1 and Appendix A, respectively.

2.2 Ultraviolet: GALEX

The Galaxy Evolution Explorer (GALEX; Martin et al. 2005) was a NASA *Small Explorer* mission designed to observe galaxies at ultraviolet (UV) wavelengths, performing the first sky-wide UV survey. It was launched in 2003, and although it was planned to be a 29-month mission, it was extended and continued to probe the sky at UV wavelengths until 2013, when it was decommissioned.

GALEX carried a 50 cm Ritchey-Chretien telescope capable of obtaining far-ultraviolet (FUV, 1350 – 1750 Å) and near-ultraviolet (NUV, 1750 – 2750 Å) photometric and spectroscopic measurements at the same time, using a dichroic coating to separate the incoming light. GALEX had two broadband filters to obtain photometric measurements, one covering the

²The Mullard Space Science Laboratory, University College London, UK; the Max-Planck-Institut für extraterrestrische Physik, Germany; the University of Leicester, UK; the Leibniz-Institut für Astrophysik, Potsdam (AIP), Germany; the Département d’Astrophysique CEA/DRF/IRFU, Saclay, France; Instituto de Física de Cantabria, Santander, Spain; the Observatoire Astronomique de Strasbourg, France and the Institut de Recherche en Astrophysique et Planétologie, Toulouse, France.

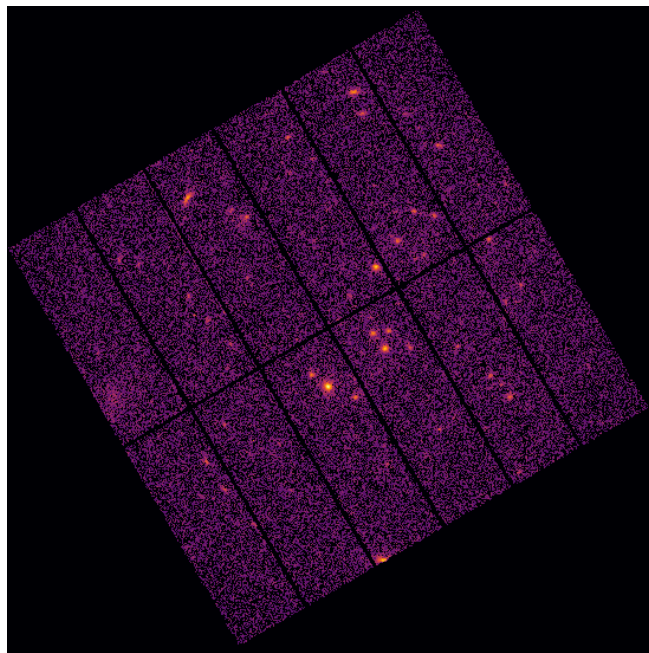


Figure 2.2: X-ray image at 0.2 – 12.0 keV energies of an XMM observation carried out with the EPIC-pn camera to observe the object 2XMMJ111606.9 + 423645 (bright source located at the bottom-left of the centre of the field-of-view). This observation is part of the fields used in the BUXS sample (see Sect. 3.1). The rest of the sources in the observation correspond to serendipitous detections. Image adapted from the XMM-Newton Science Archive: <https://nxs.a.esac.esa.int/nxs-a-web>.

FUV ($\lambda_{\text{eff}} = 1535 \text{ \AA}$) and another the NUV ($\lambda_{\text{eff}} = 2301 \text{ \AA}$), achieving an angular resolution in the first of 4.0 arcsec (FWMH) and of 5.6 arcsec (FWMH) in the second. However, the FUV detector stopped working in 2009, and subsequent observations only have NUV data. The transmission curves of the filters are shown in Fig. 2.3.

GALEX data releases are composed of several catalogues, the principal being the Nearby Galaxy Survey (NGS), Deep Imaging Survey (DIS), Medium Imaging Survey (MIS), and All Sky Imaging Surveys (AIS). The AIS is composed of observations with a sky coverage of over ~ 26000 square degrees, reaching a maximum depth of an AB magnitude of around 20 in both filters. The MIS is made of deeper observations over a smaller region of the sky of ~ 1000 square degrees, reaching a maximum depth of an AB magnitude of 23 in both filters. In this work, we used data drawn from the GUVCat source catalogue (Bianchi et al., 2014, 2017, 2019), built from AIS and MIS observations of the last data release, the GR6/7, published in 2013. Access to the AIS and MIS observations is available on its MAST website³ and access to the GUVCat catalogue is available at <https://archive.stsci.edu/hlsp/guvcat>.

³<https://galex.stsci.edu/GR6/>

2.3 Optical: Sloan Digital Sky Survey

The Sloan Digital Sky Survey (SDSS) is an international collaboration that aims to obtain a public database of photometry and spectrometry at optical and near-infrared wavelengths of the whole sky. The SDSS has relied on three different telescopes to achieve it: the Sloan Foundation 2.5m telescope at Apache Point Observatory (located in the Sacramento Mountains in Sunspot, New Mexico), the 2.5m Irénée du Pont Telescope at Las Campanas Observatory (located in the Atacama Desert, Chile) and the 1m NMSU 1-Meter Telescope at Apache Point Observatory. These telescopes have mounted several instruments, but in this thesis, we have worked with observations taken by the SDSS photometric camera, the SDSS-I/-II spectrograph and the Baryon Oscillation Spectroscopic Survey (BOSS) spectrograph:

- The SDSS photometric camera (Gunn et al., 1998), now decommissioned, was mounted in the Sloan Foundation 2.5m telescope and was used from 1998 to 2009 to collect photometric data of half of the northern sky in five different optical filters. It was composed of an array of 30 SITE/Tektronix 2048×2048 pixel CCDs distributed in six columns. Each of the rows was covered by one of the five SDSS broadband optical filters: u ($\lambda_{\text{eff}}^4 = 3551 \text{ \AA}$), g ($\lambda_{\text{eff}} = 4686 \text{ \AA}$), r ($\lambda_{\text{eff}} = 6165 \text{ \AA}$), i ($\lambda_{\text{eff}} = 7481 \text{ \AA}$) and z ($\lambda_{\text{eff}} = 8931 \text{ \AA}$). The camera was able to achieve a maximum depth in AB magnitudes of 22.0, 22.2, 22.2, 21.3 and 20.5, respectively, over 14555 square degrees with an angular resolution of 1.3 arcsec. The response curves of the five filters are shown in Fig. 2.3.
- The SDSS-I/-II spectrographs (Smee et al., 2013) are the old and now decommissioned two spectrographs used for the two first SDSS surveys. Each one was mounted in a different hemisphere to cover the whole sky. These spectrographs were able to collect spectra for 640 points in the focal plane simultaneously. For every point, an optical fibre of $3''$ diameter carried and splitted the detected light into two SITE/Tektronix 2048×2048 CCDs, one covering the bluest wavelengths ($3800 - 6150 \text{ \AA}$) and the other the reddest ($5900 - 9100 \text{ \AA}$), having a combined total coverage of 3800 to 9100 \AA . The SDSS-I/-II spectrographs were able to achieve spectral resolution values in the range from $R = 1560$ to $R = 2560$.
- The BOSS spectrographs (Smee et al., 2013) are a rebuilding of the two old SDSS spectrographs. The number of fibres was increased to a thousand, and their diameter reduced to $2''$. Similar to its predecessor, each of the two constituents has a red channel, relying on a fully depleted $4K \times 4K$ LBNL CCDs and covering $5650 - 10000 \text{ \AA}$, and a blue channel, using $4K \times 4K$ e2V CCDs covering $3600 - 6350 \text{ \AA}$. The spectral resolution of BOSS ranges from $R = 1850$ at 6000 \AA to $R = 2650$ at 9000 \AA in the red

⁴ λ_{eff} is defined as

$$\lambda_{\text{eff}} = \frac{\int \lambda T(\lambda) d\lambda}{\int T(\lambda) d\lambda}$$

where $T(\lambda)$ is the filter transmission.

arm and from $R=1560$ at 3700 \AA to $R=2270$ at 6000 in the blue arm.

The SDSS has published over the years incremental data releases made of the combination of several catalogues. The DR1 was released in June 2003 (Abazajian et al., 2003), and nowadays, the last data release is DR18, published in 2023 (Almeida et al., 2023).

We have used DR17, released in 2021 (Abdurro'uf et al., 2022). The data published was a combination of all spectra taken with BOSS and the SDSS-I/-II spectrographs up to the publication date. Optical spectra can be accessed through <https://dr17.sdss.org/optical/spectrum/search>. To get the optical photometric information, we relied on the Legacy imaging catalogue available in the DR14, published in 2017 (Abolfathi et al., 2018). It is composed of observations taken from 1998 to 2009 with the old SDSS photometric camera covering 14055 square degrees. Imaging data is available at <https://skyserver.sdss.org/dr14/en/tools/crossid/crossid.aspx>.

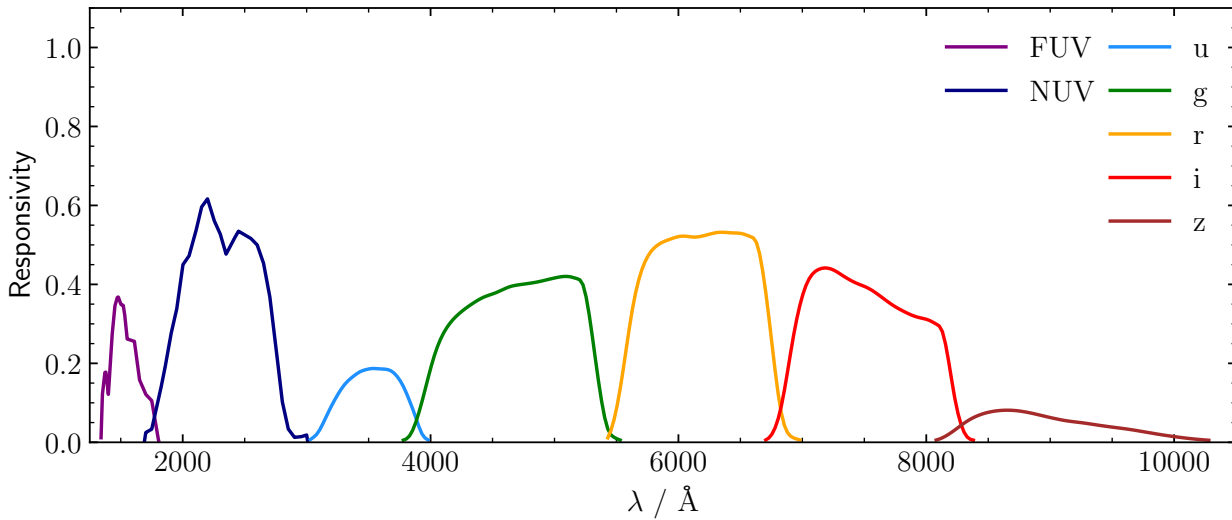


Figure 2.3: Full responsivity (filter transmission + detector response) of the ultraviolet filters (FUV, NUV) used by GALEX and the optical filters (u, g, r, i, z) used by SDSS.

2.4 Near-infrared

2.4.1 VISTA

The Visible and Infrared Survey Telescope for Astronomy (VISTA; Emerson et al. 2006) is a 4.3m telescope part of the Paranal Observatory. Since its first light in 2009, it has been surveying the southern sky at NIR wavelengths.

VISTA has mounted the VISTA InfraRed CAMera (VIRCAM; Dalton et al. 2006) composed of sixteen HgCdTe 2048×2048 pixel arrays covering a wavelength range of $0.9 - 2.4 \mu\text{m}$ with an angular resolution of 0.51 arcsec. To obtain the photometric measurements, VIRCAM was used with six NIR broadband filters: Z ($\lambda_{\text{eff}} = 0.88 \mu\text{m}$), Y ($\lambda_{\text{eff}} = 1.02 \mu\text{m}$), J ($\lambda_{\text{eff}} =$

1.25 μm), H ($\lambda_{\text{eff}} = 1.65 \mu\text{m}$), Ks ($\lambda_{\text{eff}} = 2.15 \mu\text{m}$). It also has three narrow filters at 0.98 μm , 0.99 μm and 1.18 μm . We have worked only with measurements done with the broad filters, whose transmission curves are shown in Fig. 2.4. VIRCAM has been performing observations until March 2023.

VISTA has carried out six public surveys using VIRCAM. We have used data from two of these: the VISTA Kilo-Degree Infrared Galaxy Survey (VIKING; Edge et al. 2013), whose latest data release (DR4) covers 1500 square degrees and reaches a maximum depth in AB magnitudes of $J = 22.1$, and the second data release of the VISTA Hemisphere Survey (VHS; McMahan et al. 2013), that reaches a maximum depth in AB magnitudes of $J = 21.2$ and covers all the southern hemisphere sky, except for those sky regions already covered by other VISTA surveys. Processed data of both catalogues can be accessed from the ESO Archive Science, <https://archive.eso.org/scienceportal/home>.

2.4.2 2MASS

The Two Micron All Sky Survey (2MASS; Skrutskie et al. 2006) was a project running from 1997 to 2001 to survey all the sky at NIR wavelengths uniformly. To achieve it, 2MASS relied on two 1.3 m highly automated telescopes: one placed in Mt. Hopkins, Arizona, and another at the Cerro Tololo Interamerican Observatory, Chile.

Both telescopes used a three-channel camera, and every channel was composed of a 256×256 array of HgCdTe detectors. The cameras were able to simultaneously observe at three different broadband filters (J, H, and K_s with $\lambda_{\text{eff}} = 1.25 \mu\text{m}$, 1.65 μm and 2.17 μm , respectively) with an angular resolution of $\sim 2.5 - 2.7$ arcsec. The transmission curves of the three filters are shown in Fig. 2.4.

All observations were released in the All-Sky Data Release in 2003. It covers 99.998% of the sky up to a maximum depth in Vega magnitudes of $J = 15.8$, containing positional and photometric information for more than 400 million sources. The data can be accessed from <https://irsa.ipac.caltech.edu/data/2MASS/docs/releases/allsky/>.

2.4.3 UKIRT

The United Kingdom Infrared Telescope (UKIRT; Lawrence et al. 2007) is a 3.8 m telescope placed on Mauna Kea, Hawaii. Starting from 1979, it has been surveying the north hemisphere at infrared wavelengths, ranging from 1 to 30 μm , and continues nowadays. We have used NIR measurements taken with the Wide Field Camera (WFCAM; Casali et al. 2007).

The WFCAM is a wide-field camera imager with an HgCdTe detector composed of four 2048×2048 pixel arrays able to cover a total sky area of 0.2 square degrees per observation. The WFCAM has obtained photometry measurements using five broadband filters; Z ($\lambda_{\text{eff}} = 0.88 \mu\text{m}$), Y ($\lambda_{\text{eff}} = 1.03 \mu\text{m}$), J ($\lambda_{\text{eff}} = 1.25 \mu\text{m}$), H ($\lambda_{\text{eff}} = 1.63 \mu\text{m}$) and K ($\lambda_{\text{eff}} = 2.21 \mu\text{m}$), and two narrow band filters; H_2 ($\lambda_{\text{eff}} = 2.14 \mu\text{m}$) and Br_γ ($\lambda_{\text{eff}} = 2.18 \mu\text{m}$). As with VISTA,

we have only used data taken with the broad filters. Their transmission curves are shown in Fig. 2.4. UKIRT has completed several surveys using WFCAM, with the most relevant ones for this thesis being the UKIRT Deep Sky Survey (UKIDSS; Warren et al. 2007) and the UKIRT Hemisphere Survey (UHS; Dye et al. 2018).

The UHS is a survey of 12700 square degrees of the north hemisphere using only the J and K filters, taking measurements up to a depth of 19.6/17.6 with an angular resolution of 0.75/1.1 arcsec, respectively. Its most recent data release is the DR2. UKIDSS is instead a composition of five smaller surveys, three of them based on observations of extragalactic sources using the JHK filters: the Large Area Survey (LAS), the Deep Extragalactic Survey (DXS) and the Ultra Deep Survey (UDS). Each of them has a different surveyed area (3792, 31 and 0.77 square degrees, respectively) and depth (20.2, 22.5 and 25.0 in Vega magnitudes in J, respectively). The LAS also took data in the Y filter. Data from these surveys can be accessed at the WFCAM Science Archive: <http://wsa.roe.ac.uk/index.html>.

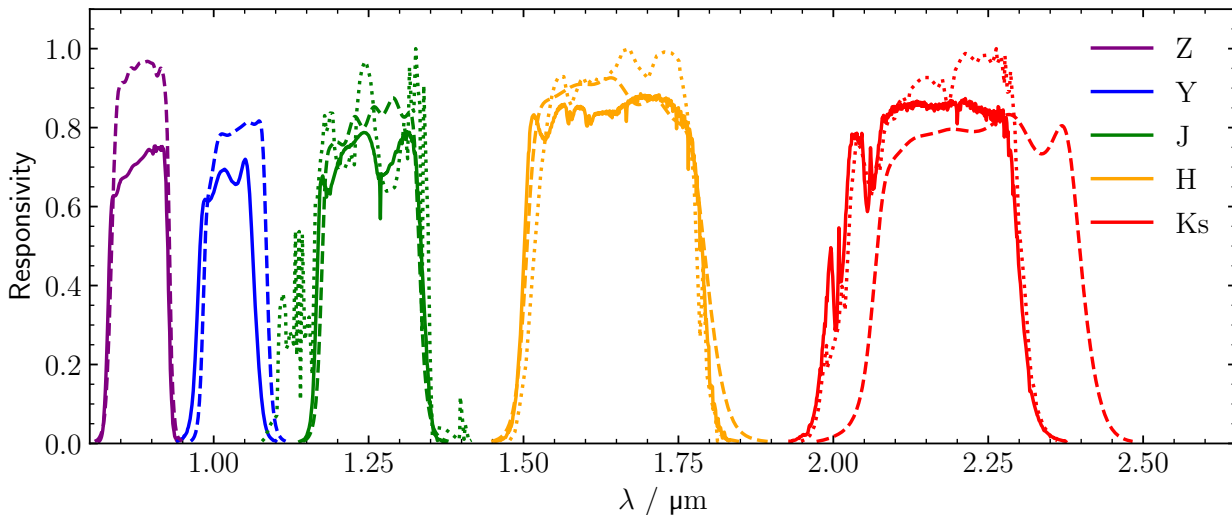


Figure 2.4: Responsivity curves of the broad NIR filters (Z, Y, J, H, K_S) used by VISTA (solid line), 2MASS (dotted line) and UKIRT (dashed line).

2.5 Mid-infrared: WISE

The Wide-field Infrared Survey Explorer (WISE; Wright et al. 2010) is a NASA *Medium-Class Explorers* mission composed of a 0.4 m space telescope launched in 2009 to study the whole sky at mid-infrared (MIR) wavelengths. WISE is equipped with four broad band filters centered at 3.4 μm (W_1), 4.6 μm (W_2), 12 μm (W_3) and 22 μm (W_4). The responsivity curves of the filters are shown in Fig. 2.5.

To carry out the observations in the long-wavelength channels (W_3 and W_4) WISE employed Si:As arrays with 1024×1024 pixels as detectors. These detectors need extremely low temperatures (below 8 K) to work and need a solid hydrogen cryostat. The refrigerant

was depleted in August 2010, meaning observations after this date were done only with W_1 and W_2 . But before the exhaustion of the refrigerant, WISE was able to map the whole sky, leading to the publication of the WISE All-Sky Source Catalogue in 2012 (Cutri et al. 2012).

The All-Sky Data Release is a combination of all the sources detected during the full-cryogenic phase that have a signal-to-noise ratio (SNR) ≥ 5 in at least one of the four filters, including more than 500 million objects and attaining a sky coverage of $> 99\%$. WISE was able to achieve sensitivities better than 0.08, 0.11, 1 and 6 mJy and angular resolutions of 6.1, 6.4, 6.5 and 12 arcsec at 3.4, 4.6, 12 and 22 μm respectively. The astrometric precision is better than 0.15 arcsec for high SNR sources (SNR > 20). The All-Sky Source Catalogue can be accessed at <https://wise2.ipac.caltech.edu/docs/release/allsky/>.

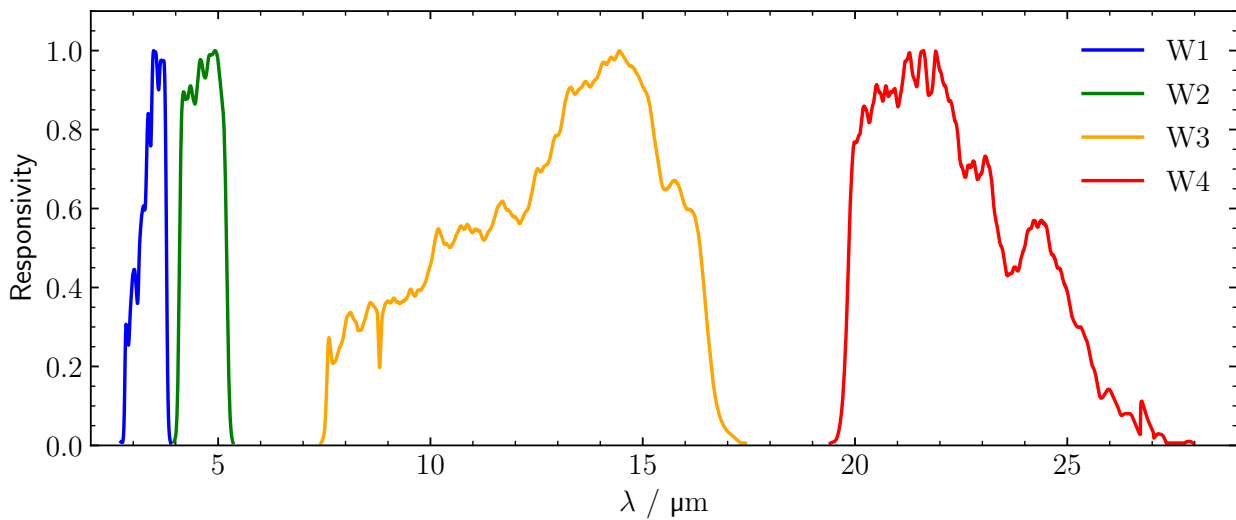


Figure 2.5: Responsivity curves of the four WISE filters (W_1 , W_2 , W_3 , W_4).

In Tab. 2.1 we show the effective wavelengths of the filters in the surveys used in this thesis, along with the depth achieved in each of them

Survey	Filter	$\lambda_{\text{eff}} / \mu\text{m}$	Depth / mag	Survey	Filter	$\lambda_{\text{eff}} / \mu\text{m}$	Depth / mag
(1)	(2)	(3)	(4)	(1)	(2)	(3)	(4)
AIS	FUV	0.153	20.5	VHS	Y	1.02	21.2
	NUV	0.231	20.5		J	1.25	21.2
MIS	FUV	0.153	23.0		H	1.64	20.6
	NUV	0.231	23.0		K _S	2.15	23.5
SDSS	u	0.359	22.0	<i>UKIDSS</i>	Y	1.03	20.2
	g	0.464	22.2	J	1.24	20.0	
	r	0.612	22.2	H	1.62	18.8	
	i	0.744	21.3	K _S	2.21	18.2	
	z	0.890	20.5	<i>UHS</i>	J	1.24	19.6
zMASS	J	1.25	15.8	<i>WISE</i>	W ₁	3.4	16.6
	H	1.65	15.1	W ₂	4.6	15.6	
	K _S	2.17	14.3	W ₃	12	11.3	
VIKING	Z	0.88	23.1	W ₄	22	8.0	
	Y	1.02	22.3				
	J	1.25	22.1				
	H	1.65	21.5				
	K _S	2.15	21.2				

Table 2.1: Summary of the effective wavelength and depth of the filters used by the photometric surveys. **Col. 1:** name of the survey; **Col. 2:** filter name; **Col. 3:** effective wavelength; **Col. 4:** maximum depth in AB magnitudes. For surveys in italics, it corresponds instead to Vega magnitude. The UKIDSS values correspond to the Large Area Survey, the survey with the largest fraction of the sky covered.

Chapter 3

The BUXS AGN Sample

In this thesis, we have analysed how the properties of AGN impact their optical spectroscopic classification. To achieve this, we required a sample composed of bright AGN to obtain accurate constraints of their physical properties and large and well-defined to derive robust statistical results. The sample must also be selected at high-energy X-rays so it is not biased against the most obscured AGN. As such, we have used the Bright Ultra-Hard XMM-Newton Survey (BUXS¹; Mateos et al. 2012, 2015), a unique X-ray-selected AGN sample with optical classifications (type 1/2) and accurate spectroscopic redshift values.

In this chapter, we will first introduce the definition and main properties of BUXS in Sect. 3.1. Next, in Sect. 3.2 we will detail the follow-up spectroscopic identification program of the sample. Then, we will describe the procedure followed for building the spectral energy distributions in Sect. 3.3.

3.1 Sample definition

BUXS is a flux-limited sample of 258 X-ray bright sources detected by XMM-Newton at energies above 4.5 keV. The sources have 4.5 – 10 keV fluxes greater than $6 \times 10^{-14} \text{ erg s}^{-1} \text{ cm}^{-2}$. High-energy ($E > 4.5 \text{ keV}$) X-rays were used for AGN selection, as indicated before, to reduce the strong detection bias against AGN with high levels of absorption ($\log_{10}(N_{\text{H}} / \text{cm}^{-2}) > 23$). At the same time, the flux limit ensures that the sample includes only bright enough objects so that a reliable classification and redshift can be derived from their optical spectra. BUXS contains a total of 255 AGN after removing Galactic stars and BL Lacs (1.2%), making it one of the largest X-ray-bright flux-limited AGN samples among the existing XMM-Newton and Chandra samples to date. BUXS have an almost complete ($> 98\%$) optical (type 1/2) classification and redshift determination from either SDSS or dedicated optical/NIR spectroscopic observations. Thanks to the work of this thesis, it also includes a uniform intermediate optical classification up to $z = 0.75$, allowing us to study the subtype of non-local AGN.

¹<https://buxs.unican.es/>

The BUXS sample was built from a subset of the observations used in the production of the XMM-Newton serendipitous source catalogues that fulfilled the following criteria:

- High galactic latitude, $|b| > 20^\circ$, to minimize the contamination from Galactic stars and the high Galactic absorbing column densities.
- Free of bright and/or extended X-ray sources where most of the field of view can be used for serendipitous source detection.
- More than 10 ks of clean exposure time with the EPIC-pn camera.

Additionally, the BUXS sky area was selected to overlap with the SDSS imaging survey. The total sky area encompassed is 44.43 square degrees distributed over 381 XMM-Newton observations.

The source detection was carried out with the same pipeline as in the 2XMM catalogues (Watson et al., 2009; Rosen et al., 2016; Traulsen et al., 2019; Webb et al., 2020). Briefly, for every observation, the area of the detector suitable for source detection was defined with the SAS task `emask`². Then, `eboxdetect`³ was used to search for the sources, and finally, `emldetect`⁴ determined their parameters by performing a simultaneous maximum likelihood PSF fitting. For further details, see Mateos et al. (2008).

To ensure the good quality of the data, only sources with a likelihood $\mathcal{L} > 15$ were kept as detections. This roughly translates to a significance of detection greater than 5σ (Cash, 1979). Sources close to CCD gaps were also masked. The X-ray spectra were extracted and modelled using empirically and physically motivated models for all objects. This allowed us to obtain their intrinsic (absorption-corrected) X-ray luminosity at rest-frame 2 – 10 keV energies, L_X . The fitting process was carried out by collaborators of the Galaxies and AGN group of the Instituto de Física de Cantabria (IFCA). However, as L_X was used in our analysis, a brief description of the X-ray fitting process is included in Appendix A.

3.2 Optical counterpart identification and spectroscopic follow-up

In order to obtain the optical spectra required to determine the AGN redshift and classification, it was necessary to identify the optical counterparts of our X-ray detections. As the BUXS sample was defined to match the sky area covered by SDSS, the optical counterpart identification was carried out using the SDSS imaging catalogue together with the likelihood-ratio crossmatching algorithm of Pineau et al. (2011). This algorithm, based on the likelihood ratio of De Ruiter et al. (1977), calculates the probability of an optical counterpart candidate to be the actual counterpart of the X-ray detection. Optical detections were found for 250 of the 255 BUXS sources ($\sim 98\%$). For the remaining five objects, the opti-

²Documentation at <https://xmm-tools.cosmos.esa.int/external/sas/current/doc/emask/>

³Documentation at <http://xmm-tools.cosmos.esa.int/external/sas/current/doc/eboxdetect/>

⁴Documentation at <http://xmm-tools.cosmos.esa.int/external/sas/current/doc/emldetect/>

cal counterparts were identified by carrying out deeper observations (up to 24 – 25 mag) with the Telescopio Nazionale Galileo (TNG) and performing a simple crossmatching with search radius of $3''$. The mean distance between the X-ray sources and their optical counterparts is $\lesssim 2$ arcsec. The fraction of spurious matches is expected to be similar to that of the MIR sources ($\lesssim 1\%$, see next section), given their proximity ($\lesssim 1$).

A total of 176 objects had SDSS optical spectra (69% of the sample); 60 of them were taken with the BOSS spectra, and the 116 remaining with the old SDSS-I/-II spectrograph. To complement the SDSS spectra and improve those with the lowest SNR, an intensive campaign of optical spectroscopic follow-up was carried out. To do so, the following telescopes and associated instruments were employed. The configuration used in every instrument, associated characteristics and number of spectra obtained are summarised in Table 3.1.

- **The Gran Telescopio CANARIAS (GTC)** is a 10.4 m optical-IR telescope situated at the Roque de los Muchachos Observatory on the island of La Palma. For the optical spectroscopic follow-up, the Optical System for Imaging and low-Intermediate-Resolution Integrated Spectroscopy (OSIRIS) was used. OSIRIS is an optical spectrograph capable of obtaining low-to-mid ($R = 360\text{--}2500$) resolutions mounted at the Namyth-B focus of the GTC.
- **The Very Large Telescope (VLT)** of the ESO is a facility composed of four Unit Telescopes (UT) of 8.2 m situated at Cerro Paranal, Chile. In the Cassegrain focus of the UT1, also known as Antu, is installed the FOcal Reducer/low dispersion Spectrograph 2 (FORS2). FORS2 is an optical spectrograph that is able to reach low to medium ($R = 260\text{--}2600$) spectral resolutions.
- **Subaru** is an 8.2 m optical-IR telescope of the National Astronomical Observatory of Japan (NAOJ) situated at Mauna Kea, Hawaii. The Faint Object Camera and Spectrograph (FOCAS), mounted in the Cassegrain focus of the Subaru Telescope, was used. FOCAS is an optical spectrograph capable to obtain low-to-mid ($R = 900\text{--}2700$) resolution spectra.
- **The William Herschel Telescope (WHT)** is a 4.2 m optical telescope part of the Isaac Newton Group of Telescopes (ING) situated at the Roque de los Muchachos Observatory in La Palma. To collect the optical spectra, two instruments mounted at the WHT Cassegrain focus were used:
 - The Auxiliary-port CAMera (ACAM) was an optical spectrograph used to obtain low ($R = 230\text{--}770$) resolution spectra.
 - The Intermediate-dispersion Spectrograph and Imaging System (ISIS) was a double-arm optical spectrograph capable of obtaining low-to-high ($R = 500\text{--}11000$) resolution spectra.

- **The New Technology Telescope (NTT)** is a 3.58 m optical-NIR telescope of ESO at La Silla observatory, Chile. The instrument used was the ESO Faint Object Spectrograph and Camera version 2 (EFOSC2), which is mounted at the Nasmyth B focus. EFOSC2 is an optical-NIR spectrograph designed to obtain low-resolution ($R \sim 100 - 1200$) spectra.
- **The Telescopio Nazionale Galileo (TNG)** is a 3.6 m optical-NIR telescope of the Istituto Nazionale di Astrofisica (INAF) operating at the Roque de los Muchachos Observatory in La Palma. The observations were carried out with the Device Optimized for the LOw RESolution (DOLORES), an optical spectrograph designed for the acquisition of low-resolution ($R = 585 - 715$) spectroscopy observations.
- **The Nordic Optical Telescope (NOT)** is a 2.56 m optical telescope located at the Roque de los Muchachos Observatory in La Palma. The Alhambra Faint Object Spectrograph and Camera (ALFOSC) was used. ALFOSC is a low-resolution ($R = 100 - 1000$) optical spectrograph.
- **The University of Hawaii telescope (UH88)** is an optical 2.2m telescope located near the summit of Mauna Kea, in Hawaii. The UH88 was used in combination with the Wide Field Grism Spectrograph (WFGS), an optical spectrograph working at low ($R = 620 - 730$) resolutions.

After combining all observations, we had optical spectra for 254 AGN ($> 99\%$). The typical optical spectra extend up to 9000\AA . This means that at redshifts higher than $z \sim 0.4$, $H\alpha$ ($\lambda_c^5 = 6562\text{\AA}$) will not be covered. As we want to obtain a classification based on the same set of lines ($H\alpha$, $H\beta$ and $[\text{OIII}]5007\text{\AA}$) for all objects, this is especially a problem for those AGN for which we are not able to detect a broad component of $H\beta$, as we can not distinguish between 1.9s and 2s.

To mitigate it, a spectroscopic follow-up at NIR wavelengths was also carried out for those AGN. This allowed us to have a complete and uniform optical spectroscopic classification up to $z = 0.75$. The following telescopes and instruments were used to perform these observations:

- **The GTC** was used in conjunction with the Infrared Multi-Object Spectrograph (EMIR, in its Spanish acronym). EMIR is a NIR ($0.9 - 2.5\text{ }\mu\text{m}$) spectrograph working at low ($R = 987$) and medium ($R = 4000 - 5000$) resolutions.
- **The WHT** was employed again to use the Long-slit Intermediate Resolution Infrared Spectrograph (LIRIS). LIRIS is a NIR (0.8 to $2.5\text{ }\mu\text{m}$) spectrograph capable of taking spectra with low to medium resolutions ($R = 700 - 2500$).

⁵ λ_c corresponds to the rest-frame wavelength of the indicated emission line.

The configurations for the NIR instruments and the number of spectra obtained for each one are also shown in Table 3.1.

Telescope (1)	D_T/m (2)	Instrument (3)	N (4)	Grism (5)	$\lambda/\text{\AA}$ (6)	Slit / " (7)	Seeing / " (8)	R ($\lambda / \Delta\lambda$) (8)
GTC	10.4	OSIRIS	30	R500R	4800 – 10000	1.0	0.9	352
						1.23	1.1	286
		EMIR	18	YJ	8500 – 13500	1.0	0.9	987
VLT	8.2	FORS2	32	300V	4450 – 8650	1.0	0.7	440
						1.3	1.0	338
Subaru	8.2	FOCAS	4	300B	4700 – 9100	0.8	0.5	500
WHT	4.2	ACAM	3	V400	3300 – 9500	1.0	0.8	570
						1.5	1.5	380
		ISIS	17	R300B	3200 – 5300	1.46	0.9	640
						1.52	0.9	620
		R158R			5300 – 9300	1.46	0.9	640
						1.52	0.9	620
LIRIS	4	lr_hk	8870 – 15310	1.0	0.8	700		
NTT	3.58	EFOOSC2	18	Grism 4	4085 – 7520	1.0	0.7	370
				Grism 13	3685 – 9315	1.5	1.1	210
TNG	3.6	DOLORES	62	LR-B	3000 – 8430	1.0	0.8	585
						1.5	0.9	390
						2.0	0.8	293
NOT	2.5	ALFOSC	5	Grism 4	3200 – 9600	1.0	1.1	360
						1.3	1.5	277
						1.8	1.5	200
						Grism 7	3650 – 7110	1.0
UH	2.2	WFGS	3	Green(400)	3800 – 9700	1.6	0.6	300

Table 3.1: Summary of the properties of the telescopes and associated instruments used. **Col. 1:** name of the telescope; **Col. 2:** diameter of the telescope in meters; **Col. 3:** name of the instrument; **Col. 4:** number of sources observed; **Col. 5:** grism; **Col. 6:** wavelength range covered; **Col. 7:** width of the slit used; **Col. 8:** average seeing of the observation nights; **Col. 9:** spectral resolution. Instrument names in italics correspond to NIR spectrographs.

3.3 Spectral energy distribution construction

In this thesis, we have studied the effect on the optical spectroscopic classification of several observational parameters (AGN luminosity, reddening...), whose reliable determination requires a proper decomposition of the observed emission of AGN and host galaxy. Although these properties could be derived from the optical spectra in 1.0, 1.2 and 1.5, it is no longer possible when the host galaxy dominates. To obtain estimations of these parameters from the same origin for all sources, the rest-frame UV-to-mid-IR spectral energy distribution (SED) of our AGN were built. As they cover a higher wavelength range than the spectra, they allow to constrain the AGN extinction and luminosity even when the host galaxy dominates. To do so, the UV, optical, NIR, and MIR counterparts of our X-ray sources were identified, and the observed fluxes were extracted from the photometric magnitudes available in the catalogues introduced in Chapter 2. The process followed will be described below.

We corrected the fluxes obtained for the Milky Way extinction using the model of Allen (1985). To derive the value of A_V associated with the sky coordinates of an object. First we obtained the Galactic N_H from the LAB map of Kalberla et al. (2005). Then, we converted it to an optical reddening assuming a standard Galactic gas/dust ratio of $A_V/N_H = 5.3 \times 10^{-22} \text{ cm}^{-2}$ (Bohlin et al., 1978) and $R_V = 3.1$. The fraction of sources detected at the different spectral bands used is shown in Tab. 3.2.

Filter	Detection	Filter	Detection	Filter	Detection	Filter	Detection
(1)	(2)	(1)	(2)	(1)	(2)	(1)	(2)
NUV	36%	u	98%	Z	2%	W ₁	100%
FUV	23%	g	98%	Y	45%	W ₂	100%
		r	100%	J	90%	W ₃	99%
		i	98%	H	69%	W ₄	96%
		z	98%	K _S	73%		

Table 3.2: From left or right, fraction of sources detected at UV, optical, NIR and MIR spectral bands. Upper-limits have been considered as detections for the calculation of the fraction of sources detected. The Z filter has a low detection fraction because only VIKINGS measurements were carried out with this filter.

UV photometry

At rest-frame UV wavelengths, the observed SED of unobscured or mildly obscured AGN shows a strong emission from the accretion disk. As UV emission is especially affected by dust, obtaining photometric points at these wavelengths allows for a better determination of the level of extinction of the disk. We looked for UV counterparts using the GUVCat catalogue. The coordinates of the optical counterparts of our objects were cross-correlated with GUVCat using a simple position matching with a search radius of 5 arcsec to account for the less precise astrometry of GALEX compared to the other catalogues. We used the

coordinates of the optical counterparts, as their astrometry is more accurate than the X-ray sources, and the estimated fraction of spurious matches is low.

GUVCat offers Kron, isophotal and fixed aperture AB magnitudes. For all objects, we used the Kron magnitudes, which were selected as the best magnitude for our objects by the GALEX pipeline. For all detections in the NUV and FUV filters, the SNR was at least > 2 . All magnitude flags associated with artefacts were rejected. In total, we had UV photometry for 91 objects. The mean distance between the UV identification and its optical counterpart is ~ 1 arcsec.

As GUVCat is composed of two catalogues with overlapping sky area, in some objects a clean observation from both the AIS and the MIS were available. In these cases, the MIS observations were kept, as they are deeper. Calibrated magnitudes provided by the GUVCat were converted into fluxes using the zero-points provided by GALEX.

Optical photometry

Optical photometry is fundamental to understanding whether the observed emission is AGN or host-galaxy dominated. The SDSS catalogues were used to obtain the optical magnitudes in the u, g, r, i and z filters. As our sample is composed of bright AGN, it is expected to have an optical counterpart for almost every object. Indeed, photometry observations were obtained for 250 of the 255 BUXS sources ($\sim 98\%$; see Tab. 3.2).

The SDSS legacy imaging catalogue has different magnitudes (`modelMag`, `petroMag`, `psfMag`...) depending on how the flux of each object is extracted. A full description can be found on the SDSS website⁶. In this work, the `modelMag` were used. The aperture used for the flux determination is obtained from the best fit of the two-dimensional light profile of the image of the object in the r-filter. The best fit between a de Vaucouleurs and a pure exponential profile model is selected. The `modelMag` magnitude provides reliable estimates for extended objects and at the same time, they are indistinguishable from the standard PSF magnitudes for point-like objects.

The SDSS magnitudes and errors were converted to fluxes following the procedure detailed in the SDSS website⁷. This has two main differences from the typical translation from magnitudes to fluxes. First, the magnitudes defined in the SDSS catalogues are inverse hyperbolic sine (`asinh`) magnitudes (Lupton et al., 1999). These are used because they behave better at low SNR or even negative fluxes than the typical Pogson magnitudes, while both are indistinguishable at high SNR. The `asinh` magnitudes are defined as:

$$m = -\frac{2.5}{\ln(10)} \times \left[\operatorname{asinh} \left(\frac{f_m/f_0}{2b} \right) + \ln(b) \right] \quad (3.1)$$

⁶<https://www.sdss3.org/dr10/algorithms/magnitudes.php>

⁷<https://www.sdss3.org/dr10/algorithms/fluxcal.php>

where f_m corresponds to the flux in the band under consideration, f_0 corresponds to the flux of an object with a conventional magnitude of 0, while b is softening parameter of the photometric band and correspond to the 1σ noise of the sky in a PSF aperture in $1''$ seeing. The values of b are measured relative to f_0 and are tabulated by SDSS on their website⁷. Secondly, the SDSS magnitudes are not exactly on the AB system, as intended, and had to be corrected following the SDSS recommendations⁶. Additionally, a 2 per cent error was added in quadrature to the flux uncertainties to account for systematic uncertainties in the zero-points (Padmanabhan et al., 2008).

MIR photometry

The torus is the main responsible for the emission in the MIR region. Hence, MIR photometry allows us to constrain the intensity of its emission and, by extension, the AGN luminosity. The same cross-matching algorithm used to identify the optical counterparts was employed to select the MIR counterpart of our AGN in the WISE bands. The detection rate on the MIR filters is shown in Tab. 3.2. Detections with $\text{SNR} > 2$ were available at W_1 , W_2 and W_3 for 249 AGN ($> 97\%$) and for 186 AGN ($> 72\%$) at W_4 . All WISE magnitudes are in the Vega system. The mean distance between the X-ray source and its MIR counterpart is $\lesssim 2$ arcsec. The fraction of spurious matches was estimated to be $< 1\%$, from the cross-matching of X-ray and WISE sources using a large offset of 3 arcmin in either the RA or Dec. in the MIR coordinates.

For 10 objects, a non-zero value of the photometric quality flag was found, indicating that the fluxes may be contaminated by a nearby source. However, after a careful visual revision of the WISE images, it was concluded that there were not any issues with the measured fluxes and decided to keep them in the sample.

The flux of the WISE magnitudes has been calculated using profile-fitting photometry except for six objects flagged as extended, for which elliptical aperture magnitudes were used. To do so, the zero-points of the Vega magnitude system were used. A 1.5 per cent error was added in quadrature to account for the systematic uncertainty associated with the zero-points and an additional 10 per cent to the W_3 and W_4 bands for the uncertainties associated with the red and blue calibrators used for the conversion from magnitudes to janskys (Wright et al., 2010).

NIR photometry

The NIR emission of the host galaxy reaches its maximum at $\sim 1 \mu\text{m}$. The addition of photometry at these wavelengths allows for a better determination of the luminosity of the host galaxy. Accurate positions for all sources from the optical and MIR counterparts were already obtained. To identify the counterparts, the coordinates of the optical counterparts were cross-correlated to the NIR catalogues introduced in Sect. 2.4 using a simple position matching with a search radius of 2 arcsec, except for 2MASS. For these, the counterparts of

our sources were already provided directly by the AllWISE catalogue. To identify the point sources, the closest 2MASS source within a 3 arcsec radius in the point source catalogue (PSC) was selected. In all our point sources, a unique match was returned at a separation $< 1''$. For the extended sources, the 2MASS extended source catalogue (XSC) was matched with the AllWise extended detections with a matching radius equal to 1.1 times the Ks isophotal of the 2MASS XSC sources.

A total of 239 of the 255 AGN ($\approx 94\%$) have at least one photometric observation in the NIR from any of the catalogues. Both UKIDSS, 2MASS and UHS magnitudes were in the Vega system, while VHS and VIKING magnitudes were in the AB system. The mean distance between the optical sources and their NIR counterpart is smaller than 1 arcsec and is well below the radius for which multiple matches started to be found ($\sim 5''$). The fraction of spurious matches for the NIR sources is expected to be similar to that of the MIR sources, given their proximity ($\lesssim 1''$ for more than $> 90\%$).

When we had magnitudes from more than one survey, we first prioritised photometry from UKIDSS and VIKING. If they were not available, we used data from VHS. If no other was available, we used 2MASS or UHS.

The Petrosian magnitudes were obtained from the UKIDSS observations for extended sources and the default aperture magnitudes for point sources. For the rest, fixed aperture magnitudes for point sources and profile-fitting magnitudes for extended sources were used. Magnitudes from the different NIR catalogues were converted into fluxes using the corresponding zero-points. Similar to the SDSS photometry, a 2 per cent error was added in quadrature to account for uncertainties in the zero-points.

Chapter 4

Data reduction and fitting

To achieve the scientific goals of this thesis, we needed to obtain a robust determination of the optical spectroscopic classification of our AGN. We had to disentangle the emission of our AGN into continuum and emission line components, identify the lines of interest and determine their emission properties as flux and width. To do so, we have fitted the optical and NIR spectra of our sample sources. These NIR spectra were a new addition to the ensemble of BUXS data, obtained during this thesis.

But we also need to extract the optical extinction suffered by the AGN emission or the luminosity of the AGN and the host galaxy. To obtain this information fitted the UV-to-MIR spectral energy distributions of our AGN in a decomposition process similar to that of our spectra.

In this chapter, we will first summarise the optical spectral reduction process in Sect. 4.1. Next we will introduce the procedure followed to reduce the raw data from EMIR in Sect. 4.2. Then, we will describe the models and fitting process used to identify the lines and derive their fluxes in Sect. 4.3. Finally we will describe the photometric fitting process carried out in Sect. 4.4.

4.1 Optical spectral reduction

Members of the Galaxies and AGN group at IFCA already reduced the optical spectra using standard procedures and the Image Reduction and Analysis Facility (IRAF) software (Tody, 1986). However, we briefly describe the reduction process here for completeness.

First, the bias was subtracted from the spectra, the flat field was corrected, and cosmic rays effect were removed with the `lacos_spec` method (Van Dokkum, 2001). Then, the 2D to 1D spectral conversion was carried out. In the process, the error for each spectrum was estimated. Finally, the wavelength calibration was carried out using the arc-lamp spectra and the flux calibration was performed using spectrophotometric standard stars that were observed the same night with each grism, to calibrate the spectra in physical units. The

spectra of six objects were reduced by collaborators, and we only had flux values without error for them. To estimate the flux uncertainty in these cases, we used the fluctuations of the continuum using the algorithm of [Stoehr et al. \(2008\)](#).

4.2 EMIR spectral reduction

As introduced in Sect. 3.2, additional observations were carried out at NIR wavelengths to complement the optical spectra and have a complete and uniform classification up to $z = 0.75$. These were done with the LIRIS and EMIR spectrographs. While the spectra taken with the first were reduced by a collaborator, the EMIR observations were reduced by the author of this thesis. In total, 34 observations were carried out with EMIR, 18 to observe the target AGN and 16 to obtain the spectra of reference stars used for the flux calibration of the scientific targets (see below). The 34 observations were done on visitor time observations on the nights of the 8th to the 10th of May 2018 and service time observations through 2019. All observations were in the long-slit mode with an aperture of $1''$ using the EMIR low-resolution normal grism and the spectroscopic filter YJ covering $0.85 - 1.35 \mu\text{m}$. The arc files were obtained using HgAr, Xe and Ne arc lamps covering wavelengths of $\sim 0.9 - 1.3 \mu\text{m}$.

For every observation, one or more observation blocks following an ABBA pattern were obtained. When following this image capture patron, two 2D spectra were acquired, with the target displaced alternatively between two positions, A and B, in the slit (see Figure 4.1). This pattern allowed to easily remove the sky background as we can directly subtract the B 2D spectra from the A 2D spectra to obtain four traces of the object without sky background, two positive and two negative.

To carry out the combination of images, calibration and reduction we used the IRAF software and its Python interface, PyRAF ([Science Software Branch at STScI, 2012](#))¹. The first step was to identify the Y-axis position of the observed traces of the object in the raw 2D spectrum files and determine the extraction aperture needed. To carry out both tasks, we used the display and visualization software SAOImageDS9 ([Joye & Mandel, 2003](#)). For every observation, we directly measured the position of the traces in the A and B 2D spectra.

We used the routines `identify` from IRAF and the arc files of our observations to calibrate the wavelength. We added additional lines to the standard reference file of emission lines at $\lambda > 13 \mu\text{m}$ to improve the calibration at long wavelengths. Before carrying out the wavelength calibration, we corrected the dispersion on the field-of-view using the `dispcor` procedure. We removed cosmic rays replacing the affected pixels with an average of nearby points using the method `cosmicrays`². After this process, we obtained four 2D wavelength-calibrated images.

¹Access to the documentation of IRAF and PyRAF is available at <https://iraf.readthedocs.io/en/latest/index.html>

²Documentation is available <https://iraf.readthedocs.io/en/latest/tasks/noao/imred/crutil/cosmicrays.html>

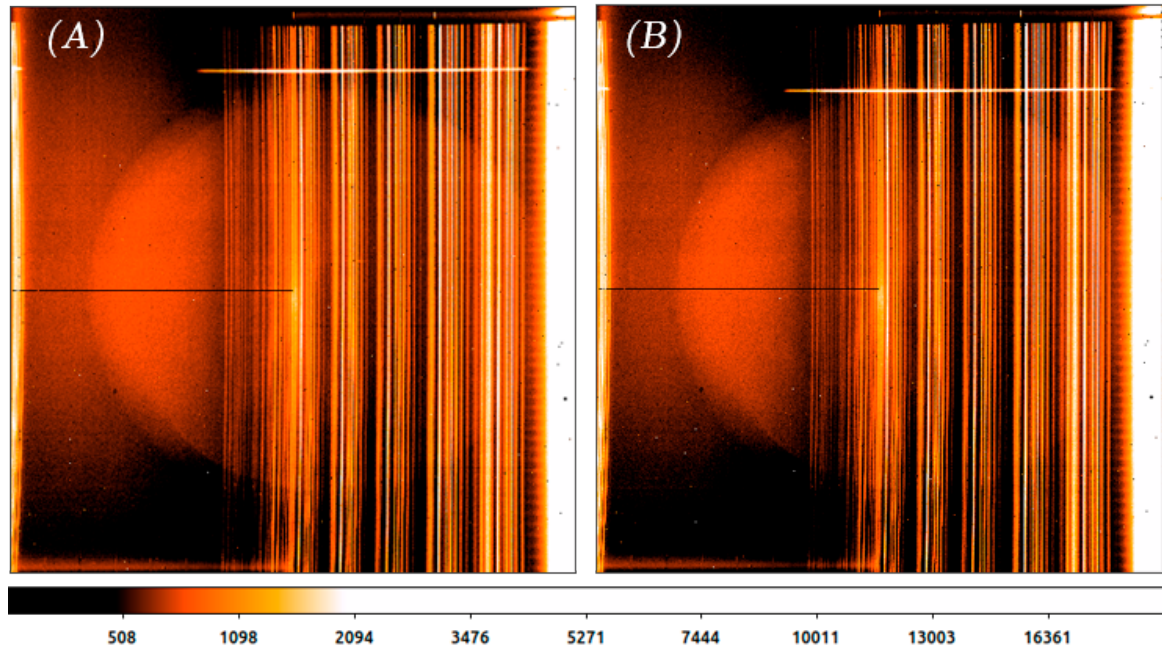


Figure 4.1: Example of images A and B taken from EMIR. The colour bar indicates the number of counts per pixel. The bright horizontal line corresponds to the trace of the object. The trace in image A is at a different Y pixel ($Y \sim 1820$) than the trace in image B ($Y \sim 1743$). Bright vertical lines correspond to telluric emission, while the central circular emission is a vignetting effect. Both features are correctly removed when the ABBA is performed.

We then combined every ABBA block, adding the A images and subtracting the B images, obtaining a single 2D spectra calibrated in wavelength with a total of 4 traces of the object, two positives from the A images and two negatives from the B images.

To obtain the extraction aperture of the trace, we integrated along the X-axis for every pixel in the Y-axis, obtaining its intensity curve. We got a first visual estimation in pixels from the width for which the trace blends into the background. To refine it, we carried out the reduction for different aperture values in the range of the initial estimation, ± 5 pixels, using a step of 1 pixel. We obtained the resultant SNR for all values and kept the aperture that maximised it. The resultant extraction apertures are in the range of 10 – 16 pixels ($\approx 2 - 3''$) for AGN observations and around 28 pixels ($\approx 5.4''$) for the reference stars.

We then extracted and combined the four traces, obtaining 1D spectra. We corrected them for the detector response, filter transmission and telluric absorption. In the NIR, the atmosphere absorption effect is more severe than in the optical range and must be corrected. To correct these three effects, we followed the standard approach of observing a reference star with a non-variable spectrum, which is easy to model (shape dominated by black-body emission and with a small number of spectral features) like A0V, B0V–B9V and G2V–G4V stars. Then, a response curve, $R(\lambda)$, can be modelled by comparing the observed spectra with the tabulated spectra of a star of the same spectral type. The reference star observation

should be taken immediately after or before the observation of the scientific target to ensure the atmospheric properties remain constant between both observations.

We selected stars of spectral types A0V and B8V–B9V from the Extended Hipparcos Compilation (Anderson & Francis, 2012) and used the tabulated spectra of HD074721 (for A0V) and HD130095 (for B8V–B9V). We obtained $R(\lambda)$ as the ratio between the tabulated and observed star, and smoothed it with a Savitzky-Golay filter, as the EMIR reduction documentation³ recommended.

The last step of the reduction process was the absolute flux calibration of the spectra. To do so we applied a calibration factor such that the J magnitude measured from the spectra is equal to the one tabulated in the UKIDDS catalogue, a typical approach when reducing NIR spectra.

To estimate the associated error, we fitted the continuum of a 750 Å-width region free of emission lines with a linear model and calculated the root-mean-square error (RMSE). We used the resultant value as the constant error of all observed fluxes of the spectra. We discarded all data at $\lambda < 9000$ Å, as the transmission of the filter decreases sharply below this wavelength. An example of a reduced EMIR spectrum is shown in Fig. 4.2

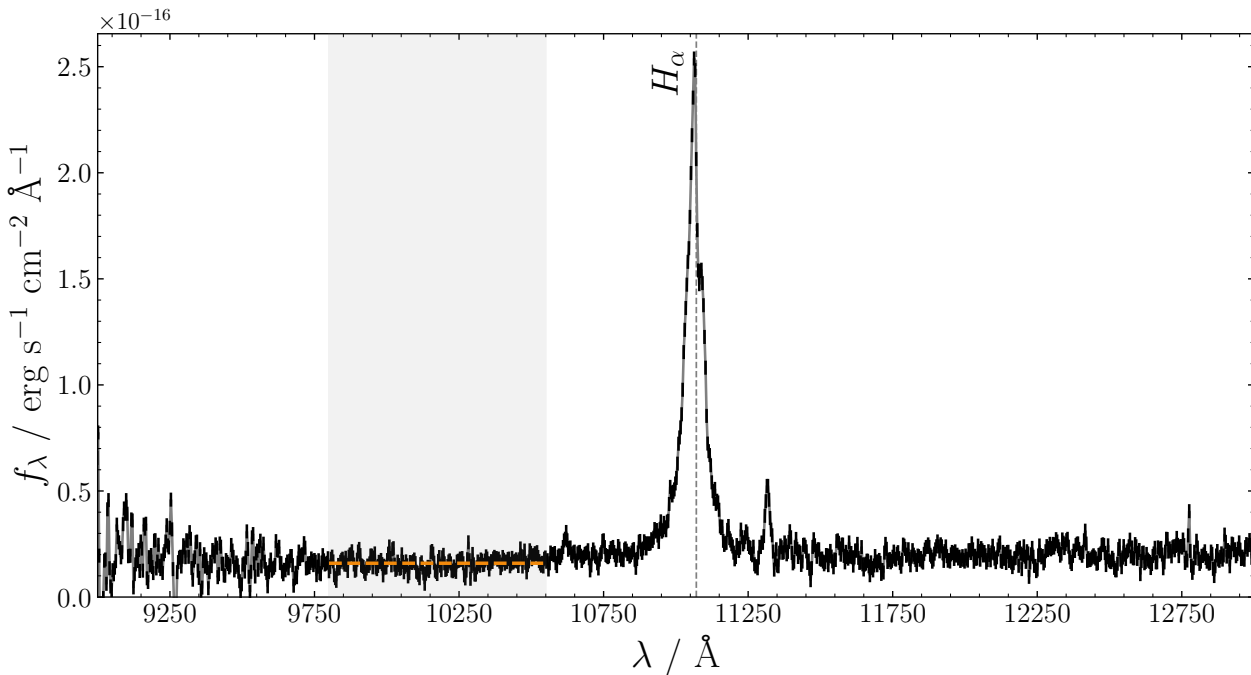


Figure 4.2: Example of a reduced and calibrated EMIR spectrum with $\text{SNR} = 5.49$. It corresponds to the AGN 1375 with $z = 0.692$ and subtype 1.9. The shadowed area and orange dashed line represent the wavelength range and continuum fit used to derive the RMSE.

³<https://pyemir.readthedocs.io/en/latest/index.html>

4.3 Analysis of the optical/NIR spectra

To determine the AGN subtype and obtain their emission line properties we obtained flux and widths values for the [OIII]5007Å, H β , H α and MgII λ 2798 emission lines, both for narrow and broad components. To do so, we carry out the fit of our optical and NIR spectra using a combination of continuum and emission line components.

However, this could not be done for all AGN in the BUXS sample. For the determination of the intermediate classification, the emission lines of interest are H β ($\lambda_0 = 4861 \text{ \AA}$) and H α ($\lambda_0 = 6563 \text{ \AA}$). Typically, the maximum wavelength at which H β can be observed such that a reliable intermediate classification can be derived in our spectra is 8500 \AA , which corresponds to $z \approx 0.75$. In order to have a complete sample with uniform classification criteria, we have restricted our studies to AGN below $z = 0.75$. The resulting 165 AGN will be referred to as the working sample forward, and the analysis of SED and optical/NIR spectra will focus only on them.

The same effect can be expected for H α at an even lower redshift ($z \approx 0.4$) because of its higher emission wavelength. This does not affect the class determination if broad H β is detected, but it becomes a fundamental problem for AGN without the detection of broad H β since we cannot distinguish 1.9s and 2s. However, we overcame this caveat in the working sample with the addition of the NIR spectra.

Our sample consists of spectra from different spectrographs. To minimize effects related to the cross-calibration between instruments, we will not compare absolute fluxes derived from spectrograph normalizations between objects, but rather flux or luminosity ratios. In 56 AGN, we have more than one available optical spectra. When this happened, we kept the spectra with the highest SNR for the fitting. However, for 10 AGN, the selected spectra did not have detection of broad H β and lacked coverage of H α . In these cases, we instead kept the lower SNR spectra since they had coverage of H α . We checked that selecting the spectra with the lowest SNR did not significantly change the fitted values but only increased the associated uncertainty ranges. The optical and NIR spectra used for all AGN of the working sample are shown in Tab. C.1, in the Appendix C.

Before fitting the optical/NIR spectra, we had to do some preparation steps. First, the SDSS spectra have their wavelengths defined in vacuum, while in the rest of our spectra were defined in air. To make all the available spectra and templates uniform, we converted them to the vacuum reference system using the implementation of the Ciddor (1996) formula by the Python package PyAstronomy (Czesla et al., 2019). However, we will refer to any emission line wavelength by the one defined in air as usual in the optical range.

Second, all spectra were corrected for the Milky Way extinction by applying the Allen (1985) extinction law. As with the SED correction, we extracted the Galactic N_H associated with the position of each source from the LAB map of Kalberla et al. (2005) and assumed a standard

Galactic gas/dust ratio of $A_V/N_H = 5.3 \times 10^{-22} \text{ cm}^{-2}$ (Bohlin et al., 1978) and $R_V = 3.1$ to derive the optical reddening.

Third, we had to correct for the instrumental broadening produced by the spectrograph. In spectral observations, a perfectly narrow emission line would be detected with a certain width, as it would be broadened by the diffraction of the light by the grism of the spectrograph. It means that the measured width of the emission lines is the convolution of the intrinsic broadening associated to the kinematics of the BLR/NLR and the instrumental broadening.

The procedure we followed differs for spectra obtained from SDSS and those from our follow-up campaign. The spectra from SDSS include an instrumental broadening curve, $w(\lambda)$, for every spectrum so we deconvolved the width of the emission lines by the values of $w(\lambda)$ at the centroid of such emission lines. However, we did not have $w(\lambda)$ curves for our follow-up spectra. We used the atmospheric emission lines to estimate its value at specific wavelengths in these cases. These lines have intrinsic widths significantly smaller than the instrumental broadening. Consequently, they can be used as an estimate of the instrumental broadening.

We fitted five strong sky emission lines on the observed wavelength range 5500 – 7200 Å: OI $\lambda\lambda$ 5579, 6302, Na λ 5890 and two OH transitions centred at 6836 and 7246 Å, respectively. They were modelled with a combination of a single Gaussian and a linear continuum defined in a small region around the lines. After checking that the fitted width remained similar for all five lines in all spectra, we estimated a constant instrumental width for a certain object as the median of the measured values and corrected the measured width of the AGN emission lines by it.

4.3.1 Fitting software

In this thesis, we have used the Sherpa application and its Python framework (Freeman et al., 2001; Doe et al., 2007) to develop the software needed to carry out our spectral fitting. Sherpa is the modelling and fitting application of the Chandra Interactive Analysis of Observations (CIAO) software package. Sherpa allows for the definition of complex models from simple individual components and the fitting of those models using a variety of different statistics and optimization techniques. The full documentation can be found at <https://cxc.cfa.harvard.edu/sherpa/>. We have minimized the χ^2 statistic to fit our spectra and looked for its minimum value using the Sherpa implementation of the Levenberg-Marquardt (Moré, 1978) optimization method. All uncertainties obtained from the spectral fit are the 1σ confidence intervals, calculated using the `conf` implementation of Sherpa.

We opted to fit the continuum locally around the lines as in previous works (Shang et al., 2007; Dong et al., 2008; Shen et al., 2011; Trakhtenbrot & Netzer, 2012; Mejía-Restrepo et al.,

2016; Koss et al., 2017; Coffey et al., 2019). We defined a region free of the influence of strong emission lines and another containing them. Both continuum and emission line regions were defined in the same way as in Shen et al. (2011). A detailed explanation of the specific fitting approach for every region will be presented in Sect. 4.3.3.

The optical spectra from SDSS were already corrected for telluric absorptions by the SDSS pipeline. However, we refrained from applying similar corrections in our follow-up optical spectra to avoid miscorrecting the atmospheric absorption, as it depends on the specific sky conditions during the night of the observations. We masked the affected regions to avoid them having an impact in our fits. Six optical telluric absorption bands were defined and masked: 6840 – 6950Å, 7580 – 7700Å, 8100 – 8350Å, 8900 – 9010Å, 9050 – 9175Å and 9250 – 9800Å. This process was not necessary for the NIR spectra as the corrections for the telluric absorptions are part of the typical reduction process at these wavelengths.

When carrying out the fit, to avoid over-fitting and adding non-necessary components, we increased gradually the complexity of the emission line model. We started with the simplest possible model consisting of continuum components and narrow emission lines. Then, we added additional components only if their inclusion produced an improvement to the fit with a 5σ significance, according to the results of an F-test (see Appendix B.2 for a description of the test). As the components and models fitted varied among the fitting regions, a detailed explanation of such models will be introduced in Sect. 4.3.3 and of the individual components in Sect. 4.3.2.

We obtained an initial redshift estimation for all spectra from a visual fit of at least one of the Balmer emission lines or the [OIII] doublet using the software GUISpec (Rodríguez Martínez, 2012). Briefly, GUISpec allows to plot a spectrum and superpose templates of AGN, different types of galaxies and the typical AGN emission lines and galaxy absorption lines for a given redshift. For two type 2 AGN there was no clear detection of any prominent emission lines, even though their nature as AGN was confirmed using the X-ray information. In these cases, we estimated the redshift from the CaII K and H absorption lines, as both AGN showed a galaxy-like optical spectrum. This initial estimation of the redshift was let to vary slightly for all components in the fitting process to obtain a more accurate value.

In the end, using the Python interface of the Sherpa as a basis, we developed a complete multithread software for spectral fitting. It implemented not only all the previously stated characteristics but also the capability of modifying the default initial values of all or certain models fitted, the definition of additional wavelength ranges to be masked for the fitted data or even the inclusion of regions normally excluded. The main code and associated library developed in this work ended composed of more than 7000 code lines.

4.3.2 Spectral models

We modelled the continuum using up to three components: the AGN disk continuum emission, the host galaxy integrated emission and the FeII pseudo-continuum. We also modelled the broad and narrow emission lines with a combination of Gaussian functions. The description of models for both continuum and emission lines is as follows:

- **Disk continuum:** As introduced in Sect. 1.1, the emission of the AGN accretion disk can be well described by a power law. Consequently, we modelled it using a local power law, similar to previous works in the literature (Dong et al., 2008; Shen et al., 2011; Calderone et al., 2017; Koss et al., 2017; Coffey et al., 2019). The power law is defined as:

$$f_{\lambda} = A \left(\frac{\lambda}{5100 \text{ \AA}} \right)^{\alpha} \quad (4.1)$$

The spectral index, α , was let to take values in the range $[-6, 6]$. The normalisation factor, A , was left free to take any positive or zero value and was defined to correspond to the value of the power law at rest-frame 5100 Å. As the disk continuum is fitted independently in local regions around H α , H β and MgII λ 2798, the extinction effect on the disk emission would be poorly constrained. Consequently, we decided not to include in the spectral fits extinction as a free parameter, leaving the extinction determination for the SED fits (see Sect. 4.4).

- **Iron emission:** AGN show a pseudo-continuum FeII emission across the UV and optical ranges. This emission is the result of the blending of a large number of individual emission lines from the transitions of FeII. Their blending and resultant appearance as a continuum is produced by the high-velocity movement of the gas in which they originated. In some AGN, the FeII emission can have a significant contribution to the continuum in the H β and MgII λ 2798 fitting regions, and its subtraction is fundamental to estimate their fluxes, especially if the width of the broad lines is small (Boroson & Green, 1992).

To model the FeII emission, we used the theoretical model from Verner et al. (2009). It reproduces the emission from rest-frame 1000Å to 10 000Å using an 830-level model atom for FeII. There are different templates available that differ in the column density, N_H , the microturbulence, χ , and the ionizing flux, Φ . Here we used the template with the values that best fit I ZW 1, the prototypical FeII emission of AGN, as it is usually done in the literature (Dong et al., 2008; Trakhtenbrot & Netzer, 2012; Jin et al., 2012; Calderone et al., 2017; Coffey et al., 2019). Those values were: $\log_{10}(N_H/\text{cm}^{-3}) = 11$, $\chi = 30 \text{ km s}^{-1}$ and $\log_{10}(\Phi/\text{cm}^{-2} \text{ s}^{-1}) = 20.5$. The FeII template employed is shown in Fig. 4.3.

The FeII template was then convolved with a Gaussian function to model the blending of the lines. The width of the Gaussian could take values from 1000 km s^{-1} to 10000 km s^{-1} . The other two free parameters of the model were the normalisation, which can take any positive value or zero and correspond to its emission at rest-frame 5100 \AA , and a wavelength shift up to $\pm 1800 \text{ km s}^{-1}$, which allows for a refinement of the initial redshift.

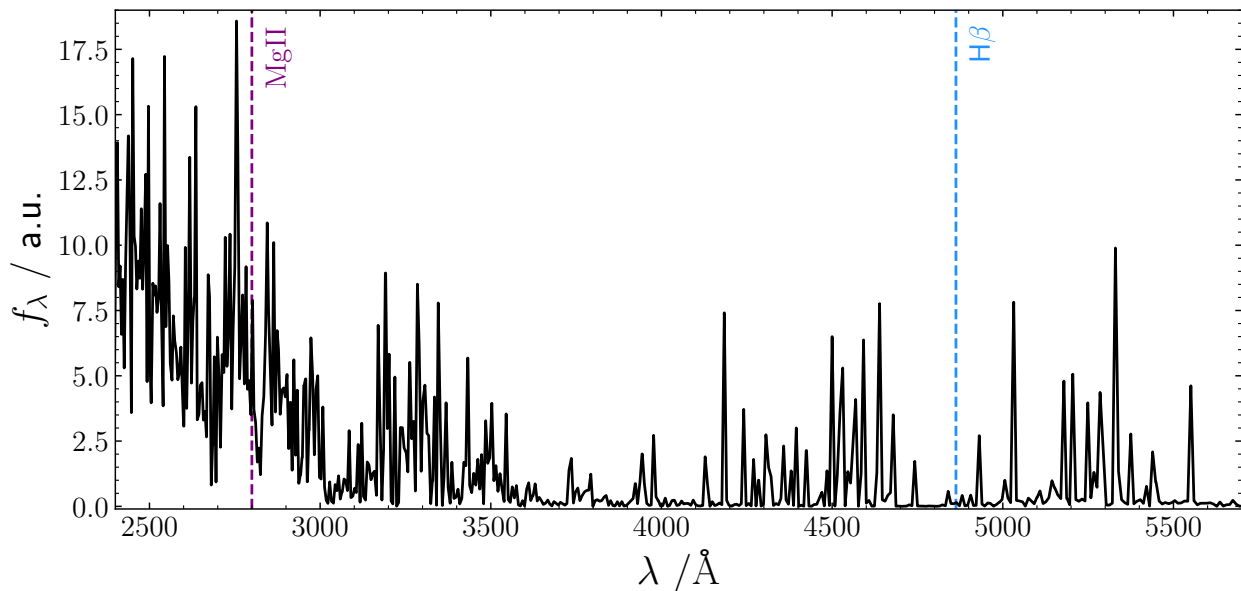


Figure 4.3: Zoom in the rest-frame $2400\text{--}5600 \text{ \AA}$ range of the FeII pseudo-continuum template employed in the spectral fitting.

- **Host galaxy emission:** Previous works showed that luminous AGN, as the ones in our sample, are most likely hosted by elliptical galaxies and that their emission can be fitted using a template of a galaxy of such kind (Floyd et al., 2004; Grogin et al., 2005; Jin et al., 2012; Calderone et al., 2017; Coffey et al., 2019). Following the same approach, we have used a composite spectrum obtained from ~ 2000 early-type galaxies from SDSS DR7 (available at <http://classic.sdss.org/dr7/algorithms/spectemplates/> as template number 23) to model the host galaxy contribution in our spectra. The template is shown in Fig. 4.4.

As this template was obtained from a combination of spectra measured with the SDSS spectrograph, we needed to correct it for the difference in spectral resolutions of the spectrographs used in our sample. To do so, we first deconvolved the template using a Gaussian with width equal to the mean instrumental broadening of our SDSS spectra, 2.98 \AA . We then convolved the resultant spectrum with a Gaussian with a width equal to that of the instrumental broadening associated with the AGN spectra fitted.

The host galaxy template was fitted allowing the flux normalization, defined at 5100 \AA , to take any positive or zero values. Additionally, the template could take a wavelength

displacement of up to $\pm 1800 \text{ km s}^{-1}$ to allow for a refinement of the initial redshift.

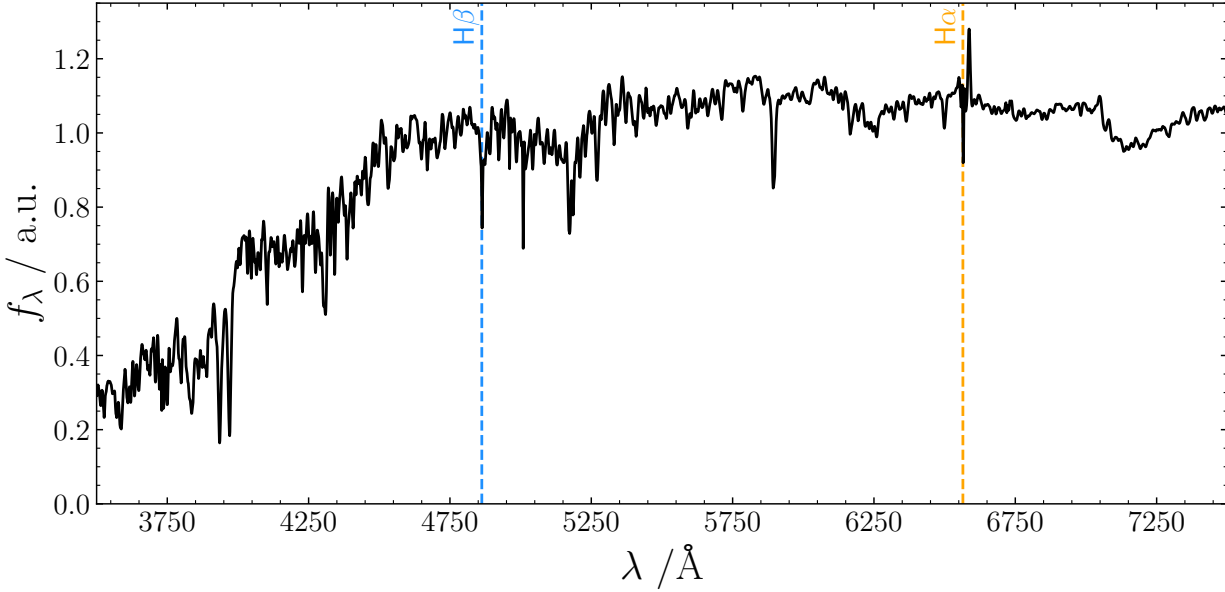


Figure 4.4: Host galaxy template used for the spectral fitting. Wavelength is in rest-frame.

- **Broad emission lines:** We have fitted the broad components of the $\text{MgII}\lambda 2798$, $\text{H}\beta$ and $\text{H}\alpha$ emission lines using the same model. Initially, we fitted a single Gaussian function. However, in some cases this simple model was not enough to correctly fit their profile, as they may show complex profiles (Netzer & Trakhtenbrot, 2007). We added an additional Gaussian component when it improved the χ^2 of the fit by 5σ according to a F-test (See Appendix B.2). Both Gaussian components were defined as:

$$f_\lambda = \frac{A}{\sqrt{2\pi}\sigma} \times e^{-(\lambda-\lambda_0)^2/2\sigma^2} \quad (4.2)$$

where λ_0 is the expected observed wavelength of the emission line, A is the normalization and σ the width of the Gaussian. The normalization could take any positive or zero value and was defined as the integrated flux of the emission line. The width was set to take values in the range 1000 km s^{-1} – 20000 km s^{-1} . Additionally, both components could have a shift with respect to the expected observed wavelength of up to $\pm 3500 \text{ km s}^{-1}$, to allow the fit of the most complex profiles.

- **Narrow emission lines:** We fitted the narrow components of $\text{MgII}\lambda 2798$, $\text{H}\alpha$ and $\text{H}\beta$ and the doublets of $[\text{OIII}]\lambda\lambda 4960, 5007$, $[\text{NII}]\lambda\lambda 6549, 6585$ and $[\text{SII}]\lambda\lambda 6718, 6732$. We modelled these narrow emission lines with a Gaussian function.

All emission lines in a spectral region were fitted simultaneously. We fixed the separation between the centroid of every set of narrow emission lines to their theoretical values. We also imposed all of them to have the same width, with an upper limit of

2000 km s⁻¹, and the same displacement with respect to their theoretical centroids up to ± 600 km s⁻¹. Additionally, the flux ratio of the [OIII] and [NII] doublets were fixed to their theoretical values of 2.98 (Storey & Zeppen, 2000) and 2.96 (Acker et al., 1989), respectively.

The narrow emission lines H α , [OIII], [NII] and [SII] can show a core component and broad blue wings or other complex profiles with a broad base (Boroson, 2005; Shen et al., 2011; Shimizu et al., 2018; Rojas et al., 2020). To properly fit them, we included an additional Gaussian component when it improved the χ^2 of the fit by 5σ according to a F-test (See Appendix B.2). As with the core components, all emission lines in a certain region share width, displacement and have the distance between centroids fixed. The flux ratios of [OIII] and [NII] were also set to their theoretical values. All parameters are equal to those of the core component except for the displacement that was allowed to take values up to 1800 km s⁻¹, to account for the wavelength shift with respect to the core components. In those AGN with fits including both a core and a wing component of the narrow emission lines, we checked afterwards if the core component was the narrowest. If this was not the case, we inverted the parameter values between the core and wing components.

For both components we allowed values of the width of the narrow emission line to be larger than the minimum value of the width of the broad component. These allowed us to fit cases with exceptionally wide narrow emission lines (> 1000 km s⁻¹) or unusually narrow broad emission lines (< 2000 km s⁻¹). However, we checked that for no AGN fit the narrow emission lines were broader than the broad emission lines.

4.3.3 Fitting regions

Using the individual models introduced in the previous section, we have defined a collection of local models to fit in the MgII, H α and H β regions, respectively. In this section, we will define those regions, describe the models used in each region, and describe any specific setup the regions require.

MgII λ 2798

We did not use the properties of the MgII λ 2798 emission lines. However, whether we detected the broad component of MgII or not was used to identify the AGNs classified as type 1. x and 2. x (see Sect. 5.1). So for completeness, the description of the procedure to fit them is included. We had coverage of the MgII region for 41 AGN ($\sim 26\%$ of the working sample).

The region of MgII emission was defined as [2700, 2900] Å and the continuum fitting regions were [2200, 2700] Å and [2900, 3090] Å. We modelled the continuum locally using a combination of a power law and the FeII pseudo-continuum template. Since we were modelling the MgII continuum in a relatively narrow region, we did not include a model for the Balmer continuum, assuming it to be blended with the disk continuum. As we did not

intend to obtain strong constraints of the MgII properties, we assumed the combined emission of the host-galaxy and the disk could be approximated locally by a power law and the FeII template.

MgII is actually a doublet composed of the emission lines MgII λ 2796, 2803. However, the close proximity of the two lines combined with the significant line broadening causes it to be detected as a single line at the resolution of our observations. Consequently, we followed the same approach as previous works (Shen et al., 2011, 2016; Coffey et al., 2019) and modelled both narrow and broad emission lines as being one single line. Both components were modelled with one single Gaussian, similarly to H β and H α .

Usually, the MgII emission region is close to the bluest limit of the spectra where the SNR of the spectra decreases significantly. To avoid misfitting continuum features and as we did not intend to compare MgII fluxes but only determine their detection, we decided not to include a second component for broad MgII in any case.

Combining the continuum and emission line components, we defined two fitting models:

- **Model 1:** disk continuum + FeII pseudo-continuum + narrow emission lines
- **Model 2:** model 1 + broad emission line

We accepted the second model only if it improved the fit with a 5σ significance according to an F-test. Examples of a fit of both models in the MgII (with and without a broad component) are shown in Fig. 4.5

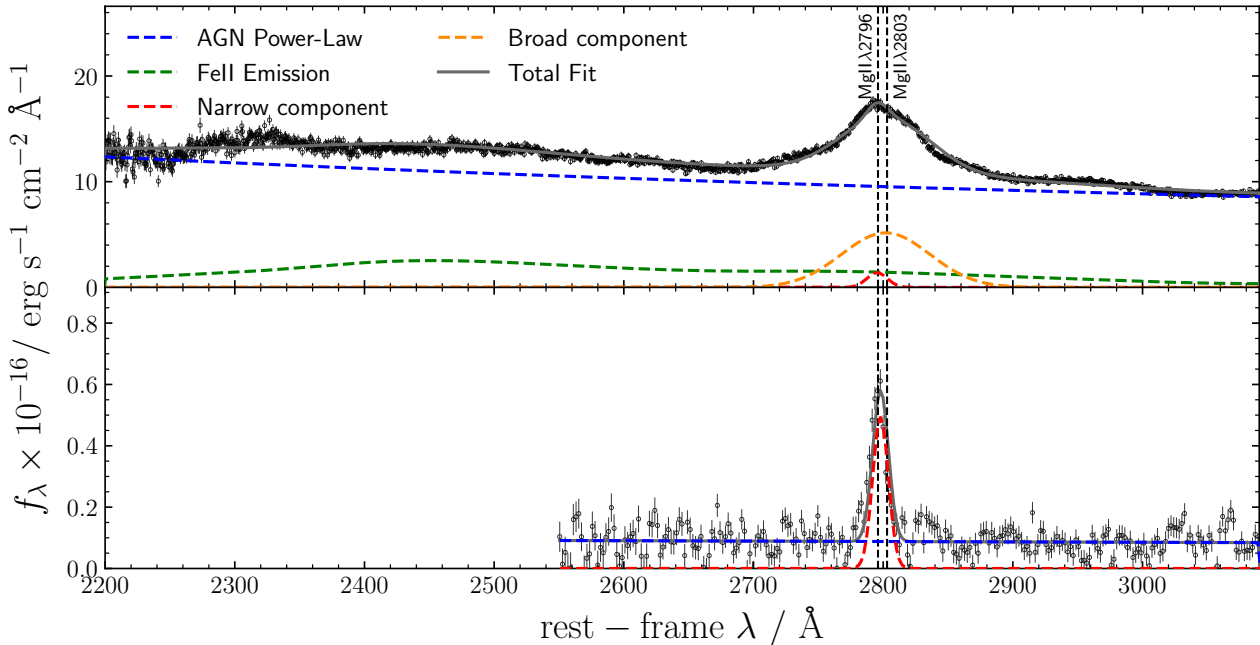


Figure 4.5: Examples of two typical best-fits in the MgII region. **(Top)** Best fit of AGN 8923 using the model 1. **(Bottom)** Best fit of AGN 3307 with the model 2.

H β

The region to fit the H β emission was defined as [4700, 5100] Å and the continuum fitting regions were [4435, 4700] Å and [5100, 5535] Å. We modelled the continuum using a combination of the host galaxy template, the accretion disk power law and the FeII template. We had coverage of the H β region for 164 AGN (> 99% of the working sample).

As in the MgII region, we gradually increased the complexity of the model in the H β region. To do so, we defined six different models:

- **Model 1:** disk continuum + FeII pseudo-continuum + narrow emission lines
- **Model 2:** Model 1 + broad emission line
- **Model 3:** Model 2 + 2nd broad emission line
- **Model 4:** Model 1 + wings of the narrow emission lines
- **Model 5:** Model 2 + wings of the narrow emission lines
- **Model 6:** Model 3 + wings of the narrow emission lines

In order to optimize the code, we did not fit all models, but only those strictly necessary to obtain the best model. We started with a simple model of continuum and narrow emission lines, and checked if the fit improved with a 5σ significance when adding a broad component, a second broad component, and wings to the narrow emission lines (Models 1 \rightarrow 2 \rightarrow 3 \rightarrow 6). If we found the best-fit model did not need a second component of a broad emission line, we checked instead if a wing component of the narrow emission lines improved the fit (Models 1 \rightarrow 2 \rightarrow 5). Finally, if no broad emission line was detected, we checked for the presence of a wing component of the narrow emission lines (Models 1 \rightarrow 4). Examples of fits in the H β region with models 6 and 1 can be seen in Fig. 4.6.

We carried out a visual screening of the results to check the reliability of our fits. We found that in 7 cases the additional broad component of H β was misused to fit emission unrelated to the broad emission line. We identified two ways in which this could happen:

- The additional Gaussian component had a width equal to the top of the range of allowed values. When this happened, the the extra broad Gaussian instead models a continuum with a broad convex bump.
- A line fit with the lowest possible width modelled small continuum features close to the central wavelength of H β .

In both cases, the additional H β component was significantly displaced ($\approx \pm 3500$ km s $^{-1}$) with respect to the expected wavelength. We identified all these non-physical artefacts and forced a new fit without this additional component, even if the former combination was formally improving the fit by more than 5σ .

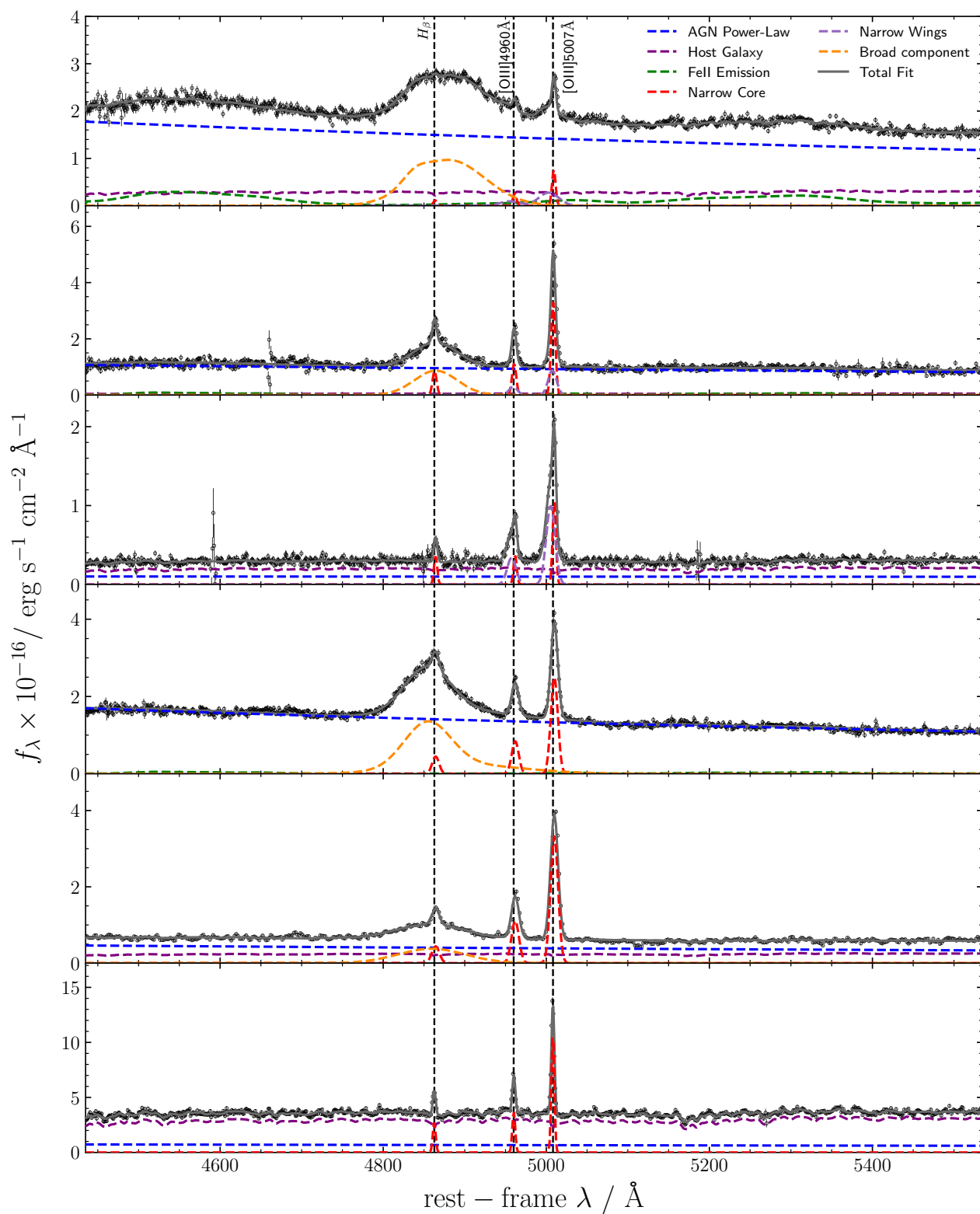


Figure 4.6: Examples of typical spectral fittings in the $H\beta$ region. Plots correspond from top to bottom to models 6 (AGN 1036), 5 (AGN 7967), 4 (AGN 4946), 3 (AGN 1450), 2 (AGN 4450), and 1 (AGN 1638), respectively.

H α

We defined the region of the H α emission line as [6400, 6800] Å. The continuum fitting regions were [6000, 6250] Å and [6800, 7000] Å. We modelled the continuum as in the H β region, but without adding an FeII pseudo-continuum, as its contribution is negligible at these wavelengths. We had coverage of the H α region for 130 AGN (79% of the working sample).

To fit all the emission lines in this spectral region (H α , [NII] and [SII]) we used the same approach as for H β . However, as the narrow emission lines [NII] and H α are heavily blended, the determination of the wings is problematic. The blending of the wings of the narrow components could be misinterpreted as a broad component, as shown in [Shimizu et al. \(2018\)](#). To overcome these problems, we considered only models 1 to 3 in the H α region, and we added a component of the wings of the narrow emission lines it had been previously detected in the [OIII] doublet. In this case, we forced them to have the same width and wavelength shift as the wings. Two examples of fits are presented in [Fig. 4.7](#).

As the flux of the broad components of H α are larger than those of H β , their properties are usually better constrained. To confirm the goodness of the fit of H β and reject non-physical fits, we compared the fitted values of the line parameters of H β and H α . If for two fitted parameters we found inconsistencies between broad H β and H α (understood as the best-fit values being incompatible at a 1σ level) we considered the fitted broad component of H β to be non-physical and rejected its detection.

To compare the flux of the broad H α and H β components we used the Balmer decrement. Although the intrinsic value is still a debated topic in literature ([Dong et al., 2008](#); [Gaskell, 2017](#); [Lu et al., 2019](#)), one of the lowest values of its intrinsic distribution proposed is $f(\text{bH}\alpha)/f(\text{bH}\beta) = 2.5$ (lower 5σ range of the intrinsic distribution of [Gaskell 2017](#)). Lower values are not expected so any AGN with a Balmer decrement lower than that was marked as inconsistent according to the flux of the broad components.

We also compared the widths and displacement with respect to the expected central wavelength of the broad emission lines. We considered both lines to be consistent if their values and 1σ errors were compatible. We did the same with the width of both lines, but we took into account that H β is systematically slightly broader (around 10 – 20% more) than H α ([Greene & Ho, 2005](#); [Shen et al., 2011](#)) and compared them using the relation of [Greene & Ho \(2005\)](#). Using this method we were able to correct a total of 18 spurious fits of broad H β .

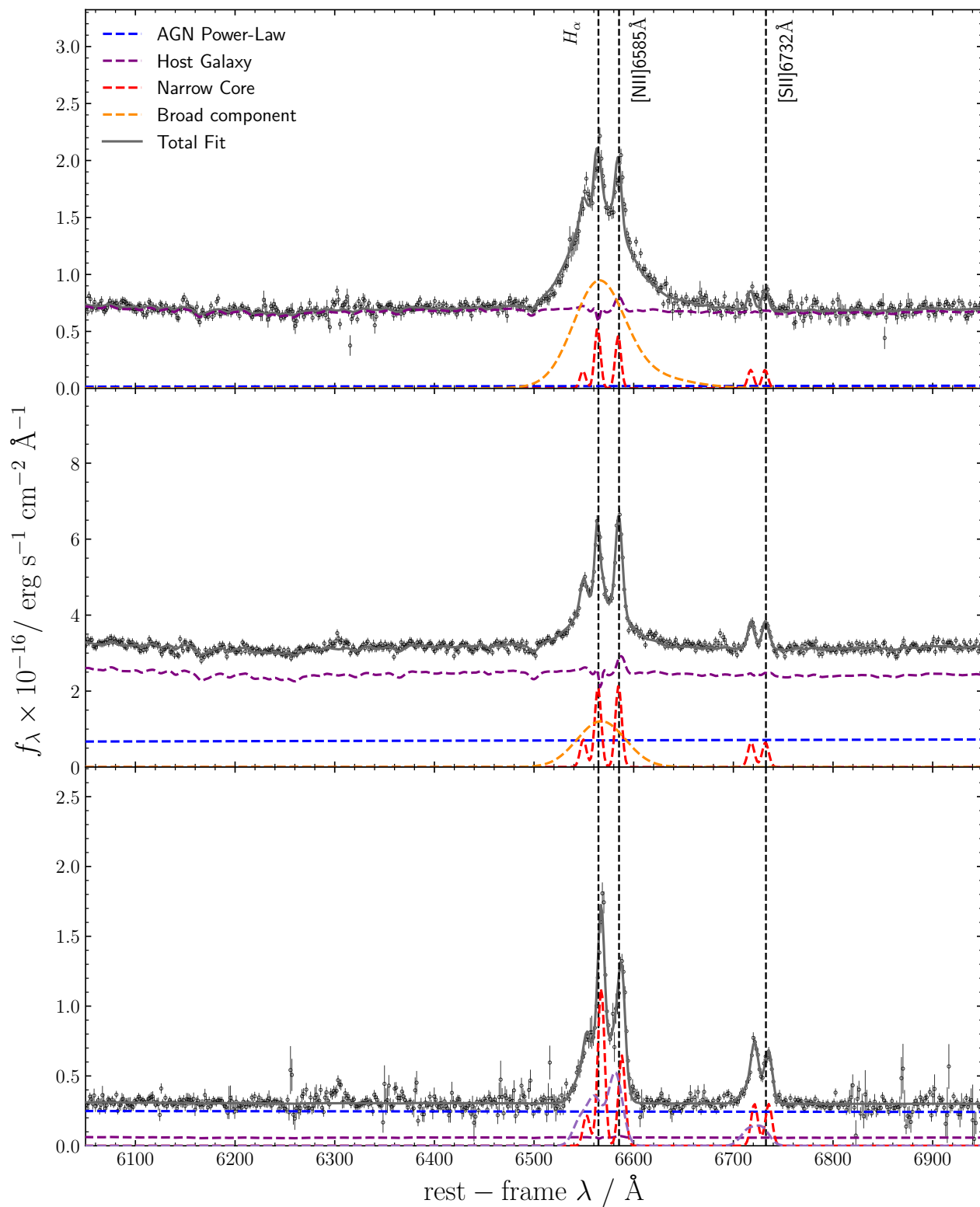


Figure 4.7: Examples of typical spectral fittings in the $H\alpha$ region. Plots correspond from top to bottom to models 3 (AGN 5405), 2 (AGN 9899), and 1 (AGN 4946), respectively.

In total, we detected and determined the flux of [OIII]5007Å in 160 AGN (97% of the working sample), for narrow H β in 149 (90%), for broad H β in 85 AGN (52%), for the narrow H α in 126 AGN (76%), and for broad H α in 88 AGN (53%). The total flux of these lines is presented in Tab. C.2 in Appendix C.

4.4 Analysis of the SEDs

In this thesis, we wanted to study differences of observational properties (such as the optical extinction or the AGN and the host galaxy optical luminosities) between AGN subtypes. In our spectral fits the observed continuum was modelled locally, consequently the AGN luminosity or the total optical extinction would be poorly constrained. Instead, to obtain reliable estimates of the luminosity and the optical extinction we have fitted the rest-frame UV-to-mid-infrared SEDs. This way we obtained the optical/UV reddening, $E(B - V)$, and the continuum luminosity of both AGN, L_{AGN} , and host galaxy, L_{Gal} , at rest-frame 5100 Å. This is a usual reference wavelength in the literature to trace the bolometric luminosity of the AGN (Richards et al., 2006; Shen et al., 2011; Koss et al., 2017), which is also close to H β . Although $E(B - V)$ is not the optical extinction, A_V , it is directly related to it through the absolute extinction to colour excess ratio, R_V . As we assume $R_V = 3.1$, we used $E(B - V)$ as a direct proxy of A_V .

To carry out the SED fits we have utilised the program *SEd Analysis using Bayesian Statistics* (SEABASs; Rovilos et al. 2014). SEABASs is a Java-based SED decomposition code that combines up to two sets of SED templates provided by the user, plus a library of synthetic stellar templates, to describe the observed photometry of a source through a set of filters set by the user. To carry out the fit SEABASs uses a maximum likelihood method that compares the flux of the templates fitted through the filters with the observable data. SEABASs uses a Monte Carlo Markov chain procedure to carry out the sampling of the different parameters. By default, SEABASs allows the fit of an AGN and host galaxy from a set defined by the user. However, we used a modified version, allowing for the fit of two AGN templates describing the emission of the accretion disk and the torus.

To model the torus emission, we employed the templates from Silva et al. (2004). These templates were constructed by combining the nuclear MIR spectra of a large sample of AGN with clear signatures of non-stellar nuclear emission detected in the NIR and MIR. After the subtraction of the host galaxy, the composite SEDs were interpolated using the smooth-density dust emission radiative transfer model from Granato & Danese (1994). The resultant torus SEDs were normalized by the X-ray luminosity and divided between type 1 and type 2 AGN with different column densities: $\log_{10}(N_H/\text{cm}^{-2}) = \{< 22, 22 - 23, 23 - 24, 24 - 25\}$. We show the four torus templates in Fig. 4.8. We have not selected the torus model to be fitted based on the optical classification or the best-fit column density derived from X-rays (see Sect. A), but instead we considered all four templates for both type 1 and type 2 AGN, to have greater flexibility when fitting the shape of the global AGN SED.

To describe the disk emission we used the mean type 1 quasar SED from [Richards et al. \(2006\)](#) up to $\lambda = 0.7 \mu\text{m}$. Since we were modelling separately the contribution from the torus, at higher wavelengths we extrapolated the disk emission with a power law $\lambda f_\lambda \propto \lambda^{-1}$. Then, we reddened the disk template following the Small Magellanic Cloud extinction law from [Gordon & Clayton \(1998\)](#) for $\lambda < 3300\text{\AA}$ and the Galactic extinction law from [Cardelli et al. \(1989\)](#) for $\lambda > 3300\text{\AA}$, as it best represents the nuclear reddening of quasars. To redden the templates we have used values of $E(B - V)$ ranging from 0 to 2, with a grid of $\Delta E(B - V) = 0.01$ up to 0.65 and a grid of $\Delta E(B - V) = 0.15$ onwards. We generated a total of 84 disk templates with different extinction levels. Some examples are in Fig. 4.8.

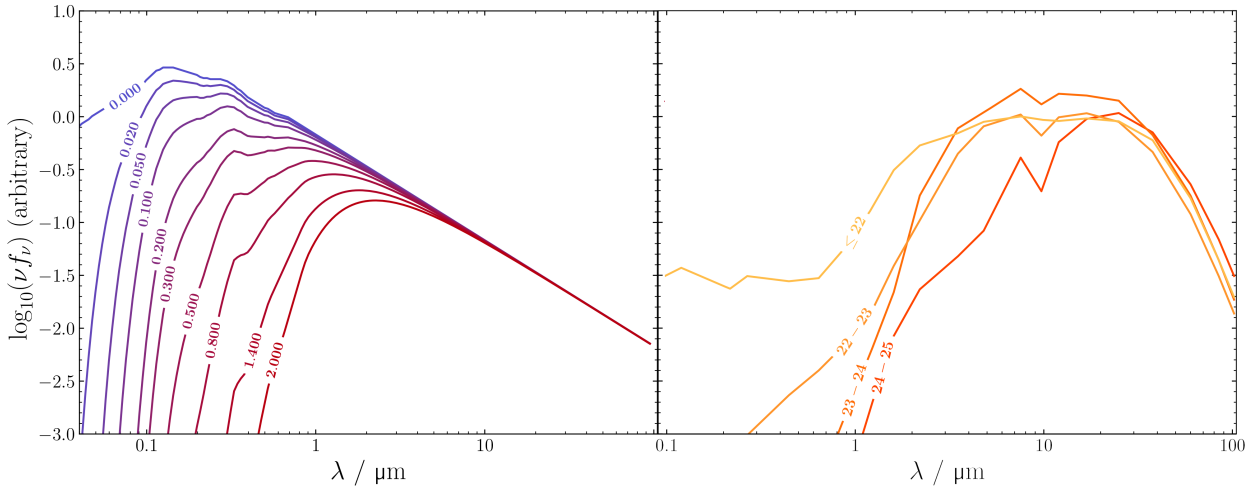


Figure 4.8: **Left:** ten examples of disk templates ranging from no extinction, $E(B - V) = 0$, to the maximum allowed value, $E(B - V) = 2$. Emission is normalised to the unobscured disk emission at rest-frame 5100\AA . **Right:** the four torus templates used in this work and their associated $\log_{10}(N_H / \text{cm}^{-2})$ values. Emission is normalised to that of the $\log_{10}(N_H / \text{cm}^{-2}) < 22$ template at rest-frame $6 \mu\text{m}$.

While fitting both torus and disk components independently is possible for subtype 1.0 – 8 AGN, where the disk is directly detected, the procedure is not suitable for subtype 1.9 and type 2 AGN. In these cases, the disk becomes fainter until being completely undetected, and a direct constrain of their emission is increasingly difficult. To overcome this problem we have fixed the relative contribution of the disk with $E(B - V) = 0$ and torus with $\log_{10}(N_H / \text{cm}^{-2}) = 0$. In particular, we fixed the flux ratio between both components at rest-frame $6 \mu\text{m}$, $C_{6\mu\text{m}}$, to the observed median value for subtype 1.0, the population expected to suffer the lowest values of extinction. This way, we could constrain the disk normalization with that of the torus emission, always visible for both type 1 and type 2 AGN, leaving only the extinction (and the normalization of the global template) as a free parameter.

To calculate $C_{6\mu\text{m}}$ we first carried out the fit of all subtype 1.0 SEDs with the disk and torus normalization free. Then, we obtained the intrinsic $C_{6\mu\text{m}}$ value from these fits after correcting the fitted templates for the associated extinction. From these initial fits, we obtained

$C_{6\mu\text{m}} = 0.10 \pm 0.04$, a value compatible with that of the templates from [Richards et al. \(2006\)](#) and [Assef et al. \(2010\)](#). We checked if imposing a fixed $C_{6\mu\text{m}}$ affects our extinction determination of the subtype 1.0 sample and found no significant changes.

The $C_{6\mu\text{m}}$ parameter is equivalent to the $L_{\text{IR}}/L_{\text{BOL}}$ ratio, a typical quantity used in several studies in the literature as a proxy of the covering factor of the torus. However, we point out that the relation between $L_{\text{IR}}/L_{\text{BOL}}$ and the covering factor is complex, as shown by [Stalevski et al. \(2012\)](#), and depends on many other parameters, including the type of the AGN. Therefore, imposing a constant $C_{6\mu\text{m}}$ does not translate to a constant covering factor. The conversion between $C_{6\mu\text{m}}$ and $L_{\text{IR}}/L_{\text{BOL}}$ depends only on the torus template used and the optical bolometric correction assumed. Applying the bolometric correction of [Duras et al. \(2020\)](#), we translated our $C_{6\mu\text{m}}$ to $L_{\text{IR}}/L_{\text{BOL}} = 0.39 \pm 0.15$, a value similar to that of previous studies ([Lusso et al., 2013](#); [Roseboom et al., 2013](#)). Furthermore, [Ichikawa et al. \(2019\)](#) also showed that it is similar for all AGN types.

After fixing $C_{6\mu\text{m}}$, we obtained a library of 304 AGN templates mixing all possible combinations of $E(B - V)$ and $\log_{10}(N_{\text{H}}/\text{cm}^{-2})$ to account for all possible shapes of the AGN emission. The value of $E(B - V)$ estimated with our SED fits accounts for the combined contribution of nuclear and host galaxy-associated components. As such, in the rest of the thesis, this total line-of-sight optical/UV extinction towards the AGN will be simply referred to as extinction, unless otherwise stated explicitly.

We have used the library of 75 stellar templates from [Bruzual & Charlot \(2003\)](#) included in SEABASs to model the host galaxy emission. The templates have solar metallicity and a Chabrier initial mass function ([Chabrier, 2003](#)). To generate the templates, ten exponentially decaying star formation histories were used, with characteristic times $\tau = 0.1 - 30$ Gyr, a model with constant star formation, and a set of ages in the range 0.1 - 13 Gyr. The host galaxy templates were later reddened using the [Calzetti et al. \(2000\)](#) dust extinction law with $E(B - V)_{\text{Gal}}$ from 0 to 2.

We decided not to add a contribution from dust heated by star formation to avoid potential degeneracies between AGN and host galaxy templates. Deblending both components in our sample is not possible as star formation emission peaks at far-infrared wavelengths, while our data covers up to $\lambda \sim 12 \mu\text{m}$ for all AGN and to $\lambda \sim 22 \mu\text{m}$ for a small fraction. [Mateos et al. \(2015\)](#) obtained conservative upper-limits for the star formation contamination at $6 \mu\text{m}$ for the BUXS sample. For more than 90% of the objects with $L_{\text{X}} > 10^{42} \text{ erg s}^{-1}$, contamination was estimated to be below 15%, consequently having a negligible effect on our results. Examples of two fitted SEDs, a type 1.0 and a type 2, are shown in Fig. 4.9.

SEABASs does not allow for the estimation of uncertainties in the best-fit parameters used to generate the templates fitted, such as extinction. To estimate the significance of the detection of extinction with respect to certain threshold levels, we have studied the variation of the χ^2 statistic. We forced a refit, imposing the $E(B - V)$ values used as threshold, and calculated

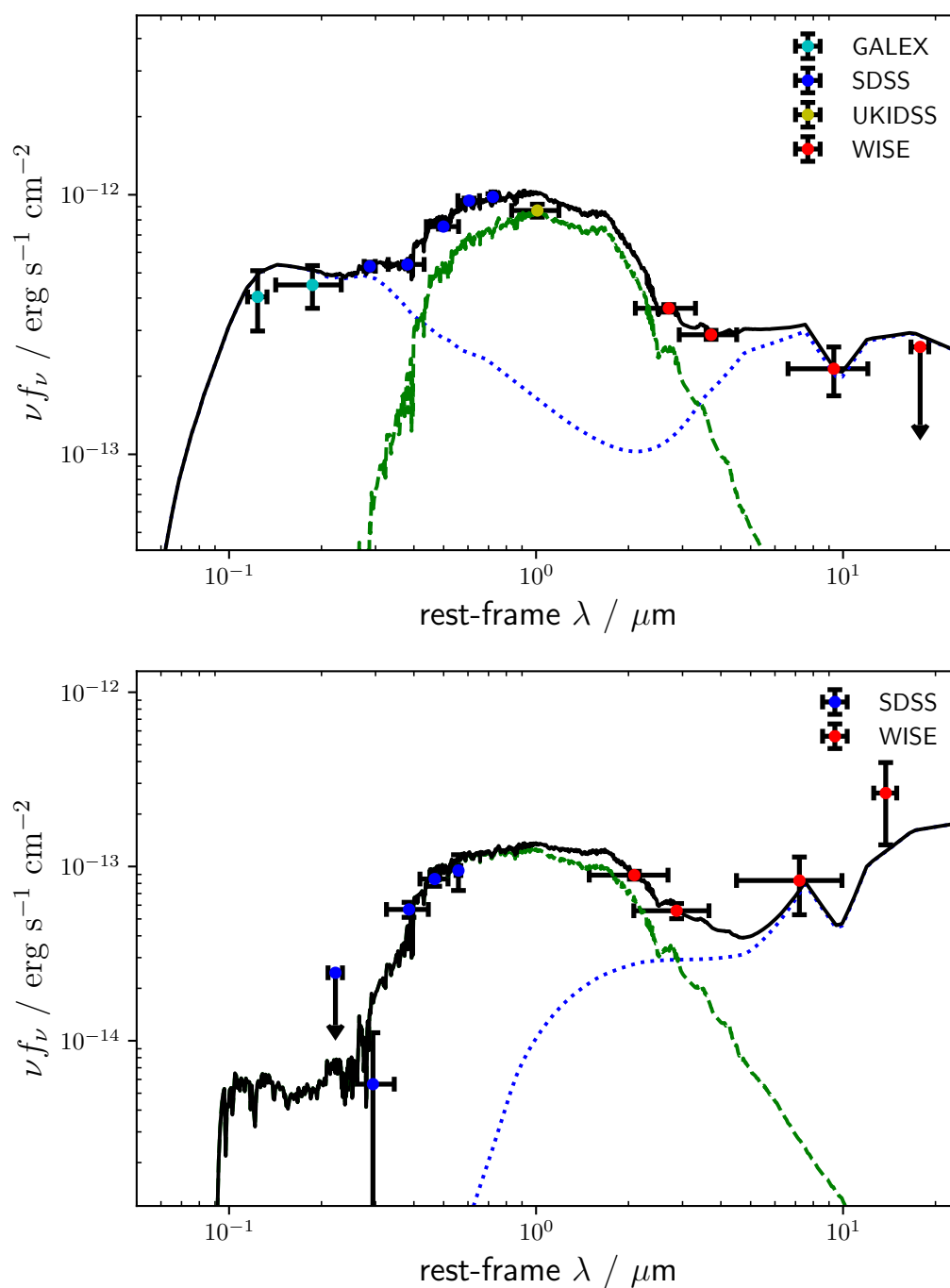


Figure 4.9: (Top) Example of SED fit of a subtype 1.0 AGN. The blue dotted line corresponds to a reddened accretion disk with $E(B - V) = 0.02$ plus a torus template with $\log_{10}(N_H/\text{cm}^{-2}) < 22$, while the dashed-green line corresponds to the host galaxy component with $E(B - V)_{\text{Gal}} = 0.057$. **(Bottom)** Example of a SED fit of a type 2 AGN with a reddened accretion disk with $E(B - V) = 2.0$ plus a torus template with $\log_{10}(N_H/\text{cm}^{-2}) = 23\text{--}24$ and a host galaxy component with $E(B - V)_{\text{Gal}} = 0.062$. In both plots the coloured symbols correspond to the photometry used.

how much our original fit improved. If the significance was less than 90% ($\Delta\chi^2 < 2.71$), the detection was considered as not significant.

In particular, we followed this approach to determine which extinction values are significant with respect that proposed by [Caccianiga et al. \(2008\)](#) as large enough to suppress the broad component of $H\beta$, $E(B - V) = 0.65$ (for more details see Sect. 5.3.2).

The same methods were used to determine which fits were compatible with no extinction at all, using $E(B - V) = 0$ as the threshold value. Additionally, if the extinction is comparable to the uncertainty of the Galactic correction we also marked these fits as compatible with no extinction. We have found that 70% of the objects with $0 < E(B - V) < 0.05$ (equivalent to the mean Galactic extinction) were compatible with no obscuration at all. We kept the fitted values for the sake of obtaining the best possible fit, but marked them in all plots with a triangle pointing down.

In some cases, the best fit SED resulted in a combination of a very bright and blue galaxy and a heavily extinguished disk to describe what should be fitted with an unobscured disk at rest-frame UV wavelengths, a known degeneracy ([Calistro Rivera et al., 2016](#); [Suh et al., 2019](#); [Marshall et al., 2022](#)). We have compared the SED fit with the optical spectrum to identify these cases. If we concluded that the continuum was dominated by the AGN emission, we limited the maximum extinction to $E(B - V) = 0.1$ to favour the fit of an unobscured disk. This was necessary for 13 objects (8%): six subtype 1.0, six subtype 1.2 and one subtype 1.5 AGN.

We have obtained the values of $E(B - V)$ from the fit of the SED. Still, alternative ways exist to estimate the extinction; one is using the Balmer decrement. As the intrinsic value of the Balmer decrement of the broad emission lines is expected to be similar for all AGN and the extinction affects broad $H\beta$ and $H\alpha$ differently, any deviation from the intrinsic ratio can be used to determine the extinction. This method has its significant limitations. First, the measured intrinsic ratio does not correspond to the theoretical value of the Baker-Menzel Case B and is still debated, with values ranging typically from 2.7 to 3.4 ([Dong et al., 2008](#); [Gaskell, 2017](#); [Lu et al., 2019](#)). Second, extinction values can only be obtained for AGN for which broad $H\beta$ and $H\alpha$ are detected, i.e., subtypes 1.0, 1.2, 1.5, and 1.8.

Nevertheless, as Balmer decrement-based extinctions are frequently used in the literature, we checked if they correlated well with those derived from the SED fits. We obtained the Balmer decrements for those 1.0 – 5s with broad components of $H\beta$ and $H\alpha$ detected and coming from the same spectra (55 objects). To convert it to an extinction value, we assumed the frequently used intrinsic ratio of $f(bH\alpha)/f(bH\beta) = 3.06 \pm 0.03$, from [Dong et al. \(2008\)](#). In Fig. 4.10, we can see how the two estimates of the optical extinction show a broadly agreement with a important dispersion, a combination of the uncertainty of our extinction values and the dispersion of the intrinsic ratio of $f(bH\alpha)/f(bH\beta)$. From this point on, any future reference to $E(B - V)$ will refer exclusively to the values obtained from the SED fits.

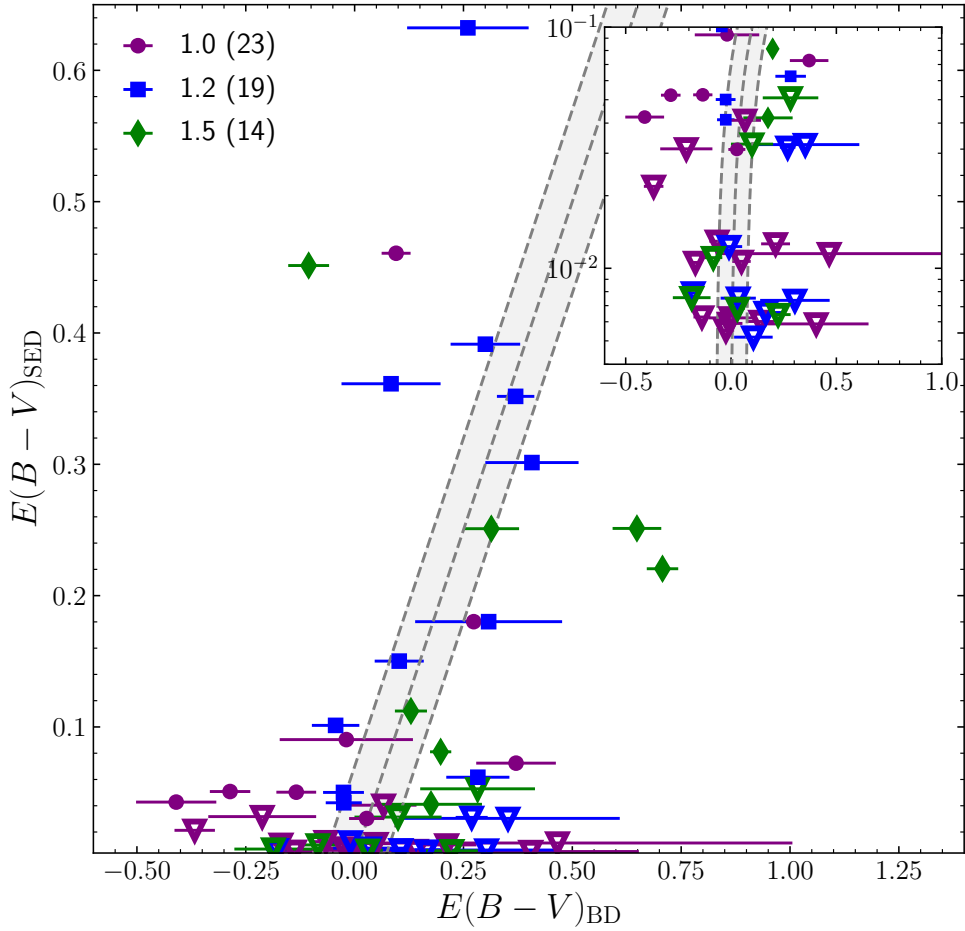


Figure 4.10: Optical extinction of the accretion disk derived from the SED fit ($E(B - V)_{\text{SED}}$) versus the one derived from the Balmer decrement of the $H\alpha$ and $H\beta$ broad emission lines ($E(B - V)_{\text{BD}}$). The grey area represents the 1 : 1 relation and its 1σ uncertainty from Dong et al. (2008). A random contribution of ± 0.003 has been added to $E(B - V)_{\text{SED}}$ to avoid the superposition of points with the same value. The inset shows a zoom of those objects with $E(B - V)_{\text{SED}} < 0.1$. AGN with $E(B - V)$ compatible with no obscuration have been represented with empty triangles pointing down. Please note that other values in the literature deviate significantly from the central value assumed, suggesting the intrinsic dispersion is most probably much larger than the one reported in Dong et al. (2008).

We obtained from the SED fit the observed flux of the total AGN component at rest-frame 5100 \AA . As the torus emission is a reprocessed emission from the nuclear region, we had to subtract it from the total AGN component before obtaining the AGN luminosity. Since we imposed $C_{6\mu\text{m}}$, we obtained the ratio of the observed disk flux over the total AGN template flux at 5100 \AA for any extinction value. Then, we multiplied it by the fitted normalization of the total AGN template to get the observed disk flux. Finally, we corrected it by the optical extinction and obtained the intrinsic luminosity of the AGN component at rest-frame 5100 \AA , L_{AGN} , using the cosmology introduced in Sect. 1.5.

Chapter 5

Results of this thesis

After the spectral and photometric fitting process, we obtained a well-defined sample with extensive characterization in the optical range, including a robust intermediate classification for almost all AGNs. This makes our sample ideal for studying the dependence of the subtype with AGN properties.

To shed light on this issue, we will compare the distributions of several parameters (observed AGN-host contrast, optical extinction, AGN and host galaxy luminosity, and narrow and broad emission line relative luminosities with respect to the AGN luminosity) between subtypes and look for significant differences.

To determine the statistical significance of any difference between distributions, we will rely on the Kolmogorov-Smirnov test (from now on, the KS test). All comparisons will also be repeated using the Anderson-Darling (AD) test, which is more sensitive to tails, to confirm the significance level. We will also use the Kendall rank correlation coefficient (hereafter Kendall- τ) to determine the statistical significance of potential correlations between variables. We will reject the null hypothesis¹, H_0 , when the p-value, p , is lower than 0.003, i.e., the statistical significance is greater than 3σ . A comprehensive description of these definitions and statistical tests is presented in Appendix B.

In this chapter, we will first introduce the properties of the working sample in Sect. 5.1. We will explore the dependence of our subtype determination on the projected aperture of the spectra in Sect. 5.2. We will compare the AGN-host contrast and contrast-related properties (both observed and intrinsic properties) between subtypes in Sect. 5.3, summarising the results of the KS test in Tab. 5.2. Finally, in Sect. 5.4 we will compare between subtypes the relative luminosity with respect the AGN luminosity of the broad and narrow emission lines relevant to our classification scheme: $H\beta$ and $[\text{OIII}]5007\text{\AA}$. Similarly, we will summarise the results of KS and Kendall- τ tests in Tab. 5.3 and Tab. 5.4, respectively.

¹The null hypothesis for the KS and AD tests assumes that both samples were drawn from the same parent distribution, while for the Kendall- τ , it assumes that both parameters are independent.

5.1 AGN sample properties

Using the results of our optical/NIR spectral fitting, we classified our AGN into 1.0, 1.2, 1.5, 1.8 and 1.9 subtypes and type 2 using the flux ratio of [OIII] λ 5007Å and the broad H β emission lines, as introduced in Sect. 1.2. In order to do so, we obtained all the components fitted to describe the broad component of H β (all Gaussians in case of complex profiles) and [OIII] λ 5007Å (core and wing components) and obtained the total flux, f . This way, we obtained robust classifications for 159 AGN (96% of the working sample). In Tab. 5.1, we summarise the results. We got similar results using the classification scheme of Whittle (1992), which considers the whole profile (narrow plus broad components) of H β instead of only the broad component, as in our work, to determine the subtype.

As the sample of 1.8 AGN is too small (only two objects) to obtain any statistically significant result, we merged the 1.8s with the 1.9s. From now on, we will refer to the merged sample as 1.8 – 9. Additionally, when carrying out comparisons between properties we have also grouped and compared 1.0s, 1.2s and 1.5s (1.0 – 5 hereafter) and 1.8 – 9s and 2s (1.8 – 9/2), it is usual in the literature (Bassani et al., 1999; Akylas & Georgantopoulos, 2009; Burtscher et al., 2016; Schnorr-Müller et al., 2016; Shimizu et al., 2018; Oh et al., 2022; Mejía-Restrepo et al., 2022).

We could not determine an intermediate classification for six AGNs. In one of those, we detected a broad component of the MgII emission line, but we did not have spectral coverage of H β nor H α available. In another, we detected a broad component of H β , but strong atmospheric absorption in the spectral region made it impossible to measure the flux of [OIII] λ 5007 reliably. These two cases have been labelled as 1.x, as given the detection of a broad component of H β or MgII, we know for certain they are not type 2. There are also three AGN for which we did not detect a broad component of H β , and we did not have coverage of the H α region, impeding us from determining whether they are subtype 1.9 or type 2 AGN. Additionally we have one case where we have a detection of broad H α but no coverage in H β . They were labelled as 2.x.

All 1.x and 2.x AGN (less than 4% of the total) were removed from the sample. For the rest of this thesis, we derive our results for the remaining 159 AGN in any analysis using the working sample. We will consider the subtypes as numerical values for the rest of the work. So increasing subtype means going from 1.0 to 2 in the order 1.0 \rightarrow 1.2 \rightarrow 1.5 \rightarrow 1.8 \rightarrow 1.9 \rightarrow 2, and decreasing classification the opposite.

To determine the impact of the uncertainty of the emission line fluxes in the subtype determination, we studied the possible cross-contamination between 1.0/1.2/1.5 associated with the error in R . To this end, we plotted R against SNR, with threshold values superposed, in Fig. 5.1. The SNR ($\text{SNR} = f/\Delta f$) corresponds to the median value of the individual points of the whole spectra. The following results remain the same if we calculate the SNR using only the continuum fitting region for H β (see Sect. 4.3).

The contamination between subtypes is small; up to 9 AGN have R values compatible with another classification inside the 1σ uncertainty. Four are placed in the frontier between 1.0 and 1.2, and five between 1.2 and 1.5. Also, there is no evident strong correlation between SNR and R . This result is confirmed by a Kendall- τ test, returning a $p = 0.705$. As such, we can be sure the quality of the individual spectra does not play a significant role in determining the subtype.

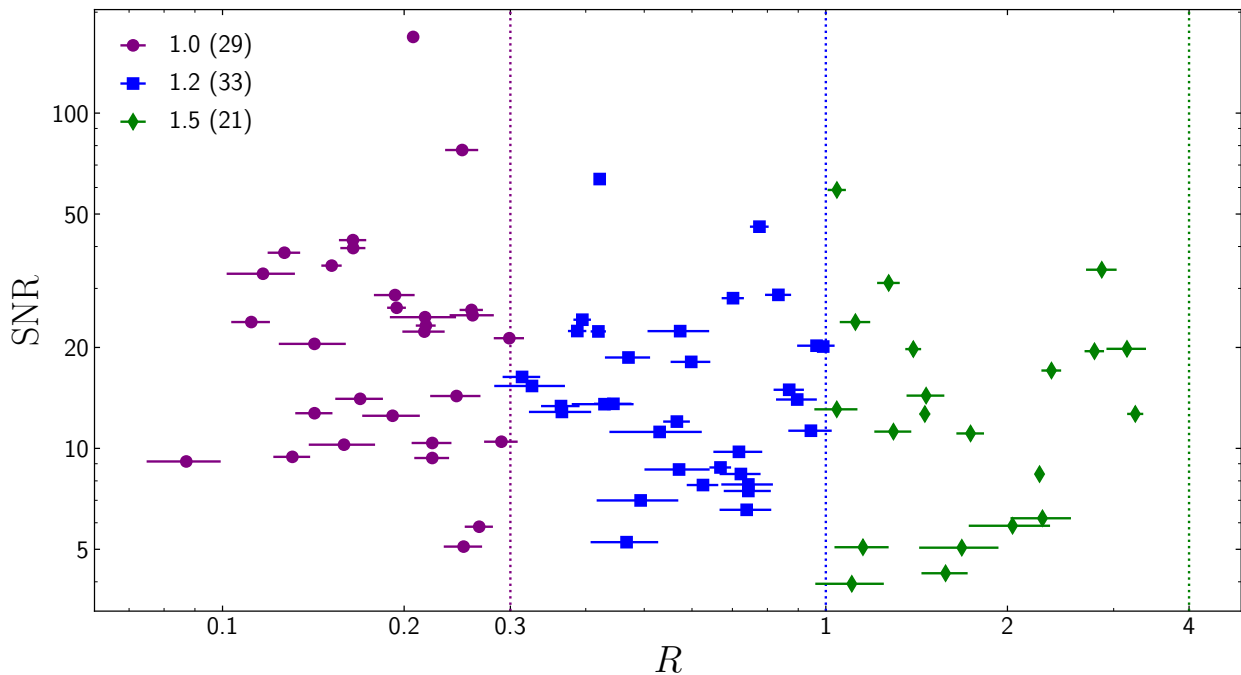


Figure 5.1: SNR of the 1.0 (purple dots), 1.2 (blue squares) and 1.5 (green diamonds) AGN versus R . The dotted vertical lines correspond to the limit values between one subtype and the following.

Detecting broad $H\beta$ becomes increasingly difficult as its flux decreases, especially in the spectra with the lowest SNR. Then, as long as we detect a broad $H\alpha$, we cannot discard the presence of a very weak, undetected broad $H\beta$. To estimate the impact of the 1.5 contamination in our 1.8 – 9 AGN sample, we checked those fits that initially included a broad component of $H\beta$, but it was below our detection significance threshold (5σ). After a thorough visual check-up, we found a maximum of three objects which could have a genuine broad component of $H\beta$, translating into a variation in the 1.8 – 9 sample no higher than 10%. We also checked for the impact of 1.8 – 9s with low significance $H\alpha$ detections in the type 2 AGN sample. Following a similar approach, we found the variation would be no higher than six objects (14% of the type 2 sample).

From the X-ray spectral fitting, we obtained the intrinsic X-ray luminosity of our AGN in the rest-frame 2 – 10 keV energy range, L_X (see Sect. A). Our sample was selected and defined in X-rays. So the first diagram we made to characterise it was the relation between L_X and

Class	Number	$\langle L_X \rangle$	$\sigma(L_X)$	$\langle z \rangle$	$\sigma(z)$
(1)	(2)	(3)	(4)	(5)	(6)
1.0	29	43.88	0.47	0.36	0.16
1.2	33	43.74	0.72	0.34	0.20
1.5	21	43.71	0.67	0.34	0.20
1.8 – 9	32	43.22	0.56	0.25	0.18
2.0	44	43.51	0.56	0.25	0.16
1.x	2	44.09	0.15	0.52	0.01
2.x	4	44.05	0.41	0.52	0.08

Table 5.1: Col. 1: AGN classes; Col. 2: total number of sources; Cols. 3, 4: mean value and standard deviation of the rest-frame 2 – 10 keV luminosity; Cols. 5, 6: mean value and standard deviation of the redshift.

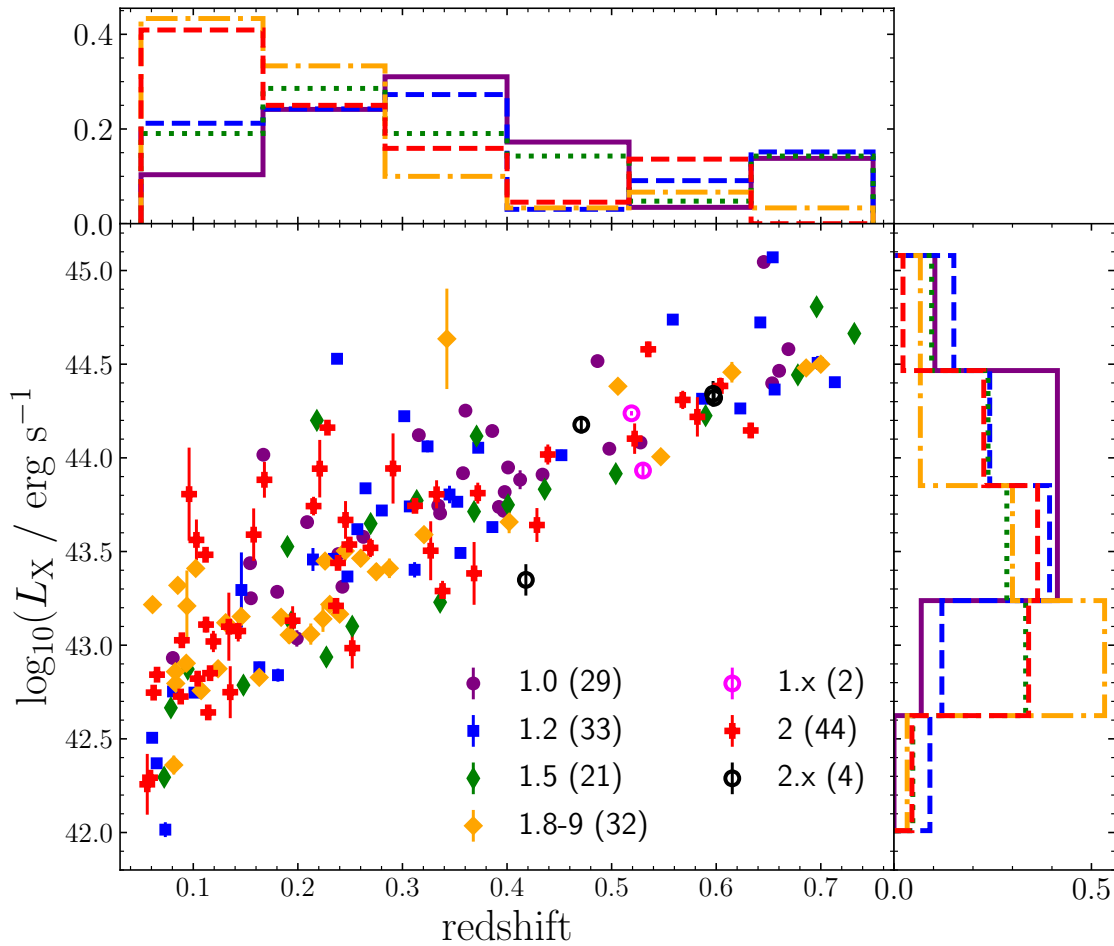


Figure 5.2: Decimal logarithm of the intrinsic rest-frame 2–10 keV X-ray luminosity versus redshift and the projected distributions of these quantities for different subtypes of AGN (see text). Distributions are normalised such that the sum of the heights for each subtype equals one. Symbols, line styles and colour codes depend on the subtype (see Sect. 1.2) and will remain the same for the rest of the work.

redshift, shown in Fig. 5.2. The mean values and their associated standard deviations are available in Tab. 5.1. The sample covers three orders of magnitude in X-ray luminosities. It seems that 1.0s, and 1.2s are slightly more luminous than 1.5s and 2s, and 1.8 – 9 are less luminous than all the other subtypes. We will investigate luminosity differences in detail later in Sect. 5.3.3.

When comparing the redshift distributions, we clearly saw differences. Subtype 1.8 – 9 and type 2 AGN have preferentially lower redshifts than subtype 1.0, 1.2, and 1.5 AGN. With a KS test, we checked that the difference between both groups was statistically significant at a 3σ level, and the difference between means was $\Delta z = 0.10 \pm 0.03^2$. This difference in redshift distributions was taken into account when comparing luminosity distributions.

5.2 Analysis of aperture effect in subtype determination

The classification of our sources, as defined in Sect. 1.2, may be dependent on the projected aperture of our spectra. The fraction of the host galaxy light collected by the spectrograph increases with the projected aperture because of its extended nature (\sim several kiloparsecs), while the unresolved emission from the AGN (\sim hundreds of parsecs) remains constant. This could translate into two observable effects:

- As the host galaxy also emits the [OIII]5007Å emission line, its observed flux would increase at larger projected apertures favouring the classification of higher subtypes (1.0 \rightarrow 1.2 \rightarrow 1.5 \rightarrow 1.8) because it would add to the line flux coming from the AGN.
- The increased host-galaxy contribution will hamper the detection of broad emission lines, favouring the classification of 1.9 and 2 AGN at larger projected apertures.

We briefly studied both effects. First, we calculated the angular distance of our objects, in kpc $''$, from their redshifts, using the cosmology described in the Sect. 1.5. We then obtained the projected aperture by multiplying it by the size of the slit or fibre in arcseconds.

We first checked for an increase in the host galaxy contribution to the measured [OIII]5007Å luminosity with increasing aperture. We obtained the luminosity ratio between the AGN continuum at rest-frame 5100 Å (L_{AGN} , see Sect. 4.4) and the [OIII]5007Å emission line to measure the [OIII]5007Å strength relative to the AGN. The former ratio is equivalent to the equivalent width of [OIII]5007Å. We have used L_{AGN} as it is a good tracer of the bolometric luminosity. We have compared this ratio against the projected aperture, as shown in Fig. 5.3. Any significant increase in host galaxy contribution associated with an aperture effect should increase such ratio with the projected aperture. The lack of a significant correlation is confirmed with a Kendall- τ test ($p \sim 0.29$).

²Uncertainties correspond to the standard error of the mean, σ/\sqrt{N} , with σ the standard deviation and N the number of object in the sample.

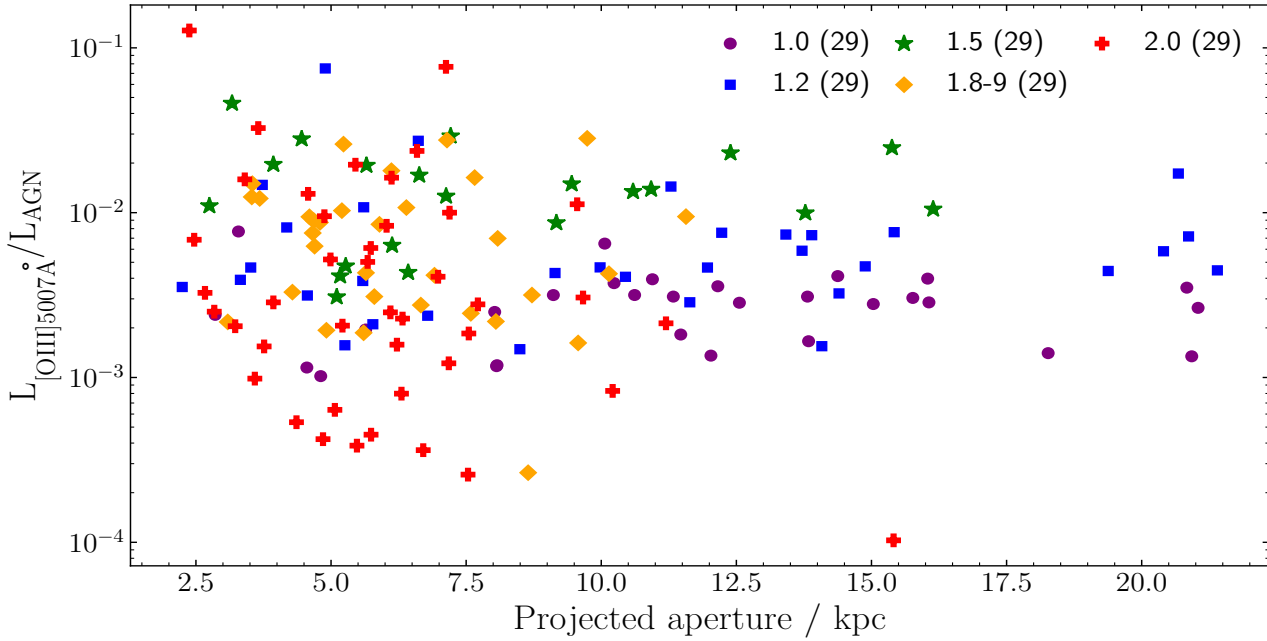


Figure 5.3: $[\text{OIII}]5007\text{\AA}$ luminosity over intrinsic AGN luminosity at rest-frame 5100\AA versus the projected aperture for the working sample. Symbol and colour codes as in Fig. 5.2.

We have followed two approaches to check for any additional potential effect of host galaxy dilution on the detectability of the broad emission lines. First, we compared the AGN luminosity (again, using the AGN luminosity at rest-frame 5100\AA) versus the projected aperture (left plot of Fig. 5.4). Second, we compared the fraction of host-galaxy light inside the projected aperture by subtypes (right plot of Fig. 5.4). We would expect $1.9/2$ at higher projected apertures for a given luminosity and with higher fractions of host-galaxy light. If we do not observe either, we can confidently affirm that the effect of aperture on our subtype determination would be negligible.

We found that at a given luminosity $1.9/2$ s are preferentially placed at the lowest apertures of our sample. This is a selection effect. To obtain spectroscopic redshifts for our AGN sample, we first collected all available SDSS spectra and then did a follow-up of the remaining sources. In this second phase, we used long-slit observations with typical sizes $\sim 1''$, so the projected apertures are smaller than those of the $2''/3''$ fibre-based SDSS spectra. The SDSS spectroscopic survey is biased towards blue type 1 AGN and identified preferentially $1.0 - 5$ s. As such, the identification of $1.8 - 9/2$ s in BUXS has been carried out mainly with our observations, which explains the position of $1.0 - 5$ s in the diagram.

To check for differences between the fraction of host-galaxy light captured inside the projected aperture, ϕ_{Gal} , we calculated it assuming that the surface brightness is well-modelled with a De Vaucouleurs profile with a $R_e = 3\text{ kpc}$, the typical value for early-type galaxies in our range of luminosities (Shen et al., 2003). We integrated the profile differently for a

fibre-based (from SDSS-I/II and BOSS) or a slit spectrum (the rest of the spectrographs). In the first case, we radially integrated the profile using half the projected aperture as the integration radius. For the latter, we carried out a 2D integration over a rectangular area. The size of one side of the rectangle was the projected aperture previously obtained, while to determine the other, we used the projected aperture associated with the extraction size of the spectra of $2''$.

A behaviour similar to that of the left plot of Fig. 5.4 is found when comparing the fraction of host-galaxy light in the spectra by subtypes in the right plot of Fig. 5.4. As it can be seen, 1.9s and 2s AGN have lower values of ϕ_{Gal} than 1.0 – 5s overall, being the difference between mean values is $\Delta\phi_{\text{Gal}} = 0.10 \pm 0.02$, in opposition with the expected behaviour for a significant aperture effect on subtype determination. The difference is also confirmed with a 3σ significance according to the KS test results. This is an immediate consequence of the previous results, as 1.9s and 2s have lower projected apertures than 1.0 – 5s, a smaller part of the host galaxy falls inside the slit of the spectrograph, resulting in smaller ϕ_{Gal} values.

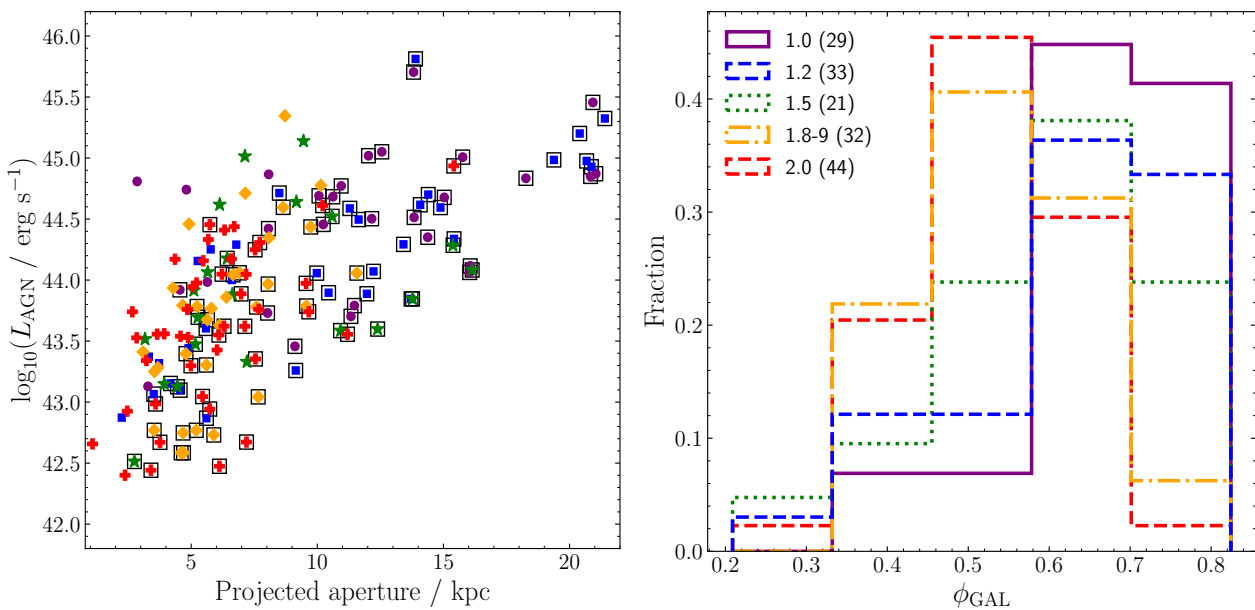


Figure 5.4: (Left) Decimal logarithm of the intrinsic AGN luminosity at rest-frame 5100 \AA versus the projected aperture. Sources with fibre spectrum from SDSS are marked with empty dark squares. (Right) Distributions of the fraction of light of a galaxy collected by the slit by subtypes. Line, symbol and colour codes as in Fig. 5.2.

Additionally, we have checked if the detectability of broad $H\beta$ and $H\alpha$ emission lines in 1.9s and 2s changed depending on whether we used a fibre or slit spectrum. In total, we had eight 1.9s and ten 2s for which we obtained the classification using a fibre spectrum, and we also had slit spectra covering $H\beta$ or $H\alpha$ emission lines, respectively. In all cases, we did not detect a broad component of $H\beta$ or $H\alpha$ emission lines when carrying out the fit using the slit spectra.

The combined evidence of these analyses is enough to conclude that any effect of dilution by aperture does not significantly influence the subtype determination of our sample: neither hampering the detection of the broad component nor increasing the observed flux of [OIII]5007Å.

5.3 Contrast related properties

We first compared the observed contrast between AGN and total emission and then we investigated which properties affected it: the optical extinction, AGN and host galaxy luminosity, and their ratio. The p-values of the KS tests are summarised in Tab. 5.2. The magnitude of the statistically significant differences will be shown in their respective sections and will be described as the difference between the mean values of the distributions.

Sample 1	Sample 2	C_{obs}	$E(B - V)$	$f(nH\alpha)/f(nH\beta)$	L_{AGN}	L_{Gal}	L_{AGN}/L_{Gal}
(1)	(2)	(3)	(4)	(5)	(6)	(7)	(8)
1.0	1.2	<i>0.007</i>	0.117	0.383	0.074	0.113	<i>0.029</i>
1.2	1.5	0.506	0.534	0.637	0.815	0.245	0.462
1.5	1.8 – 9	0.000	0.000	0.422	0.855	0.000	<i>0.005</i>
1.8 – 9	2.0	0.086	0.607	0.055	0.184	0.072	0.880
1.0	1.5	<i>0.009</i>	<i>0.014</i>	0.331	<i>0.012</i>	0.339	<i>0.020</i>
1.2	1.8 – 9	0.000	0.000	0.458	0.939	0.056	<i>0.009</i>
1.5	2.0	0.000	0.000	0.086	0.918	0.000	<i>0.005</i>
1.0 – 5	1.8 – 9/2.0	0.000	0.000	0.856	0.062	0.001	0.000
1.0 – 5*	1.8 – 9/2.0*	<i>0.009</i>	0.000	0.000

Table 5.2: KS test p-value results for the null hypothesis that the samples under consideration have the same distribution for the tested parameter. We reject the null-hypothesis with a 3σ significance if $p < 0.003$. In this case, we mark the result in bold. If the result lies between a 3σ and 2σ significance ($0.003 < p < 0.05$), we display it in italic. Significance levels remains the same if we use instead the AD test. **Cols. 1, 2:** samples evaluated by the KS test; **Col. 3:** observed contrast of the AGN over the total flux at rest-frame 5100 Å; **Col 4:** extinction of the AGN emission; **Col 5:** Balmer decrement of the narrow emission lines; **Col 6:** absorption-corrected luminosity of the AGN at rest-frame 5100 Å weighted by redshift distributions (see Sect. 5.3.3); **Col 7:** host-galaxy luminosity at rest-frame 5100 Å weighted by redshift distributions (see Sect. 5.3.3); **Col 8:** ratio between AGN and host galaxy optical luminosity at rest-frame 5100 Å. (*) These comparisons are limited to AGN with $E(B - V) < 0.65$.

5.3.1 Observed contrast

The starting point of the analysis is the comparison of the observed contrast between the AGN and the total (AGN + host galaxy) observed fluxes. In a classification scheme based

on the detectability of broad emission lines, like the one used in this thesis, intuitively, we would expect to detect a change in contrast with higher subtype as the predominance of AGN emission decreases. In this work, we have defined the observed contrast, C_{obs} , as

$$C_{\text{obs}} = f_{\text{AGN}} / (f_{\text{AGN}} + f_{\text{Gal}}). \quad (5.1)$$

where f_{AGN} and f_{Gal} are the observed (i.e. not corrected for obscuration) AGN and host galaxy flux density at rest-frame 5100 Å, respectively. The values of f_{AGN} and f_{Gal} were directly measured from the SED best-fit AGN and host galaxy templates (see Sect. 4.4).

The distributions of C_{obs} are shown in Fig. 5.5. It can be seen that there is an apparent decrease of C_{obs} with increasing subtype and a substantial decrease from 1.5 to 1.8 – 9 AGN. The KS results (see Tab. 5.2) indicated two significantly different groups: 1.0 – 5 and 1.8 – 9/2.0 AGN, with the former having an overall higher observed contrast than the latter, $\Delta C_{\text{obs}} = 0.52 \pm 0.04$. No statistically significant differences were found between individual subtypes within these groups, although our results hinted at smaller differences between 1.0s and 1.2s ($p = 0.006$) and 1.0s and 1.5s ($p = 0.009$), with $\Delta C_{\text{obs}} = 0.24 \pm 0.07$ and $\Delta C_{\text{obs}} = 0.20 \pm 0.07$ respectively.

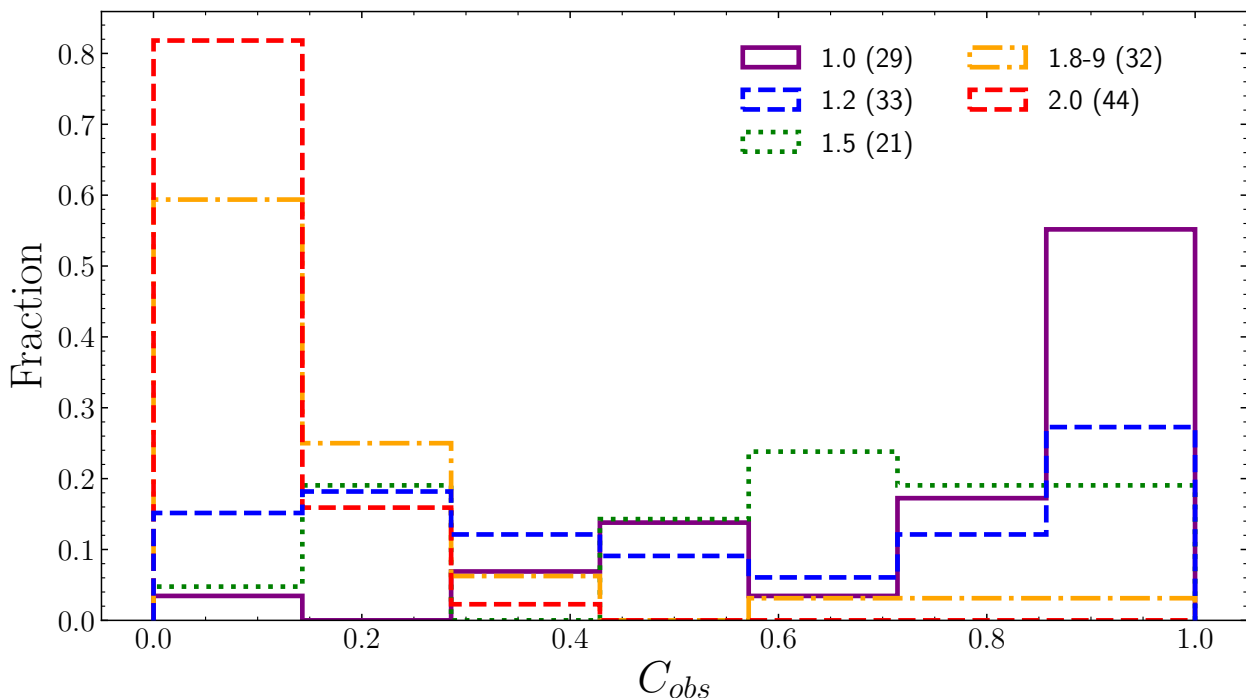


Figure 5.5: Distributions of the observed contrast at rest-frame 5100 Å. Line styles as in Fig. 5.2.

To properly explain the change in subtype, we needed to identify what is leading to this decrease in contrast. Potential drivers are an increase in extinction, changes in the intrinsic luminosity of the host galaxy or AGN, or even a combination of both. The first physical parameter we checked was optical extinction.

5.3.2 Optical extinction

If the line-of-sight optical extinction increases with higher subtype, the AGN observed flux would decrease accordingly, and consequently, the observed contrast would also decrease. To identify if this is the situation, we compared the distributions of optical reddening ($E(B - V)$), a direct proxy of A_V , see Sect. 4.4) obtained from the SED best-fit disk template.

Distributions of $E(B - V)$ by subtype are shown in Fig. 5.6. According to the results of the KS test, we found two different groups composed of 1.0 – 5s and 1.8 – 9/2s AGN, with the latter being AGN are significantly more extinguished than the former, $\Delta E(B - V) = 0.89 \pm 0.09$. This difference translates into an absorption 15 times greater at rest-frame 5100 Å. We did not find any significant differences between finer subtypes. The results do not change if we assign $E(B - V) = 0$ to the fits compatible with no extinction. Furthermore, the difference in observed contrast previously hinted between 1.0s and 1.2s is no longer significant at a 2σ level ($p = 0.117$) when comparing $E(B - V)$. Consequently, even if 1.0s have actually higher contrast than 1.2 – 5, this is unlikely to be consequence of an extinction effect.

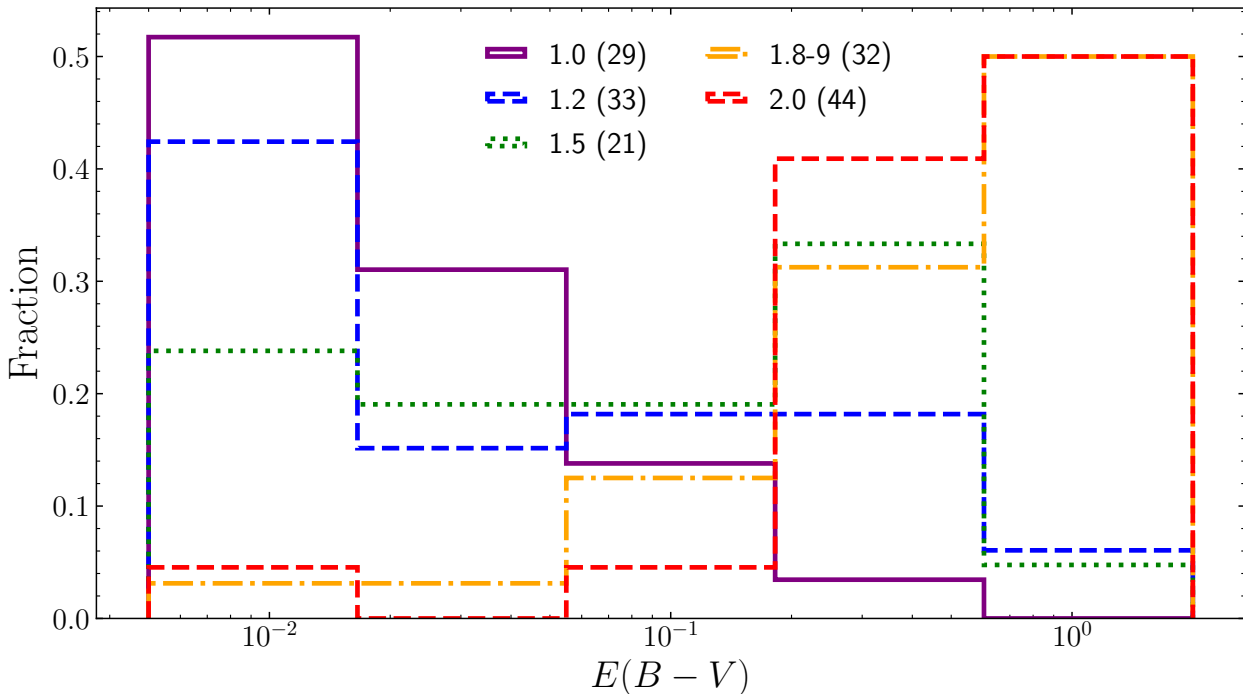


Figure 5.6: Line-of-sight optical extinction of the AGN. $E(B - V) = 0$ values have been added to the lowest bin. Line styles as in Fig. 5.1.

To look for additional insight and a potential relationship between observed contrast and extinction, we have plotted one against the other in Fig. 5.7. To have a quantitative definition of what we can call high and low extinction, we have used as threshold value $E(B - V) = 0.65$, which was found by Caccianiga et al. (2008) as the amount of extinction that was able to suppress the broad component of $H\beta$ enough to be undetected. It can be seen that the highest values of extinction concentrate at the lowest values of contrast while at the lowest extinction, the contrast shows a much wider range of values. This trend is again related to AGN classification in the same direction as before, 1.0/1.2/1.5s with lower extinctions overall and 1.8 – 9/2s with higher extinctions overall.

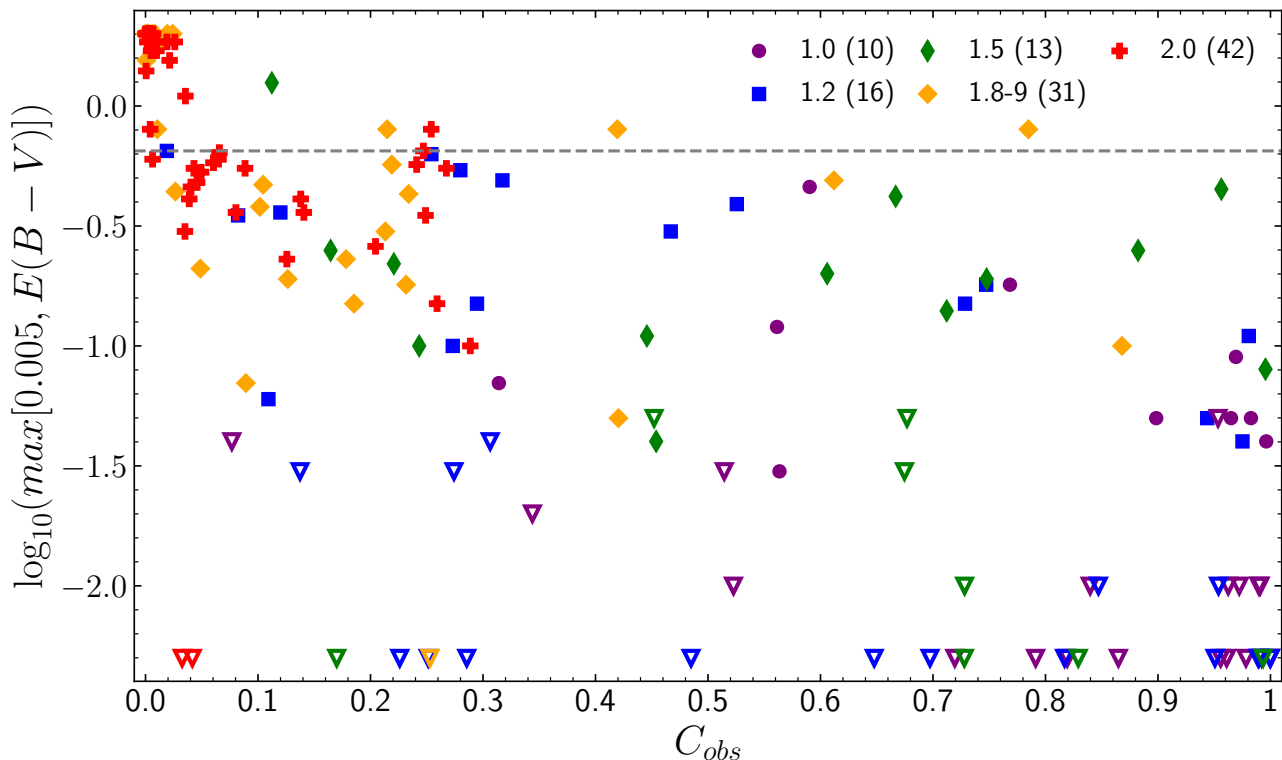


Figure 5.7: AGN optical extinction versus contrast. To represent $E(B - V) = 0$ values in a logarithmic axis, they have been approximated as $E(B - V) = 0.005$. The grey dashed line represents the $E(B - V) = 0.65$ limit defined by Caccianiga et al. (2008). Symbol and colour codes as in Fig. 5.2, except for AGN with $E(B - V)$ compatible with no obscuration, represented with empty triangles pointing down.

Despite this trend, there is a significant fraction of 1.8 – 9s and 2s with low extinction, comparable to 1.0 – 5s. We have 16 1.8 – 9s (50%) and 22 2s (50%) with low extinction, insufficient to explain the non-detection of the broad component of the emission lines and, consequently, their intermediate classification. We have checked that all these objects have a probability of at least 90% to be below the extinction threshold using $\Delta\chi^2$ (see Sect. 4.4). A similar fraction of 1.8 – 9 with low extinction is found in previous works in the literature (Caccianiga et al., 2004; Trippe et al., 2010). For these objects, an additional effect should

decrease the observed contrast enough to explain their optical subtype. We will explore this in Sect. 5.3.3.

The extinction measured from the SED fits accounts for the total extinction along the line of sight. Consequently, it could be associated exclusively with AGN material at circumnuclear scales (Pogge & Martini, 2002; Lyu et al., 2014; Calistro Rivera et al., 2021), the gas and dust of the host galaxy (Maiolino & Rieke, 1995; Alonso-Herrero et al., 2003a; Dunn et al., 2015; Baron et al., 2016) or be a combination of both (Hickox & Alexander, 2018). To clarify which situation we are in, we have investigated whether there are differences in extinction associated with the host galaxy between subtypes.

The extinction value from the SED best-fit host-galaxy template is unreliable for this analysis. In AGN with high observable contrast, the host-galaxy extinction would be poorly constrained as the bluest part of its emission would be out-shined by the accretion disk emission. It would affect mostly 1.0 but also an important part of 1.2 and 1.5, making comparisons between subtypes equally unreliable.

Instead, to estimate the extinction caused by the host galaxy, we have calculated the Balmer decrement of the $H\alpha$ and $H\beta$ narrow emission lines, $f(nH\alpha)/f(nH\beta)$. These lines originate far from the nuclear region of the AGN, at hundreds or even thousands of parsecs (See Sect. 1.3). Consequently, their emission is not affected by circumnuclear extinction (Heard & Gaskell, 2016), but they can still suffer extinction from the gas and dust of the host galaxy. Furthermore, the intrinsic narrow line Balmer decrement distribution is not expected to change between subtypes (Gaskell & Ferland, 1984). Therefore, any differences should be related to changes in the host galaxy extinction.

To derive $f(nH\alpha)/f(nH\beta)$ we obtained the total flux of the narrow components of $H\beta$ and $H\alpha$, adding up the flux from the core and wing components. We used only AGN with detection for both emission lines and, to avoid uncertainties related to cross-calibration between different spectrographs, AGN for which both emission lines are measured in the same spectrum. In total, we obtained $f(nH\alpha)/f(nH\beta)$ for 107 AGN (67% of the working sample).

The distributions of narrow line Balmer decrement are shown in Fig. 5.8. They are visually similar for all subtypes, exhibiting a clear peak around $\log_{10}[f(nH\alpha)/f(nH\beta)] = 0.62$, the median value for the whole sample, which is comparable with previous findings in the literature (Baron et al., 2016; Lu et al., 2019; Selwood et al., 2023). Only the 1.0s distribution differs slightly, showing a secondary peak at high values. We checked that the AGN corresponding to this peak are associated with $H\beta$ profiles completely dominated by the broad component. In these cases, narrow $H\beta$ is detected but poorly constrained as its shape is diluted in the total profile. In these cases, the correspondent values of narrow $H\alpha$ are generally better fitted due to constraints imposed by the [NII] doublet. Regardless, KS tests confirm no significant differences are found between any subtypes or groups, including 1.0s.

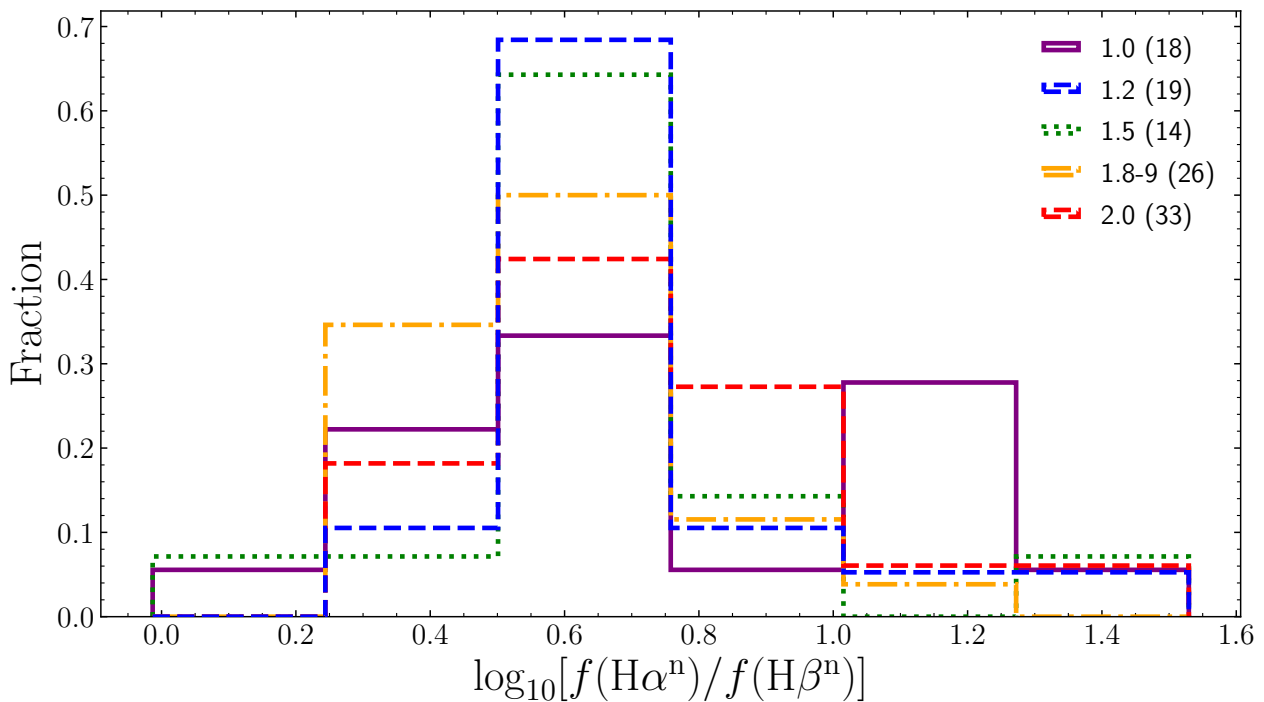


Figure 5.8: Distribution of the Balmer decrement of the narrow components of $H\alpha$ and $H\beta$ for AGN with detection of both narrow emission lines. Line styles as in Fig. 5.1.

The best overall value of the intrinsic ratio of the narrow line Balmer decrement is $f(nH\alpha)/f(nH\beta) = 3.1$ and, unlike with the broad emission lines, it has been long indicated that it can be used to estimate the reddening (Gaskell, 1982; Gaskell & Ferland, 1984; Wysota & Gaskell, 1988). We then derived the extinction suffered by the NLR and compared it with our values from the SED, as shown in Fig. 5.9.

We found that most AGNs with line-of-sight $E(B-V) < 0.65$ have overall extinction values compatible with those derived from the narrow line Balmer decrement. For this population, most, if not all, of the line-of-sight extinction could arise in material in the host galaxy. However, for those $1.8-9/2s$ with $E(B-V) > 0.65$, there must be an important contribution of material at circumnuclear scales, which is likely playing the leading role in the contrast decrease and consequently in the subtype determination.

According to our results, extinction is an essential actor behind the contrast change and, consequently, the determination of the AGN subtype. It increases from $1.0-5$ to $1.8-9/2s$ and follows the same trend as contrast. The high extinction for those $1.8-9/2s$ with $E(B-V) > 0.65$ can be associated with a circumnuclear component, while for the rest, it can be explained by material in the host galaxy. However, for about half of the $1.8-9/2$ group, the extinction, whatever its origin, is not enough to explain their low observed contrast and, consequently, classification.

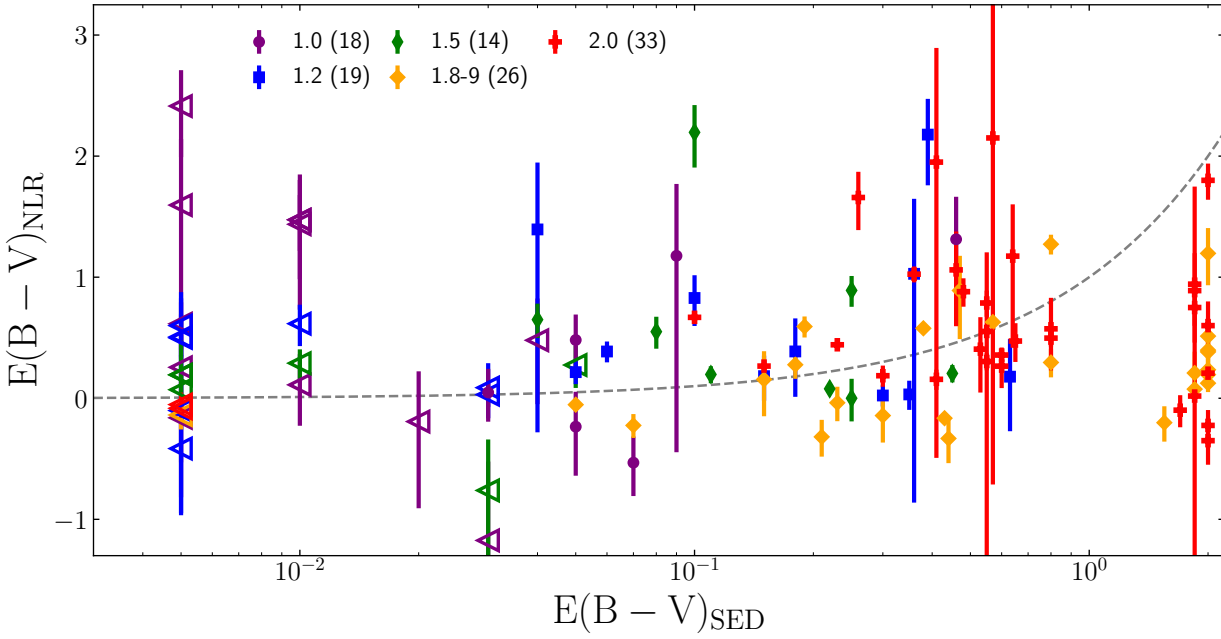


Figure 5.9: Extinction from the Balmer decrement of the narrow lines, $E(B - V)_{\text{NLR}}$, versus the value from the SED fitting, $E(B - V)_{\text{SED}}$. The grey dashed line corresponds to the 1:1 relation. Symbol and colour codes as in Fig. 5.2, except for AGN with $E(B - V)_{\text{SED}}$ compatible with no obscuration, represented with empty triangles pointing left.

5.3.3 AGN and host galaxy luminosity

As shown before, extinction can not be the only parameter driving the subtype determination. An additional explanation would be a decrease in the AGN luminosity or an increase in the galaxy luminosity with subtype or both, resulting in a decline in the observed contrast.

Previous works have reported that type 1 AGN have higher intrinsic luminosity than type 2 AGN. This trend has been detected at different wavelengths, but mostly in X-rays (Della Ceca et al., 2008; Burlon et al., 2011; Ueda et al., 2014; Lacy et al., 2015; Koss et al., 2017). Additionally, Stern & Laor (2012) found a decrease in the AGN luminosity with increasing subtype. To look for any dependence with classification in our sample, we have used the extinction-corrected AGN luminosity at rest-frame 5100 \AA , L_{AGN} , calculated in the Sect. 4.4.

To properly compare luminosities between subtypes, we need to account for the differences in the redshift distributions (shown in Fig. 5.2). To correct our luminosity distributions, we assigned to each object a weight following the same procedure as in Mendez et al. (2016) and Mountrichas et al. (2021). First, we obtained the distribution of redshift of the entire sample and divided it into bins of $\Delta z = 0.125$, the smaller bin size for which all bins have the same width and have at least one object of every subtype. Then, we repeated the same process for the distribution of each subtype. Finally, for each AGN in a particular bin i of a certain subtype, s , the weight, w_{is} , is calculated as the number of AGN in that bin, N_i , over the overall number of AGN of that certain subtype in the same bin, N_{is} .

$$w_{is} = \frac{N_i}{N_{is}}. \quad (5.2)$$

From now on, all discussions about L_{AGN} and L_{Gal} refer to the redshift-corrected distributions. We also accounted for the redshift correction when conducting the KS test. We weighted the luminosity cumulative distributions involved by these same weights. To implement it, we adapted the unweighted KS test code available in the Numpy package (Harris et al., 2020) to follow the procedure shown in Monahan (2011).

The distributions of L_{AGN} are presented in Fig. 5.10. The lowest p-values obtained correspond to 1.0s with 1.2s, and 1.0s with 1.5s. However, no comparison between individual subtypes or groups returned a statistical significance greater than 3σ . Similar results are found if we use X-ray luminosities instead. These results suggest that L_{AGN} is unlikely to play a key role in the AGN classification.

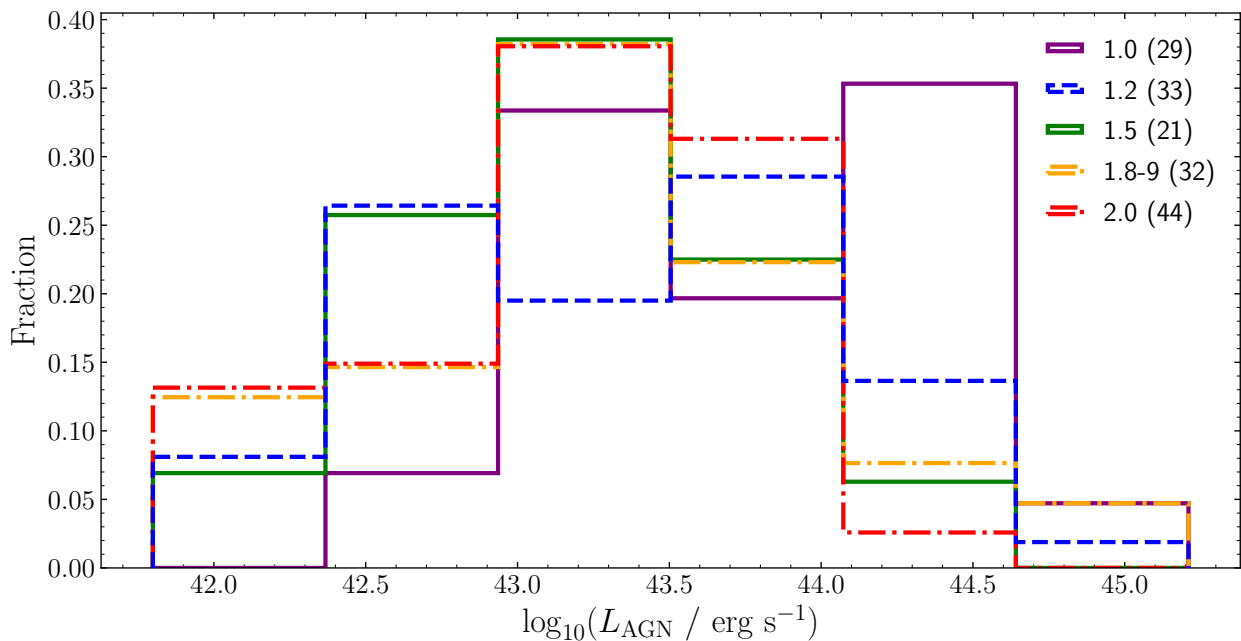


Figure 5.10: Redshift weighted distributions of AGN luminosity at rest-frame 5100 Å. Line, symbol and colour codes as in Fig. 5.2.

Previous studies in the literature found that the stellar mass of the host galaxies of type 2s is slightly larger than that of type 1, a difference that may or may not appear statistically significant (Zou et al., 2019; Mountrichas et al., 2021; Koutoulidis et al., 2022), although, other studies found types 1 and 2 to have host galaxies with similar stellar masses (Kauffmann et al., 2003; Merloni et al., 2014; Bornancini & García Lambas, 2018b). The most massive host galaxies are expected to be more luminous than the rest, and their observed contrast of the hosted AGN will be smaller. In this thesis, we directly derived the host galaxy luminosity at rest-frame 5100 Å from the SED fitting. With this approach, we are focusing on

the parameter directly affecting the observed contrast. We show the distributions of host galaxy luminosity, L_{Gal} , in Fig. 5.11.

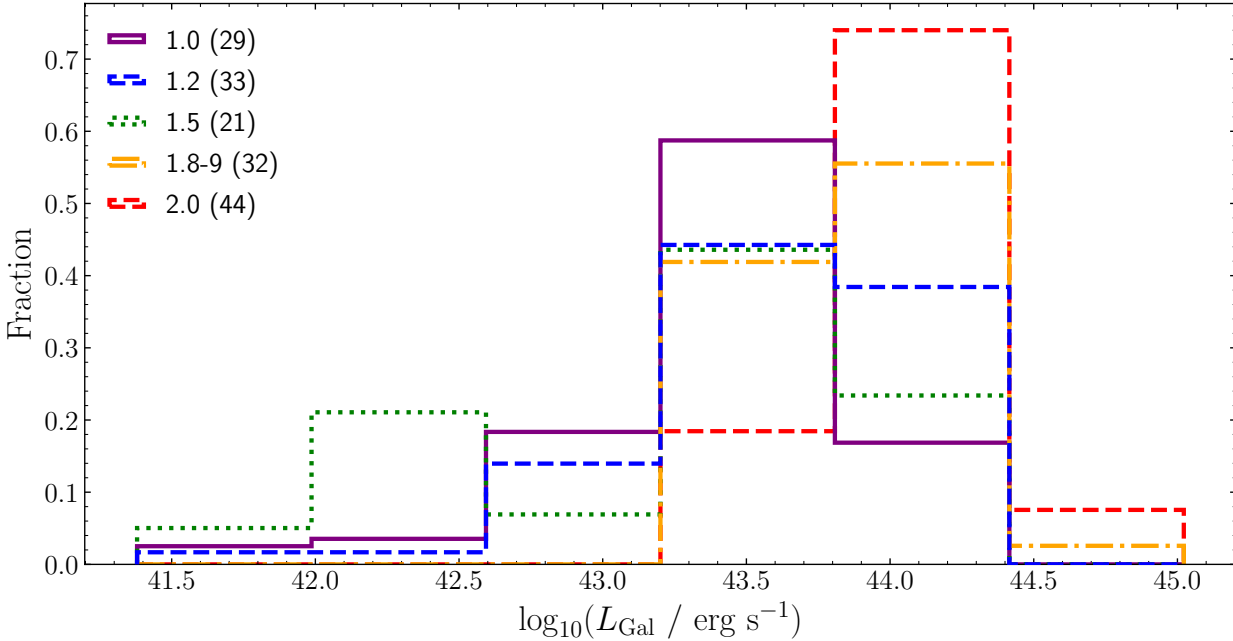


Figure 5.11: Redshift weighted distributions of the luminosity of the host galaxy at rest-frame 5100 Å. Line, symbol and colour codes as in Fig. 5.2.

According to the KS results, we found significant differences when comparing 1.5s with 1.8 – 9s and 2s (see Col. 7 of Table 5.2) and this extends to a difference the 1.0 – 5 and 1.8 – 9/2 groups. The difference between these two big groups is significant, $\Delta\log_{10}(L_{\text{Gal}}) = 0.68 \pm 0.09$ dex, and could partially explain the decrease of observed contrast.

As shown in Sect. 5.2, the projected apertures of the spectra of 1.0–5s are larger than those of 1.8 – 9/2s. This means that although we detected a L_{Gal} difference using photometric data, which collects the light of the whole galaxy, the difference may be diluted in the optical spectra and did not impact the subtype determination. So, we checked if the observed difference remains if we compare the light of the host-galaxy collected by the spectrograph instead. To do so, we multiplied the host galaxy luminosity by the fraction of light collected by the spectrograph, ϕ_{Gal} (see Sect. 5.2).

The the KS results remain when comparing groups and the previously reported difference still persist, decreasing only slightly, $\Delta\log_{10}(L_{\text{Gal}}) = 0.51 \pm 0.09$ dex. We also checked that the results did not change if we compare instead the host-galaxy luminosity at rest-frame 1 μm , the wavelength at which its luminosity peaks.

Our results reveal that the AGN luminosity does not play a significant role in subtype determination and could be affecting it only as a secondary effect. The host galaxy of 1.8 – 9/2s, however, are clearly more luminous than those of 1.0 – 5s, even when taking into considera-

tion the redshift and aperture difference between both groups. This difference may explain the reduced observed contrast in low-extinction $1.8 - 9/2s$ as a dilution effect.

5.3.4 AGN over host galaxy luminosity ratio

The observed contrast does not depend only on the AGN or host galaxy luminosity; it involves both. So we have also investigated their combined effect using the ratio of the AGN over host galaxy luminosities, $L_{\text{AGN}}/L_{\text{Gal}}$. This ratio has the additional advantage over the individual luminosities of being a value that does not need a redshift correction. The results are presented in Fig. 5.12. We compared the individual and grouped distributions as before.

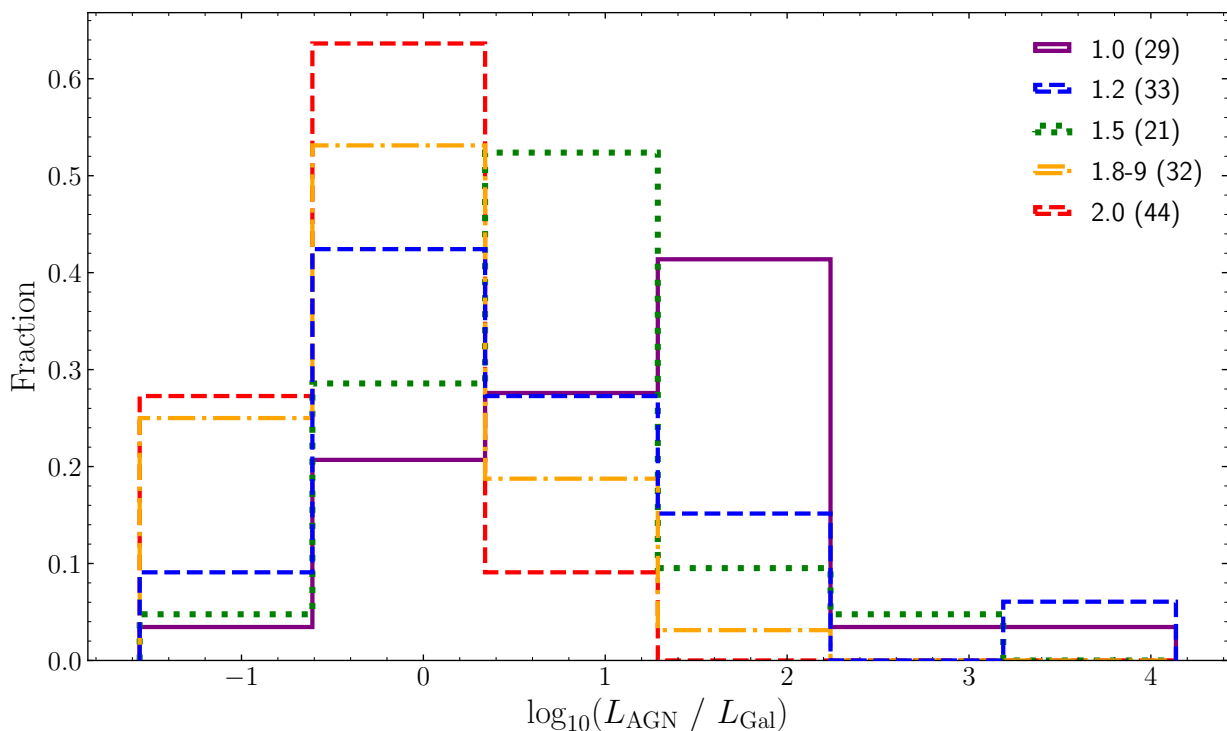


Figure 5.12: AGN over host galaxy luminosity ratio at rest-frame 5100 \AA . Line styles as in Fig. 5.1.

Once again, the KS test revealed a 3σ significance when comparing $1.0 - 5s$ versus $1.8 - 9/2s$, the latter having an overall lower intrinsic AGN over host galaxy luminosity ratio than the first. The mean values of $\log_{10}(L_{\text{AGN}}/L_{\text{Gal}})$ for the $1.0 - 5$ and $1.8 - 9/2$ samples are -0.23 ± 0.08 and 0.84 ± 0.11 , respectively. The resultant difference is of more than one order of magnitude, 1.08 ± 0.19 dex, greater than when comparing L_{Gal} alone.

Additionally, the combined effect of AGN and host galaxy luminosities enhanced the KS results for several individual comparisons, although all remained below 3σ . However, the results hinted at individual differences between subtypes 1.0 and $1.2 - 5$, with similar results to those of the observed contrast distributions. We also compared the main groups limiting

to $E(B - V) < 0.65$ to focus on the $1.8 - 9/2$ s not explained by the extinction alone. We found an even more significant difference with the difference between mean values being 1.3 ± 0.2 dex, with a mean value of 0.87 ± 0.11 for $1.0 - 5$ s and of -0.41 ± 0.08 for $1.8 - 9/2$ s.

So far, we have considered the effects of extinction and intrinsic luminosities separately. To identify if there is a relation between both, we have represented them in Fig. 5.13. The stars shown correspond to the mean point of the $1.0 - 5$ and $1.8 - 9/2$ with $E(B - V) < 0.65$. It can be shown how $1.8 - 9/2$ s with low extinctions are both preferentially found at the extinctions closer to the $E(B - V) = 0.65$ limit and at $L_{\text{AGN}}/L_{\text{Gal}}$ lower values than those of $1.0 - 5$ s. This revealed that in these cases, the lower $L_{\text{AGN}}/L_{\text{Gal}}$ combined with an extinction close to the $E(B - V) = 0.65$ limit reduces the contrast enough to change its subtype.

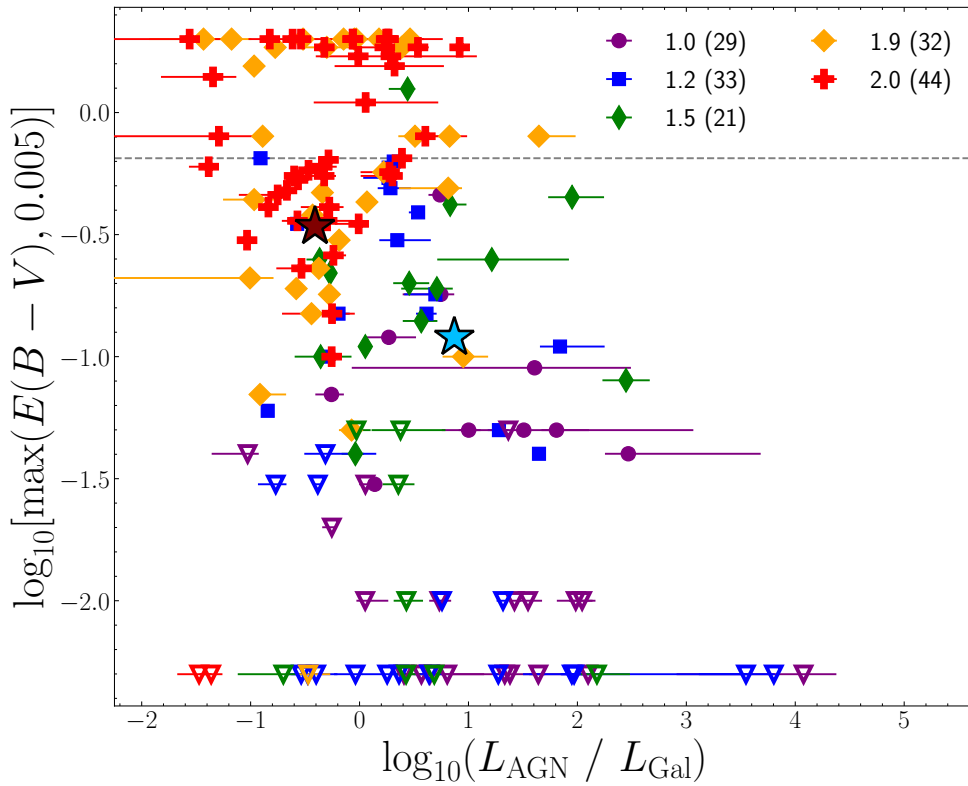


Figure 5.13: Intrinsic AGN over host galaxy contrast at rest-frame 5100 \AA versus the optical extinction. To represent $E(B - V) = 0$ values in a logarithmic axis, they have been approximated as $E(B - V) = 0.005$. Large stars correspond to the mean values of extinction and $\log_{10}(L_{\text{AGN}}/L_{\text{Gal}})$ for $1.0 - 5$ (blue star) and $1.8 - 9/2$ (red star). Symbol and colour code as in Fig. 5.2, except for AGN with $E(B - V)$ compatible with no obscuration, represented with empty triangles pointing down.

These results suggest the following scenario: half the $1.8 - 9/2$ objects lack enough extinction to provoke their change from $1.0 - 5$ to $1.8 - 9/2$ by itself. In these objects, a low value of $L_{\text{AGN}}/L_{\text{Gal}}$, consequence mainly of a high value of L_{Gal} , is enough to provide the extra reduction in observed contrast necessary for that change between groups.

5.4 Emission line luminosities

In the previous section, we found the parameters driving the dichotomy between the 1.0 – 5 and 1.8/9 – 2 groups. However, we still did not obtain a proper explanation for the origin of the subtype determination of 1.0s, 1.2s, and 1.5s.

So far, we have only considered properties measured from the continuum emission. However, the classification criterion is based on the flux ratios of emission lines and, consequently, depends on their strength. Therefore, in this section, we focused on studying the relative luminosity with respect to the AGN luminosity at rest-frame 5100 Å, L_{AGN} , of both the broad emission lines H β ($r_{\text{bH}\beta} = L_{\text{H}\beta}/L_{\text{AGN}}$) and H α ($r_{\text{bH}\alpha} = L_{\text{H}\alpha}/L_{\text{AGN}}$) and narrow emission lines (focusing on [OIII]5007Å, $r_{[\text{OIII}]} = L_{[\text{OIII}]} / L_{\text{AGN}}$) of subtypes 1.0, 1.2, and 1.5.

For $r_{\text{bH}\beta}$ and $r_{[\text{OIII}]}$, the reference rest-frame wavelengths of both luminosities are close between them and are affected by comparable $E(B - V)$. Consequently, the ratio should not be strongly affected by extinction, so we used the directly observed luminosities. In the case of $r_{\text{bH}\alpha}$, this was not possible, and we corrected both luminosities by the total line-of-sight extinction value. Given their definitions, $r_{\text{bH}\beta}$ and $r_{[\text{OIII}]}$ should be proportional in first approximation to the equivalent width of their respective emission lines.

As in the previous section, we summarised the significance of the null hypothesis when comparing distributions with the KS test and the correlation between two parameters with the Kendall- τ test in Tab. 5.3 and in Tab. 5.4, respectively, while the magnitude of the differences or trends are described in their respective sections.

Sample 1	Sample 2	$r_{\text{bH}\beta}$	$r_{\text{bH}\alpha}$	$r_{\text{bH}\beta}^{z < 0.4}$	$r_{\text{bH}\beta - \alpha}$	$r_{[\text{OIII}]}$
(1)	(2)	(3)	(4)	(5)	(6)	(7)
1.0	1.2	0.492	0.306	0.483	0.415	0.000
1.2	1.5	0.462	0.545	0.319	0.739	0.000
1.5	1.8	-	-	-	0.001	-
1.0	1.5	0.167	0.156	0.074	0.080	0.002
1.2	1.8	-	-	-	0.000	-

Table 5.3: KS test p-values for the null hypothesis for different parameters of the emission lines. Style code for significance remains as in Tab. 5.2. **Cols. 1, 2:** samples evaluated by the KS test; **Col 3:** relative luminosity of the broad component of H β ; **Col 4:** relative luminosity of the broad component of H α using only AGN with $z < 0.4$; **Col 5:** relative luminosity of the broad component of H β using only AGN with $z < 0.4$; **Col 6:** same as Col. 3 but adding up 1.9s with $E(B - V) < 0.65$ for which broad H β was estimated from H α observations assuming an intrinsic Balmer decrement of 3.06 (Dong et al., 2008). For this comparison, the 1.9s were reclassified as 1.0 – 8 using [OIII]5007Å and the estimated flux of H β ; **Col. 7:** relative luminosity of the [OIII]5007Å emission line.

Parameter 1	Parameter 2	p-value
(1)	(2)	(3)
R	$r_{\text{bH}\beta}$	0.385
L_{AGN}	$r_{\text{bH}\beta}$	0.835
R	$r_{[\text{OIII}]}$	0.000
L_{AGN}	$r_{[\text{OIII}]}$	0.003

Table 5.4: Kendall- τ test p-values results for the null hypothesis for the whole 1.0 – 5 subsample. Style code for significance remains as in Tab. 5.2. **Cols. 1, 2:** parameters evaluated; **Col. 3:** p-value for the comparison.

5.4.1 Relative luminosity of the broad emission lines

One explanation for the subtypes 1.0s, 1.2s and 1.5s could be that they correspond to a sequence of decreasing relative luminosity of the broad H β emission line with subtype. In fact, Elitzur et al. (2014) found a small decrease in the relative luminosity of the broad H α emission line with increasing subtype and an increase with the bolometric luminosity of the AGN. This was interpreted as a decrease in the covering factor of the BLR, postulating in Elitzur & Ho (2009) even the disappearance of the BLR at the lowest luminosities. This is one of the models usually proposed to explain the behaviour of changing look AGN (Denney et al., 2014; LaMassa et al., 2015; McElroy et al., 2016; Li et al., 2022). However, results such as the detection of a broad component in the true type 2 candidate NGC 3147 (Bianchi et al., 2019), whose bolometric luminosity is below the minimum value inferred for forming a BLR, challenge this model.

To determine if the broad H β relative luminosity decreases with increasing subtype, we studied the relation of R with $r_{\text{bH}\beta}$ and the distributions of $r_{\text{bH}\beta}$, both shown in Fig. 5.14. A visual inspection suggests no significant correlation between $r_{\text{bH}\beta}$ and R , confirmed by the results of a Kendall- τ test ($p = 0.385$). We used the Bayesian fitting technique LinMix³, described in Kelly (2007), to gain additional insight. We fitted the data with a linear relationship $r_{\text{bH}\beta} = m \times R + b$. LinMix returns the Markov chain for every fitted parameter, so we used the median as the representative value and obtained the 1σ error as those for which the described range encompassed 68.27% of the values of the chain. The best fit returned a slope $m = -0.03 \pm 0.08$ and a intercept $b = -1.84 \pm 0.04$. The almost zero fitting value of the slope reinforces the absence of any dependence.

According to the KS results, we did not find any significant differences when comparing $r_{\text{bH}\beta}$ distributions between any of the three AGN subtypes. The combined evidence suggests that if there is any decrease of $r_{\text{bH}\beta}$ with subtype, it is rather small and cannot play a key role in determining the subtype.

³A Python implementation is available in <https://github.com/jmeyers314/linmix>

To further confirm the absence of any change of $r_{\text{bH}\beta}$ in our sample, we studied the relation between $r_{\text{bH}\beta}$ and L_{AGN} . An effect regulated by AGN luminosity should be easier to detect since our sample covers three orders of magnitude in L_{AGN} . The relation between these two magnitudes is shown in the top right plot of Fig. 5.14. The absence of any dependence of $r_{\text{bH}\beta}$ with luminosity is clear and confirmed with the Kendall- τ test returning $p = 0.835$. The LinMix best fit returned a best-fit slope $m = 0.01 \pm 0.04$ and intercept $b = -2.4 \pm 1.9$, compatible with no dependence.

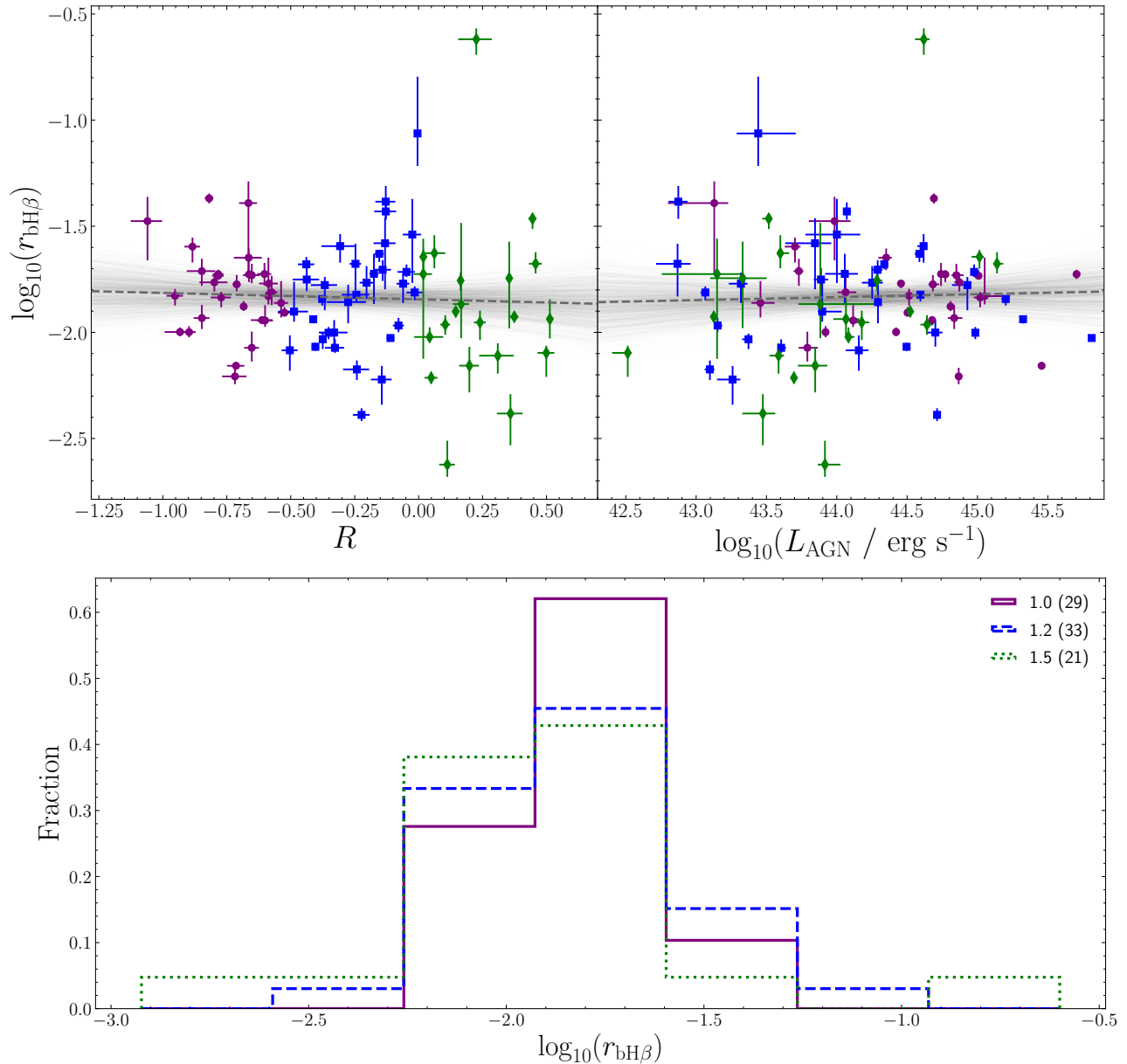


Figure 5.14: (Top left) $r_{\text{bH}\beta}$ versus R . (Top right) $r_{\text{bH}\beta}$ versus L_{AGN} . The dashed grey lines correspond to the best fit of a linear relationship. The shadowed areas correspond to the fitting tuples obtained from the posterior chains of the fit carried out using LinMix. (Bottom) Distributions of $r_{\text{bH}\beta}$. Symbol and colour codes as in Fig. 5.2 for both plots.

We have also checked if the absence of any trend remains if we use instead the broad component of the $H\alpha$ emission line, $r_{bH\alpha}$, which is stronger and better constrained than $H\beta$. As we did not have $H\alpha$ coverage for all AGN, we considered only AGN with redshifts up to $z = 0.4$ in this analysis to cover similar redshift ranges for 1.0s, 1.2s and 1.5s. The distributions, shown in the left plot of Fig. 5.15, may suggest a wider distribution for 1.5s. However, our KS results show that the difference between 1.5s and 1.0s or 1.2s, or any other comparison, is not statistically significant. We also repeated the $r_{bH\beta}$ analysis imposing $z < 0.4$ (right plot of Fig. 5.15) and found no significant differences.

The absence of the previously hinted trend could be partly due to how our samples of intermediate types were compiled. The sample used by Elitzur et al. (2014) was the same as that of Stern & Laor (2012), and both used the same criteria to classify AGN: the flux ratio between the broad and narrow components of $H\alpha$. If we reclassify our sample with their classification criterion, only 55% of the 1.0s, 42% of the 1.5, and 53% of the 1.8 – 9 would remain classified as such. At the same time, 1.2s with $H\alpha$ coverage would be distributed among the rest of the classes. This makes a direct comparison between works difficult.

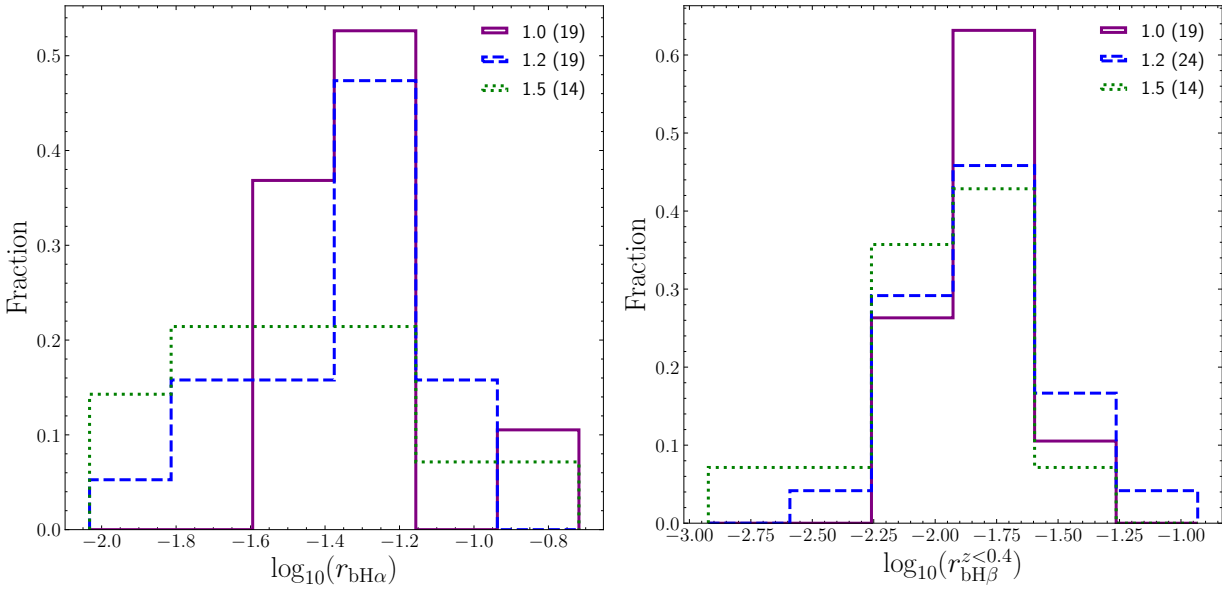


Figure 5.15: (Left) Distributions of $r_{bH\alpha}$ for 1.0s, 1.2s, 1.5s with $z < 0.4$. (Right) Distributions of $r_{bH\beta}$ for 1.0s, 1.2s, 1.5s with $z < 0.4$. Symbol and colour codes as in Fig. 5.2.

Additionally, they performed a spectral fitting process in which the continuum was fitted over the whole spectrum with a model for the host galaxy that is more complex than ours. This may have allowed the detection of broad lines weaker than those in our sample. To check if the lack of detection of the weakest broad components of $H\beta$ could explain why we are not detecting a trend of decreasing $r_{bH\beta}$, we have estimated the expected observed flux of broad $H\beta$ from broad $H\alpha$ for the 1.9s with low extinction (14 AGN). Broad $H\beta$ is undetected in these AGN mainly because of the low intrinsic AGN over host galaxy luminosity ratio,

so we expect the weakest broad H β lines to be found in these objects.

To estimate the expected broad H β line luminosity, we used the flux of the broad H α emission line corrected for extinction, applying the Galactic extinction law of Cardelli et al. (1989). Then, we obtained the flux of broad H β , assuming the intrinsic flux ratio between both components to be $f_{bH\alpha}/f_{bH\beta} = 3.06$ (Dong et al., 2008). We checked that all 1.0s, 1.2s and 1.5s have similar $f_{bH\alpha}/f_{bH\beta}$ (see Fig. 5.16) and found they have distributions peaking around the expected intrinsic value. Then, we applied the extinction to $f_{bH\beta}$ using the same extinction law as before and derived the intermediate subtype for the 14 1.9s with low extinction. We also checked that for 1.0s, 1.2s and 1.5s with both H β and H α coverage, the value of the observed $f_{bH\beta}$ retrieved from the spectra matches well with the estimated value using this method. The overall good correlation between both quantities can be seen in Fig. 5.16. However, we acknowledge the intrinsic value of $f_{bH\alpha}/f_{bH\beta}$ is still debated, as previously stated, and results derived from this analysis should be taken as hints but not as strong conclusions.

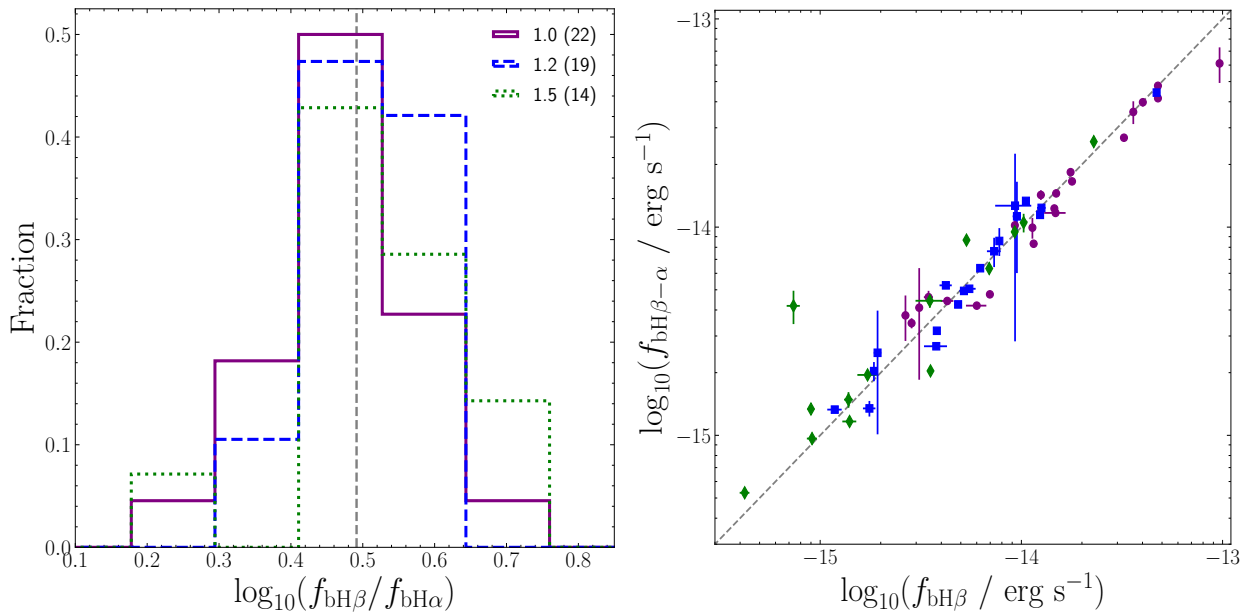


Figure 5.16: (Left) Distribution of the intrinsic (extinction corrected) ratio between broad H β and H α emission lines. The vertical dashed line corresponds to the intrinsic value $f_{bH\alpha}/f_{bH\beta} = 3.06$. **(Right)** Observed fluxes of the broad component of H β versus the expected values estimated from H α . The grey dashed line corresponds to the 1:1 relation. Symbol and colour codes as in Fig. 5.2 for both plots.

Out of the initial 14 1.9s, six were classified as 1.2s, five as 1.5s and three as 1.8s. We repeated the previous analysis; the results are presented in Fig. 5.17. Due to the increased sample size of 1.8s, we treated them as an independent group. The comparison of $r_{bH\alpha}$ between 1.0s, 1.2s and 1.5s are still not significant in any case; neither the Kendall- τ ($p = 0.22$) nor the KS results are significant. However, when including the 1.8s, we found a significant decrease in their $r_{bH\beta}$ compared to 1.0 – 5s. The mean $r_{bH\beta}$ of 1.8s is almost one order of

magnitude smaller (0.79 ± 0.11 dex) than that of $1.0 - 5s$, which translates to a reduction of the observed flux of the broad component of $H\beta$ by a factor of six. This is enough to explain their classification as 1.8 and their observed extreme values of R .

However, this result remains only a hint due to the small size of the 1.8s sample. For the same reason, we refrain from further investigating its origin. A potential explanation could be a reduced covering factor of the BLR.

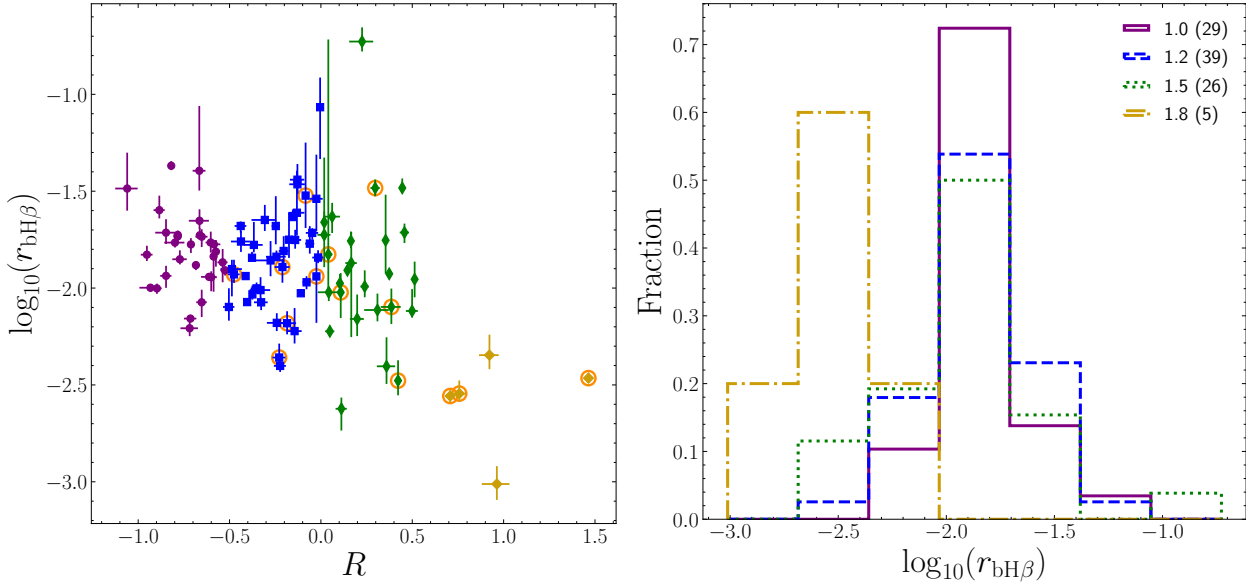


Figure 5.17: (Left) $r_{bH\beta}$ versus R . AGNs for which $r_{bH\beta}$ has been estimated from the broad $H\alpha$ are marked with empty circles. (Right) Distribution of $r_{bH\beta}$. Symbol and colour codes as in Fig. 5.2 except for 1.8s, now represented using a dark yellow colour.

5.4.2 Relative luminosity of the $[OIII]5007\text{\AA}$ emission line

Another origin of the change in subtype for $1.0 - 5$ AGN could be an increase in the narrow emission line relative luminosity. Stern & Laor (2012) found a gradual decrease in the relative luminosity of $[OIII]5007\text{\AA}$ with increasing AGN bolometric luminosity. This trend was linked to the intermediate optical classification of AGN, suggesting that the detected subtype was driven by this effect.

Consequently, we have also checked for a dependence of the relative luminosity of the $[OIII]5007\text{\AA}$ emission line with both subtype and L_{AGN} . As with the relative luminosity of broad $H\beta$, we have used the ratio between $[OIII]5007\text{\AA}$ luminosity and the AGN luminosity at rest-frame 5100\AA , $r_{[OIII]} = L_{[OIII]}/L_{AGN}$. Similarly to $r_{bH\beta}$, $r_{[OIII]}$ should be proportional in first approximation to the equivalent width of $[OIII]5007\text{\AA}$.

In Fig. 5.18, we show both the relation of $r_{[OIII]}$ with R for the $1.0 - 5s$ (left plot) and their $r_{[OIII]}$ distributions (right plot). The first plot shows a strong relation between $r_{[OIII]}$ and R . The results of Kendall- τ confirmed the presence of a correlation with a significance of

more than 3σ . The distributions of $r_{[\text{OIII}]}$ by subtypes also show clear differences, and the KS results confirmed that the comparisons between all three subtypes have a significance greater than 3σ .

As in the previous section, we also fitted the 1.0 – 5s with a linear regression using `LinMix`. We obtained a positive relation between both parameters, with slope $m = 0.97 \pm 0.07$ and intercept $b = -1.86 \pm 0.04$. The increase in the relative luminosity of $[\text{OIII}]5007\text{\AA}$, by around a factor of ten between the lowest and largest values, is sufficient to explain the change in subtype from 1.0s to 1.5s.

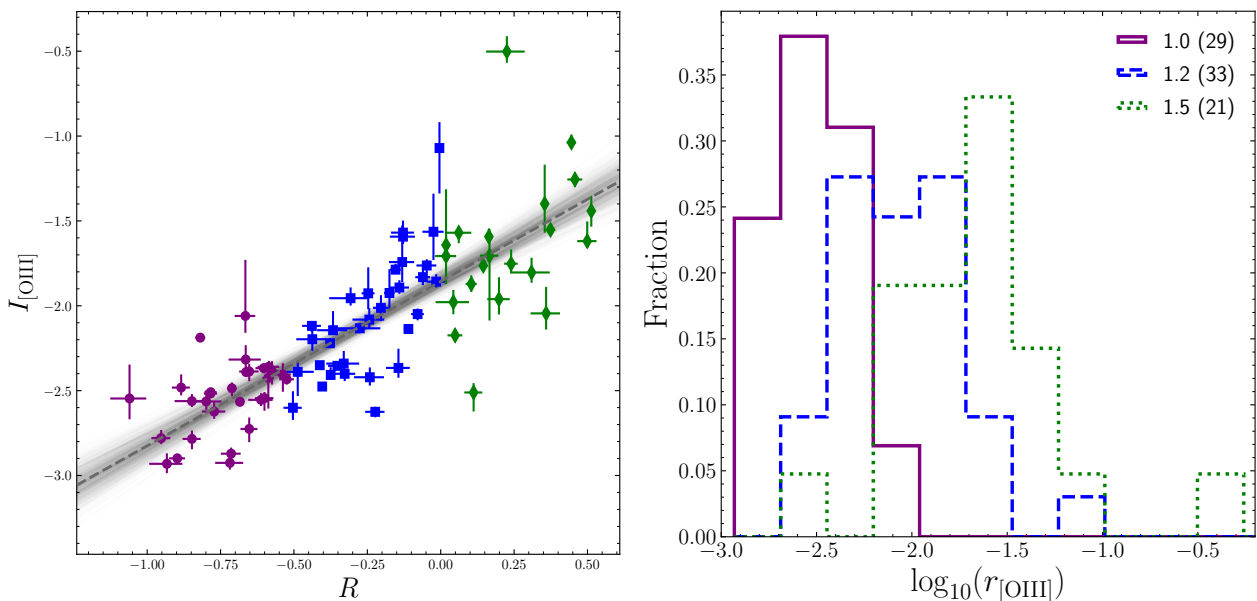


Figure 5.18: (Left) $r_{[\text{OIII}]}$ versus R . The dashed grey line corresponds to the best fit of a linear relationship. The shadowed area corresponds to the fitting tuples obtained from the Markov chains. (Right) Distribution of $r_{[\text{OIII}]}$. Symbol and colour codes as in Fig. 5.2.

Fig. 5.19 shows the relation between $r_{[\text{OIII}]}$ and L_{AGN} . A clear decrease of $r_{[\text{OIII}]}$ with luminosity seems to be visible. This trend was confirmed with a 3σ significance according to a Kendall- τ test. In this case, we also carried out a `LinMix` fit, with best-fit slope $m = -0.19 \pm 0.07$ and intercept $b = -6.61 \pm 3.19$, suggesting a weak, decreasing trend. However, even if there is a luminosity effect, Fig. 5.19 shows that at a given AGN luminosity, the relative luminosity of $[\text{OIII}]5007\text{\AA}$ generally increases with subtype.

Our results show that $r_{[\text{OIII}]}$ increases with increasing subtypes. This trend is independent of the detected dependency with L_{AGN} , showing an increasing $r_{[\text{OIII}]}$ with subtype for a given AGN luminosity. The found difference is strong enough to produce the change in subtype between 1.0s, 1.2s, and 1.5s by itself.

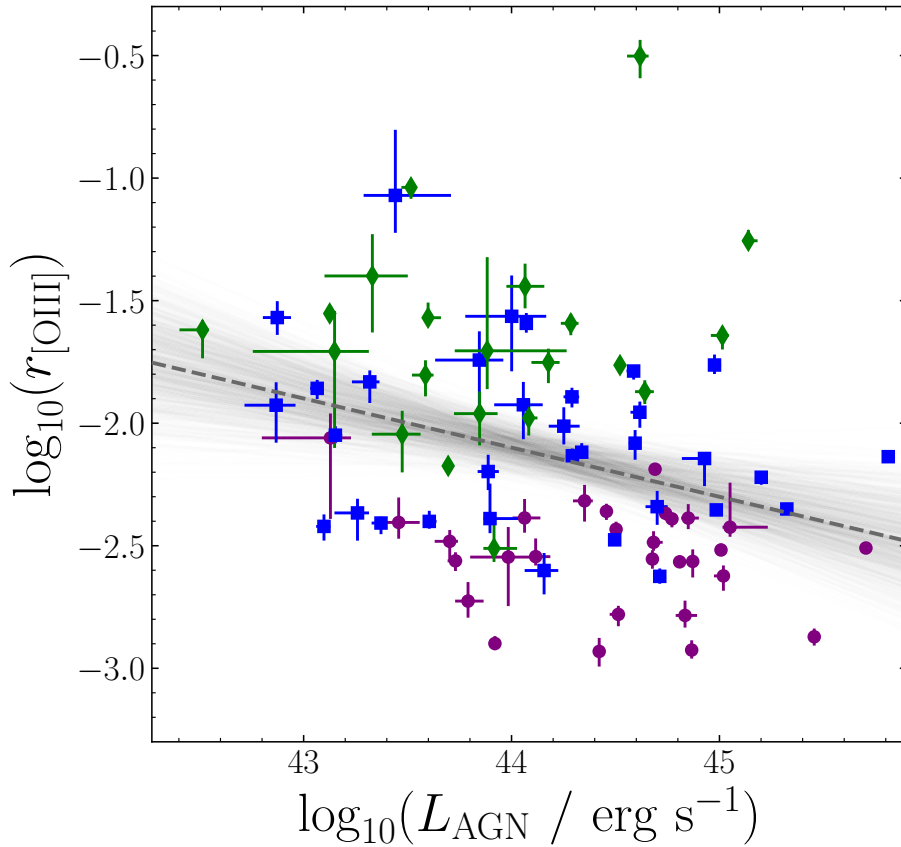


Figure 5.19: $r_{[\text{OIII}]}$ versus L_{AGN} . The dashed grey line corresponds to the best fit of a linear relationship. The shadowed area corresponds to the possible fitting tuples obtained from the chains. Symbol and colour codes as in Fig. 5.2.

5.4.3 Origin of the [OIII]5007Å relative luminosity increase with subtype

In this section, we review some mechanisms that may be behind the increase of $r_{[\text{OIII}]}$ with subtype and discuss them.

Host galaxy emission

Differences in the stellar contribution to the [OIII]5007Å total flux could explain the detected increase in its relative luminosity with subtype. The results of Sect. 5.3.3 suggest this is improbable, as we found no differences in the galaxy luminosity distributions between 1.0s, 1.2s and 1.5s.

To further confirm it, we plot $r_{[\text{OIII}]}$ versus the luminosity of the galaxy at rest-frame 5100 Å, L_{Gal} , in Fig. 5.20. If the emission line flux from the stellar origin increases, we should detect a correlation between both. We do not find such a trend, in agreement with our previous results of host galaxy contribution to [OIII]5007Å with aperture in Sect. 5.2.

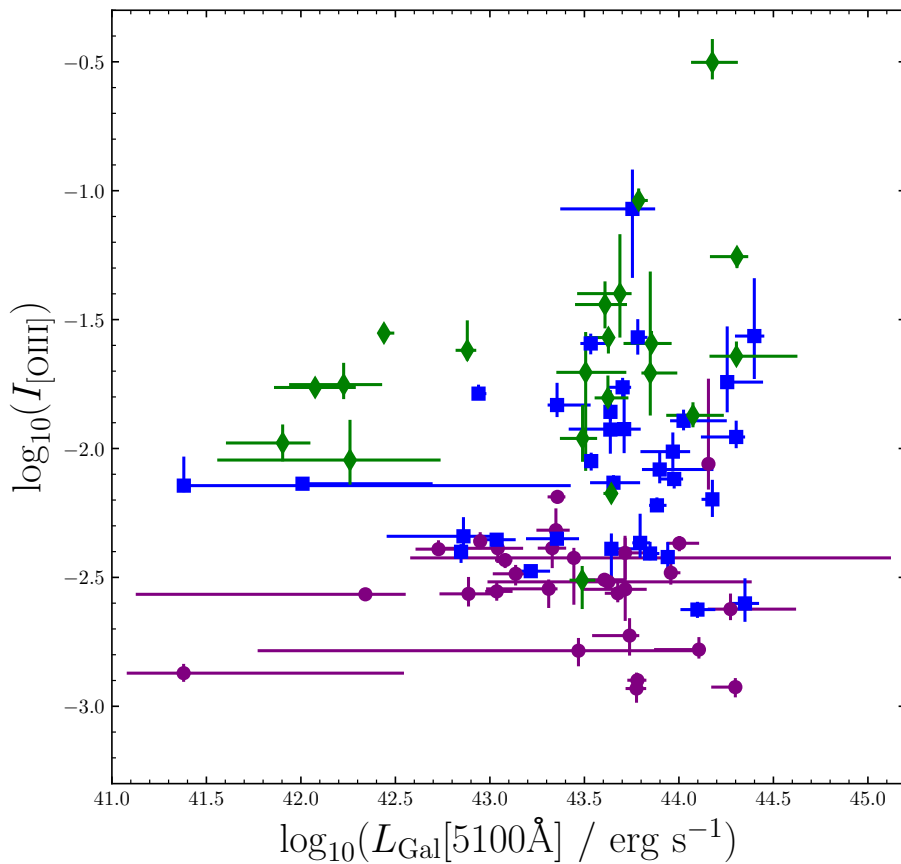


Figure 5.20: $r_{[\text{OIII}]}$ versus L_{Gal} . Symbol and colour codes as in Fig. 5.2.

NLR obscuration

Another possible explanation for the observed trend is that the obscuration of the NLR changes with subtype. However, we found no differences between the Balmer decrement of the narrow emission lines between subtypes (see Sec. 5.3.2), suggesting that the extinction of the NLR is similar in all sources.

Variability

As the NLR is further from the SMBH than the disk, it traces the AGN emission on temporal scales much longer than the nuclear emission and short variability effects will not impact its emission. Therefore, 1.2/1.5s could be AGN in a low emission state, where the emission of $[\text{OIII}]5007\text{\AA}$ remains unchanged while the nuclear emission decreases. However, as stated by Stern & Laor (2012), in this scenario, the AGN classified as 1.2/1.5 should be rare, in clear contraposition to the demographics of our sample.

NLR properties

If the electron density, ionization parameter or covering factor of the NLR changes, it would impact the luminosity of the $[\text{OIII}]5007\text{\AA}$ emission line. However, as shown by Baskin &

Laor (2005), the luminosity of [OIII]5007Å is mainly regulated by the covering factor of the NLR, which contributed twice as much as the ionization parameter and electron density. As we discarded all the other potential explanations, the change in luminosity could be related to changes in the covering factor of the NLR.

Stern & Laor (2012) obtained an expression for the covering factor of the NLR using the luminosity of the narrow component of H α . The expression for [OIII]5007Å would be similar except for a multiplying constant, $CF_{\text{NLR}} \propto L_{[\text{OIII}]} / L_{\text{BOL}} \propto r_{[\text{OIII}]}$. Assuming a similar ionization and density of the NLR for 1.0 – 5s, our results would also be consistent with an increase in the covering factor of the NLR.

Chapter 6

Conclusions and future work

As we introduced in Chapter 1, the Unification Model of AGN has been able to give, in first approximation, a satisfactory explanation for the origin of type 1 and 2 AGN. However, it does not address which physical properties are driving the subclassification of type 1 into subtypes (1.0, 1.2, 1.5, 1.8, and 1.9). Although previous works have studied AGN samples with intermediate optical classification, there is a lack of a systematic study of all the possible properties driving the subtype determination in the same sample with a well-defined selection function. We shed light on this issue by studying the difference in the distributions of several observable and intrinsic properties of AGN subtypes. In particular, we studied the observed AGN contrast at rest-frame 5100 Å, the line-of-sight UV/optical extinction, the optical luminosity of the AGN and host galaxy at rest-frame 5100 Å (L_{AGN} and L_{Gal} , respectively), and the relative luminosity of broad and narrow emission lines with respect to the luminosity of the AGN, using photometric and spectroscopic observations ranging from X-ray energies to MIR wavelengths. We described all datasets employed in Chapter 2.

To carry out this work, we used the BUXS sample, a unique flux-limited sample of 255 bright X-ray-selected AGN described in Chapter 3. From BUXS, we drew a working sample of 165 AGN covering a rest-frame 2–10 keV X-ray luminosity range of $10^{42} - 10^{46}$ erg s⁻¹ and $z = 0.05 - 0.75$. Using this redshift range, we ensured that we had both a high spectroscopic identification completeness (96%) and a uniform classification criterion based on the same set of emission lines for all objects since H β leaves the coverage range of our optical spectra at higher redshifts. These properties ensure our study will not suffer from biases related to classification incompleteness, which is more severe for sub-types 1.9 and 2, as they are fainter and more difficult to determine class and redshift. The large sample size ensures we can extract robust statistical conclusions from comparing sub-types. Both features make this sample ideal for studying the AGN subtype dependence with AGN and host galaxy properties.

For all objects in the working sample, we fitted the H β , H α and MgII regions of the optical and NIR spectra to obtain their emission line properties and to classify our AGNs. We also

calculated the Balmer decrement of the narrow and broad emission lines using the flux ratios $H\beta$ and $H\alpha$. We fitted the rest-frame UV-to-mid-infrared SEDs with galaxy and AGN components to obtain the observed AGN over total flux contrast, the line-of-sight extinction, and AGN and host galaxy luminosities. We described the fitting processes in Chapter 4.

We then compared the distributions of all properties by subtypes in Chapter 5. With this approach, we looked for significant differences to reveal the driving parameters behind the AGN intermediate optical spectroscopic classification. In particular, we focused on differences between $1.0 - 5$ and $1.8 - 9/2$ and between 1.0, 1.2, and 1.5. We used the KS test to calculate the statistical significance of the differences between subtypes and the Kendall- τ test to determine the significance of correlations between two parameters (see Appendix B for a description of these tests).

In this chapter, we will summarize in Sec. 6.1 the main conclusions derived from the study of the contrast and contrast-related properties (extinction, AGN and host galaxy luminosity) and their impact on our understanding of the $1.0 - 5$ versus $1.8 - 9/2$ dichotomy (see Sect. 5.3). Then, in Sec. 6.2, we will draw the conclusions of the analysis of the relative luminosity of the broad and narrow emission lines relative to the AGN luminosity for different AGN subtypes (see Sect. 5.4). Finally, in Sect. 6.3, we will propose some lines of research that can be followed up based on the results of this thesis.

6.1 Contrast-related properties as main drivers of $1.0/1.2/1.5$ and $1.8 - 9/2$ classes

The main results of this part of the work can be summarized as:

1. A clear decrease of the observed AGN over total AGN+galaxy contrast with subtype was found, identifying two main groups of high ($1.0 - 5$) and low ($1.8 - 9/2$) contrast with $\Delta C_{obs} = 0.52 \pm 0.04$. This difference is significant for the main groups and for any comparison between subtypes in the $1.0 - 5$ and $1.8 - 9/2$ groups. A difference is hinted for subtypes 1.0 and $1.2 - 5$.
2. We found an increase in extinction with subtype, showing $1.8 - 9/2$ s to have overall higher extinctions than $1.0 - 5$ s, $\Delta E(B - V) = 0.89 \pm 0.09$, which agrees with previous results in the literature. No significant change between subtypes inside these groups is identified. The relation found between observable contrast and extinction reveals the latter as a key actor behind the classification into $1.0 - 5$ to $1.8 - 9/2$.
3. We found a population of $1.8 - 9$ s (50%) and 2 s (50%) with insufficient extinction to suppress the BLR emission enough to change the classification of the AGN only by itself.
4. The extinction in the host galaxy, gauged from the Balmer decrement of the narrow lines, is not significantly different between subtypes. However, for most $1.0 - 5$ s and

for the low extinction 1.8 – 9/2.0s, most, if not all, of the extinction they suffer can be explained by material in the host galaxy.

5. No significant difference is found in L_{AGN} , between AGN subtypes. If there is such a difference in our sample, it must be small and, at most, a secondary effect.
6. When comparing L_{Gal} between subtypes, we found a difference between 1.0 – 5s and 1.8 – 9/2s, with lower values for the former group, $\Delta\log_{10}(L_{\text{Gal}}) = 0.68 \pm 0.09$ dex.
7. Differences in L_{Gal} produce a decrease in the intrinsic ratio between AGN and host galaxy luminosity, $L_{\text{AGN}}/L_{\text{Gal}}$, for 1.8 – 9/2s, $\Delta\log_{10}(L_{\text{AGN}}/L_{\text{Gal}}) = 1.08 \pm 0.19$. Furthermore, for a given extinction, 1.8 – 9/2s have lower values of $L_{\text{AGN}}/L_{\text{Gal}}$ than 1.0 – 5s.

Based on the results presented, the subtype classification into the main groups 1.0 – 5s and 1.8 – 9/2 is driven by a decreasing contrast effect. As the observed contrast decreases, the ability to detect the broad component of H β and H α is hampered until it is no longer possible to detect them, resulting in the change of subtype.

Extinction explains the classification of 50% of the 1.8 – 9/2s. The change cannot be explained for the rest without an additional effect of a decreasing $L_{\text{AGN}}/L_{\text{Gal}}$ ratio (which we found mainly driven by a higher L_{Gal} in 1.8 – 9/2.0). For those 1.8 – 9/2s with high extinction, the dominant component must be associated with circumnuclear material. However, the host galaxy material could significantly contribute to the total line-of-sight extinction for the rest of the sample. These findings imply the need to include of the host galaxy properties parameters in the Unification Model to explain the observations.

We find no significant difference in the studied parameters between subtypes within the big groups of 1.0 – 5 and 1.8 – 9/2. We only found a hint at a potential contrast effect for type 1.0 with respect to 1.2 and 1.5 with a 2σ significance. It could be associated with a higher $L_{\text{AGN}}/L_{\text{Gal}}$ value than 1.2 – 5, or less probably, to slightly smaller $E(B - V)$ overall values. Nevertheless, this remains only a potential hint of a weak, secondary effect, not strong enough to explain the subtype change.

6.2 Differences in relative luminosity of [OIII] for 1.0s, 1.2s and 1.5s

We found no contrast-related property driving the different classifications for 1.0s, 1.2s, and 1.5s. So, we looked for differences in the relative luminosity of the broad and narrow emission lines with respect to L_{AGN} between these subtypes in Sect. 5.3. The main results of this analysis can be summed up as follows:

1. The relative luminosity of the broad component of H β remains constant between 1.0s, 1.2s and 1.5s and does not change with L_{AGN} . The lack of dependence remains if we consider the broad component of H α instead.

2. If we estimate broad $H\beta$ from broad $H\alpha$ for the AGN without detection of the 1.9s with low extinction and we reclassify those sources, the results do not change. However, we detected a hint of a decrease in the relative luminosity of broad $H\beta$ for 1.8s, $\Delta\log_{10}(r_{bH\beta}) = 0.79 \pm 0.11$ dex, with this method.
3. A clear, positive correlation of the relative luminosity of $[\text{OIII}]5007\text{\AA}$ with R was found, $m = 0.97 \pm 0.07$ and $b = -1.86 \pm 0.04$. The decrease of approximately one order of magnitude for $r_{[\text{OIII}]}$ is enough to explain the change in the observed subtype between 1.0, 1.2 and 1.5.
4. We found a weak but significant decrease $r_{[\text{OIII}]}$ with L_{AGN} , $m = -0.19 \pm 0.07$ and $b = -6.61 \pm 3.19$. However, intrinsic differences between subtypes remain for any given range of AGN luminosities.
5. We discarded several origins for the observed increase of the relative luminosity of $[\text{OIII}]5007\text{\AA}$ using our results or theoretical arguments, leaving only an increase of the covering factor of the NLR with subtype as the most likely explanation.

After combining the obtained results, we conclude that the subtype determination inside the 1.0 – 5 group is mainly regulated by the intrinsic strength of the $[\text{OIII}]5007\text{\AA}$ emission line with respect to L_{AGN} . In contrast, the broad emission line relative luminosity remains similar for all subtypes. The previously reported trends in [Elitzur et al. \(2014\)](#) may be only significant at the end-tail of low luminosity AGN or correspond to a change in regime instead of a gradual change. After discarding other possibilities, we conclude that the most probable reason for the change of the relative luminosity of $[\text{OIII}]5007\text{\AA}$ must be an increase in the covering factor of the NLR with subtype. These results may suggest that the Unification Model must take into account for intrinsic differences in the NLR properties to explain the subtype diversity between 1.0 – 5.

We found, however, a hint of a decrease in the relative luminosity of the broad $H\beta$ for 1.8s with respect to 1.0 – 5, $\Delta\log_{10}(r_{bH\beta}) = 0.79 \pm 0.11$ dex. However, the small sample size (only 5 AGN) prevented us from further trying to explain the origin behind this apparent behaviour. A possibility explaining this decrease would be an intrinsically weak BLR (for example, because of a reduced covering factor).

6.3 Future work

We have provided several results that have helped to shed light on the parameters driving the optical spectroscopic intermediate classification of AGN. Nevertheless, various topics related to the classification still need better understanding. In the following, we propose some research lines that would help to complete and expand the results presented in this work.

Impact of SMBH mass and Eddington ratio

Elitzur et al. (2014) hinted at a trend of increasing equivalent width of the broad H α emission line with $L_{\text{BOL}}/M^{2/3}$, an amount close to the Eddington ratio. To clarify the effect of both the SMBH mass and the Eddington ratio in the subtype determination, our results could be extended by obtaining both parameters for our sample and carrying out an analysis similar to that done for the relative luminosity of the emission lines.

For this study, we could derive single-epoch SMBH mass estimations for our 1.0 to 1.9 from the emission line best-fits of the broad component of H β and H α emission lines, using the Greene & Ho (2005) relations. For the type 2 AGN, we can derive the SMBH mass from the host galaxy properties, like for example their stellar masses, using the relation from Suh et al. (2020).

Determine the covering factor of the narrow line region

Although we have proposed the increase of the NLR covering factor as the leading effect in the increase of $r_{[\text{OIII}]}$, we did not confirm it through the comparison of the distribution of the subtypes, as with the rest. We also did not confirm that its effect in the subtype determination is bigger than the ionization parameter and electron density.

A technique similar to the one Baskin & Laor (2005) used could be employed to derive the NLR properties. Their approach compares the predictions of the theoretical values of the equivalent widths of [OIII]5007Å [OIII]4363Å and the narrow component of H β obtained with the CLOUDY code (Ferland et al., 1998), with the measured values. From this comparison, they obtained the ionization parameter, electron density and covering factor of the NLR. We can easily extend our spectral fitting process to fit also [OIII]4363Å in our optical spectra and replicate the process to directly compare the distribution of the covering factor of the NLR between subtypes.

However, to obtain precise values of the weakest narrow components of H β but also [OIII]4363Å, sensibly less intense than [OIII]5007Å and blended with H γ , we would re-observe the objects with the spectra with the SNR and/or lowest spectral resolution. Additionally, we would improve the current fitting code to include a more detailed decomposition of the host-galaxy using the Penalized Pixel-Fitting method (pPXF, Cappellari (2012)), to better determined the emission line fluxes when the host galaxy dominates.

Appendices

Appendix A

X-rays spectral analysis

To correctly characterize the BUXS sources, their X-ray properties need to be constrained. In particular, the X-ray spectra were fitted to obtain the intrinsic, absorption-corrected, X-ray luminosity in the rest-frame 2 – 10 keV range (from this point L_X). This appendix summarises the process followed to fit the X-ray spectra.

The X-ray spectra were extracted for every object using the same pipeline that the SSC used to build the source catalogues from the observations taken with the three EPIC cameras (MOS1, MOS2, and pn). A complete description of the process can be found in [Rosen et al. \(2016\)](#). The spectral products from both MOS cameras were merged for every object. Then, every pn and MOS spectra from multiple observations were combined, so in the end, there were at most only two X-ray spectra for each object. Due to the different instrumental responses of the detectors, MOS and pn spectra were not merged. Instead, both spectra were fitted simultaneously, adding a normalization correction factor to account for the small difference in flux cross-calibration between cameras ([Mateos et al., 2009](#)). Only the energy range from 0.25 to 10 keV was used to carry out the fit. The quality of the spectra is good; the distribution of net (background-subtracted) counts for the whole sample is shown in [Fig. A.1](#).

The X-ray spectra of AGN are complex and had to be modelled with different components representing the multiple sources of X-ray emission and absorption effects. To this end, the software Xspec v12.10 ([Arnaud, 1996](#)) was used to carry out the fit of the emission. The components described using the Xspec implementations¹ are:

- **Power law:** as introduced in [Sect. 1.1](#), the emission from the corona is well reproduced by a power law. To describe it, a `zpowerlaw` component (`zpo` from this point) was used, a redshifted photon power law defined as:

$$A(E) = K[E(1+z)]^{1-\Gamma} \quad (\text{A.1})$$

¹Documentation is available at <https://heasarc.gsfc.nasa.gov/xanadu/xspec/manual/Models.html>

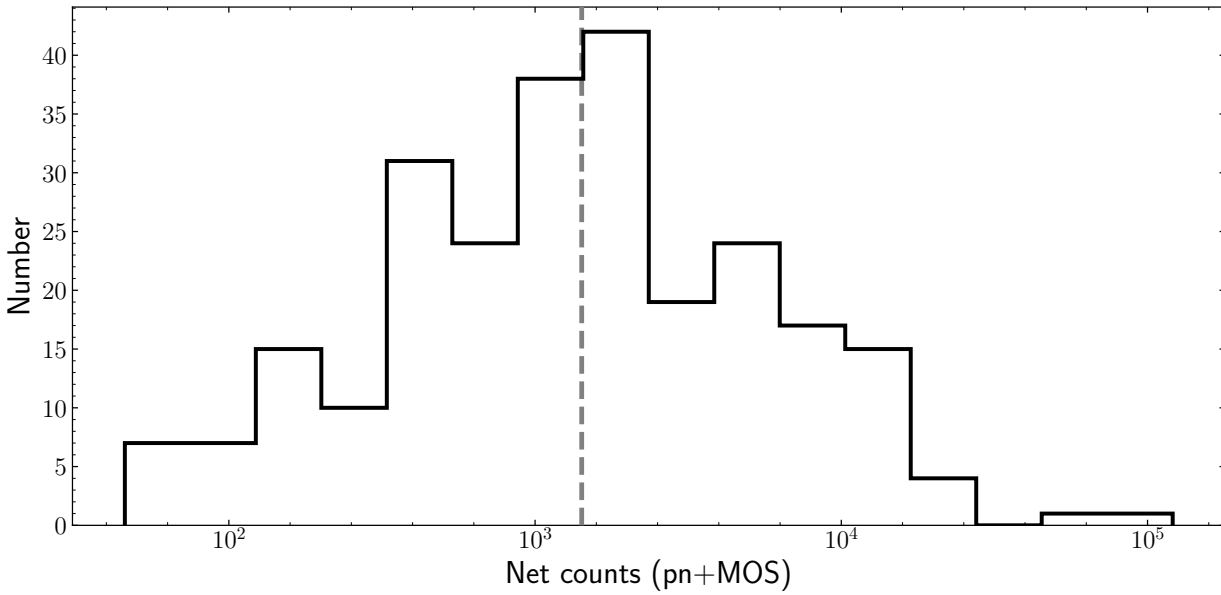


Figure A.1: Distribution of the number of total (pn+MOS) net counts in the 0.25–10 keV range. The vertical dashed line corresponds to the mean number of counts of 1420.

being the fitting parameters K , the normalization in photons/keV/cm²/s, Γ the photon index of the power law, and z the redshift.

A `clumin` model was included to derive the probability distribution for L_X . `clumin` is a convolution model designed to calculate the luminosity of other models. With this approach, the normalization of the `zpowerlaw` component is overridden with the `clumin` normalization.

- **Intrinsic absorption:** The AGN X-ray emission could be intercepted by the torus depending on our line of sight. A `zfabs` component modelling the photoelectric absorption was incorporated to model the absorption the X-rays suffer by this structure. It is defined as:

$$M(E) = e^{-N_H \times \sigma(E)} \quad (\text{A.2})$$

where N_H is the column density of the torus and $\sigma(E)$ is the photoelectric cross-section. Only the first is a free parameter, while the latter is defined by the `Wisconsin` cross-sections (Morrison & McCammon, 1983). The `zfabs` model was used to affect only the direct emission from the corona, i.e., the `zpo` component.

- **Reflection component:** to model the reflection of X-rays by the circumnuclear material, an extra `zpo` was added. A `zfabs` was not applied to this component, as it is not affected by the obscuration of the circumnuclear material.

- **Collisionally-ionized diffuse gas:** Below 2 keV, in around 50% of AGN an excess with respect to the extrapolation of the power laws is detected, the so-called soft-excess [Beckmann & Shrader \(2012\)](#). An apec component was included to fit it. apec describes the emission spectrum from collisionally-ionized diffuse gas calculated from the AtomDB atomic database from [Foster et al. \(2012\)](#). The model is parametrized by the plasma temperature, kT, and the metal abundances in the emitting gas. The latter were fixed to the values of [Anders & Grevesse \(1989\)](#).
- **Black body:** In some cases, a phenomenological black body model, zbb, was used instead to model the soft excess. It is defined by only its temperature, T . A zbb model is used if it improves the fitting of an apec component or to avoid overfitting a featureless soft excess.
- **Galactic absorption:** all radiation coming from AGN has to cross the material of the Milky Way and is partially absorbed before reaching our detectors. To model it, a wabs component was used. This model is similar to a zwabs component but without applying a redshift displacement in energies. The Galactic N_{H} densities were determined at the coordinates of our objects using the Leiden/Argentine/Bonn (LAB) Survey of Galactic HI ([Kalberla et al., 2005](#)) and the routine nh from HEASOFT². They were allowed to vary inside the 3σ uncertainty range, being σ defined as the standard deviation of the N_{H} values measured in a 4×4 degrees box centred in the object. The measured N_{H} and the 3σ uncertainty range were also used as the centroid and width of the Gaussian prior in the Bayesian fit (see below).

The redshift has been fixed in all sources. The free parameters of the models and their allowed fitting values are shown in Table A.1. The best-fit models were obtained from the combination of these components, and they are in order of increasing complexity:

- **Absorbed power law:** wabs*zwabs*clumin*zpo
- **Absorbed double power law:** wabs*(zpo+zwabs*clumin*zpo)
- **Absorbed power law plus a black-body:** wabs*(zbb+zwabs*clumin*zpo)
- **Absorbed power law plus ionized gas emission:** wabs*(apec+zwabs*clumin*zpo)
- **Abs. double power law plus ionized gas emission:** wabs*(apec+zpo+zwabs*clumin*zpo)

To carry out the fit, the spectra were grouped to 1 count/bin, and then an initial spectral fit using Cash statistics (implemented as C-stat in Xspec; [Cash 1979](#)) was performed. The initial guesses of the fitting values for a latter and definitive Bayesian fit were obtained from its results. The priors used in the Bayesian fit for every parameter are shown in Tab. A.1. To derive the posterior probability of the best-fit parameters, Markov Chain Monte Carlo simulations (MCMC) were run using the Goodman-Weare method ([Goodman & Weare, 2010](#)).

²<https://heasarc.gsfc.nasa.gov/docs/software/lheasoft/>

A chain length of 100000 was selected, rejecting the 10000 first values to ensure convergence. The convergence was also tested by visually checking the MCMC chains obtained. Whenever we talk about the X-ray luminosity, we will refer to the value of the mode obtained from the chain, and its associated 1σ uncertainty corresponds to the range encompassing 68.27% of the values of the chain.

The best-fit model was selected as the one that minimizes the Deviance Information Criterion (DIC; Spiegelhalter et al. 2002). However, the intrinsic dispersion of the chain for different MCMC runs was also taken into account. By obtaining multiple chain realizations for the same source and model, the dispersion was estimated to be $\lesssim 3$ per cent. Then, adopting a conservative approach, a model more complex than the unabsorbed power law was selected as the best only if its resulting DIC improvement was better than 5 per cent. In Fig. A.2, we show an example of an X-ray fitting with these models and the L_X posterior distribution obtained from it. This process was followed for all AGN with a few exceptions.

Component (1)	Parameter (2)	Prior type (3)	Limits (4)
zpo	Norm.	Flat logarithmic	$10^{-7} - 1 \frac{\text{counts}}{\text{keV cm}^2 \text{ s}}$
	Γ	Gaussian ($\mu = 1.9, \sigma = 0.25$)	0–4
clumin	$\log_{10}(L_X / \text{erg s}^{-1})$	Gaussian ($\mu = 44, \sigma = 2$)	39 – 47
apec	Norm.	Flat logarithmic	$10^{-7} - 1 \frac{\text{counts}}{\text{keV cm}^2 \text{ s}}$
	kT	Flat	0.01 – 1 keV
zbb	Norm.	Flat logarithmic	$10^{-7} - 1 \frac{\text{counts}}{\text{keV cm}^2 \text{ s}}$
	kT	Flat	0.01 – 1 keV
wabs	$N_{\text{H,Gal}}$	Gaussian (see text)	(see text)
zwabs	N_{H}	Flat logarithmic	$10^{19} - 10^{25} / \text{cm}^{-2}$

Table A.1: **Col. 1:** Components used in the different X-ray models fitted; **Col. 2:** free parameters; **Col. 3:** prior type set for the free parameter; **Col. 4:** allowed values for the fit.

The best-fit column density for nine AGN was higher than $N_{\text{H}} = 10^{23} \text{ cm}^{-2}$, so it was necessary to refit these spectra using a p1cabs component instead. This model considers not only photoelectric absorption but also Compton scattering and reprocessed radiation of the Compton-thick material around the central engine. A detailed description of the physics of the models, approximations used, and other details are available in Yaqoob (1997). The models defined using p1cabs were:

- plcabs
- zpo+plcabs
- apec+plcabs
- zpo+apec+plcabs

The plcabs additional parameters were fixed to typical values to avoid over-fitting (a complete list of such parameters and values is in Tab. A.2). The rest (normalization, Γ and N_{H}) were left to vary freely. Their corresponding priors are the same as those used for previous models. When fitting a plcabs model, applying a clumin is not possible. In these cases, L_{X} was recovered from the posterior distributions of the normalization, Γ and N_{H} . For every iteration of the chain, the intrinsic flux in the 2 – 10 keV energy range was obtained, and it was translated to a luminosity applying the cosmology presented in Sect. 1.5. An example of a fit and its associated L_{X} posterior distribution is shown in A.3.

Parameter (1)	Description (2)	Fixed value (3)
N_{Max}	Maximum no. of scatterings to consider	5
$n(\text{Fe})$	Iron abundance	1
$E(\text{FeK})$	Iron K edge energy	7.11 keV
E_{Max}	High-energy cut-off threshold energy	150 keV
f_{E}	High-energy cut-off e-folding energy	150 keV
A_{Crit}	Critical albedo for switching to elastic scattering	0.1

Table A.2: Fixed parameters of the plcabs model. **Col. 1:** parameter; **Col. 2:** descriptions; **Col. 3:** value.

One AGN was a Compton-thick candidate and showed a very intense FeK α emission line at rest-frame 6.4 keV, so it was necessary to use instead the torus model of Brightman & Nandra (2011). The torus model is described by four parameters: the redshift, the absorption, the opening angle of the torus (defined as the vertex angle formed by the torus and the vertical axis) and its inclination with respect to the line of sight. The associated fitted model was apec+zpo+torus.

In this case, the maximum scattering fraction (ratio between the zpo and torus normalization) was limited to values under 0.05. Also, the Γ of the zpo and torus models was fixed at 1.9, the typical photon index value in AGN (Caccianiga et al., 2004; Tozzi et al., 2006; Mateos et al., 2010; Corral et al., 2011). Otherwise, with the addition of an apex and zpo component to the torus model, the Γ value would be heavily degenerated. Additionally, the opening and inclination angles were fixed at 40 and 80 degrees, respectively. The normalization and column density of the torus component had the same priors and fit limits as those for the zpo and zwabs models, respectively. Similarly to the fits carried out with a

plcabs model, applying a clumin component to the torus model and retrieving a posterior distributions of $\log_{10}(L_X)$ was impossible. To obtain them, we followed the same procedure as for the plcabs fits. The fit of the AGN with the torus model and the associated L_X posterior distribution is shown in A.4.

Besides, for 13 AGN, the photon index of the power law could not be well constrained. All of them correspond to the spectra with the lowest count values in the sample, either because of low counts or high absorbing column density. In these cases, the photon index was also fixed to $\Gamma = 1.9$.

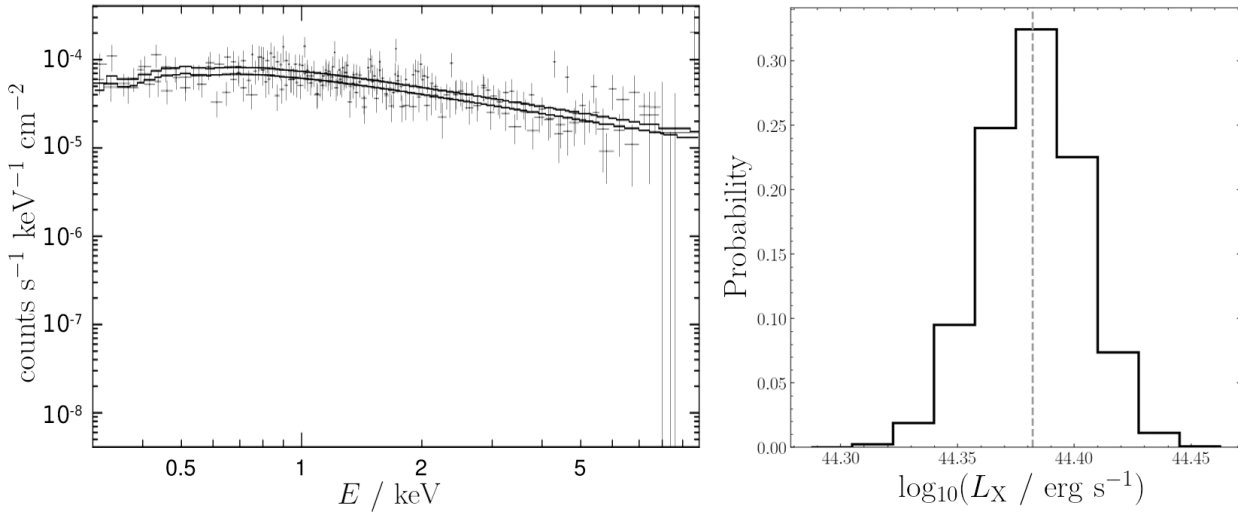


Figure A.2: (Left) Example of the X-ray fitting of an AGN (ID 1859, 2110 total counts) modelled with an absorbed power law. (Right) L_X posterior distribution. The dashed line correspond to the mode of the distribution, $\langle \log_{10}(L_X / \text{erg s}^{-1}) \rangle = 44.38$.

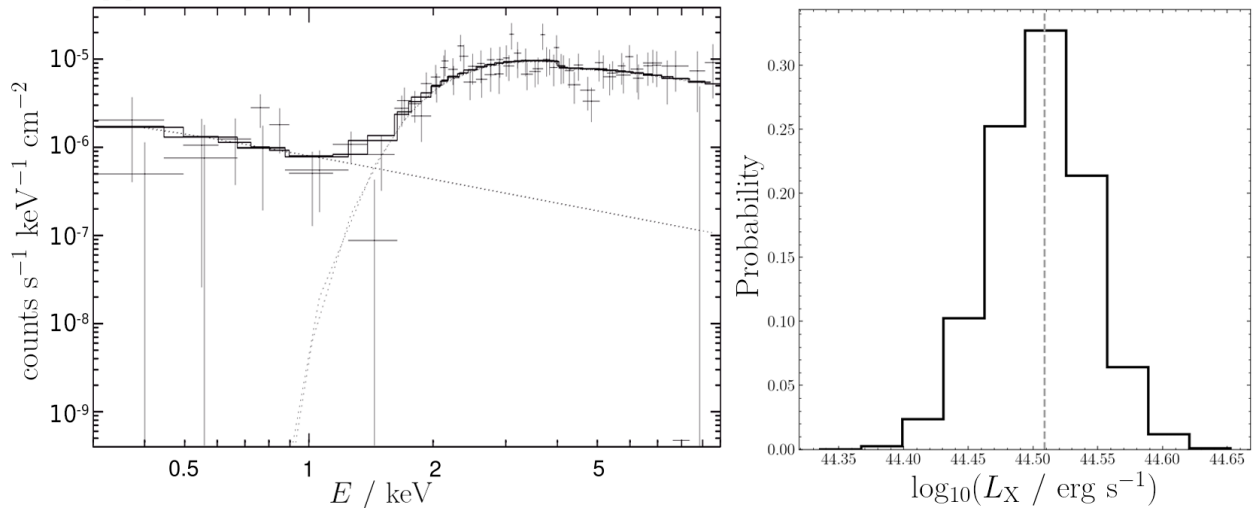


Figure A.3: (Left) Example of the X-ray fitting of an AGN (ID 2822, 522 total counts) modelled with plcabs model plus a power law. (Right) L_X posterior distribution obtained. The dashed line correspond to the mode of the distribution, $\langle \log_{10}(L_X / \text{erg s}^{-1}) \rangle = 44.51$.

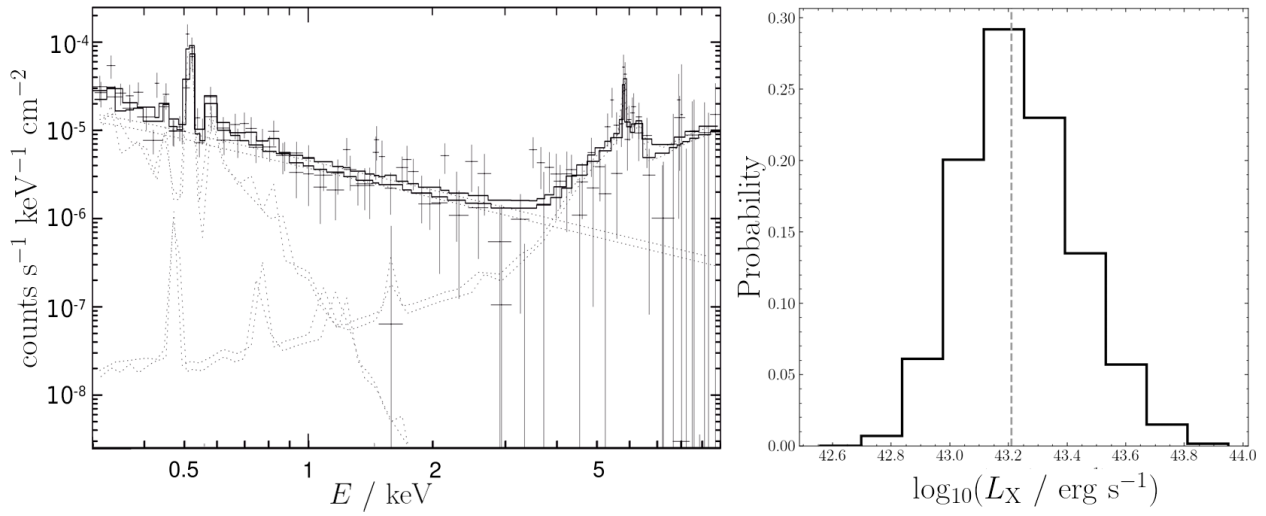


Figure A.4: (Left) X-ray fitting of an AGN (ID 9487, 956 total counts) modelled with the torus model. (Right) L_X posterior distribution obtained. The dashed line correspond to the mode of the distribution, $\langle \log_{10}(L_X / \text{erg s}^{-1}) \rangle = 43.21$.

Appendix B

Statistical tests

In this appendix, we will first briefly explain in Sect. [B.1](#) the significance levels used in this work to consider a difference, trend or improvement in a spectral fit as statistically significant. Then, we will describe in Sect. [B.2](#) the test of Fisher, used to determine the significance of a component detection in the X-ray and optical spectral fits. Then, we will introduce the tests used to determine the significance of a difference between distributions, the Kolmogorov-Smirnov and the Anderson-Darling tests in Sects. [B.3](#) and [B.4](#), respectively. Finally, in Sect. [B.5](#), we will describe the Kendall rank correlation coefficient test, used to determine the significance of a linear correlation between two parameters.

B.1 Significance levels

Through this work, we have used a 3σ confidence level to consider a difference or trend evaluated by a test to be statistically significant. This corresponds to a p-value¹ equal to $p = 0.003$. If the significance level is greater than 2σ (corresponding to $p = 0.05$) but less than 3σ , we considered it only a hint. Using the standard limit of 3σ ensured that we identified only differences or trends with a strong statistical significance.

When we fitted the optical and NIR spectra, we considered an additional component to be significant only if it improved the fit by 5σ according to the results of an F test (see below). The high significant level imposed was selected to reduce to a minimum the spurious detections of broad components of the emission lines, especially in the presence of complex continuum or in spectra with low SNR, and to avoid overfitting the spectra with unnecessary additional components.

When X-ray spectra were fitted, the Deviance Information Criterion (DIC; [Spiegelhalter et al. 2002](#)) was used to select the best fit. After taking into account the intrinsic dispersion of the MCMCM chains of the X-ray spectra fit ($\leq 3\%$), a more complex model was only selected if it improved the DIC by at least a 5%.

¹The p-value corresponds to the probability that the statistical variable under consideration is equal to or greater than the value of our sample, assuming the null hypothesis is true.

B.2 F test

The F test of Fisher is a parametric test used to determine the probability of the variance of two samples being equal. However, it can also be used to study if a model 2 fits the data significantly better than a model 1. This method can only be employed when model 2 is an extension of model 1, i.e., model 2 is the same as model 1, plus some additional parameters. When used to compare models, the F statistic is defined as:

$$F = \frac{\frac{\chi_1^2 - \chi_2^2}{\nu_1 - \nu_2}}{\frac{\chi_2^2}{\nu_2}} \quad (\text{B.1})$$

where χ_1^2 and χ_2^2 correspond to the chi-square and ν_1 and ν_2 to the degrees of freedom of the original and extended model, respectively. The associated p-value, p , for the null hypothesis of no improvement using the more complex model is defined as:

$$p = I_{\frac{\nu_2}{\nu_2 + (\nu_1 - \nu_2)F}} \left(\frac{\nu_2}{2}, \frac{\nu_1 - \nu_2}{2} \right) \quad (\text{B.2})$$

where I corresponds to the incomplete beta function.

B.3 Kolmogorov-Smirnov test

The Kolmogorov-Smirnov (KS) test is a non-parametric test used to study whether a sample has been drawn from a parent sample (N) described by a reference function with only one independent variable (one-sample KS test). It can be also use to determine is two samples (N_1 and N_2 , two-sample KS test) have been drawn from the same parent sample (Press et al., 1986).

The KS test compares their cumulative distribution functions, $S_N(x)$, to determine it. This function correspond to the fraction of data points in a set below a certain value, x . What sets two distributions apart is their behaviour between the common values at the lowest x (zero) and the highest x (one). Among the different statistics that could be used to compare two cumulative distributions, the KS test defines the KS statistic as the maximum value of the absolute difference between two cumulative distribution functions, D , as:

$$D = \max_{-\infty < x < \infty} |S_{N_1}(x) - S_{N_2}(x)| \quad (\text{B.3})$$

where $S_{N_1}(x)$ and $S_{N_2}(x)$ are the cumulative functions of the two samples in consideration, N_1 and N_2 . An illustration of cumulative functions for two samples and their associated D is in Fig. B.1.

The feature that makes the KS statistic useful is that for the case of the null hypothesis, it can be calculated, at least to a useful approximation, for all observed non-zero values of D . The necessary approximations are valid for samples with $N_e = N_1 + N_2 > 4$. Then, comparing this statistic with the calculated value of D , the probability of the null hypothesis can be obtained. The KS test also has the advantage of being invariant under any reparametrization of x . We used the implementation of the two-sample KS test provided by the Python package SciPy (Virtanen et al., 2020) in the method `ks_2samp`².

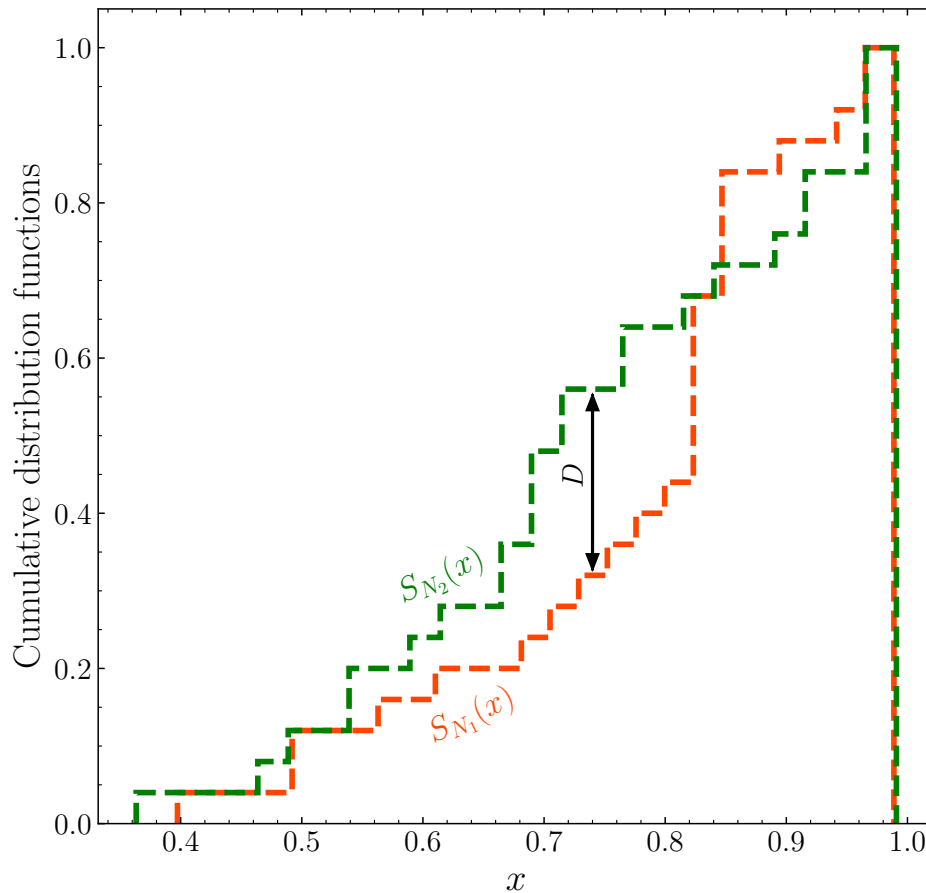


Figure B.1: Examples of the cumulative function of two samples, $S_{N_1}(x)$ (orange dashed line) and $S_{N_2}(x)$ (green dashed line), and the associated maximum value of the absolute difference between them, D .

We weighted the distributions of host galaxy and AGN luminosities when comparing them to account for the different redshift distributions between subtypes. In these two cases, we modified the original SciPy KS method to apply the same weights to cumulative functions (Monahan, 2011).

²Documentation available at https://docs.scipy.org/doc/scipy/reference/generated/scipy.stats.ks_2samp.html

B.4 Anderson-Darling test

The KS test is less responsive to differences in the tails of distributions. This is because the KS statistic is not independent of x and tends to be more sensitive around the median value. An alternative that is better at detecting differences in the tails of distributions is the Anderson-Darling (AD).

The AD test uses a *stabilized* statistic to remove the influence of x . As there is no simple analogue for the AD test of Eq. B.3, we refer the reader to [Scholz & Stephens \(1987\)](#) for a full description of the mathematics behind the test. In this work, we have used the AD two-sample test implementation in the method `anderson`³ of the Scipy package [Virtanen et al. \(2020\)](#) to reinforce the KS test results. We checked that the significance levels reported in Sect. 5 remained the same either we use the KS test or the AD test.

B.5 Kendall rank correlation coefficient test

The Kendall- τ test is a non-parametric rank correlation test that replaces values in x and y by ranks: a series of integers ranging from 1 to the maximum number of data points ordered by the original values. The advantage of this test is that if a correlation is demonstrated to be present between the ranks, for which a useful statistic is easier to define, then it is also present in the original data set ([Press et al., 1986](#)).

The Kendall- τ uses what is called concordant and discordant pairs. Two pairs (x_i, y_i) and (x_j, y_j) with $j > i$ are concordant (C) if both classification orders agree, i.e., $x_j > x_i$ and $y_j > y_i$, and discordant (D) if not. Additionally, if there is a tie in only y (T_y) or x (T_x), it is counted independently, while if there is a tie in both parameters, it is not counted at all. A visual definition of concordant and discordant pairs is shown in Fig. B.2. The Kendall- τ statistic is defined as:

$$\tau = \frac{C - D}{\sqrt{C + D + T_y} \sqrt{C + D + T_x}} \quad (\text{B.4})$$

τ can take only values in the interval $[-1, 1]$ by definition. Depending on the approach used to account for the ties in x and y , different variations of the τ statistic can be defined. The previous expression, known as $\tau - \alpha$, does not consider ties in x or y . It was used in this work to estimate the significance of linear relations between different parameters in Sect. 5.4. To work with the Kendall- τ test, we used the implementation defined in the method `kendalltau`⁴ of the SciPy package.

³Documentation available at https://docs.scipy.org/doc/scipy/reference/generated/scipy.stats.anderson_ksamp.html

⁴Documentation available at <https://docs.scipy.org/doc/scipy/reference/generated/scipy.stats.kendalltau.html>

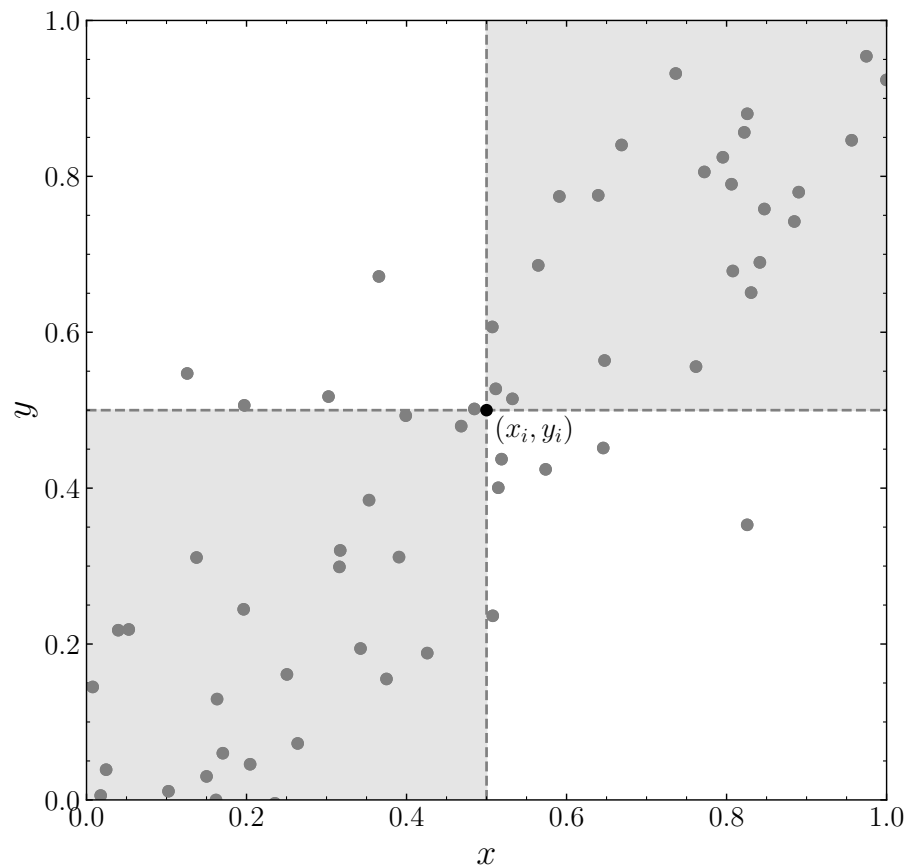


Figure B.2: Example of a random distribution of points defined by the independent variable x and the dependent variable y . For a point (x_i, y_i) , any other point that is in the shadowed areas will be considered concordant, while any point falling in the white areas it will be considered discordant. Points in the horizontal dashed line will be ties in y while points in the vertical dashed line will be ties in x .

Appendix C

Working sample spectra and results lists

In this appendix, we will first introduce Tab. C.1, which displays the instruments that were used to obtain the optical and IR spectra of all AGN of the working sample. Then, we will present Tab. C.2, which shows the main numerical results (see Chapter 5) obtained from this thesis for all the objects in the working sample. Each object is identified by its internal identification, redshift, and observed magnitude in the SDSS r filter.

ID	Opt. Spec.	Aperture / ''	NIR Spec.	ID	Opt. Spec.	Aperture / ''	NIR Spec.	ID	Opt. Spec.	Aperture / ''	NIR Spec.
(1)	(2)	(3)	(4)	(1)	(2)	(3)	(3)	(1)	(2)	(3)	(4)
10	BOSS	2.0	-	3315	SDSS-I/-II	3.0	-	6825	SDSS-I/-II	3.0	-
11	BOSS	2.0	-	3546	SDSS-I/-II	3.0	-	6848	SDSS-I/-II	3.0	-
170	BOSS	2.0	-	3554	ISIS	1.0	-	6867	EFOC	1.0	-
247	FORS2	1.3	-	3579	FORS2	1.3	-	6921	DOLORES	1.5	EMIR
261	SDSS-I/-II	3.0	-	3667	SDSS-I/-II	3.0	-	6961	DOLORES	1.5	-
289	SDSS-I/-II	3.0	-	3724	ISIS	1.0	-	6962	BOSS	2.0	-
346	OSIRIS	1.0	-	3838	BOSS	2.0	-	7005	SDSS-I/-II	3.0	-
347	BOSS	2.0	-	3867	FORS2	1.0	-	7150	FORS2	1.0	-
450	SDSS-I/-II	3.0	-	4031	FORS2	1.0	-	7215	BOSS	2.0	-
635	SDSS-I/-II	3.0	-	4269	DOLORES	1.5	-	7216	BOSS	2.0	-
636	SDSS-I/-II	3.0	-	4277	Subaru	0.8	EMIR	7308	SDSS-I/-II	3.0	-
754	FORS2	1.0	EMIR	4360	SDSS-I/-II	3.0	-	7309	ISIS	1.0	-
851	DOLORES	1.0	-	4361	SDSS-I/-II	3.0	-	7409	SDSS-I/-II	3.0	-
900	WFGS	1.6	-	4364	FORS2	1.0	-	7427	SDSS-I/-II	3.0	-
1035	BOSS	2.0	-	4450	DOLORES	1.0	-	7509	SDSS-I/-II	3.0	-
1036	SDSS-I/-II	3.0	-	4487	ISIS	1.0	-	7528	SDSS-I/-II	3.0	-
1044	OSIRIS	1.0	LIRIS	4643	BOSS	2.0	-	7697	BOSS	2.0	-
1155	SDSS-I/-II	3.0	-	4645	SDSS-I/-II	3.0	-	7734	OSIRIS	1.0	-
1261	ISIS	1.5	-	4648	SDSS-I/-II	3.0	-	7756	BOSS	2.0	-
1302	SDSS-I/-II	3.0	-	4659	OSIRIS	1.0	-	7809	SDSS-I/-II	3.0	-
1314	SDSS-I/-II	3.0	-	4740	SDSS-I/-II	3.0	-	7880	DOLORES	1.5	-
1375	OSIRIS	1.2	EMIR	4741	SDSS-I/-II	3.0	-	7967	SDSS-I/-II	3.0	-
1378	DOLORES	1.5	-	4797	SDSS-I/-II	3.0	-	8104	DOLORES	1.5	-
1437	ISIS	1.0	-	4799	FORS2	1.3	-	8178	ACAM	1.0	-
1450	BOSS	2.0	-	4812	BOSS	2.0	-	8405	SDSS-I/-II	3.0	-
1527	SDSS-I/-II	3.0	-	4946	BOSS	2.0	-	8602	SDSS-I/-II	3.0	-
1567	SDSS-I/-II	3.0	-	5059	BOSS	2.0	-	8741	BOSS	2.0	-
1585	SDSS-I/-II	3.0	-	5060	SDSS-I/-II	3.0	-	8833	FORS2	1.0	-
1638	SDSS-I/-II	3.0	-	5172	SDSS-I/-II	3.0	-	8919	SDSS-I/-II	3.0	-
1706	ISIS	1.5	-	5245	DOLORES	1.0	-	8921	SDSS-I/-II	3.0	-
1749	ALFOC-FASU	1.8	-	5287	BOSS	2.0	-	8923	EFOC	1.0	EMIR
1750	SDSS-I/-II	3.0	-	5291	BOSS	2.0	-	8929	SDSS-I/-II	3.0	-
1752	ISIS	1.0	-	5330	Subaru	0.8	EMIR	9046	SDSS-I/-II	3.0	-
1784	BOSS	2.0	-	5336	SDSS-I/-II	3.0	-	9089	DOLORES	1.5	-
1847	OSIRIS	1.0	EMIR	5405	BOSS	2.0	-	9262	FORS2	1.0	-
1859	Subaru	0.8	EMIR	5622	OSIRIS	1.0	-	9478	SDSS-I/-II	3.0	-
1863	SDSS-I/-II	3.0	-	5623	OSIRIS	1.0	-	9480	SDSS-I/-II	3.0	-
1924	ALFOC-FASU	1.0	-	5687	OSIRIS	1.0	EMIR	9487	SDSS-I/-II	3.0	-
2115	SDSS-I/-II	3.0	-	5688	DOLORES	1.5	-	9507	SDSS-I/-II	3.0	-
2116	ISIS	1.0	-	5689	SDSS-I/-II	3.0	-	9514	SDSS-I/-II	3.0	-
2157	DOLORES	1.5	-	5986	OSIRIS	1.0	-	9639	SDSS-I/-II	3.0	-
2158	SDSS-I/-II	3.0	-	6009	SDSS-I/-II	3.0	-	9887	SDSS-I/-II	3.0	-
2159	BOSS	2.0	-	6080	SDSS-I/-II	3.0	-	9888	SDSS-I/-II	3.0	-
2289	SDSS-I/-II	3.0	-	6188	BOSS	2.0	-	9899	SDSS-I/-II	3.0	-
2291	BOSS	2.0	-	6213	SDSS-I/-II	3.0	-	9954	SDSS-I/-II	3.0	-
2408	SDSS-I/-II	3.0	-	6215	DOLORES	1.5	-	9956	ISIS	1.0	-
2424	SDSS-I/-II	3.0	-	6261	BOSS	2.0	-	9973	ISIS	1.5	-
2500	SDSS-I/-II	3.0	-	6277	BOSS	2.0	-	10027	ALFOC-FASU	1.0	-
2812	FORS2	1.3	-	6434	ISIS	1.0	-	10049	SDSS-I/-II	3.0	-
2944	FORS2	1.3	-	6458	ISIS	1.2	-	10050	OSIRIS	1.2	EMIR
3021	EFOC	1.5	EMIR	6527	SDSS-I/-II	3.0	-	10306	BOSS	2.0	-
3028	BOSS	2.0	-	6644	SDSS-I/-II	3.0	-	10381	DOLORES	1.5	-
3113	SDSS-I/-II	3.0	-	6646	OSIRIS	1.0	EMIR	10389	SDSS-I/-II	3.0	-
3144	BOSS	2.0	-	6699	SDSS-I/-II	3.0	-				
3307	BOSS	2.0	-	6781	ISIS	1.0	-				
3309	SDSS-I/-II	3.0	-	6824	ISIS	1.5	-				

Table C.1: List of the spectrographs used to collect the optical and NIR spectra of the working sample AGN. **Col. 1:** AGN identification; **Col. 2:** spectrograph employed for collecting the optical spectrum; **Col. 3:** slit width employed in the optical observations or fibre size in the case of SDSS/BOSS spectra. The slit width for all IR observations was 1''; **Col. 4:** spectrograph employed for collecting the infrared spectrum.

ID	z	m_r	SNR	$f(\text{nH}\beta)$	$f(\text{bH}\beta)$	$f(\text{nH}\alpha)$	$f(\text{bH}\alpha)$	$f(\text{[OIII]5007\AA})$	R	Class	$E(B-V)$	L_{AGN}	L_{Gal}	$\tau_{\text{[OIII]}}$	$\tau_{\text{[bH}\beta]}$	$\tau_{\text{[bH}\alpha]}$	ϕ_{Gal}
(1)	(2)	(3)	(4)	(5)	(6)	(7)	(8)	(9)	(10)	(11)	(12)	(13)	(14)	(15)	(16)	(17)	(18)
-	-	-	-	$\text{erg s}^{-1} \text{cm}^{-2}$	-	-	-	erg s^{-1}	erg s^{-1}	-	-	-	-				
10	0.163	18.23	14.0	0.62 ± 0.13	-	6.31 ± 0.59	15.44 ± 1.07	5.15 ± 0.61	-	1.9	2.00	43.30 ^{+0.14} _{-0.07}	43.82 ^{+0.06} _{-0.03}	-	-	-	0.48
11	0.343	18.87	6.0	16.43 ± 0.26	-	61.82 ± 6.00	12.03 ± 4.65	195.38 ± 4.84	-	1.9	2.00	44.44 ^{+0.08} _{-0.03}	44.26 ^{+0.02} _{-0.13}	-	-	-	0.63
170	0.429	19.57	7.3	< 0.04	-	< 0.94	-	1.15 ± 0.08	-	2.0	2.00	43.56 ^{+0.14} _{-0.19}	44.38 ^{+0.02} _{-0.06}	-	-	-	0.67
247	0.237	18.59	55.0	5.35 ± 0.21	-	25.66 ± 0.21	-	19.19 ± 0.25	-	2.0	0.23	43.53 ^{+0.05} _{-0.22}	44.06 ^{+0.07} _{-0.01}	-	-	-	0.55
261	0.401	19.81	3.9	3.53 ± 0.32	20.23 ± 0.88	-	-	22.34 ± 3.29	1.10 ± 0.14	1.5	0.00	44.08 ^{+0.04} _{-0.02}	41.90 ^{+0.15} _{-0.30}	-1.98 ^{+0.07} _{-0.07}	-2.02 ^{+0.03} _{-0.05}	-	0.76
289	0.302	18.26	11.2	3.69 ± 0.89	93.02 ± 18.93	18.75 ± 5.53	392.89 ± 13.82	49.33 ± 2.89	0.53 ± 0.09	1.2	0.00	44.29 ^{+0.02} _{-0.01}	43.65 ^{+0.14} _{-0.12}	-2.13 ^{+0.03} _{-0.03}	-1.86 ^{+0.10} _{-0.08}	-1.23 ^{+0.02} _{-0.02}	0.72
346	0.597	21.75	2.9	< 0.16	-	-	-	2.29 ± 0.08	-	5.0	1.10	44.62 ^{+0.03} _{-0.08}	43.79 ^{+0.47} _{-0.37}	-	-	-	0.65
347	0.072	18.47	19.8	2.25 ± 0.22	9.00 ± 0.35	16.84 ± 1.35	53.10 ± 2.13	28.40 ± 1.85	3.16 ± 0.24	1.5	0.25	42.51 ^{+0.03} _{-0.11}	42.88 ^{+0.05} _{-0.06}	-1.62 ^{+0.12} _{-0.04}	-2.12 ^{+0.11} _{-0.03}	-1.43 ^{+0.11} _{-0.03}	0.30
450	0.239	18.47	9.4	2.07 ± 0.40	69.74 ± 2.73	5.31 ± 2.49	150.34 ± 3.46	9.10 ± 0.53	0.13 ± 0.01	1.0	0.02	43.70 ^{+0.04} _{-0.07}	43.96 ^{+0.05} _{-0.02}	-2.48 ^{+0.08} _{-0.05}	-1.60 ^{+0.07} _{-0.04}	-1.27 ^{+0.07} _{-0.04}	0.68
635	0.065	15.46	28.5	6.34 ± 0.60	-	18.66 ± 0.73	-	7.07 ± 0.59	-	2.0	0.00	42.67 ^{+0.10} _{-0.11}	44.03 ^{+0.01} _{-0.01}	-	-	-	0.38
636	0.227	19.00	5.9	3.22 ± 0.38	17.20 ± 1.90	18.98 ± 1.43	62.90 ± 2.15	35.08 ± 4.09	2.04 ± 0.31	1.5	0.04	43.59 ^{+0.04} _{-0.06}	43.62 ^{+0.11} _{-0.07}	-1.80 ^{+0.09} _{-0.06}	-2.11 ^{+0.08} _{-0.06}	-1.56 ^{+0.07} _{-0.04}	0.67
754	0.580	20.96	9.7	2.97 ± 0.10	-	7.30 ± 0.82	-	25.64 ± 0.80	-	2.0	2.00	44.17 ^{+0.23} _{-0.61}	44.23 ^{+0.09} _{-0.59}	-	-	-	0.64
851	0.388	18.91	16.3	< 0.5	13.67 ± 0.64	-	-	4.29 ± 0.23	0.31 ± 0.02	1.2	0.15	44.16 ^{+0.07} _{-0.09}	44.35 ^{+0.07} _{-0.08}	-2.60 ^{+0.10} _{-0.07}	-2.10 ^{+0.10} _{-0.07}	-	0.58
900	0.226	18.56	15.8	5.80 ± 0.90	-	15.62 ± 1.92	81.11 ± 3.64	11.98 ± 1.00	-	1.9	0.30	43.77 ^{+0.08} _{-0.03}	43.96 ^{+0.11} _{-0.04}	-	-1.89 ^{+0.04} _{-0.08}	-	0.57
1035	0.288	19.32	8.9	1.95 ± 0.14	-	21.34 ± 0.86	17.90 ± 1.39	3.96 ± 0.27	-	1.9	0.80	44.60 ^{+0.02} _{-0.02}	43.77 ^{+0.13} _{-0.04}	-	-	-	0.60
1036	0.316	17.78	23.8	0.83 ± 0.34	148.92 ± 6.25	3.32 ± 1.17	450.10 ± 5.43	16.62 ± 0.87	0.11 ± 0.01	1.0	0.00	44.51 ^{+0.03} _{-0.04}	44.11 ^{+0.24} _{-0.24}	-2.78 ^{+0.05} _{-0.03}	-1.83 ^{+0.05} _{-0.03}	-1.35 ^{+0.04} _{-0.03}	0.73
1044	0.439	18.69	48.1	6.38 ± 0.13	-	20.72 ± 0.58	-	15.36 ± 0.30	-	2.0	0.36	44.33 ^{+0.13} _{-0.04}	44.63 ^{+0.03} _{-0.20}	-	-	-	0.61
1155	0.089	16.54	21.1	8.32 ± 0.47	-	34.84 ± 1.45	-	52.24 ± 7.87	-	2.0	0.55	43.30 ^{+0.04} _{-0.03}	43.90 ^{+0.03} _{-0.01}	-	-	-	0.45
1261	0.269	19.10	13.9	0.67 ± 0.19	-	3.12 ± 0.24	-	9.88 ± 0.25	-	2.0	0.53	43.43 ^{+0.10} _{-0.09}	43.99 ^{+0.07} _{-0.01}	-	-	-	0.59
1302	0.192	17.65	12.5	2.68 ± 0.60	-	9.69 ± 1.28	57.54 ± 3.05	9.46 ± 0.58	-	1.9	0.15	43.79 ^{+0.02} _{-0.07}	44.23 ^{+0.06} _{-0.05}	-	-2.36 ^{+0.07} _{-0.03}	-	0.63
1314	0.101	17.68	18.7	6.10 ± 0.93	125.81 ± 6.19	34.81 ± 2.37	387.31 ± 12.43	59.24 ± 3.74	0.47 ± 0.04	1.2	0.01	43.60 ^{+0.03} _{-0.01}	42.85 ^{+0.01} _{-0.03}	-2.40 ^{+0.03} _{-0.04}	-2.07 ^{+0.02} _{-0.04}	-1.59 ^{+0.02} _{-0.04}	0.48
1375	0.692	21.55	2.6	5.59 ± 0.24	-	189.23 ± 37.63	456.32 ± 326.22	33.26 ± 0.37	-	1.9	0.80	45.35 ^{+0.09} _{-0.04}	43.70 ^{+0.05} _{-0.32}	-	-	-	0.70
1378	0.193	19.21	10.2	< 0.57	-	2.23 ± 0.36	-	2.29 ± 0.25	-	2.0	0.57	43.76 ^{+0.06} _{-0.15}	43.48 ^{+0.22} _{-0.05}	-	-	-	0.53
1437	0.198	17.86	22.3	0.95 ± 0.34	42.81 ± 3.12	4.74 ± 0.96	142.52 ± 2.28	9.25 ± 0.30	0.22 ± 0.02	1.0	0.04	43.13 ^{+0.10} _{-0.33}	44.16 ^{+0.02} _{-0.03}	-2.06 ^{+0.33} _{-0.10}	-1.39 ^{+0.33} _{-0.10}	-0.89 ^{+0.33} _{-0.10}	0.46
1450	0.413	18.19	23.2	6.66 ± 0.71	175.62 ± 5.69	88.72 ± 17.53	574.87 ± 14.97	38.17 ± 0.63	0.22 ± 0.01	1.0	0.01	44.77 ^{+0.01} _{-0.03}	42.73 ^{+0.12} _{-0.12}	-2.39 ^{+0.03} _{-0.02}	-1.73 ^{+0.04} _{-0.02}	-	0.67
1527	0.245	17.60	12.8	6.79 ± 0.39	-	20.29 ± 2.58	95.40 ± 8.79	59.58 ± 5.03	-	1.9	0.23	44.06 ^{+0.08} _{-0.08}	44.43 ^{+0.13} _{-0.03}	-	-2.10 ^{+0.09} _{-0.09}	-	0.68
1567	0.112	16.43	17.2	4.73 ± 0.68	-	10.37 ± 1.09	-	27.33 ± 3.25	-	2.0	2.00	43.55 ^{+0.03} _{-0.03}	44.16 ^{+0.01} _{-0.01}	-	-	-	0.50
1585	0.218	17.55	19.8	16.28 ± 1.46	228.99 ± 5.44	86.98 ± 8.17	863.35 ± 8.68	319.78 ± 6.77	1.40 ± 0.04	1.5	0.08	44.52 ^{+0.01} _{-0.03}	42.08 ^{+0.22} _{-0.22}	-1.76 ^{+0.03} _{-0.01}	-1.91 ^{+0.03} _{-0.01}	-1.36 ^{+0.03} _{-0.01}	0.66
1638	0.059	15.86	23.3	13.14 ± 0.54	-	57.99 ± 0.90	-	52.88 ± 0.82	-	2.0	0.60	42.44 ^{+0.07} _{-0.18}	43.83 ^{+0.02} _{-0.01}	-	-	-	0.35
1706	0.133	18.35	19.3	4.30 ± 1.39	-	32.16 ± 1.87	141.87 ± 3.49	57.00 ± 3.03	-	1.9	0.47	43.25 ^{+0.03} _{-0.04}	43.59 ^{+0.03} _{-0.01}	-	-1.48 ^{+0.04} _{-0.04}	-	0.44
1749	0.064	16.02	7.5	1.23 ± 1.18	35.65 ± 3.03	-	-	26.52 ± 0.76	0.74 ± 0.07	1.2	0.65	42.87 ^{+0.08} _{-0.06}	43.78 ^{+0.05} _{-0.01}	-1.57 ^{+0.07} _{-0.07}	-1.44 ^{+0.08} _{-0.07}	-	0.31
1750	0.335	18.55	24.6	1.55 ± 0.22	115.08 ± 4.87	3.80 ± 1.13	271.02 ± 4.44	24.93 ± 3.24	0.22 ± 0.03	1.0	0.05	44.35 ^{+0.04} _{-0.06}	43.35 ^{+0.07} _{-0.10}	-2.32 ^{+0.08} _{-0.07}	-1.65 ^{+0.06} _{-0.04}	-1.30 ^{+0.06} _{-0.04}	0.74

ID	z	m_r	SNR	$f(\text{nH}\beta)$	$f(\text{bH}\beta)$	$f(\text{nH}\alpha)$	$f(\text{bH}\alpha)$	$f(\text{[OIII]5007\AA})$	R	Class	$E(B-V)$	L_{AGN}	L_{Gal}	$r[\text{OIII}]$	$r[\text{bH}\beta]$	$r[\text{bH}\alpha]$	ϕ_{Gal}
(1)	(2)	(3)	(4)	(5)	(6)	(7)	(8)	(9)	(10)	(11)	(12)	(13)	(14)	(15)	(16)	(17)	(18)
-	-	-	-	$\text{erg s}^{-1} \text{cm}^{-2}$	-	-	-	erg s^{-1}	erg s^{-1}	-	-	-	-				
1752	0.452	20.32	7.8	1.84 ± 0.17	7.97 ± 0.39	-	-	4.99 ± 0.17	0.63 ± 0.04	1.2	0.49	44.25 ^{+0.08} _{-0.07}	43.97 ^{+0.09} _{-0.17}	-2.01 ^{+0.07} _{-0.08}	-1.81 ^{+0.08} _{-0.08}	-	0.61
1784	0.333	19.76	4.9	2.79 ± 0.17	-	6.92 ± 0.83	-	28.77 ± 1.83	-	2.0	2.00	43.97 ^{+0.04} _{-0.10}	44.04 ^{+0.06} _{-0.04}	-	-	-	0.63
1847	0.604	21.42	6.2	< 0.17	-	3.02 ± 0.79	-	0.66 ± 0.07	-	2.0	2.00	44.44 ^{+0.36} _{-0.33}	44.17 ^{+0.15} _{-0.34}	-	-	-	0.65
1859	0.506	21.18	2.0	0.38 ± 0.02	0.61 ± 0.10	181.29 ± 18.09	350.15 ± 51.07	5.64 ± 0.21	9.18 ± 1.59	1.8	0.49	44.46 ^{+0.05} _{-0.04}	43.65 ^{+0.45} _{-0.12}	-	-3.01 ^{+0.09} _{-0.08}	-	0.58
1863	0.358	18.26	14.3	2.07 ± 0.54	124.98 ± 4.96	69.92 ± 15.24	442.41 ± 21.91	30.53 ± 2.59	0.24 ± 0.02	1.0	0.00	44.68 ^{+0.01} _{-0.01}	43.04 ^{+0.08} _{-0.06}	-2.55 ^{+0.04} _{-0.04}	-1.94 ^{+0.02} _{-0.02}	-1.39 ^{+0.02} _{-0.02}	0.75
1924	0.699	19.76	17.4	4.01 ± 0.63	7.85 ± 0.95	-	-	65.68 ± 1.42	8.36 ± 1.03	1.8	0.10	44.71 ^{+0.05} _{-0.09}	43.76 ^{+0.17} _{-0.22}	-	-2.35 ^{+0.11} _{-0.07}	-	0.67
2115	0.180	18.40	10.5	1.73 ± 0.33	34.56 ± 1.80	3.17 ± 0.45	153.16 ± 11.10	10.02 ± 0.37	0.29 ± 0.02	1.0	0.07	43.46 ^{+0.10} _{-0.06}	43.71 ^{+0.13} _{-0.05}	-2.40 ^{+0.07} _{-0.10}	-1.87 ^{+0.07} _{-0.10}	-1.24 ^{+0.07} _{-0.10}	0.62
2116	0.189	18.52	19.5	22.84 ± 0.46	53.36 ± 1.89	76.51 ± 0.97	333.88 ± 1.95	148.77 ± 1.76	2.79 ± 0.10	1.5	0.22	43.52 ^{+0.01} _{-0.05}	43.79 ^{+0.05} _{-0.01}	-1.04 ^{+0.05} _{-0.01}	-1.48 ^{+0.05} _{-0.02}	-0.76 ^{+0.05} _{-0.01}	0.45
2157	0.471	19.06	7.6	3.46 ± 0.29	-	-	-	12.91 ± 0.42	-	5.0	0.18	44.21 ^{+0.06} _{-0.07}	44.51 ^{+0.03} _{-0.08}	-	-	-	0.69
2158	0.660	17.32	28.7	67.42 ± 3.73	105.58 ± 3.73	-	-	20.40 ± 1.56	0.19 ± 0.01	1.0	0.00	45.46 ^{+0.01} _{-0.01}	41.38 ^{+1.17} _{-0.30}	-2.87 ^{+0.04} _{-0.03}	-2.16 ^{+0.02} _{-0.02}	-	0.82
2159	0.369	19.84	7.3	0.61 ± 0.12	-	3.97 ± 0.58	-	7.25 ± 0.70	-	2.0	1.85	44.61 ^{+0.06} _{-0.04}	44.07 ^{+0.08} _{-0.08}	-	-	-	0.65
2289	0.559	18.22	13.6	3.09 ± 1.05	76.65 ± 4.52	-	-	34.07 ± 1.05	0.44 ± 0.03	1.2	0.00	44.98 ^{+0.01} _{-0.01}	43.04 ^{+0.10} _{-0.12}	-2.35 ^{+0.02} _{-0.02}	-2.00 ^{+0.03} _{-0.03}	-	0.80
2291	0.281	17.52	18.1	2.06 ± 0.30	51.82 ± 2.63	7.64 ± 0.81	177.60 ± 4.30	31.00 ± 1.67	0.60 ± 0.05	1.2	0.15	44.71 ^{+0.02} _{-0.02}	44.10 ^{+0.09} _{-0.09}	-2.62 ^{+0.03} _{-0.03}	-2.40 ^{+0.03} _{-0.03}	-1.92 ^{+0.02} _{-0.03}	0.60
2408	0.081	16.30	22.4	9.39 ± 0.61	42.14 ± 2.95	42.64 ± 2.32	172.77 ± 3.04	24.17 ± 2.25	0.57 ± 0.07	1.2	0.06	43.10 ^{+0.03} _{-0.04}	43.94 ^{+0.02} _{-0.01}	-2.42 ^{+0.06} _{-0.05}	-2.18 ^{+0.05} _{-0.04}	-1.59 ^{+0.04} _{-0.03}	0.43
2424	0.146	17.49	11.4	3.56 ± 0.47	-	9.04 ± 0.54	16.34 ± 2.32	31.44 ± 0.75	-	1.9	1.55	43.04 ^{+0.09} _{-0.09}	44.01 ^{+0.02} _{-0.02}	-	-	-	0.57
2500	0.114	15.87	31.6	33.94 ± 0.68	-	203.81 ± 3.45	-	52.67 ± 4.46	-	2.0	0.10	44.05 ^{+0.02} _{-0.05}	44.30 ^{+0.02} _{-0.01}	-	-	-	0.51
2812	0.678	19.99	31.1	2.34 ± 0.12	14.90 ± 0.31	-	-	18.94 ± 0.77	1.27 ± 0.05	1.5	0.14	44.64 ^{+0.04} _{-0.05}	44.07 ^{+0.16} _{-0.14}	-1.87 ^{+0.05} _{-0.05}	-1.98 ^{+0.05} _{-0.04}	-	0.71
2944	0.732	20.16	34.1	6.47 ± 0.33	29.66 ± 2.34	-	-	85.02 ± 0.47	2.87 ± 0.17	1.5	0.42	45.14 ^{+0.04} _{-0.03}	44.31 ^{+0.06} _{-0.14}	-1.26 ^{+0.03} _{-0.04}	-1.71 ^{+0.05} _{-0.05}	-	0.72
3021	0.615	21.12	1.3	3.91 ± 0.40	-	9.35 ± 0.86	20.44 ± 1.97	16.04 ± 0.44	-	1.9	2.00	44.78 ^{+0.04} _{-0.04}	44.31 ^{+0.07} _{-0.05}	-	-	-	0.73
3028	0.356	19.99	8.8	3.37 ± 0.19	18.50 ± 0.70	10.68 ± 0.69	84.83 ± 8.35	12.38 ± 0.20	0.67 ± 0.03	1.2	0.30	44.06 ^{+0.09} _{-0.14}	43.71 ^{+0.09} _{-0.29}	-1.92 ^{+0.05} _{-0.09}	-1.75 ^{+0.14} _{-0.09}	-1.19 ^{+0.15} _{-0.10}	0.64
3113	0.080	15.91	38.3	15.92 ± 1.49	477.15 ± 18.76	51.74 ± 9.88	1524.01 ± 16.03	60.42 ± 2.86	0.13 ± 0.01	1.0	0.03	43.92 ^{+0.02} _{-0.02}	43.78 ^{+0.05} _{-0.05}	-2.90 ^{+0.03} _{-0.03}	-2.00 ^{+0.02} _{-0.03}	-1.51 ^{+0.02} _{-0.02}	0.42
3144	0.713	19.95	5.3	0.46 ± 0.15	15.31 ± 1.14	-	-	7.16 ± 0.72	0.47 ± 0.06	1.2	0.11	44.70 ^{+0.05} _{-0.06}	42.86 ^{+0.18} _{-0.41}	-2.34 ^{+0.07} _{-0.06}	-2.01 ^{+0.07} _{-0.06}	-	0.74
3307	0.646	16.70	39.6	< 0.18	532.59 ± 22.81	-	-	87.69 ± 2.73	0.16 ± 0.01	1.0	0.00	45.70 ^{+0.01} _{-0.01}	43.61 ^{+0.11} _{-0.13}	-2.51 ^{+0.02} _{-0.02}	-1.73 ^{+0.02} _{-0.02}	-	0.73
3309	0.372	18.30	3.5	< 0.79	-	1.84 ± 1.40	-	1.86 ± 0.42	-	2.0	1.85	44.94 ^{+0.03} _{-0.20}	44.70 ^{+0.06} _{-0.06}	-	-	-	0.75
3315	0.257	18.21	12.8	3.09 ± 0.39	48.48 ± 2.04	21.76 ± 3.48	145.55 ± 4.73	17.71 ± 2.05	0.37 ± 0.04	1.2	0.10	43.89 ^{+0.05} _{-0.05}	44.18 ^{+0.03} _{-0.06}	-2.20 ^{+0.08} _{-0.07}	-1.76 ^{+0.05} _{-0.05}	-1.32 ^{+0.05} _{-0.05}	0.69
3546	0.324	18.60	7.0	1.64 ± 0.32	37.76 ± 4.94	6.05 ± 1.83	154.80 ± 4.83	18.62 ± 1.74	0.49 ± 0.08	1.2	0.63	44.62 ^{+0.03} _{-0.02}	44.30 ^{+0.11} _{-0.06}	-1.96 ^{+0.06} _{-0.06}	-1.65 ^{+0.06} _{-0.06}	-1.25 ^{+0.02} _{-0.02}	0.73
3554	0.250	19.12	13.1	5.56 ± 0.36	14.00 ± 1.11	20.85 ± 0.73	36.14 ± 1.43	14.60 ± 0.29	1.04 ± 0.09	1.5	0.00	43.15 ^{+0.16} _{-0.39}	43.85 ^{+0.14} _{-0.05}	-1.71 ^{+0.07} _{-0.16}	-1.73 ^{+0.40} _{-0.17}	-1.31 ^{+0.39} _{-0.17}	0.51
3579	0.146	17.79	63.6	1.86 ± 0.57	38.00 ± 0.76	10.44 ± 0.63	98.53 ± 1.21	16.03 ± 0.12	0.42 ± 0.01	1.2	0.00	43.37 ^{+0.03} _{-0.03}	43.85 ^{+0.05} _{-0.01}	-2.41 ^{+0.05} _{-0.03}	-2.03 ^{+0.05} _{-0.03}	-1.62 ^{+0.05} _{-0.03}	0.44
3667	0.153	17.83	20.5	3.27 ± 0.58	147.84 ± 18.05	3.18 ± 2.82	373.62 ± 6.74	21.00 ± 0.76	0.14 ± 0.02	1.0	0.03	43.73 ^{+0.03} _{-0.04}	43.68 ^{+0.04} _{-0.07}	-2.56 ^{+0.04} _{-0.03}	-1.71 ^{+0.07} _{-0.06}	-1.32 ^{+0.04} _{-0.03}	0.58
3724	0.232	19.04	11.0	2.97 ± 0.30	-	8.02 ± 0.38	35.30 ± 1.19	14.62 ± 0.31	-	1.9	0.00	43.28 ^{+0.13} _{-0.10}	43.75 ^{+0.03} _{-0.15}	-	-2.02 ^{+0.10} _{-0.13}	-	0.49
3838	0.193	19.32	11.1	5.69 ± 0.31	35.35 ± 1.21	21.62 ± 0.96	98.64 ± 3.33	61.41 ± 2.58	1.74 ± 0.09	1.5	0.45	44.18 ^{+0.05} _{-0.08}	42.23 ^{+0.20} _{-0.29}	-1.75 ^{+0.08} _{-0.06}	-1.99 ^{+0.08} _{-0.06}	-1.70 ^{+0.08} _{-0.06}	0.52
3867	0.590	21.39	14.4	0.74 ± 0.11	6.15 ± 0.40	-	-	9.02 ± 0.16	1.47 ± 0.11	1.5	0.05	43.88 ^{+0.38} _{-0.16}	43.51 ^{+0.22} _{-0.16}	-1.70 ^{+0.16} _{-0.38}	-1.87 ^{+0.16} _{-0.38}	-	0.65

ID	z	m_r	SNR	$f(\text{nH}\beta)$	$f(\text{bH}\beta)$	$f(\text{nH}\alpha)$	$f(\text{bH}\alpha)$	$f(\text{[OIII]5007\AA})$	R	Class	$E(B-V)$	L_{AGN}	L_{Gal}	$\tau_{\text{[OIII]}}$	$\tau_{\text{[bH}\beta]}$	$\tau_{\text{[bH}\alpha]}$	ϕ_{Gal}
(1)	(2)	(3)	(4)	(5)	(6)	(7)	(8)	(9)	(10)	(11)	(12)	(13)	(14)	(15)	(16)	(17)	(18)
-	-	-	-	$\text{erg s}^{-1} \text{cm}^{-2}$	-	-	-	erg s^{-1}	erg s^{-1}	-	-	-	-				
4031	0.368	20.05	11.2	0.34 ± 0.11	4.22 ± 0.23	1.28 ± 0.11	16.42 ± 0.33	5.46 ± 0.24	1.29 ± 0.09	1.5	0.00	43.92 ^{+0.11} _{-0.05}	43.49 ^{+0.07} _{-0.07}	-2.51 ^{+0.06} _{-0.11}	-2.62 ^{+0.06} _{-0.11}	-2.03 ^{+0.05} _{-0.11}	0.58
4269	0.096	18.34	10.9	4.76 ± 0.52	-	13.38 ± 0.94	-	36.43 ± 0.59	-	2.0	1.70	43.53 ^{+0.02} _{-0.02}	43.24 ^{+0.01} _{-0.08}	-	-	-	0.39
4277	0.633	22.92	2.5	0.05 ± 0.01	-	< 3.38	-	0.33 ± 0.01	-	2.0	1.55	44.16 ^{+0.15} _{-0.53}	43.84 ^{+0.15} _{-0.43}	-	-	-	0.61
4360	0.642	18.45	14.0	9.73 ± 0.75	103.77 ± 3.86	-	-	93.03 ± 6.54	0.90 ± 0.07	1.2	0.00	44.98 ^{+0.03} _{-0.02}	43.70 ^{+0.04} _{-0.08}	-1.76 ^{+0.04} _{-0.04}	-1.72 ^{+0.02} _{-0.04}	-	0.82
4361	0.112	16.75	15.4	1.55 ± 0.33	-	8.70 ± 0.49	-	15.08 ± 0.53	-	2.0	2.00	42.47 ^{+0.41} _{-1.65}	44.03 ^{+0.02} _{-0.02}	-	-	-	0.51
4364	0.419	20.80	21.4	0.16 ± 0.03	-	-	-	3.92 ± 0.06	-	5.0	0.48	43.90 ^{+0.35} _{-2.15}	43.74 ^{+0.19} _{-0.39}	-	-	-	0.60
4450	0.345	20.26	20.1	6.91 ± 0.36	52.28 ± 0.99	-	-	51.77 ± 0.34	0.99 ± 0.02	1.2	0.04	43.44 ^{+0.27} _{-0.15}	43.75 ^{+0.12} _{-0.38}	-1.07 ^{+0.15} _{-0.27}	-1.07 ^{+0.15} _{-0.27}	-	0.57
4487	0.587	20.27	11.3	0.73 ± 0.23	20.48 ± 1.49	-	-	19.35 ± 0.73	0.94 ± 0.08	1.2	0.00	44.00 ^{+0.17} _{-0.22}	44.40 ^{+0.05} _{-0.10}	-1.56 ^{+0.22} _{-0.17}	-1.54 ^{+0.23} _{-0.17}	-	0.65
4643	0.487	18.43	14.1	1.22 ± 0.25	92.82 ± 1.55	< 10.90	377.78 ± 6.85	15.70 ± 1.31	0.17 ± 0.02	1.0	0.18	45.02 ^{+0.03} _{-0.05}	44.27 ^{+0.35} _{-0.12}	-2.62 ^{+0.06} _{-0.04}	-1.85 ^{+0.05} _{-0.03}	-	0.69
4645	0.116	16.28	19.9	3.54 ± 0.40	-	26.26 ± 0.67	-	9.60 ± 0.52	-	2.0	0.48	43.62 ^{+0.08} _{-0.10}	44.29 ^{+0.02} _{-0.02}	-	-	-	0.51
4648	0.246	17.46	24.2	42.40 ± 2.60	123.86 ± 3.66	162.72 ± 11.44	373.12 ± 14.04	48.90 ± 1.03	0.39 ± 0.01	1.2	0.05	44.50 ^{+0.01} _{-0.01}	43.22 ^{+0.10} _{-0.09}	-2.48 ^{+0.02} _{-0.02}	-2.07 ^{+0.02} _{-0.02}	-1.61 ^{+0.02} _{-0.02}	0.68
4659	0.436	20.48	12.7	4.26 ± 0.24	9.98 ± 0.30	-	-	32.53 ± 0.17	3.26 ± 0.10	1.5	0.20	44.07 ^{+0.09} _{-0.09}	43.61 ^{+0.12} _{-0.16}	-1.44 ^{+0.09} _{-0.09}	-1.95 ^{+0.09} _{-0.09}	-	0.60
4740	0.085	15.39	30.4	15.93 ± 0.80	-	39.56 ± 3.30	425.50 ± 4.50	121.05 ± 1.99	-	1.9	0.07	43.40 ^{+0.24} _{-0.09}	44.31 ^{+0.01} _{-0.01}	-	-1.94 ^{+0.09} _{-0.24}	-	0.44
4741	0.656	18.70	13.5	2.59 ± 0.62	76.32 ± 6.79	-	-	32.79 ± 1.80	0.43 ± 0.05	1.2	0.00	44.93 ^{+0.01} _{-0.11}	41.38 ^{+0.05} _{-0.01}	-2.14 ^{+0.11} _{-0.03}	-1.78 ^{+0.12} _{-0.04}	-	0.82
4797	0.265	19.30	7.8	1.75 ± 0.58	55.12 ± 4.12	46.71 ± 3.80	230.55 ± 9.42	41.01 ± 2.98	0.74 ± 0.07	1.2	0.39	44.07 ^{+0.03} _{-0.02}	43.53 ^{+0.08} _{-0.05}	-1.59 ^{+0.04} _{-0.04}	-1.46 ^{+0.04} _{-0.04}	-0.98 ^{+0.03} _{-0.03}	0.69
4799	0.249	17.90	58.8	0.93 ± 0.09	-	10.36 ± 0.30	-	2.99 ± 0.14	-	2.0	0.58	43.95 ^{+0.11} _{-0.04}	44.41 ^{+0.05} _{-0.03}	-	-	-	0.56
4812	0.168	18.99	11.1	0.58 ± 0.15	-	4.54 ± 0.47	-	16.35 ± 0.81	-	2.0	1.85	44.45 ^{+0.01} _{-0.01}	43.54 ^{+0.05} _{-0.04}	-	-	-	0.49
4946	0.215	19.18	7.0	2.14 ± 0.20	-	14.45 ± 0.67	-	23.22 ± 0.92	-	2.0	0.55	43.89 ^{+0.03} _{-0.14}	43.58 ^{+0.26} _{-0.04}	-	-	-	0.54
5059	0.240	18.38	11.4	4.32 ± 0.38	-	17.60 ± 1.12	48.35 ± 2.79	8.53 ± 0.83	-	1.9	0.18	43.78 ^{+0.05} _{-0.05}	44.06 ^{+0.04} _{-0.08}	-	-2.18 ^{+0.06} _{-0.06}	-	0.57
5060	0.181	18.35	9.8	3.49 ± 0.49	11.82 ± 0.97	17.87 ± 0.89	41.20 ± 1.58	8.48 ± 0.37	0.72 ± 0.07	1.2	0.00	43.26 ^{+0.06} _{-0.11}	43.79 ^{+0.05} _{-0.04}	-2.37 ^{+0.11} _{-0.06}	-2.22 ^{+0.12} _{-0.06}	-1.68 ^{+0.11} _{-0.06}	0.62
5172	0.243	18.71	9.4	1.74 ± 0.40	28.47 ± 1.08	6.02 ± 1.02	108.27 ± 6.14	6.34 ± 0.34	0.22 ± 0.01	1.0	0.01	43.79 ^{+0.07} _{-0.06}	43.74 ^{+0.05} _{-0.20}	-2.73 ^{+0.07} _{-0.08}	-2.07 ^{+0.06} _{-0.08}	-1.50 ^{+0.07} _{-0.08}	0.68
5245	0.504	20.60	5.1	2.32 ± 0.43	15.98 ± 1.24	-	-	26.86 ± 3.53	1.68 ± 0.25	1.5	1.25	44.62 ^{+0.02} _{-0.04}	44.18 ^{+0.17} _{-0.07}	-0.50 ^{+0.09} _{-0.07}	-0.73 ^{+0.07} _{-0.05}	-	0.63
5287	0.221	18.56	8.8	19.78 ± 0.36	-	62.43 ± 1.08	-	223.13 ± 4.49	-	2.0	1.85	43.62 ^{+0.03} _{-0.04}	43.94 ^{+0.02} _{-0.08}	-	-	-	0.55
5291	0.158	17.97	12.4	3.54 ± 0.20	-	12.81 ± 0.77	-	31.86 ± 2.23	-	2.0	0.41	43.05 ^{+0.06} _{-0.08}	43.88 ^{+0.03} _{-0.02}	-	-	-	0.47
5330	0.567	21.54	4.9	0.07 ± 0.01	-	4.19 ± 0.76	-	1.50 ± 0.10	-	2.0	1.70	43.98 ^{+0.23} _{-0.38}	43.99 ^{+0.09} _{-1.06}	-	-	-	0.59
5336	0.124	17.38	18.7	18.74 ± 0.55	-	108.25 ± 1.93	71.98 ± 4.99	75.59 ± 3.18	-	1.9	0.57	44.04 ^{+0.02} _{-0.06}	43.82 ^{+0.05} _{-0.01}	-	-2.54 ^{+0.07} _{-0.04}	-	0.53
5405	0.163	18.63	12.0	1.36 ± 0.25	19.29 ± 0.83	4.61 ± 0.55	79.56 ± 20.00	10.92 ± 0.30	0.57 ± 0.03	1.2	0.03	42.87 ^{+0.09} _{-0.15}	43.64 ^{+0.06} _{-0.03}	-1.93 ^{+0.15} _{-0.09}	-1.68 ^{+0.15} _{-0.09}	-1.07 ^{+0.21} _{-0.13}	0.48
5622	0.336	18.72	77.6	0.81 ± 0.17	60.01 ± 6.97	9.20 ± 3.32	205.04 ± 3.12	14.98 ± 0.78	0.25 ± 0.02	1.0	0.46	44.74 ^{+0.02} _{-0.02}	44.00 ^{+0.10} _{-0.07}	-2.37 ^{+0.03} _{-0.03}	-1.76 ^{+0.06} _{-0.05}	-1.39 ^{+0.02} _{-0.02}	0.56
5623	0.321	19.31	32.7	1.69 ± 0.06	-	4.98 ± 0.15	17.03 ± 0.42	13.82 ± 0.09	-	1.9	0.05	43.79 ^{+0.08} _{-0.10}	43.87 ^{+0.05} _{-0.06}	-	-2.48 ^{+0.11} _{-0.08}	-	0.55
5687	0.536	21.46	18.2	0.56 ± 0.05	-	0.88 ± 0.40	-	5.15 ± 0.07	-	2.0	2.00	44.41 ^{+0.28} _{-0.22}	44.15 ^{+0.10} _{-0.19}	-	-	-	0.63
5688	0.336	20.15	8.4	1.57 ± 0.23	7.37 ± 0.55	42.68 ± 8.68	143.25 ± 17.02	16.66 ± 0.22	2.26 ± 0.17	1.5	0.10	43.33 ^{+0.17} _{-0.23}	43.69 ^{+0.06} _{-0.23}	-1.40 ^{+0.23} _{-0.17}	-1.75 ^{+0.24} _{-0.17}	-0.50 ^{+0.24} _{-0.17}	0.64
5689	0.083	17.19	20.9	2.06 ± 0.32	-	4.60 ± 0.45	82.08 ± 1.94	14.13 ± 0.45	-	1.9	0.44	42.58 ^{+0.19} _{-0.29}	43.55 ^{+0.02} _{-0.01}	-	-1.52 ^{+0.27} _{-0.17}	-	0.43

ID	z	m_r	SNR	$f(\text{nH}\beta)$	$f(\text{bH}\beta)$	$f(\text{nH}\alpha)$	$f(\text{bH}\alpha)$	$f(\text{[OIII]5007\AA})$	R	Class	$E(B-V)$	L_{AGN}	L_{Gal}	$r[\text{OIII}]$	$r[\text{bH}\beta]$	$r[\text{bH}\alpha]$	ϕ_{Gal}
(1)	(2)	(3)	(4)	(5)	(6)	(7)	(8)	(9)	(10)	(11)	(12)	(13)	(14)	(15)	(16)	(17)	(18)
-	-	-	-	erg s ⁻¹ cm ⁻²	-	-	-	erg s ⁻¹	erg s ⁻¹	-	-	-	-				
5986	0.228	18.44	50.7	5.58 ± 0.11	-	21.23 ± 0.18	-	76.40 ± 0.17	-	2.0	2.00	43.56 ^{+0.03} _{-0.06}	44.09 ^{+0.02} _{-0.03}	-	-	-	0.49
6009	0.093	15.90	17.0	6.59 ± 0.61	-	30.29 ± 0.87	34.21 ± 3.47	27.82 ± 0.81	-	1.9	2.00	42.77 ^{+0.23} _{-0.50}	44.20 ^{+0.01} _{-0.01}	-	-	-	0.46
6080	0.696	17.96	22.4	24.90 ± 1.63	113.55 ± 3.59	-	-	43.98 ± 0.96	0.39 ± 0.01	1.2	0.00	45.32 ^{+0.01} _{-0.01}	43.35 ^{+0.12} _{-0.16}	-2.35 ^{+0.02} _{-0.01}	-1.94 ^{+0.02} _{-0.02}	-	0.82
6188	0.654	16.56	45.8	18.86 ± 0.73	331.21 ± 10.10	-	-	257.08 ± 3.71	0.78 ± 0.03	1.2	0.00	45.81 ^{+0.01} _{-0.01}	42.01 ^{+0.69} _{-0.03}	-2.14 ^{+0.01} _{-0.01}	-2.03 ^{+0.02} _{-0.02}	-	0.73
6213	0.156	16.61	33.2	19.39 ± 3.19	401.42 ± 13.32	110.50 ± 10.85	1233.41 ± 63.11	46.85 ± 6.07	0.12 ± 0.02	1.0	0.00	44.42 ^{+0.02} _{-0.01}	43.78 ^{+0.05} _{-0.06}	-2.93 ^{+0.06} _{-0.06}	-2.00 ^{+0.02} _{-0.02}	-1.51 ^{+0.03} _{-0.03}	0.58
6215	0.119	16.79	22.4	1.39 ± 0.51	-	12.30 ± 0.58	-	12.14 ± 0.53	-	2.0	0.46	43.34 ^{+0.12} _{-0.36}	44.09 ^{+0.02} _{-0.01}	-	-	-	0.42
6261	0.392	18.16	26.3	< 0.78	145.81 ± 1.67	40.06 ± 3.06	384.71 ± 7.50	28.34 ± 0.79	0.19 ± 0.01	1.0	0.01	44.68 ^{+0.04} _{-0.03}	43.14 ^{+0.08} _{-0.12}	-2.49 ^{+0.03} _{-0.05}	-1.77 ^{+0.03} _{-0.04}	-1.36 ^{+0.03} _{-0.04}	0.66
6277	0.260	20.08	4.5	1.27 ± 0.17	-	4.85 ± 0.64	23.43 ± 1.27	9.75 ± 0.23	-	1.9	1.85	43.97 ^{+0.05} _{-0.03}	43.58 ^{+0.04} _{-0.18}	-	-	-	0.58
6434	0.185	18.05	16.1	5.23 ± 0.42	-	29.15 ± 0.82	65.00 ± 1.90	5.81 ± 0.40	-	1.9	0.19	43.41 ^{+0.04} _{-0.07}	43.99 ^{+0.03} _{-0.01}	-	-1.93 ^{+0.08} _{-0.04}	-	0.44
6458	0.222	18.78	8.1	2.26 ± 0.33	-	8.82 ± 0.74	12.41 ± 1.42	19.59 ± 0.33	-	1.9	2.00	43.94 ^{+0.02} _{-0.04}	43.98 ^{+0.05} _{-0.03}	-	-	-	0.52
6527	0.499	18.69	12.7	0.59 ± 0.56	70.86 ± 3.89	-	-	10.07 ± 0.44	0.14 ± 0.01	1.0	0.05	44.83 ^{+0.06} _{-0.04}	43.47 ^{+0.61} _{-1.70}	-2.78 ^{+0.05} _{-0.06}	-1.94 ^{+0.05} _{-0.06}	-	0.79
6644	0.143	17.49	10.1	2.41 ± 0.35	-	44.27 ± 0.54	-	8.31 ± 0.48	-	2.0	2.00	44.25 ^{+0.03} _{-0.03}	44.00 ^{+0.01} _{-0.04}	-	-	-	0.56
6646	0.548	21.07	11.1	0.82 ± 0.04	-	4.67 ± 0.33	7.57 ± 1.41	6.50 ± 0.08	-	1.9	1.85	43.86 ^{+0.30} _{-0.21}	44.16 ^{+0.15} _{-0.13}	-	-	-	0.64
6699	0.073	16.83	28.7	11.14 ± 0.75	105.34 ± 3.67	35.57 ± 2.47	426.74 ± 8.00	87.89 ± 3.52	0.83 ± 0.04	1.2	0.03	43.15 ^{+0.03} _{-0.03}	43.54 ^{+0.02} _{-0.03}	-2.05 ^{+0.03} _{-0.04}	-1.97 ^{+0.03} _{-0.04}	-1.37 ^{+0.03} _{-0.03}	0.40
6781	0.134	17.62	12.6	16.19 ± 0.49	-	46.25 ± 0.46	-	67.74 ± 0.62	-	2.0	0.00	42.40 ^{+0.11} _{-0.20}	43.87 ^{+0.01} _{-0.01}	-	-	-	0.38
6824	0.327	18.83	23.8	0.68 ± 0.16	-	10.81 ± 0.20	-	3.85 ± 0.16	-	2.0	0.26	44.05 ^{+0.09} _{-0.12}	44.29 ^{+0.07} _{-0.07}	-	-	-	0.64
6825	0.135	17.55	11.8	1.53 ± 0.44	-	8.35 ± 0.33	-	9.76 ± 0.56	-	2.0	0.80	42.67 ^{+0.43} _{-1.97}	43.96 ^{+0.02} _{-0.04}	-	-	-	0.55
6848	0.102	16.32	17.8	13.16 ± 0.50	-	72.27 ± 1.00	68.22 ± 2.66	77.10 ± 0.81	-	1.9	0.38	43.67 ^{+0.03} _{-0.02}	44.11 ^{+0.02} _{-0.01}	-	-2.56 ^{+0.03} _{-0.03}	-	0.48
6867	0.236	19.63	15.0	5.17 ± 0.45	21.08 ± 1.19	-	-	18.33 ± 0.24	0.87 ± 0.05	1.2	0.00	43.32 ^{+0.05} _{-0.09}	43.36 ^{+0.18} _{-0.05}	-1.83 ^{+0.09} _{-0.05}	-1.77 ^{+0.09} _{-0.05}	-	0.49
6921	0.402	20.57	5.6	1.41 ± 0.26	-	2.48 ± 0.32	25.30 ± 1.52	27.15 ± 0.77	-	1.9	0.80	44.35 ^{+0.07} _{-0.11}	43.84 ^{+0.11} _{-0.13}	-	-	-	0.67
6961	0.509	19.67	4.7	-	-	-	-	-	-	3.0	0.01	44.23 ^{+0.06} _{-0.18}	44.31 ^{+0.04} _{-0.08}	-	-	-	0.71
6962	0.212	18.30	9.3	3.20 ± 0.33	-	14.49 ± 1.72	107.01 ± 9.68	36.54 ± 3.15	-	1.9	2.00	44.06 ^{+0.02} _{-0.03}	44.09 ^{+0.11} _{-0.11}	-	-	-	0.54
7005	0.373	18.47	13.4	4.27 ± 0.26	95.03 ± 4.53	11.96 ± 6.84	349.23 ± 21.86	34.59 ± 1.97	0.36 ± 0.03	1.2	0.00	44.34 ^{+0.03} _{-0.01}	43.97 ^{+0.05} _{-0.08}	-2.12 ^{+0.03} _{-0.04}	-1.68 ^{+0.02} _{-0.03}	-1.11 ^{+0.03} _{-0.04}	0.75
7150	0.696	19.24	59.0	4.25 ± 0.12	58.29 ± 0.96	-	-	60.81 ± 1.70	1.04 ± 0.04	1.5	0.19	45.01 ^{+0.03} _{-0.06}	44.30 ^{+0.32} _{-0.14}	-1.64 ^{+0.06} _{-0.03}	-1.66 ^{+0.06} _{-0.03}	-	0.67
7215	0.338	19.62	3.5	< 0.4	-	2.15 ± 0.33	-	4.41 ± 0.19	-	2.0	0.41	43.74 ^{+0.12} _{-0.20}	44.02 ^{+0.17} _{-0.06}	-	-	-	0.63
7216	0.360	17.93	35.1	1.65 ± 1.17	477.32 ± 16.59	24.75 ± 1.86	1289.41 ± 25.32	72.41 ± 1.38	0.15 ± 0.01	1.0	0.00	44.69 ^{+0.02} _{-0.02}	43.36 ^{+0.04} _{-0.05}	-2.19 ^{+0.02} _{-0.02}	-1.37 ^{+0.02} _{-0.02}	-0.94 ^{+0.02} _{-0.02}	0.64
7308	0.312	18.71	6.6	0.43 ± 0.18	17.57 ± 1.25	3.68 ± 2.69	59.61 ± 5.13	12.99 ± 0.80	0.74 ± 0.07	1.2	0.36	43.85 ^{+0.15} _{-0.16}	44.26 ^{+0.20} _{-0.01}	-1.74 ^{+0.22} _{-0.12}	-1.61 ^{+0.22} _{-0.12}	-1.20 ^{+0.22} _{-0.12}	0.72
7309	0.530	20.63	4.6	0.50 ± 0.13	2.88 ± 0.48	-	-	-	-	3.0	0.05	43.98 ^{+0.55} _{-0.18}	43.68 ^{+0.08} _{-0.09}	-	-	-	0.63
7409	0.079	18.13	17.1	33.17 ± 1.04	102.63 ± 1.84	110.27 ± 4.16	325.77 ± 4.80	242.81 ± 8.13	2.37 ± 0.09	1.5	0.00	43.13 ^{+0.02} _{-0.01}	42.44 ^{+0.05} _{-0.03}	-1.55 ^{+0.02} _{-0.02}	-1.93 ^{+0.02} _{-0.02}	-1.42 ^{+0.02} _{-0.02}	0.42
7427	0.371	18.74	12.7	10.46 ± 0.36	69.21 ± 1.04	43.20 ± 4.94	198.07 ± 7.81	100.99 ± 1.47	1.46 ± 0.03	1.5	0.01	44.29 ^{+0.04} _{-0.05}	43.85 ^{+0.11} _{-0.15}	-1.59 ^{+0.05} _{-0.04}	-1.76 ^{+0.05} _{-0.04}	-1.30 ^{+0.05} _{-0.04}	0.75
7509	0.095	16.89	23.8	10.62 ± 0.59	92.65 ± 3.23	39.99 ± 1.66	327.89 ± 3.42	103.73 ± 5.22	1.12 ± 0.07	1.5	0.11	43.70 ^{+0.02} _{-0.02}	43.64 ^{+0.03} _{-0.04}	-2.17 ^{+0.03} _{-0.03}	-2.22 ^{+0.03} _{-0.03}	-1.71 ^{+0.02} _{-0.02}	0.46
7528	0.669	18.91	10.3	1.02 ± 0.59	63.69 ± 3.24	-	-	10.13 ± 1.17	0.16 ± 0.02	1.0	0.01	44.87 ^{+0.01} _{-0.04}	42.89 ^{+0.17} _{-0.15}	-2.56 ^{+0.07} _{-0.05}	-1.77 ^{+0.04} _{-0.03}	-	0.82

ID	z	m_r	SNR	$f(\text{nH}\beta)$	$f(\text{bH}\beta)$	$f(\text{nH}\alpha)$	$f(\text{bH}\alpha)$	$f(\text{[OIII]5007\AA})$	R	Class	$E(B-V)$	L_{AGN}	L_{Gal}	$\tau_{\text{[OIII]}}$	$\tau_{\text{[bH}\beta]}$	$\tau_{\text{[bH}\alpha]}$	ϕ_{Gal}
(1)	(2)	(3)	(4)	(5)	(6)	(7)	(8)	(9)	(10)	(11)	(12)	(13)	(14)	(15)	(16)	(17)	(18)
-	-	-	-	$\text{erg s}^{-1} \text{cm}^{-2}$	-	-	-	erg s^{-1}	erg s^{-1}	-	-	-	-				
7697	0.148	19.53	6.2	2.71 ± 0.38	9.11 ± 0.52	8.39 ± 0.86	38.31 ± 0.98	20.83 ± 2.02	2.29 ± 0.26	1.5	0.25	$43.47^{+0.09}_{-0.15}$	$42.26^{+0.48}_{-0.70}$	$-2.04^{+0.16}_{-0.10}$	$-2.40^{+0.15}_{-0.09}$	$-1.87^{+0.15}_{-0.09}$	0.46
7734	0.167	16.06	168.7	52.03 ± 1.69	966.19 ± 5.08	25.19 ± 15.80	1971.27 ± 180.06	199.99 ± 1.73	0.21 ± 0.00	1.0	0.04	$44.81^{+0.03}_{-0.02}$	$42.34^{+0.21}_{-1.21}$	$-2.57^{+0.02}_{-0.03}$	$-1.88^{+0.02}_{-0.03}$	$-1.59^{+0.05}_{-0.05}$	0.42
7756	0.246	19.29	7.5	4.24 ± 0.18	-	21.51 ± 1.12	-	30.86 ± 0.69	-	2.0	0.80	$44.31^{+0.06}_{-0.03}$	$43.70^{+0.14}_{-0.38}$	-	-	-	0.57
7809	0.270	19.34	5.1	4.03 ± 0.35	35.07 ± 5.30	16.39 ± 2.41	144.25 ± 11.46	40.41 ± 0.46	1.15 ± 0.12	1.5	0.05	$43.60^{+0.06}_{-0.01}$	$43.63^{+0.02}_{-0.11}$	$-1.57^{+0.01}_{-0.06}$	$-1.63^{+0.07}_{-0.08}$	$-1.03^{+0.04}_{-0.07}$	0.70
7880	0.298	19.00	8.4	2.06 ± 0.44	22.56 ± 1.60	-	-	16.31 ± 0.53	0.72 ± 0.06	1.2	0.54	$44.29^{+0.03}_{-0.04}$	$44.02^{+0.23}_{-0.07}$	$-1.89^{+0.04}_{-0.04}$	$-1.75^{+0.05}_{-0.05}$	-	0.62
7967	0.352	18.47	8.6	7.29 ± 0.63	77.69 ± 1.52	33.15 ± 9.87	317.81 ± 52.54	44.37 ± 5.62	0.57 ± 0.07	1.2	0.18	$44.59^{+0.01}_{-0.03}$	$43.90^{+0.28}_{-0.09}$	$-2.08^{+0.07}_{-0.05}$	$-1.84^{+0.03}_{-0.02}$	$-1.29^{+0.09}_{-0.07}$	0.74
8104	0.399	17.76	12.5	2.68 ± 1.79	81.02 ± 6.40	-	-	15.51 ± 1.18	0.19 ± 0.02	1.0	0.00	$44.87^{+0.02}_{-0.01}$	$44.30^{+0.03}_{-0.13}$	$-2.93^{+0.03}_{-0.04}$	$-2.21^{+0.04}_{-0.04}$	-	0.67
8178	0.434	20.33	9.1	< 0.92	31.60 ± 1.42	-	-	2.75 ± 0.37	0.09 ± 0.01	1.0	0.12	$43.98^{+0.11}_{-0.18}$	$43.72^{+0.11}_{-0.22}$	$-2.55^{+0.20}_{-0.12}$	$-1.49^{+0.19}_{-0.11}$	-	0.60
8405	0.104	16.77	21.8	5.57 ± 0.45	-	20.77 ± 0.60	-	19.41 ± 0.60	-	2.0	0.30	$42.94^{+0.08}_{-0.09}$	$43.98^{+0.01}_{-0.02}$	-	-	-	0.49
8602	0.215	18.44	15.4	1.31 ± 0.36	73.21 ± 5.78	2.70 ± 0.82	237.41 ± 6.08	23.85 ± 2.58	0.33 ± 0.04	1.2	0.00	$43.90^{+0.14}_{-0.03}$	$43.64^{+0.22}_{-0.03}$	$-2.39^{+0.06}_{-0.14}$	$-1.90^{+0.05}_{-0.14}$	$-1.39^{+0.03}_{-0.14}$	0.65
8741	0.527	18.31	25.9	3.91 ± 1.20	113.46 ± 3.44	38.83 ± 28.66	336.82 ± 49.70	29.34 ± 0.89	0.26 ± 0.01	1.0	0.09	$45.05^{+0.18}_{-0.04}$	$43.44^{+1.68}_{-0.87}$	$-2.42^{+0.04}_{-0.18}$	$-1.84^{+0.04}_{-0.18}$	-	0.70
8833	0.291	18.66	36.6	< 0.02	-	3.02 ± 0.13	-	2.96 ± 0.11	-	2.0	0.35	$44.17^{+0.04}_{-0.17}$	$44.18^{+0.14}_{-0.07}$	-	-	-	0.53
8919	0.237	17.39	28.1	47.32 ± 1.53	469.98 ± 19.00	582.94 ± 12.07	1427.93 ± 19.63	329.78 ± 5.71	0.70 ± 0.03	1.2	0.04	$44.59^{+0.01}_{-0.03}$	$42.94^{+0.04}_{-0.02}$	$-1.79^{+0.03}_{-0.01}$	$-1.63^{+0.04}_{-0.02}$	$-1.16^{+0.03}_{-0.01}$	0.67
8921	0.387	17.26	41.8	1.82 ± 0.79	359.96 ± 12.75	4.81 ± 0.99	1107.94 ± 108.47	59.21 ± 1.96	0.16 ± 0.01	1.0	0.00	$45.01^{+0.02}_{-0.01}$	$43.63^{+0.76}_{-0.64}$	$-2.52^{+0.02}_{-0.03}$	$-1.73^{+0.02}_{-0.03}$	$-1.25^{+0.05}_{-0.05}$	0.76
8923	0.598	20.67	4.2	-	-	8.52 ± 4.23	36.68 ± 0.00	-	-	6.0	2.00	$44.84^{+0.03}_{-0.03}$	$44.48^{+0.02}_{-0.02}$	-	-	-	0.65
8929	0.108	17.48	15.1	3.02 ± 0.40	-	6.83 ± 0.48	53.22 ± 2.07	15.31 ± 0.56	-	1.9	0.21	$42.73^{+0.21}_{-1.48}$	$43.74^{+0.04}_{-0.02}$	-	$-1.83^{+1.11}_{-0.22}$	-	0.50
9046	0.061	16.37	20.2	14.02 ± 1.51	62.42 ± 2.27	44.83 ± 2.23	278.27 ± 6.20	60.24 ± 3.56	0.97 ± 0.07	1.2	0.35	$43.07^{+0.02}_{-0.03}$	$43.64^{+0.01}_{-0.01}$	$-1.86^{+0.04}_{-0.03}$	$-1.84^{+0.04}_{-0.03}$	$-1.31^{+0.04}_{-0.03}$	0.36
9089	0.081	17.93	10.3	2.58 ± 1.34	-	25.53 ± 1.92	-	36.01 ± 1.33	-	2.0	0.64	$42.93^{+0.03}_{-0.05}$	$43.21^{+0.05}_{-0.04}$	-	-	-	0.35
9262	0.252	19.34	35.6	3.25 ± 0.13	-	13.10 ± 0.11	-	5.36 ± 0.13	-	2.0	0.15	$43.56^{+0.20}_{-0.44}$	$43.81^{+0.14}_{-0.07}$	-	-	-	0.51
9478	0.654	19.13	10.4	3.88 ± 0.55	60.60 ± 2.43	-	-	13.49 ± 0.87	0.22 ± 0.02	1.0	0.05	$44.85^{+0.05}_{-0.03}$	$43.04^{+0.13}_{-0.29}$	$-2.39^{+0.05}_{-0.06}$	$-1.73^{+0.04}_{-0.05}$	-	0.82
9480	0.399	19.47	5.1	< 0.70	26.54 ± 1.11	< 2.21	116.79 ± 28.75	6.66 ± 0.40	0.25 ± 0.02	1.0	0.00	$44.12^{+0.07}_{-0.02}$	$43.31^{+0.05}_{-0.33}$	$-2.54^{+0.04}_{-0.07}$	$-1.94^{+0.03}_{-0.07}$	$-1.30^{+0.13}_{-0.11}$	0.76
9487	0.094	16.89	17.7	65.35 ± 0.92	-	172.11 ± 3.90	115.92 ± 3.99	711.75 ± 24.63	-	1.9	0.43	$43.78^{+0.02}_{-0.02}$	$43.72^{+0.05}_{-0.01}$	-	$-2.46^{+0.03}_{-0.02}$	-	0.46
9507	0.263	17.63	21.3	4.72 ± 1.05	178.56 ± 5.33	62.94 ± 19.76	519.10 ± 10.38	53.35 ± 2.56	0.30 ± 0.02	1.0	0.01	$44.50^{+0.02}_{-0.01}$	$43.08^{+0.04}_{-0.05}$	$-2.43^{+0.02}_{-0.03}$	$-1.91^{+0.02}_{-0.03}$	$-1.45^{+0.01}_{-0.03}$	0.69
9514	0.314	19.47	4.2	3.39 ± 0.38	13.83 ± 0.68	4.94 ± 2.49	47.40 ± 4.09	21.84 ± 1.60	1.58 ± 0.14	1.5	0.03	$43.85^{+0.09}_{-0.12}$	$43.49^{+0.08}_{-0.12}$	$-1.96^{+0.13}_{-0.09}$	$-2.16^{+0.13}_{-0.09}$	$-1.63^{+0.13}_{-0.09}$	0.73
9639	0.625	17.98	22.3	3.14 ± 0.42	134.04 ± 2.00	-	-	56.27 ± 0.96	0.42 ± 0.01	1.2	0.01	$45.20^{+0.01}_{-0.03}$	$43.88^{+0.05}_{-0.04}$	$-2.22^{+0.03}_{-0.03}$	$-1.84^{+0.03}_{-0.01}$	-	0.81
9887	0.061	16.60	25.0	12.00 ± 0.50	-	40.09 ± 1.46	137.64 ± 3.88	81.71 ± 1.23	-	1.9	1.85	$42.77^{+0.09}_{-0.06}$	$43.54^{+0.02}_{-0.01}$	-	-	-	0.36
9888	0.062	17.15	15.4	2.90 ± 0.32	-	11.70 ± 1.44	-	10.31 ± 1.07	-	2.0	0.60	$42.98^{+0.13}_{-0.10}$	$43.33^{+0.04}_{-0.02}$	-	-	-	0.36
9899	0.083	16.31	21.0	3.59 ± 0.47	-	18.51 ± 1.18	79.19 ± 2.63	29.42 ± 0.70	-	1.9	2.00	$42.75^{+0.18}_{-0.21}$	$43.92^{+0.01}_{-0.03}$	-	-	-	0.43
9954	0.209	17.39	24.9	12.15 ± 1.34	323.48 ± 12.18	60.64 ± 12.35	875.38 ± 22.41	84.02 ± 6.01	0.26 ± 0.02	1.0	0.05	$44.46^{+0.01}_{-0.01}$	$42.95^{+0.02}_{-0.02}$	$-2.36^{+0.03}_{-0.03}$	$-1.77^{+0.02}_{-0.02}$	$-1.36^{+0.02}_{-0.01}$	0.65
9956	0.312	19.17	11.2	2.81 ± 0.18	-	24.02 ± 0.33	-	14.24 ± 0.21	-	2.0	0.36	$43.54^{+0.11}_{-0.14}$	$44.11^{+0.03}_{-0.16}$	-	-	-	0.55
9973	0.275	19.72	12.6	2.81 ± 0.10	-	9.85 ± 0.18	20.80 ± 0.61	32.43 ± 0.17	-	1.9	2.00	$43.63^{+0.10}_{-0.03}$	$43.77^{+0.17}_{-0.05}$	-	-	-	0.60
10027	0.056	15.23	36.3	< 4.32	-	31.55 ± 3.09	-	< 5.38	-	2.0	1.40	$42.66^{+0.21}_{-0.48}$	$44.00^{+0.01}_{-0.01}$	-	-	-	0.21

ID	z	m_r	SNR	$f(\text{nH}\beta)$ erg s ⁻¹ cm ⁻²	$f(\text{bH}\beta)$ erg s ⁻¹ cm ⁻²	$f(\text{nH}\alpha)$ erg s ⁻¹ cm ⁻²	$f(\text{bH}\alpha)$ erg s ⁻¹ cm ⁻²	$f([\text{OIII}]5007\text{\AA})$ erg s ⁻¹ cm ⁻²	R	Class	$E(B - V)$	L_{AGN} erg s ⁻¹	L_{Gal} erg s ⁻¹	$r[\text{OIII}]$	$r[\text{bH}\beta]$	$r[\text{bH}\alpha]$	ϕ_{Gal}
(1)	(2)	(3)	(4)	(5)	(6)	(7)	(8)	(9)	(10)	(11)	(12)	(13)	(14)	(15)	(16)	(17)	(18)
10049	0.081	17.44	16.7	3.15 ± 0.33	-	13.06 ± 0.60	21.93 ± 1.46	22.45 ± 0.49	-	1.9	0.80	42.58 ^{+0.03} _{-0.06}	43.47 ^{+0.03} _{-0.01}	-	-	-	0.43
10050	0.522	22.25	5.7	< 0.03	-	< 0.04	-	< 0.03	-	2.0	1.10	43.76 ^{+0.18} _{-0.44}	43.70 ^{+0.19} _{-0.64}	-	-	-	0.67
10306	0.238	19.48	5.8	0.24 ± 0.21	-	1.29 ± 0.21	-	2.45 ± 0.24	-	2.0	0.55	43.35 ^{+0.11} _{-0.13}	43.68 ^{+0.15} _{-0.01}	-	-	-	0.56
10381	0.090	17.82	7.9	6.77 ± 0.83	-	33.48 ± 3.28	-	88.06 ± 7.96	-	2.0	0.65	43.74 ^{+0.01} _{-0.03}	43.35 ^{+0.07} _{-0.02}	-	-	-	0.37
10389	0.397	19.68	5.8	1.16 ± 0.26	31.06 ± 1.20	14.86 ± 6.69	128.45 ± 70.54	8.27 ± 0.31	0.27 ± 0.01	1.0	0.01	44.06 ^{+0.08} _{-0.06}	43.33 ^{+0.07} _{-0.08}	-2.39 ^{+0.06} _{-0.08}	-1.81 ^{+0.06} _{-0.08}	-1.20 ^{+0.36} _{-0.20}	0.76

Table C.2: Resulting values for the 165 AGN that conform the working sample. **Col. 1:** BUXS identifier; **Col. 2:** redshift; **Col. 3:** SDSS modelMag magnitude in the r filter; **Col. 4:** signal-to-noise ratio of the optical spectra; **Col. 5:** total observed flux for narrow H β ; **Col. 6:** total observed flux for broad H β ; **Col. 7:** total observed flux for narrow H α ; **Col. 8:** total observed flux for broad H α ; **Col. 9:** total observed flux for [OIII]5007 \AA ; **Col. 10:** ratio between the observed fluxes of [OIII]5007 \AA and broad H β ; **Col. 10:** AGN class; **Col. 12:** total optical/ultraviolet line-of-sight extinction; **Col. 13:** decimal logarithm of the AGN luminosity at rest-frame 5100 \AA ; **Col. 14:** decimal logarithm of the host galaxy luminosity at rest-frame 5100 \AA ; **Col. 15:** relative luminosity of [OIII]5007 \AA ; **Col. 16:** relative luminosity of the broad component of H β . Values in italics correspond to estimations from H α assuming a intrinsic Balmer decrement of 3.06; **Col. 17:** relative luminosity of the broad component of H α ; **Col. 18:** fraction of host-galaxy light captured inside the projected aperture.

Bibliography

- Abazajian K., et al., 2003, *AJ*, **126**, 2081
- Abdurro'uf et al., 2022, *ApJS*, **259**, 35
- Abolfathi B., et al., 2018, *ApJS*, **235**, 42
- Acker A., Köppen J., Samland M., Stenholm B., 1989, *The Messenger*, **58**, 44
- Aharonian F. A., 2000, *New Astron.*, **5**, 377
- Akylas A., Georgantopoulos I., 2009, *A&A*, **500**, 999
- Allen C. W., 1985, *Astrophysical quantities*, 3rd, repr. edn. Athlone Press, London
- Almeida A., et al., 2023, *ApJS*, **267**, 44
- Alonso-Herrero A., Quillen A. C., Simpson C., Efstathiou A., Ward M. J., 2001, *AJ*, **121**, 1369
- Alonso-Herrero A., Quillen A. C., Rieke G. H., Ivanov V. D., Efstathiou A., 2003a, *AJ*, **126**, 81
- Alonso-Herrero A., Quillen A. C., Rieke G. H., Ivanov V. D., Efstathiou A., 2003b, *AJ*, **126**, 81
- Alonso-Herrero A., et al., 2006, *ApJ*, **640**, 167
- Alonso-Herrero A., et al., 2011, *ApJ*, **736**, 82
- Alonso-Herrero A., et al., 2014, *MNRAS*, **443**, 2766
- Alonso-Herrero A., et al., 2018, *ApJ*, **859**, 144
- Alonso-Tetilla A. V., et al., 2024, *MNRAS*, **527**, 10878
- Anders E., Grevesse N., 1989, *Geochimica Cosmochimica Acta*, **53**, 197
- Anderson E., Francis C., 2012, *Astronomy Letters*, **38**, 331
- Antonucci R., 1993, *ARA&A*, **31**, 473
- Antonucci R. R. J., Miller J. S., 1985, *ApJ*, **297**, 621

Armus L., et al., 2007, [ApJ](#), **656**, 148

Arnaud K. A., 1996, in Jacoby G. H., Barnes J., eds, Astronomical Society of the Pacific Conference Series Vol. 101, Astronomical Data Analysis Software and Systems V. p. 17

Assef R. J., et al., 2010, [ApJ](#), **713**, 970

Assef R. J., et al., 2013, [ApJ](#), **772**, 26

Baade W., Minkowski R., 1954, [ApJ](#), **119**, 206

Baldwin J. A., Phillips M. M., Terlevich R., 1981, [PASP](#), **93**, 5

Baron D., Stern J., Poznanski D., Netzer H., 2016, [ApJ](#), **832**, 8

Barquín-González L., Mateos S., Carrera F., Corral A., Alonso-Herrero A., García-Bernete I., Ordovás-Pascual I., 2020, in XIV Scientific Meeting (virtual) of the Spanish Astronomical Society. p. 7

Baskin A., Laor A., 2005, [MNRAS](#), **358**, 1043

Bassani L., Dadina M., Maiolino R., Salvati M., Risaliti G., Della Ceca R., Matt G., Zamorani G., 1999, [ApJS](#), **121**, 473

Beckmann V., Shrader C. R., 2012, Active Galactic Nuclei

Beckmann V., et al., 2009, [A&A](#), **505**, 417

Bell E. F., de Jong R. S., 2001, [ApJ](#), **550**, 212

Bianchi S., Corral A., Panessa F., Barcons X., Matt G., Bassani L., Carrera F. J., Jiménez-Bailón E., 2008, [MNRAS](#), **385**, 195

Bianchi L., Conti A., Shiao B., 2014, [Advances in Space Research](#), **53**, 900

Bianchi L., Shiao B., Thilker D., 2017, [ApJS](#), **230**, 24

Bianchi S., et al., 2019, [MNRAS](#), **488**, L1

Blandford R., Meier D., Readhead A., 2019, [ARA&A](#), **57**, 467

Bohlin R. C., Savage B. D., Drake J. F., 1978, [ApJ](#), **224**, 132

Boissay R., Ricci C., Paltani S., 2016, [A&A](#), **588**, A70

Bongiorno A., et al., 2007, [A&A](#), **472**, 443

Bornancini C., García Lambas D., 2018a, [MNRAS](#), **479**, 2308

Bornancini C., García Lambas D., 2018b, [MNRAS](#), **479**, 2308

Boroson T., 2005, [AJ](#), **130**, 381

Boroson T. A., Green R. F., 1992, [ApJS](#), **80**, 109

Böttcher M., Reimer A., Sweeney K., Prakash A., 2013, [ApJ](#), 768, 54

Brightman M., Nandra K., 2011, [MNRAS](#), 413, 1206

Bruzual G., Charlot S., 2003, [MNRAS](#), 344, 1000

Burlon D., Ajello M., Greiner J., Comastri A., Merloni A., Gehrels N., 2011, [ApJ](#), 728, 58

Burtscher L., et al., 2016, [A&A](#), 586, A28

Byrd G., Valtonen M., 1990, [ApJ](#), 350, 89

Caccianiga A., et al., 2004, [A&A](#), 416, 901

Caccianiga A., et al., 2008, [A&A](#), 477, 735

Calderone G., Nicastro L., Ghisellini G., Dotti M., Sbarrato T., Shankar F., Colpi M., 2017, [MNRAS](#), 472, 4051

Calistro Rivera G., Lusso E., Hennawi J. F., Hogg D. W., 2016, [ApJ](#), 833, 98

Calistro Rivera G., et al., 2021, [A&A](#), 649, A102

Calzetti D., Armus L., Bohlin R. C., Kinney A. L., Koornneef J., Storchi-Bergmann T., 2000, [ApJ](#), 533, 682

Cappellari M., 2012, pPXF: Penalized Pixel-Fitting stellar kinematics extraction, Astrophysics Source Code Library, record ascl:1210.002

Cardelli J. A., Clayton G. C., Mathis J. S., 1989, [ApJ](#), 345, 245

Casali M., et al., 2007, [A&A](#), 467, 777

Cash W., 1979, [ApJ](#), 228, 939

Castellano M., et al., 2024, [arXiv e-prints](#), p. [arXiv:2403.10238](#)

Chabrier G., 2003, [PASP](#), 115, 763

Ciddor P. E., 1996, [Appl. Opt.](#), 35, 1566

Coffey D., et al., 2019, [A&A](#), 625, A123

Combes F., et al., 2019, [A&A](#), 623, A79

Corral A., Della Ceca R., Caccianiga A., Severgnini P., Brunner H., Carrera F. J., Page M. J., Schwobe A. D., 2011, [A&A](#), 530, A42

Cutri R. M., et al., 2012, Explanatory Supplement to the WISE All-Sky Data Release Products, Explanatory Supplement to the WISE All-Sky Data Release Products

Czesla S., Schröter S., Schneider C. P., Huber K. F., Pfeifer F., Andreasen D. T., Zechmeister M., 2019, PyA: Python astronomy-related packages (ascl:1906.010)

Dalton G. B., et al., 2006. p. 62690X, [doi:10.1117/12.670018](https://doi.org/10.1117/12.670018)

De Ruiter H. R., Willis A. G., Arp H. C., 1977, *A&AS*, **28**, 211

Della Ceca R., et al., 2008, *A&A*, **487**, 119

Den Herder J. W., et al., 2001, *A&A*, **365**, L7

Denney K. D., et al., 2014, *ApJ*, **796**, 134

Di Matteo T., Blackman E. G., Fabian A. C., 1997, *MNRAS*, **291**, L23

Doe S., et al., 2007, in Shaw R. A., Hill F., Bell D. J., eds, *Astronomical Society of the Pacific Conference Series Vol. 376, Astronomical Data Analysis Software and Systems XVI*. p. 543

Dong X., Wang T., Wang J., Yuan W., Zhou H., Dai H., Zhang K., 2008, *MNRAS*, **383**, 581

Donley J. L., Rieke G. H., Pérez-González P. G., Rigby J. R., Alonso-Herrero A., 2007, *ApJ*, **660**, 167

Donley J. L., et al., 2012, *ApJ*, **748**, 142

Dunn J. P., et al., 2015, *ApJ*, **808**, 94

Duras F., et al., 2020, *A&A*, **636**, A73

Dye S., et al., 2018, *MNRAS*, **473**, 5113

Edge A., Sutherland W., Kuijken K., Driver S., McMahon R., Eales S., Emerson J. P., 2013, *The Messenger*, **154**, 32

Elitzur M., 2012, *ApJ*, **747**, L33

Elitzur M., Ho L. C., 2009, *ApJ*, **701**, L91

Elitzur M., Ho L. C., Trump J. R., 2014, *MNRAS*, **438**, 3340

Emerson J., McPherson A., Sutherland W., 2006, *The Messenger*, **126**, 41

Fabian A. C., 2012, *ARA&A*, **50**, 455

Ferland G. J., Korista K. T., Verner D. A., Ferguson J. W., Kingdon J. B., Verner E. M., 1998, *PASP*, **110**, 761

Ferrarese L., Merritt D., 2000, *ApJ*, **539**, L9

Floyd D. J. E., Kukula M. J., Dunlop J. S., McLure R. J., Miller L., Percival W. J., Baum S. A., O'Dea C. P., 2004, *MNRAS*, **355**, 196

Foster A. R., Ji L., Smith R. K., Brickhouse N. S., 2012, *ApJ*, **756**, 128

Freeman P., Doe S., Siemiginowska A., 2001, in Starck J.-L., Murtagh F. D., eds, *Society of Photo-Optical Instrumentation Engineers (SPIE) Conference Series Vol. 4477, Astronom-*

ical Data Analysis. pp 76–87 ([arXiv:astro-ph/0108426](https://arxiv.org/abs/astro-ph/0108426)), [doi:10.1117/12.447161](https://doi.org/10.1117/12.447161)

García-Bernete I., et al., 2019, *MNRAS*, 486, 4917

García-Burillo S., et al., 2016, *ApJ*, 823, L12

García-Burillo S., et al., 2021, *A&A*, 652, A98

Gaskell C. M., 1982, *PASP*, 94, 891

Gaskell C. M., 2017, *MNRAS*, 467, 226

Gaskell C. M., Ferland G. J., 1984, *PASP*, 96, 393

Gaspari M., Brighenti F., Temi P., 2012, *MNRAS*, 424, 190

Gebhardt K., et al., 2000, *ApJ*, 539, L13

Gkini A., Plionis M., Chira M., Koulouridis E., 2021, *A&A*, 650, A75

Goodman J., Weare J., 2010, *Communications in Applied Mathematics and Computational Science*, Vol.~5, No.~1, p.~65-80, 2010, 5, 65

Goodrich R. W., 1995, *ApJ*, 440, 141

Gordon K. D., Clayton G. C., 1998, *ApJ*, 500, 816

Graham A. W., Erwin P., Caon N., Trujillo I., 2001, *ApJ*, 563, L11

Granato G. L., Danese L., 1994, *MNRAS*, 268, 235

Granato G. L., Danese L., Franceschini A., 1997, *ApJ*, 486, 147

Gravity Collaboration et al., 2023, *A&A*, 677, L10

Greene J. E., Ho L. C., 2005, *ApJ*, 630, 122

Grogin N. A., et al., 2005, *ApJ*, 627, L97

Gültekin K., et al., 2009, *ApJ*, 698, 198

Gunn J. E., et al., 1998, *AJ*, 116, 3040

Häring N., Rix H.-W., 2004, *ApJ*, 604, L89

Harris C. R., et al., 2020, *Nature*, 585, 357

Harrison C., 2014, PhD thesis, Durham University, UK

Hawkins M. R. S., 2007, *A&A*, 462, 581

Heard C. Z. P., Gaskell C. M., 2016, *MNRAS*, 461, 4227

Hernández-García L., Masegosa J., González-Martín O., Márquez I., 2015, *A&A*, 579, A90

Hickox R. C., Alexander D. M., 2018, *ARA&A*, 56, 625

- Hickox R. C., et al., 2009, *ApJ*, 696, 891
- Hirschmann M., Khochfar S., Burkert A., Naab T., Genel S., Somerville R. S., 2010, *MNRAS*, 407, 1016
- Ho L. C., 2008, *ARA&A*, 46, 475
- Hönig S. F., Kishimoto M., 2017, *ApJ*, 838, L20
- Hopkins P. F., Hernquist L., Cox T. J., Kereš D., 2008, *ApJS*, 175, 356
- Hubeny I., Blaes O., Krolik J. H., Agol E., 2001, *ApJ*, 559, 680
- Ichikawa K., et al., 2015, *ApJ*, 803, 57
- Ichikawa K., et al., 2019, *ApJ*, 870, 31
- Jaffarian G. W., Gaskell C. M., 2020, *MNRAS*, 493, 930
- Jansen F., et al., 2001, *A&A*, 365, L1
- Jin C., Ward M., Done C., Gelbord J., 2012, *MNRAS*, 420, 1825
- Joye W. A., Mandel E., 2003, in Payne H. E., Jedrzejewski R. I., Hook R. N., eds, *Astronomical Society of the Pacific Conference Series Vol. 295, Astronomical Data Analysis Software and Systems XII*. p. 489
- Kalberla P. M. W., Burton W. B., Hartmann D., Arnal E. M., Bajaja E., Morras R., Pöppel W. G. L., 2005, *A&A*, 440, 775
- Kauffmann G., et al., 2003, *MNRAS*, 346, 1055
- Kelly B. C., 2007, *ApJ*, 665, 1489
- Kimball A. E., Ivezić Ž., 2008, *AJ*, 136, 684
- Kishimoto M., Hönig S. F., Antonucci R., Barvainis R., Kotani T., Tristram K. R. W., Weigelt G., Levin K., 2011, *A&A*, 527, A121
- Koratkar A., Blaes O., 1999, *PASP*, 111, 1
- Kormendy J., Gebhardt K., 2001, in Wheeler J. C., Martel H., eds, *American Institute of Physics Conference Series Vol. 586, 20th Texas Symposium on relativistic astrophysics*. AIP, pp 363–381 ([arXiv:astro-ph/0105230](https://arxiv.org/abs/astro-ph/0105230)), [doi:10.1063/1.1419581](https://doi.org/10.1063/1.1419581)
- Kormendy J., Ho L. C., 2013, *ARA&A*, 51, 511
- Kormendy J., Richstone D., 1995, *ARA&A*, 33, 581
- Koss M., Mushotzky R., Veilleux S., Winter L. M., Baumgartner W., Tueller J., Gehrels N., Valencic L., 2011, *ApJ*, 739, 57
- Koss M., et al., 2017, *ApJ*, 850, 74

Koutoulidis L., Mountrichas G., Georgantopoulos I., Pouliaxis E., Plionis M., 2022, *A&A*, 658, A35

LaMassa S. M., et al., 2015, *ApJ*, 800, 144

Lacy M., Ridgway S. E., Sajina A., Petric A. O., Gates E. L., Urrutia T., Storrie-Lombardi L. J., 2015, *ApJ*, 802, 102

Laor A., Netzer H., 1989, *MNRAS*, 238, 897

Lawrence A., 1991, *MNRAS*, 252, 586

Lawrence A., et al., 2007, *MNRAS*, 379, 1599

Levenson N. A., Heckman T. M., Krolik J. H., Weaver K. A., Życki P. T., 2006, *ApJ*, 648, 111

Li R., Ho L. C., Ricci C., Trakhtenbrot B., Arcavi I., Kara E., Hiramatsu D., 2022, *ApJ*, 933, 70

Liu Z., et al., 2016a, *MNRAS*, 459, 1602

Liu Z., Yuan W., Lu Y., Carrera F. J., Falocco S., Dong X.-B., 2016b, *MNRAS*, 463, 684

Lu K.-X., Zhao Y., Bai J.-M., Fan X.-L., 2019, *MNRAS*, 483, 1722

Lupton R. H., Gunn J. E., Szalay A. S., 1999, *AJ*, 118, 1406

Lusso E., et al., 2010, *A&A*, 512, A34

Lusso E., et al., 2012, *MNRAS*, 425, 623

Lusso E., et al., 2013, *ApJ*, 777, 86

Lyu J., Hao L., Li A., 2014, *ApJ*, 792, L9

Madau P., Dickinson M., 2014, *ARA&A*, 52, 415

Madejski G. G., Sikora M., 2016, *ARA&A*, 54, 725

Magorrian J., et al., 1998, *AJ*, 115, 2285

Maiolino R., Rieke G. H., 1995, *ApJ*, 454, 95

Maiolino R., et al., 2023, *arXiv e-prints*, p. arXiv:2308.01230

Maiolino R., et al., 2024, *Nature*, 627, 59

Marconi A., Hunt L. K., 2003, *ApJ*, 589, L21

Marconi A., Risaliti G., Gilli R., Hunt L. K., Maiolino R., Salvati M., 2004, *MNRAS*, 351, 169

Marshall M. A., Shabala S. S., Krause M. G. H., Pimblet K. A., Croton D. J., Owers M. S., 2018, *MNRAS*, 474, 3615

Marshall A., Auger-Williams M. W., Banerji M., Maiolino R., Bowler R., 2022, [MNRAS](#), **515**, 5617

Martin D. C., et al., 2005, [ApJ](#), **619**, L1

Mason K. O., et al., 2001, [A&A](#), **365**, L36

Mateos S., et al., 2005a, [A&A](#), **433**, 855

Mateos S., Barcons X., Carrera F. J., Ceballos M. T., Hasinger G., Lehmann I., Fabian A. C., Streblyanska A., 2005b, [A&A](#), **444**, 79

Mateos S., Barcons X., Carrera F. J., Page M. J., Ceballos M. T., Hasinger G., Fabian A. C., 2007, [A&A](#), **473**, 105

Mateos S., et al., 2008, [A&A](#), **492**, 51

Mateos S., Saxton R. D., Read A. M., Sembay S., 2009, [A&A](#), **496**, 879

Mateos S., et al., 2010, [A&A](#), **510**, A35

Mateos S., et al., 2012, [MNRAS](#), **426**, 3271

Mateos S., et al., 2015, [MNRAS](#), **449**, 1422

Mateos S., et al., 2016, [ApJ](#), **819**, 166

Mateos S., et al., 2017, [ApJ](#), **841**, L18

McElroy R. E., et al., 2016, [A&A](#), **593**, L8

McMahon R. G., Banerji M., Gonzalez E., Kuposov S. E., Bejar V. J., Lodieu N., Rebolo R., VHS Collaboration 2013, *The Messenger*, **154**, 35

McNamara B. R., Nulsen P. E. J., 2012, [New Journal of Physics](#), **14**, 055023

Mejía-Restrepo J. E., Trakhtenbrot B., Lira P., Netzer H., Capellupo D. M., 2016, [MNRAS](#), **460**, 187

Mejía-Restrepo J. E., et al., 2022, [ApJS](#), **261**, 5

Mendez A. J., et al., 2016, [ApJ](#), **821**, 55

Merloni A., et al., 2014, [MNRAS](#), **437**, 3550

Monahan J. F., 2011, *Numerical Methods of Statistics*, 2 edn. Cambridge Series in Statistical and Probabilistic Mathematics, Cambridge University Press

Moran E. C., Barth A. J., Kay L. E., Filippenko A. V., 2000, [ApJ](#), **540**, L73

Moré J. J., 1978, in , Vol. 630, *Lecture Notes in Mathematics*, Berlin Springer Verlag. pp 105–116, [doi:10.1007/BFb0067700](#)

Morrison R., McCammon D., 1983, *ApJ*, 270, 119

Mountrichas G., Buat V., Georgantopoulos I., Yang G., Masoura V. A., Boquien M., Burgarella D., 2021, *A&A*, 653, A70

Mullaney J. R., et al., 2012, *ApJ*, 753, L30

Mushotzky R., 2004, in Barger A. J., ed., *Astrophysics and Space Science Library* Vol. 308, *Supermassive Black Holes in the Distant Universe*. p. 53 ([arXiv:astro-ph/0405144](https://arxiv.org/abs/astro-ph/0405144)), [doi:10.1007/978-1-4020-2471-9_2](https://doi.org/10.1007/978-1-4020-2471-9_2)

Nandra K., O'Neill P. M., George I. M., Reeves J. N., 2007, *MNRAS*, 382, 194

Nanni R., et al., 2018, *A&A*, 614, A121

Narayan R., 2005, *Ap&SS*, 300, 177

Nenkova M., Sirocky M. M., Ivezić Ž., Elitzur M., 2008, *ApJ*, 685, 147

Netzer H., 1990, in Blandford R. D., Netzer H., Woltjer L., Courvoisier T. J. L., Mayor M., eds, *Active Galactic Nuclei*. pp 57–160

Netzer H., 2015, *ARA&A*, 53, 365

Netzer H., Trakhtenbrot B., 2007, *ApJ*, 654, 754

Neufeld D. A., Maloney P. R., Conger S., 1994, *ApJ*, 436, L127

Oh K., et al., 2022, *ApJS*, 261, 4

Ordovás-Pascual I., et al., 2017, *MNRAS*, 469, 693

Osterbrock D. E., 1977, *ApJ*, 215, 733

Osterbrock D. E., 1981, *ApJ*, 249, 462

Padmanabhan N., et al., 2008, *ApJ*, 674, 1217

Padovani P., 2016, *A&ARv*, 24, 13

Padovani P., et al., 2017, *A&ARv*, 25, 2

Panessa F., et al., 2009, *MNRAS*, 398, 1951

Peterson B. M., Bentz M. C., 2006, *New Astron. Rev.*, 50, 796

Pineau F. X., Motch C., Carrera F., Della Ceca R., Derrière S., Michel L., Schwobe A., Watson M. G., 2011, *A&A*, 527, A126

Pogge R. W., Martini P., 2002, *ApJ*, 569, 624

Popović L. Č., 2003, *ApJ*, 599, 140

Press W. H., Flannery B. P., Teukolsky S. A., 1986, *Numerical recipes. The art of scientific*

computing

- Ramos Almeida C., Ricci C., 2017, *Nature Astronomy*, 1, 679
- Ramos Almeida C., et al., 2011, *ApJ*, 731, 92
- Ramos Almeida C., Martínez González M. J., Asensio Ramos A., Acosta-Pulido J. A., Hönig S. F., Alonso-Herrero A., Tadhunter C. N., González-Martín O., 2016, *MNRAS*, 461, 1387
- Ricci C., Ueda Y., Paltani S., Ichikawa K., Gandhi P., Awaki H., 2014, *MNRAS*, 441, 3622
- Ricci C., et al., 2017, *Nature*, 549, 488
- Ricci C., et al., 2023, *ApJ*, 959, 27
- Richards G. T., et al., 2002, *AJ*, 123, 2945
- Richards G. T., et al., 2006, *ApJS*, 166, 470
- Risaliti G., Elvis M., 2004, in Barger A. J., ed., *Astrophysics and Space Science Library* Vol. 308, *Supermassive Black Holes in the Distant Universe*. p. 187 ([arXiv:astro-ph/0403618](https://arxiv.org/abs/astro-ph/0403618)), [doi:10.1007/978-1-4020-2471-9_6](https://doi.org/10.1007/978-1-4020-2471-9_6)
- Rodríguez Martínez A. V., 2012, *Actualización de software : GUIspec*, <http://hdl.handle.net/10902/803>
- Rojas A. F., et al., 2020, *MNRAS*, 491, 5867
- Roseboom I. G., Lawrence A., Elvis M., Petty S., Shen Y., Hao H., 2013, *MNRAS*, 429, 1494
- Rosen S. R., et al., 2016, *A&A*, 590, A1
- Rovilos E., et al., 2014, *MNRAS*, 438, 494
- Sandoval B., et al., 2023, *arXiv e-prints*, p. [arXiv:2312.02311](https://arxiv.org/abs/2312.02311)
- Schmidt M., 1963, *Nature*, 197, 1040
- Schmidt M., Green R. F., 1983, *ApJ*, 269, 352
- Schnorr-Müller A., et al., 2016, *MNRAS*, 462, 3570
- Scholz F. W., Stephens M. A., 1987, *Journal of the American Statistical Association*, 82, 918
- Schulz S., Struck C., 2001, *MNRAS*, 328, 185
- Schutte Z., Reines A. E., Greene J. E., 2019, *ApJ*, 887, 245
- Schwartz D. A., et al., 2003, *New Astron. Rev.*, 47, 461
- Science Software Branch at STScI 2012, *PyRAF: Python alternative for IRAF*, *Astrophysics Source Code Library*, record [ascl:1207.011](https://ascl.net/1207.011)
- Selwood M., Calderone G., Fotopoulou S., Bremer M. N., 2023, *MNRAS*, 518, 130

Seyfert C. K., 1943, *ApJ*, 97, 28

Shang Z., Wills B. J., Wills D., Brotherton M. S., 2007, *AJ*, 134, 294

Shen S., Mo H. J., White S. D. M., Blanton M. R., Kauffmann G., Voges W., Brinkmann J., Csabai I., 2003, *MNRAS*, 343, 978

Shen Y., et al., 2011, *ApJS*, 194, 45

Shen Y., et al., 2016, *ApJ*, 831, 7

Shimizu T. T., et al., 2018, *ApJ*, 856, 154

Silva L., Maiolino R., Granato G. L., 2004, *MNRAS*, 355, 973

Skrutskie M. F., et al., 2006, *AJ*, 131, 1163

Smee S. A., et al., 2013, *AJ*, 146, 32

Spiegelhalter D. J., Best N. G., Carlin B. P., Van Der Linde A., 2002, *Journal of the Royal Statistical Society Series B: Statistical Methodology*, 64, 583

Stalevski M., Fritz J., Baes M., Nakos T., Popović L. Č., 2012, *MNRAS*, 420, 2756

Stern J., Laor A., 2012, *MNRAS*, 426, 2703

Stern D., et al., 2005, *ApJ*, 631, 163

Stoehr F., et al., 2008, in Argyle R. W., Bunclark P. S., Lewis J. R., eds, *Astronomical Society of the Pacific Conference Series Vol. 394, Astronomical Data Analysis Software and Systems XVII*. p. 505

Storey P. J., Zeppen C. J., 2000, *MNRAS*, 312, 813

Strüder L., et al., 2001, *A&A*, 365, L18

Suh H., et al., 2019, *ApJ*, 872, 168

Suh H., Civano F., Trakhtenbrot B., Shankar F., Hasinger G., Sanders D. B., Allevalo V., 2020, *ApJ*, 889, 32

Tody D., 1986, in Crawford D. L., ed., *Society of Photo-Optical Instrumentation Engineers (SPIE) Conference Series Vol. 627, Instrumentation in astronomy VI*. p. 733, [doi:10.1117/12.968154](https://doi.org/10.1117/12.968154)

Tozzi P., et al., 2006, *A&A*, 451, 457

Trakhtenbrot B., Netzer H., 2012, *MNRAS*, 427, 3081

Traulsen I., et al., 2019, *A&A*, 624, A77

Tremaine S., et al., 2002, *ApJ*, 574, 740

Trippe M. L., Crenshaw D. M., Deo R. P., Dietrich M., Kraemer S. B., Rafter S. E., Turner T. J., 2010, [ApJ](#), **725**, 1749

Tristram K. R. W., et al., 2007, [A&A](#), **474**, 837

Turner T. J., Miller L., 2009, [A&ARv](#), **17**, 47

Turner M. J. L., et al., 2001, [A&A](#), **365**, L27

Ueda Y., Akiyama M., Hasinger G., Miyaji T., Watson M. G., 2014, [ApJ](#), **786**, 104

Ulrich M.-H., Maraschi L., Urry C. M., 1997, [ARA&A](#), **35**, 445

Urry C. M., Padovani P., 1995, [PASP](#), **107**, 803

Van Dokkum P. G., 2001, [PASP](#), **113**, 1420

Verner E., Bruhweiler F., Johansson S., Peterson B., 2009, [Physica Scripta Volume T](#), **134**, 014006

Virtanen P., et al., 2020, [Nature Methods](#), **17**, 261

Vito F., et al., 2018, [MNRAS](#), **473**, 2378

Wang J.-M., Zhou Y.-Y., 1996, [ApJ](#), **469**, 564

Warren S. J., et al., 2007, [arXiv e-prints](#), pp astro-ph/0703037

Watson M. G., et al., 2001, [A&A](#), **365**, L51

Watson M. G., et al., 2009, [A&A](#), **493**, 339

Webb N. A., et al., 2020, [A&A](#), **641**, A136

Whittle M., 1992, [ApJS](#), **179**, 49

Winkler H., 1992, [MNRAS](#), **257**, 677

Winter L. M., Mushotzky R. F., Reynolds C. S., Tueller J., 2009, [ApJ](#), **690**, 1322

Wright E. L., et al., 2010, [AJ](#), **140**, 1868

Wysota A., Gaskell C. M., 1988, in Miller H. R., Wiita P. J., eds, , Vol. 307, Active Galactic Nuclei. pp 79–82, [doi:10.1007/3-540-19492-4_171](#)

XueGuang Z., 2023, [arXiv e-prints](#), p. [arXiv:2311.05138](#)

Yaqoob T., 1997, [ApJ](#), **479**, 184

Younger J. D., Hopkins P. F., Cox T. J., Hernquist L., 2008, [ApJ](#), **686**, 815

Yu Q., Lu Y., 2004, [ApJ](#), **602**, 603

Zou F., Yang G., Brandt W. N., Xue Y., 2019, [ApJ](#), **878**, 11